1 April 2011 | $10

Science

AAAS

Customized, Responsive, and On-Time.™

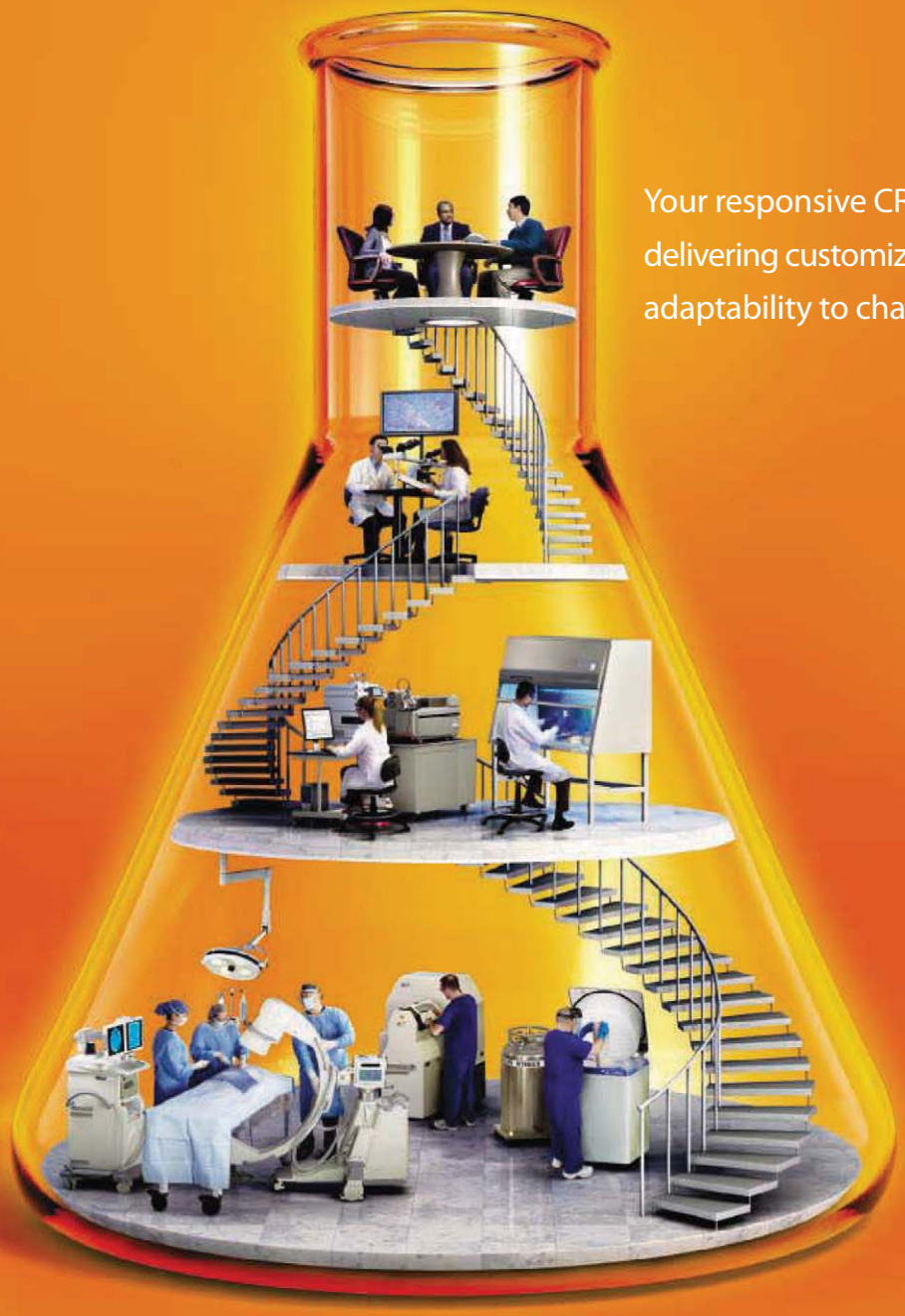

Your responsive CRO partner, delivering customized solutions and adaptability to changing needs.

MPI Research is the CRO that defines responsiveness, moving your drug development program forward with customized solutions for all your preclinical research and early clinical support needs. From discovery services to safety evaluation, including analytical and bioanalytical support, you can count on MPI Research for quick quotes, frequent updates, rapid turnaround, and scientific rigor. At every stage, and on every level, we adapt to your most exacting needs.

Explore the breadth of capabilities that make us your responsive CRO at www.MPIResearch.com.

MPI RESEARCH

Customized. Responsive. On-Time.™

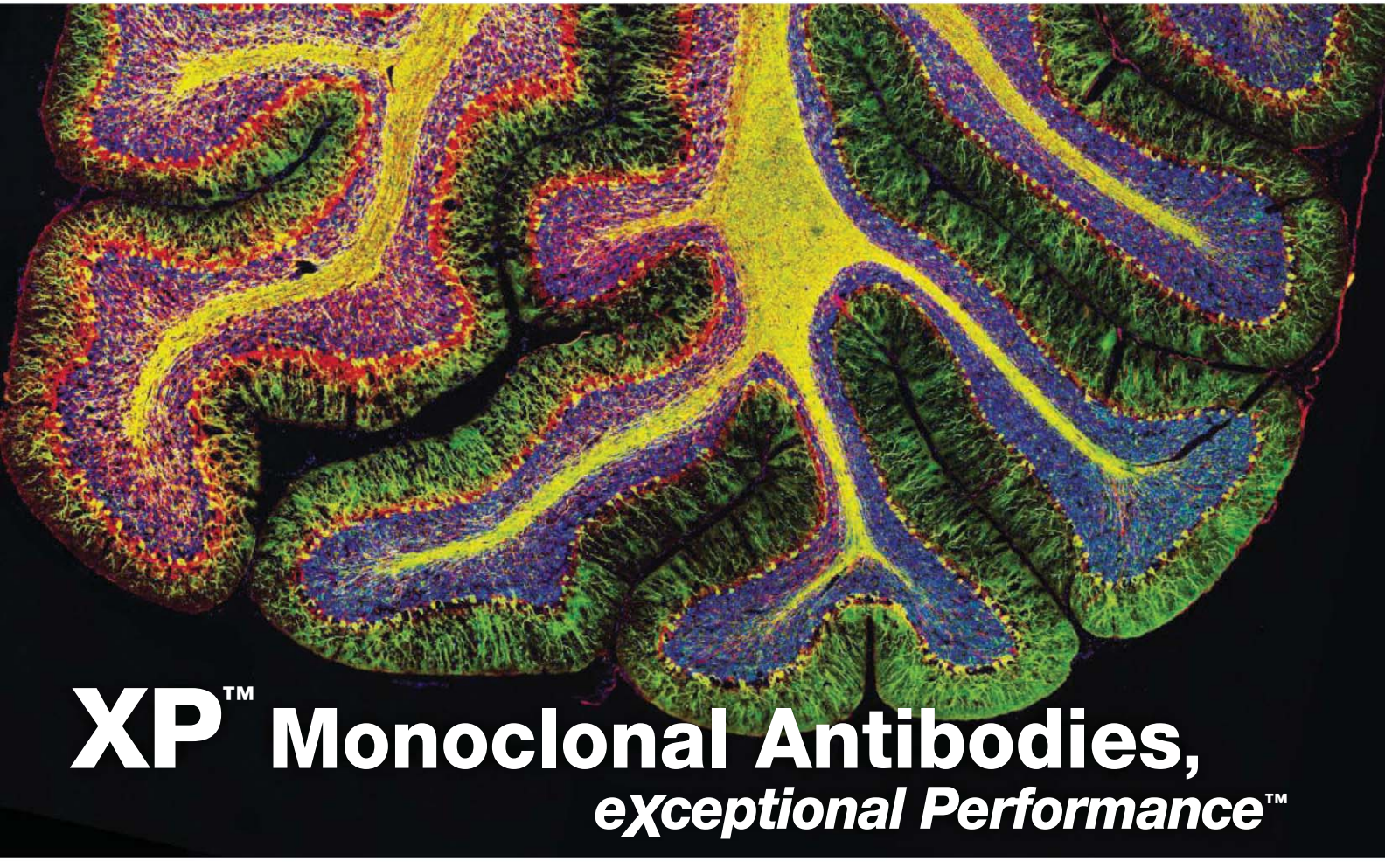

XP™ Monoclonal Antibodies, *eXceptional Performance™*

Unparalleled product quality, validation, and technical support.

XP™ monoclonal antibodies are a line of high quality rabbit monoclonal antibodies exclusively available from Cell Signaling Technology. Any product labeled with XP has been carefully selected based on superior performance in all approved applications.

XP monoclonal antibodies are generated using XMT™ Technology, a proprietary monoclonal method developed at Cell Signaling Technology. This technology provides access to a broad range of antibody-producing B cells unattainable with traditional monoclonal technologies, allowing more comprehensive screening and the identification of XP monoclonal antibodies.

eXceptional specificity
As with all of our antibodies, the antibody is specific to your target of interest, saving you valuable time and resources.

+ eXceptional sensitivity
The antibody will provide a stronger signal for your target protein in cells and tissues, allowing you to monitor expression of low levels of endogenous proteins, saving you valuable materials.

+ eXceptional stability and reproducibility
XMT Technology combined with our stringent quality control ensures maximum lot-to-lot consistency and the most reproducible results.

= eXceptional Performance™
XMT Technology coupled with our extensive antibody validation and stringent quality control delivers XP monoclonal antibodies with eXceptional Performance in the widest range of applications.

Above: Confocal IF analysis of rat cerebellum using β3-Tubulin (D71G9) XP™ Rabbit mAb #5568 (green) and Neurofilament-L (DA2) Mouse mAb #2835 (red). Blue pseudocolor = DRAQ5® #4084 (fluorescent DNA dye).

For additional information and a complete list of available XP™ Monoclonal Antibodies visit…

www.cellsignal.com

Cell Signaling TECHNOLOGY®

Orders (toll-free) 1-877-616-2355 | **Technical support** (toll-free) 1-877-678-8324 support@cellsignal.com | **Inquiries** info@cellsignal.com | **Environmental Commitment** eco.cellsignal.com

GE Healthcare
Life Sciences

Thank you ECL™ Plus, you've been great.

For every success there's a successor. It's called progress. So while we knew we had something special in Amersham™ ECL Plus, our Western blotting team was quietly working on the next generation of detection reagent. The result: a new substrate that operates with superior levels of sensitivity, signal intensity and stability than even its famous predecessor, making it an excellent choice for CCD imagers. **Welcome to ECL Prime.**

Signal intensity sustained at higher antibody dilutions

Ab dilution		**Amersham ECL Prime**		**Amersham ECL Plus**	
Primary	**Secondary**	10 µg	156 ng	10 µg	156 ng
1:3000	1:300 000				
1:10 000	1:500 000				

Comparison of Amersham ECL Prime and Amersham ECL Plus detection of ß-catenin in NIH 3T3 whole cell lysates using different dilutions of rabbit anti-ß-catenin and HRP-conjugated anti-rabbit IgG.

Find out more about Amersham ECL Prime at www.gelifesciences.com/eclprime

imagination at work

CONTENTS continued >>

page 28

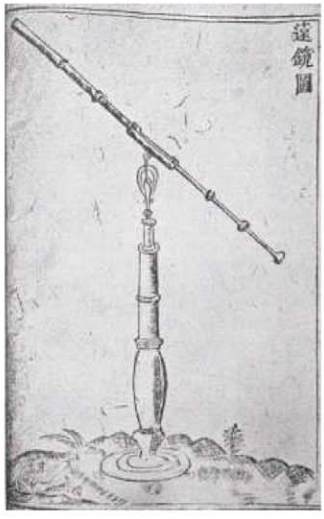

page 39

COVER

Adult sockeye salmon (weight ~2.5 kg; length ~60 cm) migrating to spawning grounds in the Adams River, British Columbia, Canada. Sockeye salmon populations in the Fraser River, British Columbia, are physiologically adapted to their specific upriver migration conditions. In a Report on page 109, Eliason *et al.* suggest that cardiac adaptations help protect one salmon population from cardiac collapse at high temperatures.

Photo: Robert Polo; robpolo.photography@gmail.com

DEPARTMENTS

Can't find the antibody you're looking for?

Let Abgent make it for you, FREE! After 10 years of manufacturing 15,000 antibodies, Abgent is giving away an unprecedented offer.

Why? Because finding the right antibody is difficult. If an antibody to a protein of interest isn't available to the scientific community, we'll start a custom project and add it to our pipeline. Together, we'll provide the research solutions the scientific community deserves. Submit your protein today!

Please visit http://www.abgent.com for complete promotion rules and to submit your protein of interest.

10239 Flanders Court, San Diego, CA 92121
Tel: (888) 735-7227 or (858) 622-0099

ABGENT

bioBAY
innovation comes home

BioBay provides total business solutions. As one of the largest biotech hubs hosting over 200 companies, we've built our dedicated, enthusiastic, and highly professional team to serve all needs for research tools innovation.

Abgent & BioBay - Partners in advancing research

RESEARCH ARTICLES

REPORTS

CONTENTS continued >>

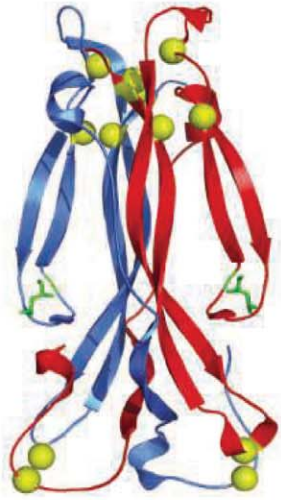

pages 47 & 65

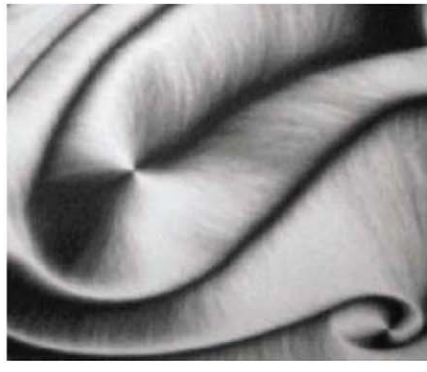

page 72

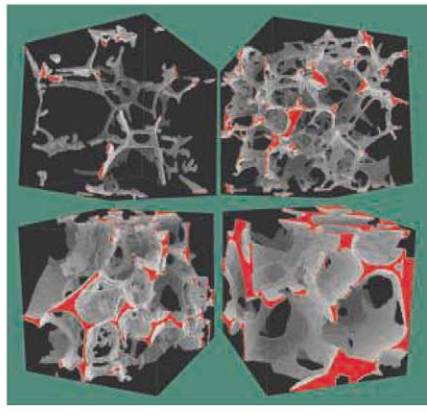

page 88

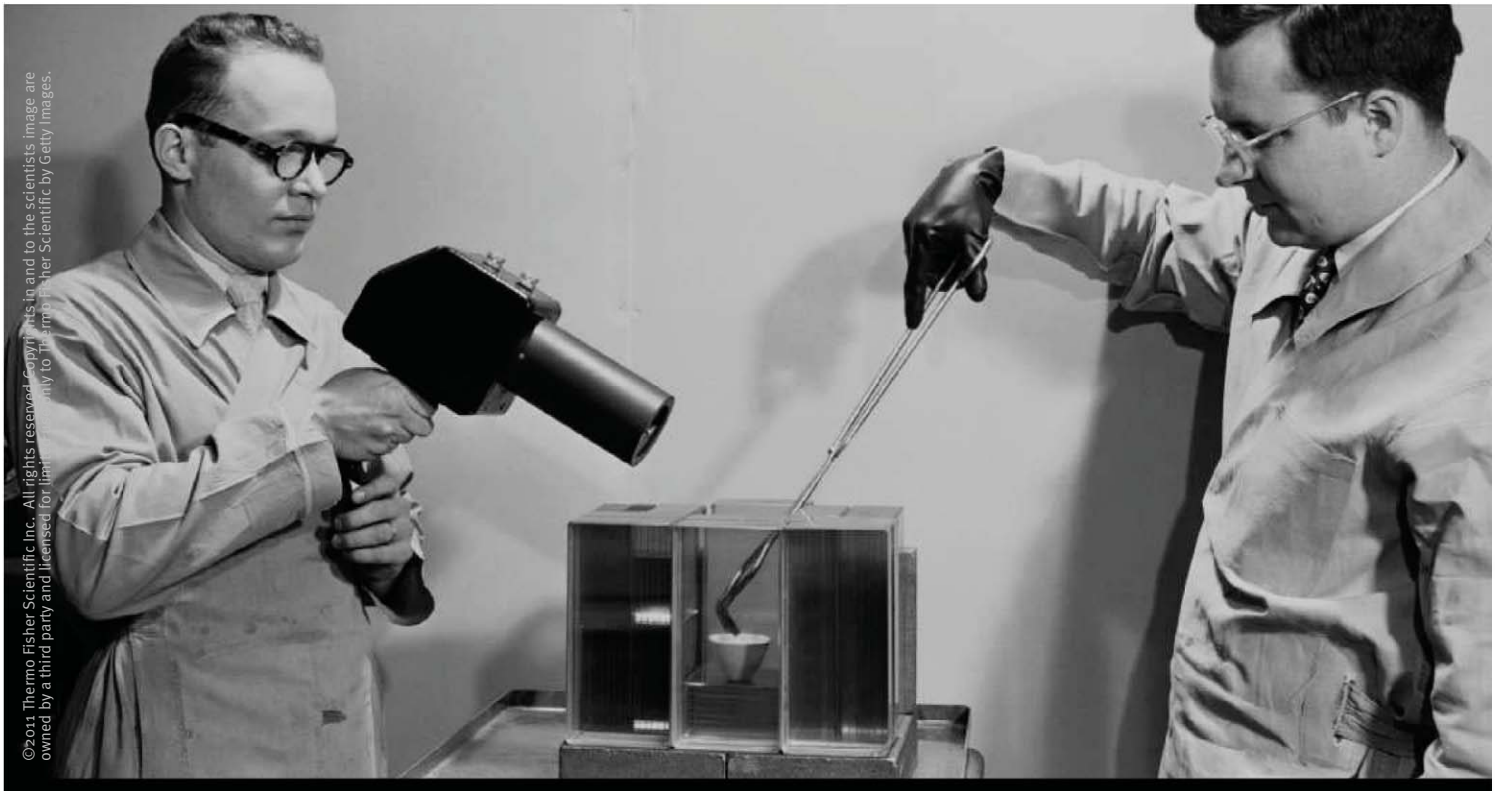

Limited by an outdated PCR system?

You can run 15 minute PCR protocols and use 50% less consumables and energy by getting away from the old standard. Choose Thermo Scientific Piko Thermal Cyclers, Phusion reagents, and ultra thin wall (UTW) plastic consumables for the most rapid and accurate PCR results. These technologically advanced components can be used individually to improve your current workflow, or as a complete solution for advanced PCR.

- Ultra fast PCR cycling protocols optimized to ‹15 minutes
- 96-well PCR runs using 50% less plastics, reagents and energy
- PCR kits that allow amplification directly from plant, blood, and tissue samples

Start your PCR experiment today
www.thermoscientific.com/advancedpcr

Everything for PCR
Thermo Scientific PCR portfolio has everything you need for successful PCR including industry leading reagents, high-quality instruments and trusted plastic consumables.

Moving science forward

Thermo SCIENTIFIC
Part of Thermo Fisher Scientific

SCIENCEONLINE

SCIENCEXPRESS
www.sciencexpress.org

Saturn's Curiously Corrugated C Ring
M. M. Hedman et al.
10.1126/science.1202238

The Impact of Comet Shoemaker-Levy 9 Sends Ripples Through the Rings of Jupiter
M. R. Showalter et al.
Spacecraft observations show that Saturn's and Jupiter's rings preserve records of recent interplanetary debris collisions.
10.1126/science.1202241

Topological Phase Transition and Texture Inversion in a Tunable Topological Insulator
S.-Y. Xu et al.
Two types of bulk insulator are realized in the same family of compounds through chemical doping.
10.1126/science.1201607

Protein Tyrosine Kinase Wee1B Is Essential for Metaphase II Exit in Mouse Oocytes
J. S. Oh et al.
Cyclin degradation is not the only mechanism that controls the exit of mouse oocytes from meiosis.
10.1126/science.1199211

Proteoglycan-Specific Molecular Switch for RPTPσ Clustering and Neuronal Extension
C. H. Coles et al.
One receptor binds two different types of proteoglycan at the same site but with divergent outcomes.
10.1126/science.1200840

SCIENCENOW
www.sciencenow.org
Highlights From Our Daily News Coverage

Damping Down Fear With Cortisol
The stress hormone enhances therapy to treat a phobia of heights.
http://scim.ag/less-fear

Sensing Organ Rejection
A new DNA test aims to detect when the body rejects a transplanted organ.
http://scim.ag/organ-test

Spinning the Sun's Rays Into Fuel
Artificial leaf makes fuel production possible wherever there's water.
http://scim.ag/sun-fuel

SCIENCESIGNALING
www.sciencesignaling.org
The Signal Transduction Knowledge Environment
29 March issue: http://scim.ag/ss29Mar2011

EDITORIAL GUIDE: Focus Issue—Rendering Resistance Futile
E. M. Adler and N. R. Gough
Understanding the pathways that mediate drug resistance is key to developing new cancer therapies.

RESEARCH ARTICLE: Amplification of the Driving Oncogene, *KRAS* or *BRAF*, Underpins Acquired Resistance to MEK1/2 Inhibitors in Colorectal Cancer Cells
A. S. Little et al.

PERSPECTIVE: Resistance to MEK Inhibitors—Should We Co-Target Upstream?
P. I. Poulikakos and D. B. Solit
Amplification of an upstream kinase in a three-kinase module confers resistance to cancer drugs that target a downstream kinase.

RESEARCH ARTICLE: c-MYC Suppresses BIN1 to Release Poly(ADP–ribose) Polymerase 1—A Mechanism by Which Cancer Cells Acquire Cisplatin Resistance
S. Pyndiah et al.

PERSPECTIVE: MYC, PARP1, and Chemoresistance—BIN There, Done That?
S. Ganesan
c-MYC promotes cisplatin resistance by enabling the increased activity of a DNA repair enzyme.

RESEARCH ARTICLE: Global Phosphoproteomics Reveals Crosstalk Between Bcr-Abl and Negative Feedback Mechanisms Controlling Src Signaling
L. Rubbi et al.

PODCAST
T. G. Graeber and A. M. VanHook
Negative feedback fails to limit Src family kinase activity in the presence of Bcr-Abl, an oncoprotein that drives leukemia.

SCIENCECAREERS
www.sciencecareers.org/career_magazine
Free Career Resources for Scientists

Experimental Error: Achieving Immortality
A. Ruben
How can we ensure that future students will read our names when, many years from now, they open their science textbooks on their iPad 15s?
http://scim.ag/jointhepantheon

Slipping Humor Into Scientific Presentations
E. Pain
Humor can be an added bonus in scientific talks, provided you know when and how to use it.
http://scim.ag/slippinghumor

SCIENCETRANSLATIONAL MEDICINE
www.sciencetranslationalmedicine.org
Integrating Medicine and Science
30 March issue: http://scim.ag/stm033011

COMMENTARY: The Precompetitive Space—Time to Move the Yardsticks
T. Norman et al.
A recent meeting of minds set into motion an open-access initiative designed to achieve proof of clinical mechanism for selected disease targets.

PERSPECTIVE: Human Pluripotent Stem Cells—Decoding the Naïve State
W. Li and S. Ding
Human stem cells exist in functionally distinct states that must be deciphered before these versatile reagents can be used to transform medicine.

RESEARCH ARTICLE: A MEK Inhibitor Abrogates Myeloproliferative Disease in *Kras* Mutant Mice
N. Lyubynska et al.
Inhibiting the Raf/MEK/ERK pathway reverses the harmful effects of oncogenic *Kras* on hematopoietic differentiation, suggesting a strategy for treating myeloproliferative neoplasms.

RESEARCH ARTICLE: Use of Mutant-Specific Ion Channel Characteristics for Risk Stratification of Long QT Syndrome Patients
C. Jons et al.
Mutations that slow the opening of potassium channels in the heart can predict risk for long QT syndrome, a heart arrhythmia that can cause sudden death.

SCIENCEPODCAST
www.sciencemag.org/multimedia/podcast
Free Weekly Show
On the 1 April *Science* Podcast: semiconductor nanocrystals, nonhuman rights, your Letters to *Science*, and more.

SCIENCEINSIDER
news.sciencemag.org/scienceinsider
Science Policy News and Analysis

SCIENCE (ISSN 0036-8075) is published weekly on Friday, except the last week in December, by the American Association for the Advancement of Science, 1200 New York Avenue, NW, Washington, DC 20005. Periodicals Mail postage (publication No. 484460) paid at Washington, DC, and additional mailing offices. Domestic individual membership and subscription (51 issues): $149 ($74 allocated to subscription). Domestic institutional subscription (51 issues): $990; Foreign postage extra: Mexico, Caribbean (surface mail) $55; other countries (air assist delivery) $85. First class, airmail, student, and emeritus rates on request. Canadian rates with GST available upon request, GST #1254 88122. Publications Mail Agreement Number 1069624. **Printed in the U.S.A.**

Change of address: Allow 4 weeks, giving old and new addresses and 8-digit account number. **Postmaster:** Send change of address to AAAS, P.O. Box 96178, Washington, DC 20090–6178. **Single-copy sales:** $10.00 current issue, $15.00 back issue prepaid includes surface postage; bulk rates on request. *Science* is indexed in the *Reader's Guide to Periodical Literature* and in several specialized indexes.

AAAS
ADVANCING SCIENCE, SERVING SOCIETY

EDITED BY STELLA HURTLEY

How Much Information Is Out There?

In the past 20 years, there have been dramatic changes in the world's ability to generate, communicate, and store information. **Hilbert and López** (p. 60, published online 10 February) conducted a survey of 60 categories of analog and digital technologies during the period from 1986 to 2007 and observed their changing contributions to global informational capacity. The capacity estimates took into account improvements in hardware performance and in software-based compression rates. The revolution in digital technology appears to have sustained an exponential increase in the global capacity to process information.

Genetics of Candidiasis

Chronic mucocutaneous candidiasis disease (CMCD) is characterized by chronic or recurring infection with *Candida albicans* and, to a lesser extent, with *Staphylococcus aureus*. The underlying cause of CMCD is unknown. **Puel *et al.*** (p. 65, published online 24 February; see the Perspective by **Dominguez-Villar and Hafler**) now report two genetic etiologies associated with CMCD. The first is an autosomal recessive mutation in interleukin 17 (IL-17) receptor A, which prevents its expression. The second is an autosomal dominant mutation in the cytokine IL-17F, which partially reduces its activity. Thus, human IL-17–mediated immunity is required for protection against these mucocutaneous infections.

Conservation: Learning from the Past

The consequences of climate change are now being taken seriously by conservation bodies and governments, just as information from fossil, historical, and present-day studies is providing new insights into how different species have responded, and could respond. **Dawson *et al.*** (p. 53) review evidence that points to a need to move beyond predictions based solely on niche models, because these models neglect many biological differences between species. The emerging challenges are to find alternative ways of anticipating and managing the biodiversity consequences of climate change and to build conservation actions around the natural mechanisms that have allowed species to persist through environmental changes in the past.

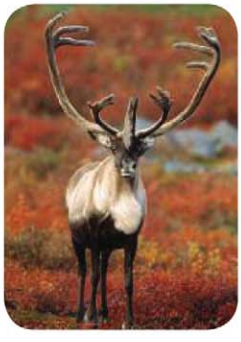

Down in the Valley >>

Breathtaking alpine landscapes illustrate the powerful nature of glacial erosion. The balance of climate-related forces on the topography and height of mountains is generally measured by the rate of erosion relative to the rate of uplift, but uncertainties related to field measurements compared to models have obscured the general mechanisms. **Shuster *et al.*** (p. 84) combined these two approaches on the mountains of Fiordland, New Zealand, to tease out these interrelationships. Isotopic dating suggests that erosion due to glacial activity removed most of the landscape that was older than 2.5 million years. Combined with a landscape evolution model, the results suggest that the modern topography of the region formed as the result of successive advances of erosion up valleys.

Cosmic Complications

Earth is constantly bombarded by cosmic rays—subatomic charged particles (mostly protons and helium nuclei) that are thought to be accelerated in the shock waves produced by stellar explosions. Using data from the satellite-borne PAMELA experiment, **Adriani *et al.*** (p. 69, published online 3 March) report spectral differences between protons and helium in cosmic rays. The results do not match predictions from models of cosmic-ray acceleration and their subsequent propagation through our Galaxy, suggesting that more complex processes need to be considered.

Charging Ahead

Polymerization resembles a chemical reaction run amok; instead of forming a single discrete product, reagents latch on to one of a slew of growing chains, which in turn can latch on to each other. Some semblance of order can be imposed in a so-called living process, in which catalysts or mediators keep all the chains in the system at more or less the same length throughout the growth period. **Magenau *et al.*** (p. 81) used electrochemistry to introduce a finer level of control. Varying an applied bias allowed for rapid modulation of the oxidation state of a copper polymerization catalyst through charge transfer. Because the catalyst is only active in one of the oxidation states, this modulation successively triggered and halted polymerization, facilitating precise control of chain structure.

The Melt Also Rises

The hot liquid rock that seeps out of mid-ocean ridges makes its way through the oceanic crust when the solid mantle below rises and depressurizes. Understanding the initial stages of melt formation and migration, however, has been based on indirect seismic measurements or limited experimental approaches. **Zhu *et al.*** (p. 88) collected three-dimensional images of melting mantle rocks using x-ray synchrotron microtomography. The images reveal the formation of an interconnected melt network at the scale of single mineral grains with a continuous increase of flow velocity of melt in partially molten rocks. Melt is thus extracted from the mantle as a function of the properties of the liquid (for example, viscosity and melt fraction) and not because of a shift in the porosity or permeability of the ocean crust.

Stress Relief

The reversible phosphorylation of proteins allows cells to adapt to sudden changes in their environment. **Tsaytler *et al.*** (p. 91, published online 3 March; see the Perspective by **Wiseman and Kelly**) describe a specific small-molecule inhibitor of a regulatory subunit of protein phosphatase 1, guanabenz. Guanabenz selectively bound to a regulatory subunit of protein phosphatase 1 and selectively disrupted the

stress-induced dephosphorylation of a subunit of translation initiation factor 2, thereby prolonging translation attenuation in stressed cells. This favored protein folding, promoting resistance to protein misfolding in the endoplasmic reticulum.

Molecular Motor

In most eukaryotes, spatial reorganization of the microtubule cytoskeleton during cell division depends crucially on microtubule cross-linking motors of the kinesin-5 family. **Roostalu *et al.*** (p. 94, published online 24 February) combined in vitro and in vivo experiments to examine Cin8, a mitotic kinesin-5 from budding yeast. Single fluorescent molecule imaging and microtubule-sliding assays on chemically functionalized surfaces, as well as in vivo imaging revealed that Cin8 is a bidirectional motor, unlike any other kinesins. Surprisingly, the "default directionality" of this motor was opposite to that of other kinesin-5 proteins. However, the motor was able to switch directionality, depending on whether it was working alone on individual microtubules or as a member of a team between antiparallel microtubules, like those found in the mitotic spindle. Cin8 may thus regulate directionality by sensing the motor-microtubule configuration.

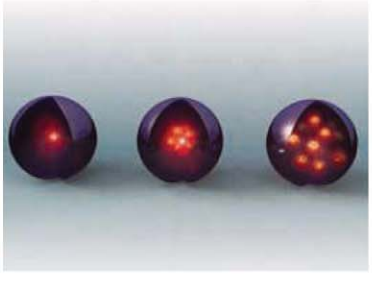

Nanoparticle Doping

The deliberate introduction of impurities into semiconducting materials is used to control their electrical properties and forms the basis of modern electronics. When considering nanometer-sized particles, the addition of only a few defect atoms can make the particle highly doped. However, forcing the foreign atoms into the nanoparticle is a challenge. **Mocatta *et al.*** (p. 77; see the Perspective by **Cao**) developed a method to add Cu, Ag, or Au impurities into InAs nanocrystals, which will be important in the fabrication of highly efficient, quantum dot–based electronic devices such as photovoltaic cells and light-emitting diodes.

Plant Ultraviolet Perception

Numerous plant photoreceptors act in the visible wavelengths of light. Now, **Rizzini *et al.*** (p. 103) report the discovery of a plant ultraviolet (UV)–B photoreceptor with distinctive mechanistic features. The plant UV-B photoreceptor, the *Arabidopsis* UVR8 protein, used a specifically positioned aromatic amino acid, tryptophan, as its chromophore. The UV-driven monomerization of UVR8 dimers signaled receptor activation. Furthermore, this plant UV perception system could be transplanted into yeast and mammalian cells.

Real-World Coevolution

In test-tube experiments using bacteria and their viruses, "arms races" evolve between hosts and parasites. **Gómez and Buckling** (p. 106) took genetically tagged bacteria and their respective phage and developed an experimental system in which soil microcosms containing a background microbial community were inoculated with the tagged microbes. Over time and locally in space, bacteria became resistant to coexisting phage. But resistance is more costly in terms of reproductive capacity in soil compared with the lab, and so the bacteria did not maintain resistance to past strains of phage. Similarly, neighboring strains of phage could not infect bacteria in other neighborhoods. Thus, in the wild, bacteria and phage rapidly coevolve.

It Takes Heart

The once-in-a-lifetime migration of sockeye salmon from the sea to their natal spawning grounds subject fish to extremely challenging physical conditions. These conditions are variable—fish that spawn in coastal tributaries have much easier journeys than those who traverse up-river for many weeks. **Eliason *et al.*** (p. 109) examined eight salmon populations that experienced a variety of migration conditions within the Fraser River in British Columbia, Canada. The fish with the most challenging journeys possessed the largest hearts and the best-developed cardiorespiratory system. Thus, local selective regimes have driven physiological adaptation to differing migratory conditions.

CREDIT: MOCATTA *ET AL.*

华大基因 BGI Premier Scientific Partner

Accurate Reliable Efficient

Sequencing

Accelerate Your Scientific Exploration

tech@genomics.cn www.genomics.cn

Locations: China (Mainland, Hong Kong), North America (Boston), Europe (Copenhagen)

When Science and the Media Mix

Christopher Reddy is a senior scientist and the director of the Coastal Ocean Institute, Woods Hole Oceanographic Institution, MA. E-mail: creddy@whoi.edu.

AS THE DEVASTATING IMPACTS OF JAPAN'S EARTHQUAKE AND TSUNAMI CONTINUE TO UNFOLD, AND concern over the Fukushima nuclear power plant grows, communication between scientists and the media has never been more vital. Fourteen years ago, journalist Jim Hartz and physicist Rick Chappell warned in their book *Worlds Apart: How the Distance Between Science and Journalism Threatens America's Future* that people are dangerously unenlightened about science's role in many aspects of life and society, in part because of the inability of scientists and journalists to understand each other. Today's relentless 24-hour media news cycle and blogosphere offer ample opportunities for both parties to provide politicians, policy-makers, and the public with scientific knowledge needed to inform their opinions and decisions. Yet the communication gap continues.

As a marine scientist who studies oil spills, I was in the fray after the Deepwater Horizon oil spill in the Gulf of Mexico last year. Journalists and scientists tried hard to communicate with each other, but I saw messages that were not delivered well to the media and/or misinterpreted by the media. In interviews, I made reference to my research on a 1969 oil spill in Falmouth, Massachusetts, which showed that oil continues to affect a small coastal marsh area, but did not anticipate many journalists' response: They extrapolated these remarks to infer potential dire, long-lasting impacts of the Gulf spill on marshes. I tried to restore perspective and reinforce that many oiled marshes have rebounded in the past, and that not all oil spills or coastal marshes are alike, but it was too late. That critical point was either missed or overlooked.

Such mistakes caused emotional damage to those living in the Gulf area, leaving people with more stress than knowledge. The research and impacts of the spill are still unfolding, and despite people's yearnings, there probably won't be quick or clear-cut answers. Nevertheless, this is no time for scientists to run back into the ivory tower and pull up the drawbridge. Scientists have to do a better job of communicating not just what they know, but also what they don't know, and what is uncertain. At their best, science and journalism both research exhaustively, discover knowledge, and communicate it accurately and objectively. For years, I have invited journalists to my laboratory to learn about field work and chemical analysis. We have defined terms, traded metaphors, and explained the perils and protocols of scholarly publishing and publishing for the public. Both parties have benefited. Journalists have come away with a greater appreciation of the research world and an increased ability to responsibly report to the public, and I have a better idea of the questions people want answers to.

How can scientists start to engage the media? Universities and colleges have press offices, but most scientists only interact with them when they have a high-profile manuscript or an inquiry from the press. However, the press office can be an invaluable conduit for explaining research to the media. In addition, scientists can reach out to general reporters and invite them into a conversation about the challenges that both parties face on a daily basis. Scientists also can encourage their institutional leaders to invest, even modestly, in outreach to the journalism community in the form of briefings, Web sites, and workshops. Fellowship programs such as those at the Woods Hole Oceanographic Institution, Marine Biological Laboratory, and the University of Rhode Island get journalists into laboratories and in the field alongside scientists for a week or more, experiences that are well worth the investment.

Communicating is risky, but not doing so is riskier. If scientists and journalists don't try harder and make continual efforts to learn each other's languages and gain confidence, knowledge will remain locked in laboratories, misunderstood, unused, or even worse, misused. When this happens, those who thirst for information are shortchanged, and the work of scientists becomes more of an interesting hobby than a critical endeavor of fundamental value to society.

– Christopher Reddy

10.1126/science.1205172

EDITED BY KRISTEN MUELLER AND JAKE YESTON

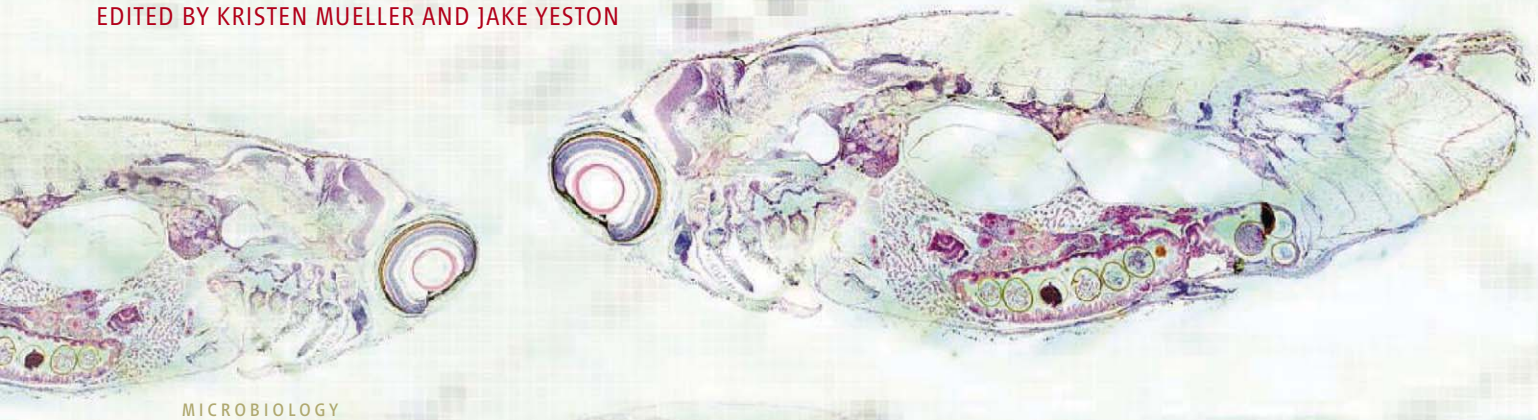

MICROBIOLOGY

TB Tolerance Exposed

One of the reasons tuberculosis (TB) continues to be a substantial public health problem is because the bacteria that cause TB, *Mycobacterium tuberculosis*, develop drug tolerance quickly. This requires patients to follow a 6-month-long drug regimen to ensure bacterial eradication, to which many patients fail to adhere. In order to identify new drug targets that may lead to shorter therapeutic regimens, Adams *et al*. dissected the development of drug tolerance in a zebrafish model of TB. Zebrafish infection with *Mycobacterium marinum* followed a similar disease course as human infection, which included the rapid development of drug tolerance. Multidrug-tolerant bacteria were present in macrophages just days after infection and were expanded and disseminated by granulomas. Bacteria acquired tolerance by replicating in macrophages, in both fish and mammalian cells. Upon infection, macrophages increased expression of bacterial efflux pumps, which can pump drugs out. Use of pump inhibitors demonstrated that these complexes mediated drug tolerance. Together, these studies suggest that adding efflux pump inhibitors to the standard TB therapies may be an effective way to reduce the course of treatment. — KLM

Cell **145**, 1 (2011).

BIOCHEMISTRY

How to Unwind

During DNA replication, ring-shaped helicases use energy from ATP hydrolysis to move along and separate DNA strands, creating space for new bases to be added to the emerging template. Initiation of replication in eukaryotes involves two key steps. First, the double hexamer Mcm2-7 helicase is loaded onto duplex DNA. Second, Cdc45 and GINS associate with each hexamer to form the active CMG helicase. To gain insight into these two steps, Costa *et al*. determined the structures of Mcm2-7 and the full CMG helicase by single-particle electron microscopy. Structural models of Mcm2-7 showed a ring that was open between Mcm2 and Mcm5 and could either be planar or form a slight spiral. The full helicase was constrained to the planar conformation, and GINS and Cdc45 bridged the gap to form a large channel. Imaging of CMG purified in the presence of an ATP analog revealed a conformational change induced by nucleotide binding; the gap between Mcm2 and Mcm5 closed and the channel was divided into two smaller pores. The tendency of Mcm2-7 to form open rings might facilitate loading onto duplex DNA. Upon binding of Cdc45 and GINS, the structural data are consistent with a model in which CMG promotes duplex opening and accommodates a single strand in each of its pores. The two helicases loaded onto DNA could then move apart, leaving the extruded DNA between them accessible for replication. — VV

Nat. Struct. Mol. Biol. **18**, 10.1038/nsmb.2004 (2011).

EDUCATION

Sizing Up Education Specialists

Attempts to include education training into already demanding science faculty schedules have been challenging. One solution is the introduction of Science Faculty with Education Specialties (SFES), scientists who take on education roles, into science departments. This may increase support for faculty development and innovation in teaching and increase departmental interest in research on teaching and learning. Minimal data are available on the purpose, structure, and outcomes of SFES, however. In order to learn more about these positions, Bush *et al*. surveyed SFES and non-SFES faculty members within the California State University System (CSU). Despite SFES existing across all science disciplines, faculty ranks, and CSU campuses, their role is still not well defined. SFES reported teaching the same amount as their non-SFES peers, and the same proportion of SFES reported being engaged in science education research as reported being engaged in basic science research. Although SFES had formal education training, the amount of actual training reported was minimal, which suggested that science departments still prefer to hire scientists trained in basic research. The majority of SFES thought that they are making a difference; however, almost 40% were considering leaving their positions because of concerns that their work in education was not supported, valued, or understood. — MM

CBE Life Sci. Educ. **10**, 25 (2011).

CELL BIOLOGY

A Less Toxic Treatment

Cells frequently tag proteins that are targeted for destruction by the proteasome with ubiquitin, a process that is important for maintaining cellular homeostasis and health. Besides defunct or aberrant cytosolic proteins, misfolded endoplasmic reticulum–derived proteins are "dislocated" back

CREDITS (TOP TO BOTTOM): ADAPTED FROM ADAMS *ET AL.*, *CELL* **145**, 1 (2011); ISTOCKPHOTOS.COM

into the cytosol, ubiquitinated, and degraded by the proteasome. Proteasome inhibitors that block various stages of these processes exist and are useful for studying this biological process, but are often quite toxic. Ernst *et al.* describe an alternative approach to interfere with the ubiquitin proteasome (UPS) pathway. A highly active ubiquitin-specific protease domain was used to remove ubiquitin preemptively from substrates about to be destroyed, and so stabilize them. The technique allowed the uncoupling of dislocation and degradation of endoplasmic reticulum–derived misfolded proteins. This approach efficiently and globally blocked the UPS pathway, but was less cytotoxic than commonly used pharmacological inhibitors. — SMH

PLOS Biol. **8**, e1000605 (2011).

NEUROSCIENCE

Obesity's Chicken or Egg

Altered reward circuitry in the brain may play a role in obesity. One change that has been observed is that overweight people have fewer dopamine D2 receptors in the brain striatum; however, it is unclear whether this is a cause or consequence of overeating. Stice *et al.* used functional magnetic resonance imaging to look at vulnerability to obesity by examining neural responses to food and related cues in high-risk though still-lean adolescents. They found that a corticostriatal network responded to food receipt, but not to anticipation of food-related cues, more strongly in these high-risk people. A related network in high-risk individuals also responded more to the receipt of money. These people also showed greater activation of the oral regions of the somatosensory cortex in response to palatable food intake, a result specific for food rather than money. Thus, youths at risk for obesity initially had a generally elevated reward region responsivity. When coupled with an increased responsivity of oral somatosensory regions, this may result in overeating that subsequently produces dopamine receptor down-regulation and elevated incentive salience of food cues. — PRS

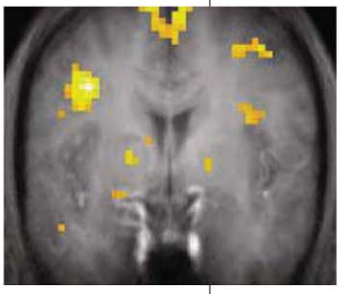

CREDIT: STICE *ET AL.*, *J. NEUROSCI.* **31**, 4360 (2011)

J. Neurosci. **31**, 4360 (2011).

GEOLOGY

Records in the River

The expansion of agriculture, mills, and deforestation after colonial settlement of eastern North America expanded erosion and greatly affected the hydrology of streams and rivers. However, Native Americans had been practicing agriculture and forest management for several centuries before that. Stinchcomb *et al.* show that river hydrology was modified by, and so records, this history as well. They focused on the Delaware River Valley, where artifacts show widespread settlement from about 1100 to 1600 CE, including expansion of maize agriculture and forest clearing. Carbon isotope, radiocarbon dating, and phytolith analyses document the increase in maize and other grasses. Analysis of sediments shows increased sedimentation during this interval in stream valleys and also an increase in flooding. Together, the data imply that perhaps half of the surrounding forests were cleared in the local floodplain. Flooding may have been further augmented by cooler and wetter conditions from 1450 to 1530 CE. Thus, pre-Columbian agriculture and deforestation also left a marked sedimentary record, at least locally in North America. — BH

Geology **39**, 363 (2011).

PHYSICS

Complex Quantum Simulation

Interactions between the charge, spin, and orbital degrees of freedom of electrons in condensed-matter systems can give rise to many complex electronic and magnetic phases. The narrow, or often fixed, range of variable materials parameters can be a limitation in probing and understanding the evolution of the order parameters of such complex correlated systems. An array of atoms trapped in an optical lattice has the potential to be extremely flexible in terms of tuning the parameters. Although the atoms tend to be isotropic, leading to somewhat trivial systems, much theoretical work has explored the possibilities of finding ways to imprint and detect more complicated order parameters on the lattice of trapped atoms. It is along such lines that Kitagawa *et al.* propose a spectroscopic technique based on two-particle interferometry that probes the phase-sensitive correlations between atom-atom interactions across the lattice. They show that the technique should allow the measurement of nontrivial order parameters in entangled ensembles of cold atoms, such as d- or p-wave pairing of electrons found in exotic superconductors and superfluids, and the realization of cold-atom systems that function as complex quantum simulators. — ISO

Phys. Rev. Lett. **106**, 115302 (2011).

www.sciencemag.org

Science

1200 New York Avenue, NW
Washington, DC 20005
Editorial: 202-326-6550, FAX 202-289-7562
News: 202-326-6581, FAX 202-371-9227
Bateman House, 82-88 Hills Road
Cambridge, UK CB2 1LQ
+44 (0) 1223 326500, FAX +44 (0) 1223 326501

Subscription Services For change of address, missing issues, new orders and renewals, and payment questions: 866-434-AAAS (2227) or 202-326-6417, FAX 202-842-1065. Mailing addresses: AAAS, P.O. Box 96178, Washington, DC 20090-6178 or AAAS Member Services, 1200 New York Avenue, NW, Washington, DC 20005

Institutional Site Licenses please call 202-326-6755 for any questions or information

Reprints: Author Inquiries 800-635-7181
Commercial Inquiries 803-359-4578

Permissions 202-326-7074, FAX 202-682-0816

Member Benefits AAAS/Barnes&Noble.com bookstore www.aaas.org/bn; AAAS Online Store www.apisource.com/aaas/ code MKB6; AAAS Travels: Betchart Expeditions 800-252-4910; Apple Store www.apple.com/eppstore/aaas; Bank of America MasterCard 1-800-833-6262 priority code FAA3YU; Cold Spring Harbor Laboratory Press Publications www.cshlpress.com/affiliates/aaas.htm; GEICO Auto Insurance www.geico.com/landingpage/go51.htm?logo=17624; Hertz 800-654-2200 CDP#343457; Office Depot https://bsd.officedepot.com/portalLogin.do; Seabury & Smith Life Insurance 800-424-9883; Subaru VIP Program 202-326-6417; VIP Moving Services www.vipmayflower.com/domestic/index.html; Other Benefits: AAAS Member Services 202-326-6417 or www.aaasmember.org.

science_editors@aaas.org	(for general editorial queries)
science_letters@aaas.org	(for queries about letters)
science_reviews@aaas.org	(for returning manuscript reviews)
science_bookrevs@aaas.org	(for book review queries)

Published by the American Association for the Advancement of Science (AAAS), *Science* serves its readers as a forum for the presentation and discussion of important issues related to the advancement of science, including the presentation of minority or conflicting points of view, rather than by publishing only material on which a consensus has been reached. Accordingly, all articles published in *Science*—including editorials, news and comment, and book reviews—are signed and reflect the individual views of the authors and not official points of view adopted by AAAS or the institutions with which the authors are affiliated.

AAAS was founded in 1848 and incorporated in 1874. Its mission is to advance science, engineering, and innovation throughout the world for the benefit of all people. The goals of the association are to: enhance communication among scientists, engineers, and the public; promote and defend the integrity of science and its use; strengthen support for the science and technology enterprise; provide a voice for science on societal issues; promote the responsible use of science in public policy; strengthen and diversify the science and technology workforce; foster education in science and technology for everyone; increase public engagement with science and technology; and advance international cooperation in science.

Information for Authors
See pages 784 and 785 of the 11 February 2011 issue or access www.sciencemag.org/about/authors

EDITOR-IN-CHIEF **Bruce Alberts**
EXECUTIVE EDITOR **Monica M. Bradford**
NEWS EDITOR **Colin Norman**
MANAGING EDITOR, RESEARCH JOURNALS **Katrina L. Kelner**
DEPUTY EDITORS **R. Brooks Hanson, Barbara R. Jasny, Andrew M. Sugden**

Editorial senior editors/commentary Lisa D. Chong, Brad Wible; **senior editors** Gilbert J. Chin, Pamela J. Hines, Paula A. Kiberstis (Boston), Marc S. Lavine (Toronto), Beverly A. Purnell, L. Bryan Ray, Guy Riddihough, H. Jesse Smith, Phillip D. Szuromi (Tennessee), Valda Vinson, Jake S. Yeston; **associate editors** Kristen L. Mueller, Jelena Stajic, Sacha Vignieri, Nicholas S. Wigginton, Laura M. Zahn (San Diego); **book review editor** Sherman J. Suter; **associate letters editor** Jennifer Sills; **editorial manager** Cara Tate; **senior copy editors** Jeffrey E. Cook, Cynthia Howe, Harry Jach, Lauren Kmec, Barbara P. Ordway, Trista Wagoner; **copy editor** Chris Filiatreau; **editorial coordinators** Carolyn Kyle, Beverly Shields; **publications assistants** Ramatoulaye Diop, Joi S. Granger, Emily Guise, Jeffrey Hearn, Michael Hicks, Lisa Johnson, Scott Miller, Jerry Richardson, Brian White, Anita Wynn; **editorial assistants** Emily C. Horton, Patricia M. Moore; **executive assistant** Alison Crawford; **administrative support** Maryrose Madrid; **editorial fellow** Melissa R. McCartney

Editorial director, web and new media Stewart Wills; **senior web editor** Tara S. Marathe; **web editor** Robert Frederick; **research associate** Corinna Cohn; **web development manager** Martyn Green; **web developer** Andrew Whitesell

News deputy news editors Robert Coontz, David Grimm (Online), Eliot Marshall, Jeffrey Mervis, Leslie Roberts; **contributing editors** Elizabeth Culotta, Polly Shulman; **news writers** Yudhijit Bhattacharjee, Adrian Cho, Jennifer Couzin-Frankel, Jocelyn Kaiser, Richard A. Kerr, Eli Kintisch, Greg Miller, Elizabeth Pennisi, Lauren Schenkman, Robert F. Service (Pacific NW), Erik Stokstad; **web developer** Daniel Berger; **intern** Sara Reardon; **contributing correspondents** Jon Cohen (San Diego, CA), Daniel Ferber, Ann Gibbons, Sam Kean, Andrew Lawler, Mitch Leslie, Charles C. Mann, Virginia Morell, Gary Taubes; **copy editors** Linda B. Felaco, Melvin Gatling, Melissa Raimondi; **administrative support** Scherraine Mack; **bureaus** San Diego, CA: 760-942-3252, FAX 760-942-4979; Pacific Northwest: 503-963-1940

Production director Wendy K. Shank; **assistant manager** Rebecca Doshi; **senior specialists** Steve Forrester, Chris Redwood, Anthony Rosen; **Preflight director** David M. Tompkins; **manager** Marcus Spiegler; **specialist** Jason Hillman

Art director Yael Fitzpatrick; **associate art director** Laura Creveling; **senior illustrators** Chris Bickel, Katharine Sutliff; **illustrator** Yana Hammond; **senior art associates** Holly Bishop, Preston Huey, Nayomi Kevitiyagala, Matthew Twombly; **art associate** Kay Engman; **photo editor** Leslie Blizard

***Science* International**

Europe (science@science-int.co.uk) **editorial: international managing editor** Andrew M. Sugden; **senior editor/commentary** Julia Fahrenkamp-Uppenbrink; **senior editors** Caroline Ash, Stella M. Hurtley, Ian S. Osborne, Peter Stern; **associate editor** Maria Cruz; **locum editor** Helen Pickersgill; **editorial support** Samantha Hogg, Alice Whaley; **administrative support** John Cannell, Janet Clements, Louise Hartwell; **news: europe news editor** John Travis; **deputy news editor** Daniel Clery; **contributing correspondents** Michael Balter (Paris), John Bohannon (Vienna), Martin Enserink (Amsterdam and Paris), Gretchen Vogel (Berlin); **intern** Jennifer Carpenter

Latin America contributing correspondent Antonio Regalado

Asia Japan Office: Asca Corporation, Tomoko Furusawa, Rustic Bldg. 7F, 77 Tenjin-cho, Shinjuku-ku, Tokyo 162-0808, Japan; +81 3 6802 4616, FAX +81 3 6802 4615, inquiry@sciencemag.jp; **asia news editor** Richard Stone (Beijing: rstone@aaas.org); **contributing correspondents** Dennis Normile [Japan: +81 (0) 3 3391 0630, FAX +81 (0) 3 5936 3531; dnormile@gol.com]; Hao Xin [China: cindyhao@gmail.com]; Pallava Bagla [South Asia: +91 (0) 11 2271 2896; pbagla@vsnl.com]

EXECUTIVE PUBLISHER **Alan I. Leshner**
PUBLISHER **Beth Rosner**

Fulfillment Systems and Operations (membership@aaas.org); **customer service supervisor** Pat Butler; **specialists** Latoya Casteel, LaVonda Crawford, Vicki Linton, April Marshall; **data entry supervisor** Cynthia Johnson; **specialists** Shirlene Hall, Tarrika Hill, William Jones

Business Operations and Administration director Deborah Rivera-Wienhold; **business systems and financial analysis director** Randy Yi; **manager, business analysis** Eric Knott; **manager, business operations** Jessica Tierney; **financial analysts** Priti Pamnani, Celeste Troxler; **rights and permissions: administrator** Emilie David; **associate** Elizabeth Sandler; **marketing director** Ian King; **marketing managers** Allison Pritchard, Alison Chandler, Julianne Wielga; **marketing associates** Aimee Aponte, Mary Ellen Crowley, Wendy Wise; **senior marketing executive** Jennifer Reeves; **director, site licensing** Tom Ryan; **director, corporate relations** Eileen Bernadette Moran; **publisher relations, eresources specialist** Kiki Forsythe; **senior publisher relations specialist** Catherine Holland; **publisher relations, east coast** Phillip Smith; **fulfillment supervisor** Iquo Edim; **marketing manager** Christina Schlecht; **marketing associate** Laura Tutino; **electronic media: director** Lizabeth Harman; **project manager** Trista Snyder; **assistant manager** Lisa Stanford; **senior production specialists** Ryan Atkins, Christopher Coleman, **computer specialist** Walter Jones, Kai Zhang; **production specialists** Antoinette Hodal, Nichele Johnston, Kimberly Oster; **director, web and new media** Will Collins

advertising director, worldwide ad sales Bill Moran
commercial editor Sean Sanders: 202-326-6430
assistant commercial editor Tianna Hicklin 202-326-6463

Product (science_advertising@aaas.org); **midwest** Rick Bongiovanni: 330-405-7080, FAX 330-405-7081; **east coast/e. canada** Laurie Faraday: 508-747-9395, FAX 617-507-8189; **west coast/w. canada** Lynne Stickrod: 415-931-9782, FAX 415-520-6940; **uk/europe/asia** Roger Goncalves: TEL/FAX +41 43 243 1358; **japan** ASCA Corporation, Makiko Hara: +81 (0) 3 6802 4616, FAX +81 (0) 3 6802 4615; ads@sciencemag.jp; **china/taiwan** Ruolei Wu: +86 1367 1015 294 rwu@aaas.org

worldwide associate director of *Science* Careers Tracy Holmes: +44 (0) 1223 326525, FAX +44 (0) 1223 326532

Classified (advertise@sciencecareers.org); **u.s.: midwest/west coast/south central/canada** Tina Burks: 202-326-6577; **east coast/industry** Elizabeth Early: 202-326-6578; **sales administrator:** Marci Gallun **sales coordinators** Shirley Young; **europe/row sales:** Susanne Kharraz, Dan Pennington, Alex Palmer; **sales assistant** Lisa Patterson; **japan** ASCA Corporation, Jie Chin +81 (0) 3 6802 4616, FAX +81 (0) 3 6802 4615; careerads@sciencemag.jp; **china/taiwan** Ruolei Wu: +86 1367 1015 294 rwu@aaas.org; **advertising support manager** Karen Foote: 202-326-6740; **advertising production operations manager** Deborah Tompkins; **senior production specialist/graphic designer** Amy Hardcastle; **production specialist** Yuse Lajiminmuhip; **senior traffic associate** Christine Hall

AAAS Board of Directors retiring president, chair Alice Huang; **president** Nina Fedoroff; **president-elect** William Press; **treasurer** David E. Shaw; **chief executive officer** Alan I. Leshner; **board** Nancy Knowlton, Stephen Mayo, Raymond Orbach, Julia M. Phillips, Sue V. Rosser, David D. Sabatini, Inder Verma, Thomas A. Woolsey

AAAS
ADVANCING SCIENCE, SERVING SOCIETY

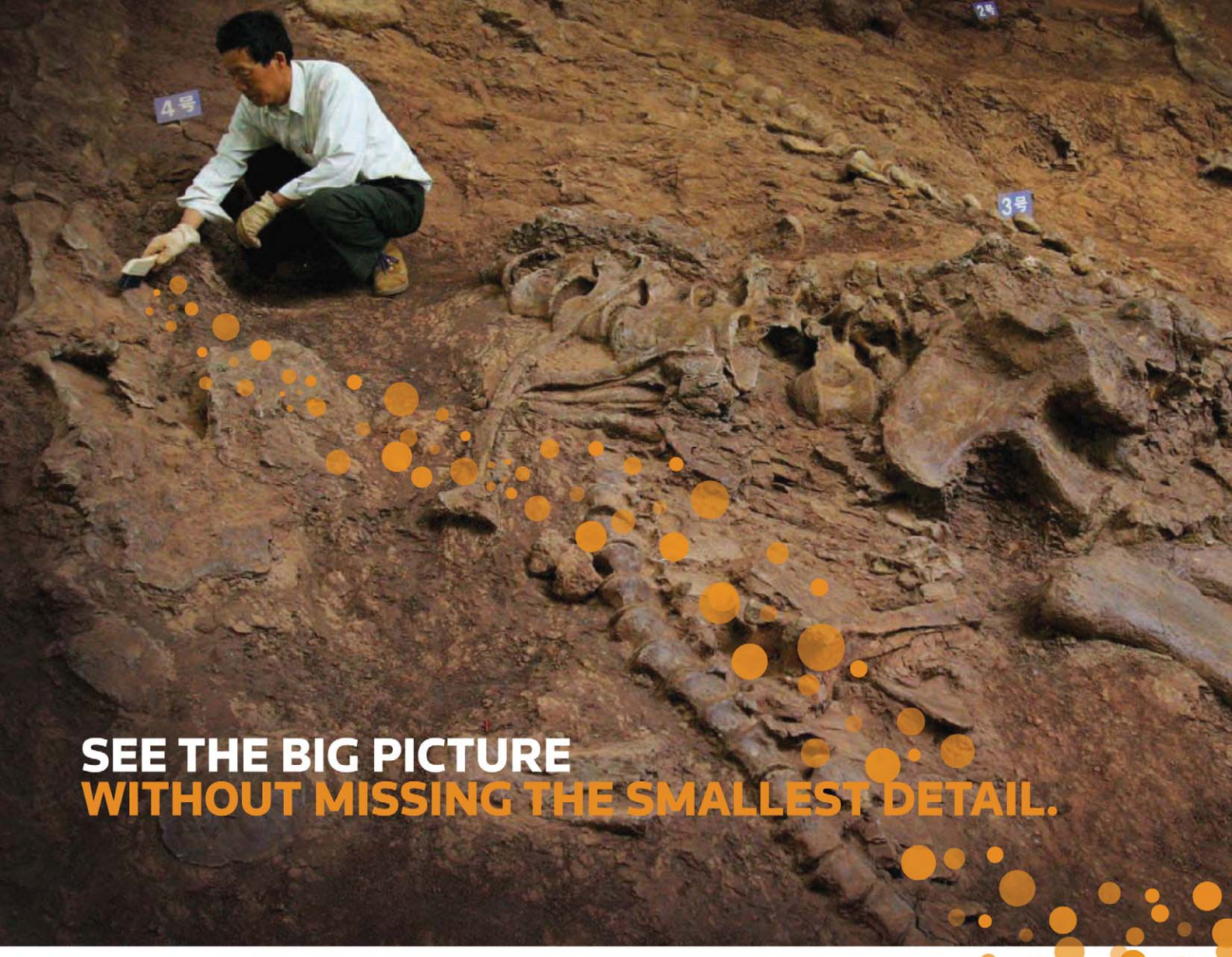

SEE THE BIG PICTURE
WITHOUT MISSING THE SMALLEST DETAIL.

INTRODUCING THE NEW *WEB OF KNOWLEDGE*

The next generation of *Thomson Reuters Web of Knowledge*℠ has arrived. With new features, enhanced functionality, and additional content, it's everything you've been searching for. The streamlined interface and more precise search options ensure you will find all the information related to your topic — quickly and efficiently. And with powerful analysis tools, you can spend less time digging into the details and more time focusing on the big picture.

DISCOVERY STARTS HERE: TheNewWok.com

THOMSON REUTERS™

AROUND THE WORLD

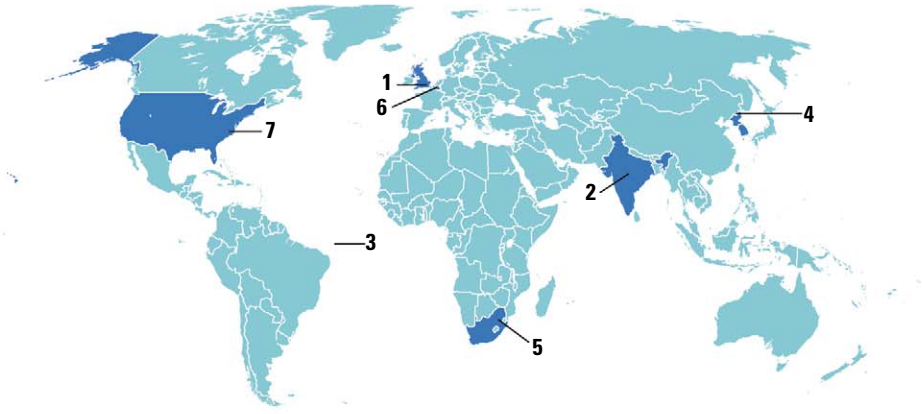

London **1**

Budget Boosts Science, Slightly

The United Kingdom's budget for 2011–12, announced last week, has a modicum of good news for scientists. Spending on capital projects got a £100 million boost, softening the cuts in last year's comprehensive spending review. In the life sciences, £44 million will go to the Babraham Research Campus near Cambridge and £26 million will go to Norwich Research Park. In the physical sciences, £10 million will fund new instruments for the ISIS spallation neutron source at the Rutherford Appleton Laboratory and a further £10 million will support the development of next-generation particle accelerators for medical and security scanning applications at the Daresbury Laboratory. Yet another £10 million will fund a new National Space Technology Program.

The budget also creates a new health research regulatory agency to streamline regulation and improve the cost effectiveness of clinical trials. Imran Khan, director of the Campaign for Science and Engineering, welcomed the new money, but warned that "labs across the country are going to be struggling to make ends meet."
http://scim.ag/uk-budget

India **2**

Tiger Numbers Up? Maybe

India is boasting about a 12% increase in the country's adult tiger population, but some tiger experts think the numbers don't add up. India today accounts for almost 60% of the world's wild tigers. A 2006 survey estimated that the country housed 1165 to 1657 tigers. The latest survey counts 1571 to 1875 tigers, including 100 tigers that were found in areas not covered during the last survey. However, tigers are now squeezed into 72,000 square kilometers, a range that has shrunk 20,800 square kilometers in 5 years.

These numbers, released earlier this week by India's environment minister Jairam Ramesh, come from a massive 18-month, $2.1 million survey that involved 800 camera traps and 476,000 people walking 625,000 kilometers looking for scat and other signs of tigers.

One expert called the results "very encouraging," but P. K. Sen, former director of the government-sponsored conservation initiative Project Tiger, called the new figures "statistical jugglery." "The habitat of the tiger has only shrunk, poaching has increased, and conservation has been diluted, so how can the numbers of tigers increase?" he says. **http://scim.ag/tiger-survey**

South Atlantic Ocean **3**

Once Again Into the Depths

In a determined effort to retrieve the flight recorders from a doomed 2009 flight, oceanographers working with French authorities are this week sending three state-of-the-art submersibles to scour the sea floor about 500 kilometers off Brazil's northeast coast. Three previous attempts to locate the downed Airbus A 330 of Air France Flight 447, including last year's by this same group from the Woods Hole Oceanographic Institution (WHOI) in Massachusetts, have failed.

The team will spend more than 3 months canvassing an area of 10,000 square kilometers, the size of Delaware and Rhode Island combined. Using sonar, each REMUS 6000 autonomous underwater vehicle (AUV) can crudely image a swath of sea floor just 1.2 kilometers wide while skimming the bottom at 5 kilometers per hour. But the AUVs can operate simultaneously and independently for up to 20 hours before returning to the mother ship to dump their data.

Oceanographers must then identify what might be a crumpled or even dismembered plane on the rocky, rugged bottom of the Mid-Atlantic Ridge and send an AUV back to take close-up photographs. WHOI researchers are hopeful of success; they've been studying that ridge for 30 years.

Mount Paektu, North Korean–Chinese Border **4**

Two Koreas Explore Volcanic Détente

Koreans cherish Mount Paektu on the North Korean–Chinese border as the birthplace of their nation. Now the venerated volcano has inspired a rare attempt at scientific partnership on the divided peninsula.

About 1000 years ago, Mount Paektu disgorged up to 30 cubic kilometers of magma—10 times as much as Krakatoa did in 1883. Smaller eruptions have occurred roughly every century since, until 1903. Mount Paektu's plumbing rumbled anew several years ago, but the volcano did not

NOTED

>If your favorite American college basketball team is in a slump, try the "Tweet 16." Cornell University's Lab of Ornithology has launched its own March Migration Madness, a Facebook popularity tournament featuring North American birds (http://scim.ag/tweet-16). The bald eagle, beloved of Americans, was left out: "We didn't want anyone to be conflicted about voting for or against our national symbol," the lab's Web site says.

CREDIT: PALLAVA BAGLA


Mount Paektu's caldera.

erupt, and since 2005 it has been largely quiet (*Science*, 30 July 2010, p. 498).

A few days after the Tohoku earthquake struck Japan on 11 March, North Korea's earthquake bureau floated the idea of a North-South project on Mount Paektu's hazards. As a result, at a highly symbolic 29 March meeting at the border village of Munsan, three scientists with North Korea's Institute of Paektu-san Volcano and four South Korean counterparts agreed to begin work on a joint research agenda.

Johannesburg, South Africa **5**

End to Partnership With Israeli University

The faculty senate of the University of Johannesburg in South Africa voted last week to terminate a collaborative research agreement on water pollution studies with its 25-year research partner, the Ben Gurion University of the Negev (BGU) in Be'er Sheva, Israel. Proponents of an international academic campaign to sever ties with Israeli researchers hailed the step as a "boycott." But University of Johannesburg Vice Chancellor and Principal Ihron Rensberg rejected the term, saying "peer-to-peer" collaborations could continue.

A petition circulated by pro-boycott supporters before the vote refers to BGU's "complicity in Israeli apartheid"—its failure to involve Palestinians in research projects—and "its direct and deliberate collaboration with the Israeli Defense Force," a reference to BGU's scholarships for military personnel. About 400 South African academics endorsed the petition.

The Jerusalem Post reported that BGU issued a statement calling the petition "a collection of lies and mistruths about BGU and the State of Israel," adding that "it would be unfortunate to cancel a research agreement that is meant solely to improve the quality of life for the residents of South Africa." **http://scim.ag/SA-Israel**

Brussels **6**

Europe Nudges Top Scientists to Market

Some of Europe's top scientists will get financial help to take their discoveries to the marketplace. The European Research Council (ERC), the European Union's funding program for frontier research, will offer scientists it already funds the chance to apply for €150,000 "Proof of Concept" grants. Researchers can use the funds to clarify intellectual property questions, do market research, and team up with venture capitalists, according to a 25 March announcement.

The idea grew out of the ERC Scientific Council's efforts to build better relations with industry, says ERC President and Scientific Council Chair Helga Nowotny. Although ERC grants are open to company scientists, "We have very, very few apply," she says. "Hopefully, where the potential is there, someone [from industry] will pick up on it."

Peter Tindemans, a Dutch physicist and E.U. science policy expert, welcomed the new grants. "The combination of the ERC focusing on very high scientific originality and quality—and stimulating people to think about what it might mean for society? I think it's a very good development," he says.

THEY SAID IT

"Now I know why they went extinct! Nature abhors a vacuum."

—Kirt, one of our online readers, who commented on a story about plant-eating sauropod dinosaurs and their improbably long necks. To find out "How a Dinosaur Is Like a Vacuum Cleaner," see p. 21.

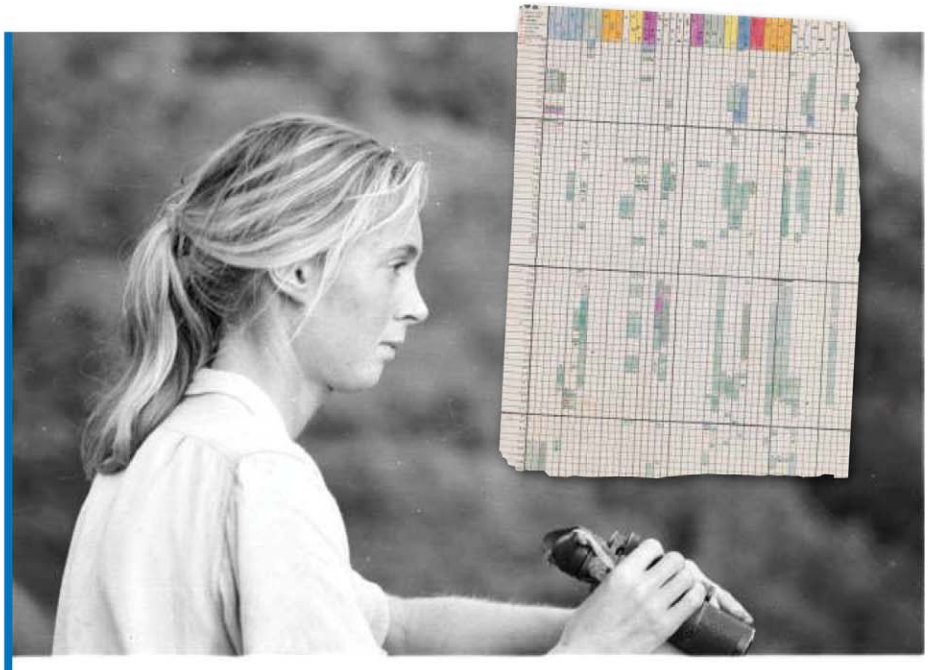

Durham, North Carolina **7**

Trove of Vintage Primate Data Goes Digital

Jane Goodall had no scientific training when she arrived in Tanzania in July 1960 to begin studying chimps, but the then 26-year-old was meticulous about recording the behavior, habits, and even personalities of her primate subjects. This week, Goodall gave a lecture at Duke University to mark the beginning of a new life for the 50 years of data collection that followed. Led by Anne Pusey, an evolutionary anthropologist who has been working with Goodall for 41 years, Duke scientists are digitizing 20 file cabinets' worth of handwritten notes, typed audio transcriptions, and color-coded check sheets (see inset) that comprise the complete life histories of more than 200 chimpanzees. Pusey hopes the effort, dubbed the Jane Goodall Institute Research Center, will open up the data to new generations of scientists.

NEWSMAKERS

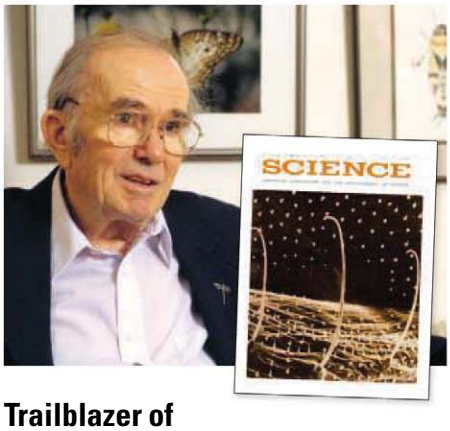

Trailblazer of Chemical Ecology Dies

Thomas Eisner, an ecologist and evolutionary biologist at Cornell University, died last week at age 81 of complications from Parkinson's disease.

In hundreds of journal articles on topics ranging from spider webs to bombardier beetles, Eisner explored how insects and arthropods defend themselves, capture prey, and attract mates in sometimes complex ways. With Cornell collaborator Jerrold Meinwald, he helped found the field of chemical ecology—the study of how animals and plants use chemicals to communicate. An outspoken conservationist, Eisner promoted the idea of allowing companies to "bioprospect" in the rainforest for useful chemicals in order to raise money to protect biodiversity.

Eisner was also a pianist, a popular science writer, and—with his wife, Maria—a nature photographer whose images of larval hooks (pictured), beetle hairs, and other minute wonders graced many pages and covers of *Science*. "He was a remarkable, amazingly accomplished individual who met every challenge with courage and grace and good humor. He was my personal scientific hero," says University of Illinois, Urbana-Champaign, entomologist May Berenbaum, who earned her doctorate at Cornell.

Pioneer of High-Dimensional Spaces Wins Abel Prize

The 2011 Abel Prize in mathematics goes to John Milnor, a topologist and dynamical systems theorist at Stony Brook University in New York state. Worth approximately $1 million and first awarded by the Norwegian Academy of Science and Letters in 2003, the prize has acquired a nearly Nobel-level cachet among mathematicians.

For Milnor, the prize caps a long and distinguished career. In 1956, he produced what others immediately recognized as a masterpiece for the ages: a seven-dimensional sphere too badly twisted to be unscrambled without creating corners and folds. By the rules of topology, two spaces are considered equivalent if one can be bent, stretched, and perhaps folded until it looks like the other. Creases are not allowed. Before Milnor, no one knew that this restriction made any difference; for spaces of three dimensions or fewer, it does not. His insight has led to decades of research in mathematics and physics.

Milnor says that what he loves most about mathematics is "a feeling of miracles." He adds, "You're working on a problem and it seems impossibly hard, but then you just put together an idea here and an idea there, and somehow the answer just drops out." **http://scim.ag/abel-prize**

Bug Expert Snags Enviro Prize

For more than 35 years, May Berenbaum has been a champion of insects, studying how they interact with plants and humans and conveying her fascination with bugs to the general public. For this work, the University of Illinois, Urbana-Champaign, entomologist will receive the 2011 Tyler Prize for Environmental Achievement.

Berenbaum helped elucidate the molecular arms race between plants trying to fend off herbivores and insects that evolve ways to sidestep, and sometimes make use of, these defenses. Ever since she was an undergraduate, she has reached out to the general public. "I serve as a self-appointed spokesperson for all things six-legged," she says. In 2006, she led a National Research

Grown on Garbage

Piles of garbage left by humans thousands of years ago in the Florida Everglades may have helped the formation of tree islands like this one, according to a new study.

Previously, scientists had presumed that the larger tree islands, which host two to three times the number of species living in the surrounding marsh, formed atop topographical high spots in underlying carbonate bedrock. But during their fieldwork, Gail Chmura and Maria-Theresia Graf, both paleoecologists at McGill University in Montreal, Canada, found instead concretelike layers of carbonate formed by water's evaporation from the peaty soil. Beneath the layers were prehistoric trash heaps, or middens.

Slightly higher and drier than the surrounding marsh, the middens could have offered a foothold for trees, shrubs, and other vegetation, the pair reported last week at a meeting of the American Geophysical Union in Santa Fe. Bones in the trash would have been a good source of phosphorus, a scarce nutrient in the Everglades. http://scim.ag/tree-island

CREDITS (TOP TO BOTTOM): MARCO MARTENS; ROBERT BARKER/CORNELL UNIVERSITY PHOTOGRAPHY; THOMAS EISNER/AAAS (INSET); GETTY IMAGES/STOCKBYTE PLATINUM

Council panel that pointed out the precarious state of pollinators in the United States. Later, her work on bee colony collapsing disorder helped focus attention on viral causes of this epidemic.

She hopes to use the $200,000 prize to promote citizen science, possibly by expanding a local Illinois bee spotting program that involves the general public in bee surveys. "I dream of taking it national," she says. **http://scim.ag/enviro-prize**

Three Q's

BEIJING—Last month, physical chemist Bai Chunli was appointed president of the Chinese Academy of Sciences (CAS), China's top research body with tens of thousands of scientists at dozens of institutes across the nation (see http://scim.ag/cas-pres). *Science* spoke with Bai about innovation, which China, like Europe and the United States, emphasizes as a crucial driver of future economic growth.

Q: What are the obstacles to China's innovation efforts?

Previously, China had hoped that by ceding market shares to foreign companies, we could in exchange obtain advanced technology and increase our capacity for innovation. However, we have realized that core technologies could not be obtained this way, nor could they be purchased. Technologies that are truly essential [to our economy] must be developed indigenously.

Q: What is your vision for CAS's "Innovation 2020" project, which sets priority R&D areas for the next decade?

The main goal is to solve science and technology problems that are of strategic importance to China's modernization and meanwhile to develop CAS into a world-class research institution. The central government's investment will emphasize stable support for talents on the one hand, and mega-projects and infrastructure development on the other.

Q: How will CAS increase its ability to innovate?

We will center around three ideas: more democracy, more openness, and [giving] more prominence to talent.

CREDITS (TOP TO BOTTOM): GETTY IMAGES; CHINESE ACADEMY OF SCIENCES (CAS)

Random Sample

Friendly Fires

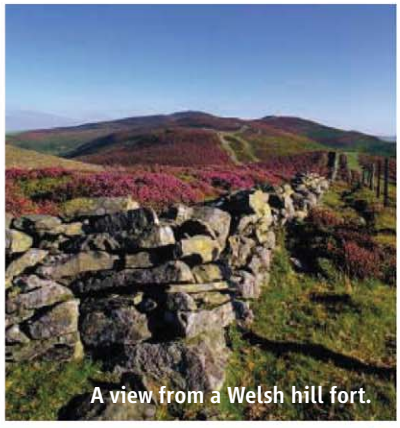

A view from a Welsh hill fort.

Just after sunset on Saturday, 19 March, archaeologist Erin Robinson waited with a small crowd of volunteers at Moel y Gaer, an Iron Age hill fort in Wales not far from the English border. They were watching another hill fort, Moel Fenlli, about 10 km to the southwest, waiting for a flare to shoot up. "There was just a huge bolt of excitement when it went off," Robinson says. "We had a huge cheer."

The volunteers were part of an experiment to see whether the people who occupied hill forts along the Welsh-English border some 2500 years ago could have seen each other and maybe even sent signals with fire. After the flare's signal, the group on Moel y Gaer shone their flashlights at the people at Moel Fenlli, who flashed theirs back, simulating light from a fire. Over the next hour, the greeting was repeated among a total of 10 hill forts.

Robinson's doctoral research at Bangor University in Wales is on the connections between the different hill forts, such as shared architectural styles. If these sites were occupied at the same time, they would have been aware of each other, the experiment shows. "The thing that I found more than anything was the emotional attachment," Robinson says. "By seeing people with a signaling light on a fellow hill fort, maybe up to 40 kilometers away, you felt the sense that you were part of one large community."

FINDINGS

How a Dinosaur Is Like a Vacuum Cleaner

The plant-eating sauropod dinosaurs, such as *Brachiosaurus* and *Apatosaurus* (formerly called *Brontosaurus*), were the largest animals ever, weighing up to 80 metric tons and stretching up to 30 meters in length. Many also sported very long necks—though researchers have debated their purpose. Now, two scientists in the United Kingdom may finally have the answer.

Evolutionary ecologists Graeme Ruxton of the University of Glasgow and David Wilkinson of Liverpool John Moores University created a simplified mathematical model of *Brachiosaurus*. By varying the dinosaur's dimensions, the duo found that its 9-meter neck gave *Brachiosaurus* an 80% energy savings in foraging compared with a 6-meter-long-neck. Like a clunky, old-fashioned vacuum cleaner with a long tube, *Brachiosaurus* could graze widely without having to move its huge body. The energy savings might even have allowed the dinosaur to browse the treetops, the pair suggest in a paper published online 23 March in *Biology Letters*.

Not so fast, says physiologist Roger Seymour of the University of Adelaide in Australia: Pumping blood to a raised head would require 50% of the animal's entire energy stores. The paper shows a long neck's advantage on the ground, he contends. "Let's just leave it there and not ask the sauropods to raise their necks." **http://scim.ag/long-necks**

Test Tells If the Heart Fits

Every year, about 4000 people worldwide get a heart transplant; roughly 40% of them experience at least one episode of acute organ rejection within a year. Usually patients must undergo regular biopsies of their new organ to monitor its health. The procedure is both painful and expensive, but now a new blood test could help.

Biophysicist Stephen Quake and his colleagues at Stanford University developed a test that monitors fragments of DNA that are released into the bloodstream when cells from the transplant tissue are broken down. When a transplant goes well, donor organ DNA typically makes up 1% of free DNA in the recipient's blood. During a rejection event, that fraction increases to an average of 3%, the team reports online this week in the *Proceedings of National Academy of Sciences*. Researchers hope that this test can eliminate the need for regular biopsies as a means of rejection monitoring. The new test is likely to be available to doctors in a year's time. **http://scim.ag/organ-test**

Over the top. The 11 March tsunami overwhelmed a coastal seawall in Miyako City designed for lesser waves.

CREDIT: REUTERS

JAPAN DISASTER

Scientific Consensus on Great Quake Came Too Late

TOKYO—Ten years ago, Koji Minoura, a geologist at Tohoku University in Sendai, and colleagues injected some science into a legendary disaster. A historical document compiled in 901 C.E. told of an earthquake in 869 C.E. that destroyed a castle town in northeastern Japan and a subsequent tsunami that inundated the surrounding area, killing 1000. Digging in rice paddies in what is now called the Sendai Plain, Minoura's team found telltale marine sediments showing that the tsunami ran as much as 4 kilometers inland. They estimated the Jogan earthquake's magnitude at 8.3 and concluded that it could recur at 1000-year intervals. "The possibility of a large tsunami striking the Sendai Plain is high," they wrote in a 2001 article in the *Journal of Natural Disaster Science*.

That obscure paper is now at the center of a growing debate about how quickly scientific findings can and should influence disaster-mitigation policies. A few years before the magnitude-9.0 Tohoku earthquake struck northeastern Japan on 11 March, a scientific consensus had begun to coalesce around the idea that a Jogan-like event could happen again. But that consensus did not influence seismic risk assessments, tsunami preparedness, or a review of the hardiness of the Fukushima Daiichi nuclear power plant.

"It's necessary to communicate research findings to society," says Yukinobu Okamura, a geologist at the Active Fault and Earthquake Research Center in Tsukuba, who led studies that independently bolstered Minoura's findings. "We tried to do that in this case, but we weren't in time."

One lesson is that incorporating geological studies of ancient earthquakes and tsunamis into risk assessments "is essential to compensate for the limitations in the current evaluation scheme," says Fumihiko Imamura, a tsunami engineer at Tohoku University in Sendai.

The need to revise earthquake probability analyses extends far beyond Japan. "There are other subduction zones, near Java and New Zealand, where people think there is no chance of a big quake" because they cling to old models of seismic processes, says Robert McCaffrey, a geophysicist at Portland State University in Oregon. But forecasts are generally based on studies covering the past several centuries—"not long enough for the cycle time for these big earthquakes," he says.

Although scientists have been interrogating geologic deposits for clues to the size and frequency of major earthquakes for several decades, efforts to apply such techniques to ancient tsunamis are more recent. In the early 1990s, "many people didn't believe tsunamis left deposits," says Joanne Bourgeois, a tsunami geologist at the University of Washington, Seattle. Minoura was among the paleotsunami pioneers when he started digging in the Sendai Plain. Recent sediment surveys have supported his Jogan findings, while studies of accumulating crustal strain in the Sendai area hinted at the possibility of a major earthquake. Even so, before the 11 March quake some scientists "did not believe" the region was primed for a big earthquake, says Yuichiro Tanioka, a seismologist at Hokkaido University in Sapporo.

Planners and engineers began to recognize the significance of geologic research for earthquake preparedness in the late 1970s, after paleoseismic studies revealed the regular recurrence of earthquakes along the San Andreas fault in California. But paleo studies didn't directly influence public policy until the mid-1990s. An early example is the Cascadia earthquake, now known to have occurred in the subduction zone off North America's Pacific Coast in 1700. In 1986, researchers reported the first geological evidence for this massive event: a sudden drop in elevation of coastal regions, inferred from sedimentary deposits, a sign of slippage on the upper side of a subduction zone. Eight years later, a revision to the Uniform Building Code required buildings in western Washington and Oregon to be 50% more earthquake-resistant. Then in 1995, partly because of the Pacific threat, the U.S. Congress passed the National Tsunami Hazard Mitigation Program, which supports studies of tsunami risk and emergency planning.

The size and timing of the Cascadia earthquake were unclear. Those pieces of the puzzle turned up in Japan, where Kenji Satake, a seismologist now at University of Tokyo, and colleagues found Japanese accounts of a tsunami without an apparent local cause. In *Nature* in 1996, they pinpointed the date of the Cascadia earthquake as 26 January 1700 and estimated a magnitude of 9.0. "There is a lot of respect for [Japan's] record-keeping diligence," says Brian Atwater, a U.S. Geological Survey geologist at the University of Washington, Seattle.

Japan's Headquarters for Earthquake Research Promotion produces seismic hazard maps for the nation; they are used to estimate potential tsunamis. The headquarters incorporates paleoseismic studies in determining earthquake risk—but only in Hokkaido, Tanioka says. Hokkaido was the last region of modern Japan settled by ethnic Japanese, and

reliable records go back only to the mid-1800s, he says. Elsewhere, the agency relies on "documents allowing the estimation of earthquake frequency and scale [going] back 400 years," Imamura says. Using those records, the earthquake research headquarters warned that the area hit by the 11 March temblor faced a 99% probability of a magnitude-7.5 earthquake occurring in the next 30 years.

Okamura and colleagues conducted more extensive surveys in the Sendai area in the mid-2000s that bolstered Minoura's original findings. According to Okamura, the earthquake research headquarters was studying whether and how to include Jogan in its risk assessment for the Tohoku region. "But the earthquake occurred before the evaluation was completed," he says.

Any upward revision is now also too late for the Fukushima plant. The first reactor was completed in 1971, long before the Jogan event appeared on the scientific radar. Planners girded for a maximum 5.7-meter tsunami; Tokyo Electric Power Co. estimates that the tsunami that took out the backup diesel generators was 14 meters high. The company missed a chance to address the deficiency when an expert panel reviewed the plant's seismic resistance in 2008. As *The Washington Post* reported, Okamura told the panel about the Jogan earthquake and warned that a bigger tsunami was possible. The panel, concerned mostly about earthquake shaking, brushed aside his concerns, he asserts.

Japan and other countries will surely rethink tsunami threats—just as Minoura intends to do. Originally, he says, he tried to "simply make clear the geological process of coastal environments." But now, "I want to meditate deeply on the future of geological work [related to] tsunamis," he says. The Tohoku temblor should convince the scientific community and authorities that magnitude-9 earthquakes can occur anywhere along subduction zones, McCaffrey says. Like a tsunami, the effects of the 11 March Tohoku earthquake will spread far and wide.

–DENNIS NORMILE

ARCHAEOLOGY

In Indus Times, the River Didn't Run Through It

SANTA FE—The Saraswati was the mother of all the holy rivers of India, flowing between the Ganges and the Indus and dispensing milk and ghee before it dried up, according to ancient Hindu scripture. Archaeologists and some devout Hindus have long tried to pinpoint its course, which the scripture puts between the Indus and Ganges rivers. For more than a century the best candidate has been the ancient channels of the now-dry Ghaggar-Hakra system in today's India and Pakistan. Along its course are scattered settlements of the Indus civilization, which some Hindus see as the progenitor of their traditions.

At a meeting* here last week, however, three independent teams offered preliminary evidence that the Ghaggar-Hakra was at most a modest seasonal stream during and after the Indus flourished from 2500 B.C.E. to 1900 B.C.E. "We need more cores, but the data suggests there was no big river here" in Indus times, said geologist Sanjeev Gupta of Imperial College London in his talk.

The findings puzzle and intrigue archaeologists. The Indus settlements along the Ghaggar-Hakra appear to have migrated over time toward the river's source. That has been interpreted by some as a sign of decreasing river flow and stress on the Indus society. If, however, the river was dry or only seasonal, it may prompt a re-evaluation of how Indus peoples acquired water for agriculture. "This is enormously important work," says archaeologist Rita Wright of New York University in New York City, who heard the presentations. "We may have to give up the idea of the Indus as a civilization based on rivers."

To determine when the Ghaggar-Hakra last was an active river, researchers looked for the youngest sediments deposited by flowing water. Each of the three groups dated sediments primarily with optically stimulated luminescence, a technique that uses the light energy stored in quartz grains to estimate when the grains were last exposed to light. Gupta's team drilled several 40-meter cores near the Indus city of Kalibangan, in today's India, and found that river sediment deposits ceased after approximately 14,000 B.C.E., long before the Indus culture. Gupta said in his talk that the river may have jumped into the bed of the Sutlej River to the west at this time. Hideaki Maemoku of Hiroshima University led a Japanese team that found that sand dunes surrounding the Ghaggar-Hakra are older than 10,000 years, another indication any river present had long since dried up by that point. Maemoku's poster gave this summation of the would-be Saraswati: "No, it wasn't mighty."

Based on work downstream in Pakistan, another team, led by geologist Peter Clift of the University of Aberdeen in the United Kingdom, agrees that little water flowed regularly in the system after 2500 B.C.E. But Clift believes the river may have simply shifted to another as-yet-unidentified channel and that there still may have been flow in the Ghaggar-Hakra during Indus times.

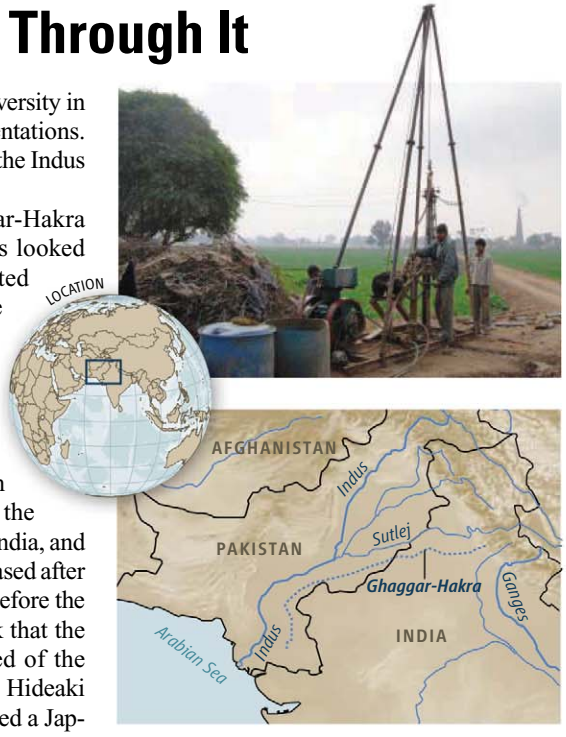

Dry hole. Researchers drill a core (*top*) in the bed of the ancient Ghaggar-Hakra River in India.

Clift says the drying of the Ghaggar-Hakra may reflect a drought that may yet help explain the civilization's mysterious decline. However, other researchers note, even though no surface water flows today, the ancient channels still provide groundwater for farmers and might have done so in the past. And a dried-up riverbed may have been a safer place to settle than the banks of a major river such as the Indus, which flooded disastrously in 2010. "Now we have more questions," Wright says.

–ANDREW LAWLER

*American Geophysical Union meeting, "Climates, Past Landscapes and Civilizations," 21–25 March 2011, Santa Fe.

CREDITS (TOP TO BOTTOM): RAJIV SINHA/IIT-KANPUR; M. TWOMBLY/*SCIENCE*

JAPAN DISASTER

Pool at Stricken Reactor #4 Holds Answers to Key Safety Questions

Of all the terrible news from the crippled Fukushima Daiichi nuclear power plant, reports about the spent fuel storage pool for reactor #4 may be among the most disconcerting for scientists. The pool held the entire complement of fuel rods from the reactor's core, which had been emptied 3 months before the 11 March earthquake and tsunami struck. And yet on 15 March the building exploded, apparently fueled by hydrogen, leaving nuclear engineers to speculate about the source. Adding to the confusion are reports of fires in the pool, a worst-case scenario that had never before occurred in a working nuclear plant.

Unraveling the mysteries surrounding the #4 pool will require discovering why water levels there fell so quickly, and whether the 230 tons of spent nuclear fuel melted in addition to catching on fire. Researchers also need to quantify how much radioactive material might have been released. The events at the #4 pool could shed light on the dangers posed by spent fuel in pools at more than 350 reactors globally, and what needs to be done to assure the public that they can be operated safely.

As *Science* went to press, extremely high levels of radiation were hampering efforts to restore power and water lines to all six reactors at the complex. And while a possibly damaged core in reactor #3 was leaking highly radioactive water, reactor #4's pool remains among the biggest potential sources of radiation. In video released early this week, what appeared to be steam continued to billow from reactor #4's blown-out frame despite continued efforts to add water.

Hot fuel

The nuclear fuel at reactor #4 is made up of uranium pellets held in 4-meter-long tubes made of zirconium alloy. The pool holds 1331 bundles of tubes, known as assemblies; 548 were removed from the reactor in January during maintenance.

Daiichi has seven spent nuclear fuel pools: one for each of its six reactors, and a central one. They serve two main purposes: to cool the fuel, which gives off heat as a result of radioactive decay, and to shield workers and the environment from radiation. In reactors with Fukushima Daiichi's design, pools are not in sealed containment vessels but are open and accessible; operators are keenly aware of the importance of keeping water levels high. (Although the pool at reactor #3 may also have produced hydrogen, the other five pools have required constant replenishment but remained stable.)

One mystery about the #4 pool is how its water level fell so quickly. During normal operation, 7 meters of roughly 40°C water sit between the top of the fuel rods and the surface of the 1425-ton pool. The water is constantly circulated and replenished.There's little doubt that temperatures in the pool would have risen steadily after power was lost. But several scientists have independently calculated that it would take much longer than 4 days—perhaps as much as 3 weeks—for the heat of the fresh fuel in the #4 pool to evaporate or boil off the water.

Could the #4 pool's structure have been damaged in the quake or subsequent explosions or both? Among possible weak points are the large doors on the side of the pool. The doors, which allow fuel to pass underwater from the reactor into the pool, are held shut by rubber gaskets inflated by electric pumps. In 1986, at the Hatch nuclear plant near Baxley, Georgia, the water level in a spent fuel pool dropped by more than a meter after the seals were left uninflated. But engineers say that the channel between the reactor and the pool is filled with water during maintenance periods, meaning that a leak would *lengthen* the time it took to empty the pool. "It's surprising to me [that] the fuel became uncovered that quickly," says Lake Barrett, a retired nuclear engineer and former U.S. Nuclear Regulatory Commission (NRC) official.

Determining the temperature of the pool has been another challenge. (It was reported to be 84°C the day before the explosion; no data have been subsequently released.) Knowing that temperatures were high enough to drive water completely from the pool could help researchers quantify how much radioactivity was released in subsequent steps. The day after the 15 March explosion, NRC Chair Gregory Jaczko said that the pool had run dry at one point, a claim that the Japanese government has disputed.

At least one fire in the pool—and possibly a second—was reported by power company officials after the explosion. Lab experiments have shown that zirconium can burn either with steam or with oxygen. Both reactions progress rapidly at roughly 800°C; the former, crucially, releases hydrogen. The hydrogen explosion at reactor #4 points to the steam reaction, which releases less energy and therefore melts the fuel more slowly. But knowing which reaction dominated could help scientists quantify how much radioactivity was released from pool #4. A 2006 study by the U.S. National Research Council said that a heat up after a loss-of-water event could melt the spent fuel, allowing the escape of volatile radionuclides, including "a substantial fraction of the cesium," into the air.

Soil samples analyzed by the Japanese science ministry last week found cesium levels roughly equivalent to 8 million becquerels per square meter near the plant. That level, if accurate, would be higher than those found near Chernobyl. (Radioactive iodine has been found in Japanese tap water, but its 8-day half-life means that it couldn't have come from the older spent fuel in pool #4. Reactor #3 may be the source.) Scientists also don't know what fraction of the radioactive cesium released is from reactors or from spent fuel. Scientists hope more detailed isotopic measurements will shed light on the age and, therefore, the source of the radioactive particles.

CREDIT: REUTERS

Minding the pools

Some experts believe that governments and the nuclear power industry have done a poor job of sharing information on the risk of zirconium fires. Critics of NRC say that studies conducted for the agency likely contain relevant data but have been kept classified to keep the information away from terrorists. "To the extent that any experiments have been done at all, the public doesn't know about them," says spent-fuel expert Gordon Thompson of Clark University in Worcester, Massachusetts. The National Research Council study called on NRC to "improve the sharing of pertinent information" on pool risks.

The calamity at Fukushima Daiichi has raised particular concerns about U.S. spent nuclear fuel pools, which are thought to be packed more tightly than those in Europe or Asia. "Spent nuclear fuel may be more vulnerable than we thought," says Edwin Lyman of the Union of Concerned Scientists in Washington, D.C. The nuclear industry has added additional sprayers to pools and now mixes hot, fresh spent fuel with older fuel in the pools to redistribute the heat. But it balked at a 2008 recommendation by Jaczko—speaking in an unofficial capacity—to transfer U.S. fuel older than 5 years to dry concrete casks, where the cooled fuel is highly unlikely to catch fire. Still, the industry has begun a safety review of U.S. reactors, and NRC has launched two studies into U.S. plant safety that could lead to new rules on spent fuel.

–ELI KINTISCH

With reporting by Dennis Normile in Tokyo.

REACTOR #4: THE SECRETS OF A SPENT FUEL POOL

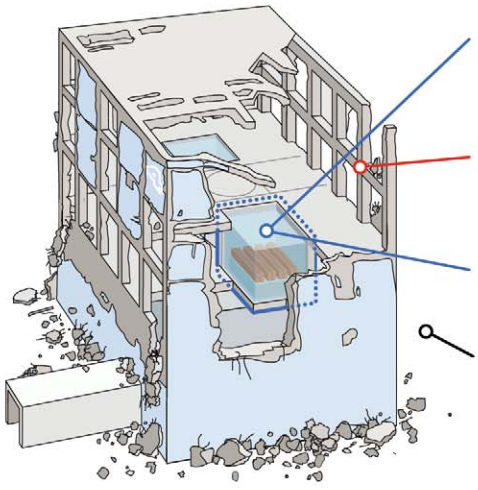

What caused the loss of water in the pool, and how low did the water level get?
Whether the water drained, evaporated, or boiled off would provide key clues.

What caused the hydrogen explosion?
Zirconium alloy, which makes up the tubes holding the uranium fuel pellets, reacts with steam to form hydrogen, which can ignite in the presence of oxygen.

What temperature was the water?
The zirconium reaction progresses at temperatures above 800°C.

What do recorded levels of cesium-137 outside the plant mean?
Melted and aerosolized long-lived radionuclides suggest a hot fire in the pool.

CHEMISTRY

Artificial Leaf Turns Sunlight Into a Cheap Energy Source

ANAHEIM, CALIFORNIA—Nearly all the energy we use on this planet starts out as sunlight that plants use to knit chemical bonds. Now, for the first time, researchers at the Massachusetts Institute of Technology (MIT) have created a potentially cheap, practical artificial leaf that does much the same thing.

The new device is a silicon wafer about the shape and size of a playing card. Different catalysts coat each side of the wafer. The silicon absorbs sunlight and passes that energy to the catalysts to split water into molecules of hydrogen (H_2) and oxygen (O_2). Hydrogen is a fuel that can be either burned or used in a fuel cell to create electricity, reforming water in either case. This means that, in theory, anyone with access to water can use it to create a cheap, clean, and available source of fuel.

"It's spectacular," says Robert Grubbs, a chemist at the California Institute of Technology in Pasadena, who saw the presentation here last weekend at the biannual meeting of the American Chemical Society. "There's still obviously a long way to go" to make the new device into a rugged, real-world technology, Grubbs says. But the approach is important because its potential low cost could make it widely available. It "has a chance of being scalable," Grubbs says.

Three years ago, an MIT team led by chemist Daniel Nocera devised a special cobalt and phosphorus-based catalyst that breaks water molecules apart and knits pairs of oxygen atoms into O_2 molecules (*Science*, 1 August 2008, p. 620). Researchers had previously made H_2-forming catalysts. But these were expensive. Earlier this week, Nocera reported devising a cheap catalyst that uses three different metals to form H_2.

The splits. A new silicon wafer can make hydrogen fuel from sunlight and water.

Nocera didn't reveal the makeup of the new catalyst, as the work is not yet published, and he is in the process of patenting it. But he notes that finding his new H_2-forming catalyst was made easier by the fact that his O_2 catalyst works in water, a more benign environment than existing H_2-generating compounds typically face.

To make its artificial leaf, the MIT team spread its catalysts on opposite sides of a silicon wafer. The silicon absorbs sunlight and passes energetic, negatively charged electrons and positively charged electron vacancies to the catalysts on opposite sides that use them to make H_2 and O_2. When the device is placed in a clear jar and exposed to sunlight, the setup converts 5.5% of the energy in sunlight into hydrogen fuel. "You literally walk outside, hold it up, and it works," Nocera says.

Nocera says he hopes to commercialize the new technology within 2 to 3 years. Later this year, a company he founded, Sun Catalytix, expects to produce a prototype electrolyzer using the cobalt catalyst and an external electricity source to split water to generate hydrogen. Sunlight-to-fuel water splitters using both new catalysts will likely follow after that, he says. In addition, Nocera is teaming up with Ratan Tata, chair of Tata Group, an Indian conglomerate, in hopes of producing a refrigerator-sized power plant capable of converting sunlight and water into electricity. The goal is cheap, renewable power for vast numbers of people lacking access to large amounts of energy.

–ROBERT F. SERVICE

CREDITS (TOP TO BOTTOM): M. TWOMBLY/*SCIENCE*; ISTOCKPHOTO

www.thermoscientific.com/nanodrop

FREE tee-shirt offer

"If it wasn't for this little machine, I'm not sure what I would have done." —Armen M. Abramian

Emotional reactions to instrumentation from scientists are rare. Yet with Thermo Scientific NanoDrop Spectrophotometers, they are becoming commonplace. That's because scientists who own a NanoDrop™ are passionate about its simplicity. These instruments reduce analysis time and minimize sample waste with fast, easy and accurate micro-volume nucleic acid and protein sample quantitation. Just ask Armen Abramian:

"NanoDrop is really easy to use. I don't have to deal with cuvettes. We use this machine to measure a number of different types of samples—DNA, RNA, Protein—and it calculates purity too. It's small, easy to use, and I trust the results."

Learn about our special offers including a FREE tee-shirt promotion
www.thermoscientific.com/nanodrop

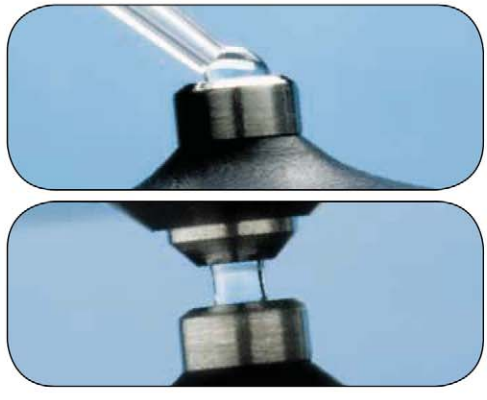

Thermo Scientific NanoDrop UV-Vis Spectrophotometers offer easy, reliable micro-volume analysis, with sample size as low as 0.5 µl and measurement time of less than 5 seconds—no dilutions.

Moving science forward

Thermo SCIENTIFIC
Part of Thermo Fisher Scientific

ANTHRAX INVESTIGATION

Army Missed Warning Signs About Alleged Anthrax Mailer

A new report detailing the mental health problems of U.S. Army researcher Bruce Ivins, the alleged perpetrator of the 2001 anthrax attacks, blames the U.S. Army Medical Research Institute of Infectious Diseases (USAMRIID) for not scrutinizing Ivins's background adequately before hiring him and providing him with the security clearances that allowed him to work with anthrax at the institute in Frederick, Maryland. The report says that if USAMRIID managers had looked at Ivins's psychiatric records, which they had the authority to access, they would have spotted behavioral red flags that would have automatically disqualified him from working in a biocontainment suite. The report's findings have rekindled a debate over how funding agencies, institutions, and labs should screen and monitor researchers with access to dangerous pathogens.

Ivins, who worked at USAMRIID for 35 years, committed suicide on 29 July 2008 as federal investigators were preparing to go public with the charges against him. The Department of Justice (DOJ) has since released thousands of pages of investigative material supporting its conclusion that Ivins was the killer. That material included scientific evidence linking the anthrax in the letters to a flask of spores under Ivins's control and other evidence such as the scientist's long nighttime stays at his lab in the months before the attacks. But former colleagues of Ivins's and many others have challenged the government's conclusion. And a recent review by a panel of the National Research Council found that the scientific evidence isn't as ironclad as claimed by federal officials (*Science*, 18 February, p. 835).

By contrast, the latest report—written by a panel of nine experts from fields such as psychiatry, medicine, and organizational systems—unambiguously endorses the government's implication of Ivins. The report was ordered in September 2009 by Chief Judge Royce Lamberth of the U.S. District Court in Washington, D.C., after DOJ requested a study of Ivins's sealed psychiatric records. The panel's findings were submitted to the court on 23 August 2010 and released publicly last week. "Dr. Ivins was psychologically disposed to undertake the mailings; his behavioral history demonstrated his potential for carrying them out; and he had the motivation and the means," the report concludes. "The psychiatric records offer considerable circumstantial evidence in support of the DOJ's finding."

Drawing upon 3 decades of mental health records, the panel—chaired by Gregory Saathoff, a psychiatrist at the University of Virginia, Charlottesville—describes Ivins as a deeply disturbed individual who projected a "benign eccentricity" that "masked his obsessions and criminal thoughts." After being rejected by a woman from the Kappa Kappa Gamma sorority during his undergraduate days at the University of Cincinnati, Ivins developed a lifelong obsession with KKG, breaking into the sorority's buildings several times. The mailbox where the anthrax letters were mailed is situated within 200 feet of a KKG office at Princeton University.

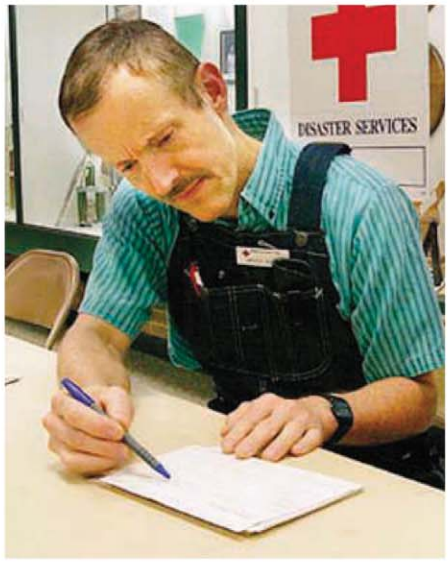

Troubled. Ivins juggled at parties and volunteered for the Red Cross but was also plagued by strange obsessions and criminal thoughts, says a new report.

CREDIT: AP

The report says Ivins's mental health issues stemmed in part from a traumatic childhood during which his mother stabbed and beat his father, his mother physically abused Ivins, and his father mocked him publicly. Over the years, Ivins revealed his criminal behaviors and obsessions selectively to mental health professionals; in the 1990s, a therapist became so alarmed that she made tentative inquiries with the local police department. Yet, when filling out medical forms with his employer, Ivins omitted critical information to conceal his history of behavioral problems. The report faults USAMRIID for not following up on these discrepancies in Ivins's paperwork, which would have brought his psychiatric problems to light.

USAMRIID has declined to comment on the panel's findings. However, Department of Defense officials have stated in the past that the Ivins affair has led to enhanced background checks and stricter monitoring of all personnel working with dangerous pathogens and toxins. Those new procedures, which have been in place since 2008, include psychological evaluations and periodic drug tests.

Whether the same standards of screening and monitoring will eventually be applied to biodefense labs in academia and industry remains an open question. Academic researchers who work with any of the 82 pathogens and toxins on the so-called select-agent list currently undergo a basic background check limited to screening the applicant's name against a set of criminal and terrorist databases. Last year, the White House announced an initiative to overhaul the entire security framework for research involving select agents: under this plan, the government will rank select agents by risk and apply tougher security measures for those in the top tier.

Biodefense researchers are opposed to tougher screening and monitoring procedures. Microbiologist David Relman of Stanford University in Palo Alto, California, a member of the National Science Advisory Board for Biosecurity (NSABB), says that some testing might be counterproductive because "it may lull us into a sense of security and wrongfully impugn creative, eccentric, but harmless individuals." NSABB has recommended that institutions enhance biosecurity by encouraging scientists to report suspicious behaviors of lab mates.

Richard Ebright, a biologist at Rutgers University in New Brunswick, New Jersey, does not believe in NSABB's self-governance model, noting that the new report suggests that well-meaning colleagues and supervisors are unlikely to be a good defense against an insider threat. "It is absolutely clear that the 2001 anthrax attacks would not have occurred if any one of three security measures had been implemented," Ebright says, citing video monitoring of biocontainment areas, a two-person rule requiring that nobody work alone in a biocontainment facility, as Ivins did, and psychological background checks. The way to enhance biosecurity and prevent another insider attack, he says, is for the government to mandate each of those measures.

–YUDHIJIT BHATTACHARJEE

The Rise of Animal Law

Will growing interest in how the legal system deals with animals ultimately lead to changes for researchers?

AT THE OREGON NATIONAL PRIMATE RESEARCH CENTER IN Beaverton, some 20 law students tour the outdoor enclosures that house breeding colonies of macaque and rhesus monkeys and talk with the veterinarian in charge of their care. "It's a very powerful trip for the students," says Kathy Hessler, who teaches a course on animal law at Lewis & Clark Law School in nearby Portland. "Some of them are really shaken." That's not because they see violations of the law, Hessler explains: "The primate center is working very hard to meet the requirements under the law, but there's a disconnect between what the law provides and what the students think the animals need."

Hessler and her class are part of the rapidly growing field of animal law, a relatively new area of study that examines—and often challenges—how the law treats animals. As recently as 2000, only a handful of law schools in the United States offered courses in animal law. Now roughly 120 do. These include several of the nation's premier law schools, including Harvard, Stanford, and Columbia, which have established endowed programs in animal law thanks to $1 million donations from TV celebrity and longtime animal rights activist Bob Barker (see table). Some of those who teach animal law courses, including Hessler, describe themselves as activists. Others shy away from that label. But many take issue with a legal system that treats animals as property and provides few mechanisms for protecting their interests in court.

Some of these legal scholars have proposed strategies for advancing animal rights through steppingstone cases that erode the notion of animals as property and grant them some of the same protections people have. Others, drawing inspiration from antislavery and civil rights movements, advocate a more direct effort to establish fundamental rights for animals—at least for more cognitively sophisticated species such as great apes and cetaceans (see sidebar, p. 30). No one is arguing that orangutans should be given the right to vote, but some legal scholars see no reason why apes shouldn't have rights similar to those of a child or a person in a coma. Whether these efforts will succeed remains to be seen. But if they do, there could be repercussions for everyone who works with animals—including scientists.

"It's a developing area of law, and we're monitoring it closely to see how it may evolve," says Andrew Cardon, director of state and legal affairs for the National Association for Biomedical Research, an advocacy group in Washington, D.C. "Our concern is that incremental changes in the law could have negative consequences for lifesaving research."

A movement is born

Joyce Tischler has loved animals since she was a child. After graduating from law school in 1977, she began searching for a way to use her law degree to help animals. She and a like-minded colleague put an ad in a San Francisco legal newspaper to see whether anyone else shared their interests. "About six people showed up to our first meeting," Tischler says. "We formed a little group and met for several years to educate ourselves about the laws that relate to animals." That group grew into the Animal Legal Defense Fund (ALDF), a Cotati, California, organization that has been a driving force in the growth of animal law.

ALDF's efforts include litigation, legislation, and education. The group has filed scores of civil lawsuits to protect animals and assists with hundreds of criminal prosecutions each

CREDITS: (TOP LEFT PHOTO) TED S. WARREN/AP; (OTHER PHOTOS) THINKSTOCK

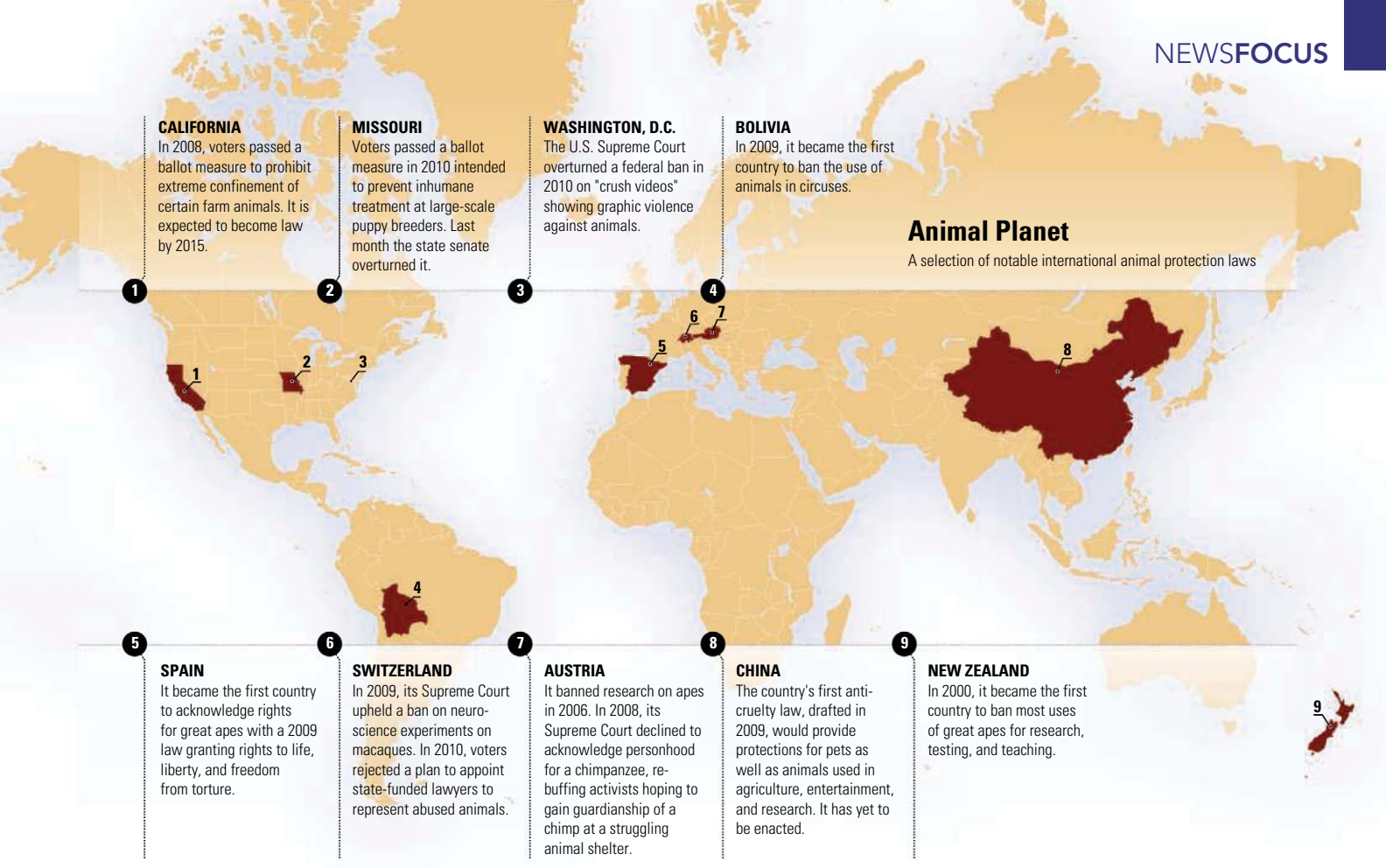

1 CALIFORNIA
In 2008, voters passed a ballot measure to prohibit extreme confinement of certain farm animals. It is expected to become law by 2015.

2 MISSOURI
Voters passed a ballot measure in 2010 intended to prevent inhumane treatment at large-scale puppy breeders. Last month the state senate overturned it.

3 WASHINGTON, D.C.
The U.S. Supreme Court overturned a federal ban in 2010 on "crush videos" showing graphic violence against animals.

4 BOLIVIA
In 2009, it became the first country to ban the use of animals in circuses.

5 SPAIN
It became the first country to acknowledge rights for great apes with a 2009 law granting rights to life, liberty, and freedom from torture.

6 SWITZERLAND
In 2009, its Supreme Court upheld a ban on neuroscience experiments on macaques. In 2010, voters rejected a plan to appoint state-funded lawyers to represent abused animals.

7 AUSTRIA
It banned research on apes in 2006. In 2008, its Supreme Court declined to acknowledge personhood for a chimpanzee, rebuffing activists hoping to gain guardianship of a chimp at a struggling animal shelter.

8 CHINA
The country's first anti-cruelty law, drafted in 2009, would provide protections for pets as well as animals used in agriculture, entertainment, and research. It has yet to be enacted.

9 NEW ZEALAND
In 2000, it became the first country to ban most uses of great apes for research, testing, and teaching.

year. In 2010, ALDF and other animal protection groups successfully sued to stop BP from carrying out "controlled burns" of spilled oil in the Gulf of Mexico that would have endangered sea turtles. ALDF drafted a 2008 Virginia law that toughened penalties for dogfighting in the wake of the Michael Vick scandal. (Vick, an American football star, was convicted in 2007 on dogfighting charges.) Tischler says she's especially excited about a current project in which ALDF lawyers are working with scientists and leaders from government and industry on strategies for implementing a 2007 National Research Council report urging companies to adopt alternatives to toxicity testing in animals. ALDF's Web site encourages visitors to petition Congress to adopt an Animal Bill of Rights, which includes "The right of laboratory animals not to be used in cruel or unnecessary experiments."

ALDF now has student chapters at 155 of the 200 U.S. law schools accredited by the American Bar Association (ABA). ALDF student chapters help establish animal law courses, arrange talks and symposia, and produce articles for law review journals.

Mainstream legal establishments are taking notice. ABA created a committee on animal law under its Tort Trial and Insurance Practice Section in 2004. The committee sponsors continuing education courses for practicing lawyers and develops policy proposals aimed at improving animal welfare. The Association of American Law Schools started a section on animal law in 2008 to promote education and professional development.

Tischler and other animal law pioneers attribute the field's rapid growth to a combination of societal change and scientific advances in animal cognition. "Pets are becoming of increasing importance to individuals and considered part of the family circle," says David Favre, a leading animal law scholar who teaches at Michigan State University College of Law in East Lansing. People's bonds with their pets tend to foster protective attitudes toward other animals, Favre says. That's reflected in a spate of recent state laws that punish not only animal cruelty but also neglect. Fourteen states now have laws that explicitly prohibit leaving animals in an unattended vehicle in hot or cold weather, for example.

The Price Is Right: $1 Million. As the game show's host for 35 years, Bob Barker gradually eliminated fur and leather prizes and signed off each episode with a plea for viewers to spay and neuter their pets. More recently, he's written $1 million checks to eight leading law schools to endow programs in animal rights law, plus two to his alma mater, Drury University in Springfield, Missouri, for undergraduate animal rights studies.

YEAR	SCHOOL
2001	Harvard Law School
2004	Duke University School of Law
2004	Stanford Law School
2004	Columbia Law School
2004	UCLA School of Law
2005	Northwestern University School of Law
2006	Georgetown University Law Center
2008	Drury University (undergraduate)
2009	University of Virginia School of Law
2009	Drury University (undergraduate)

CREDIT (BOTTOM): GENE BLEVINS/*LA DAILY NEWS*/CORBIS

At the same time, books such as *The Omnivore's Dilemma* and movies such as *Food, Inc.* have increased public concern about how animals are raised and slaughtered for food, and the law is changing in this arena, too. In 2008, for example, California voters approved a ballot measure that will outlaw cages that restrict the movement of egg-laying hens, calves raised for veal, and pregnant sows (see map, p. 29).

In parallel with these societal changes, research with a wide range of nonhuman animals has demonstrated behaviors and traits once thought to be the exclusive domain of humans, including cooperation, altruism, empathy, and a sense of fairness. "Science is incredibly important to animal law," says Mariann Sullivan, a New York City lawyer who chairs the ABA's Animal Law Committee. "Cognitive ethology is really what animal lawyers rely on in arguing that conditions for animals in any area should be improved."

According to animal law scholars and practitioners, the law has not kept up with science and society. "The legal and even moral distinctions we make about how we treat [animals] are based on the choices humans make about using animals and have nothing to do with the scientifically determined capacity of animals to feel pain or be self-aware or any of those things," Hessler says. A pet rat, a lab rat, an endangered wild rat, and a city rat that gnaws its way into someone's basement all have a similar interest in staying alive and avoiding pain, Hessler says, but the law now treats them very differently. "Inclusion of the interests of the animals themselves is what is novel in the animal law approach," she says.

Case studies

Some students may take animal law courses because they're already interested in animal protection, but instructors say many more sign up simply because the field is new and fast-moving. Coursework includes studying potentially precedent-setting cases. One of the most active areas involves monetary awards for emotional distress suffered by pet owners, says Bruce Wagman, a lawyer who teaches at the University of California (UC) Hastings College of the Law in San Francisco and developed the first casebook on animal law. "That's a hotbed of litigation and judicial opinions," Wagman says.

Historically, in cases in which a pet has been killed, U.S. courts have limited awards to the purchase price or replacement cost of the animal—typically a few hundred dollars. In recent years, grieving pet owners have argued that emotional bonds with pets are comparable to those with family, and they've sought monetary compensation for emotional distress. Courts often award damages for emotional distress after the death of an immediate family member, but not for loss of property, Wagman says. Pet owners have had some success when the pet's death was caused intentionally. In 2006, for example,

A Road Map for Animal Rights

In 1772, a slave named James Somerset won his freedom in an English court. Months earlier, three people acting on his behalf applied to the Court of King's Bench for a writ of habeas corpus, which would require Somerset's captor—he'd escaped his owner and been recaptured—to bring Somerset before the court to determine the legality of his imprisonment. In deciding that English common law provided no basis for holding Somerset, the court brought an end to slavery in that country.

The case is a potential blueprint for establishing personhood and legal rights for animals, says Steven Wise, a lawyer and legal scholar in Coral Gables, Florida, and founder of the Nonhuman Rights Project (NHRP). In the eyes of the law, animals are considered things to be owned, as slaves once were, Wise notes: "The story of James Somerset is a metaphor for how any legal thing [such as an animal] can use the court system to become a legal person."

That's a goal Wise has been working toward for 30 years, and he now says his group is close to filing lawsuits on behalf of intelligent animals such as chimpanzees and dolphins in an attempt to convince courts that at least some nonhuman animals meet the requirements of legal personhood and should be accorded certain basic rights. "We're hoping to file the first suits, if everything goes right, in 2012, and if everything goes wrong, in 2013," Wise says.

As improbable as it may sound, there's a chance he will succeed, says Richard Cupp, a legal scholar at Pepperdine University in Malibu, California. "Steven is a very smart guy, and he'll choose his jurisdictions very carefully," Cupp says. "In the short term, I suspect he won't be successful, but I could be wrong."

Rattling cages. Steven Wise wants courts to acknowledge "dignity" rights for some animals.

CREDIT: ASSOCIATED PRESS

In law review articles and books, Wise has laid out a philosophical framework for animal rights. He argues that some nonhuman animals, particularly great apes and cetaceans, are cognitively complex in many of the same ways that humans are: They can have desires, act intentionally, and have some sense of self. Therefore, Wise asserts, they deserve basic "dignity" rights, such as the right not to be harmed or held in a distressing environment. Human infants and people in a vegetative state have such rights, and Wise argues that a chimpanzee of similar or greater intelligence should be granted them as well.

Getting a judge or jury to consider these arguments is the goal of NHRP. Since 2007, Wise has recruited more than 50 volunteers, including lawyers and sociologists, who are working to identify potential plaintiffs and determine which jurisdictions are most likely to be sympathetic to their arguments and which legal strategies are most likely to be effective. He estimates that they've spent a cumulative 20,000 hours analyzing dozens of legal and sociological issues in all 50 states.

The first case will likely involve an animal being held in substandard conditions: perhaps a dolphin kept in a small pool at an aquarium or a chimpanzee confined to a small cage at a zoo or research facility. NHRP will file a lawsuit in trial court, probably using habeas corpus or another common law writ, *de homine replegiando*, used centuries ago in slavery cases.

If the trial court dismisses the case, Wise says he will appeal all the way to the state's highest court. NHRP is combing over the judicial decisions of state appellate court and high court judges to determine their judicial philosophies. Volunteers are also looking for courts sympathetic to civil rights and animal welfare issues, as well as those that have ruled in favor

a Washington state judge awarded a woman $5000 for emotional distress after a boy stole her cat from her porch and took it to a nearby schoolyard, where he doused it in gasoline and set it on fire. However, when a pet dies as a result of negligence—due to veterinary malpractice, for example—few if any courts have been willing to award damages for emotional distress, Wagman says: "That's the dividing line now, but people are constantly trying to push that envelope."

The law is also changing rapidly in how animals are dealt with in the establishment of trusts and custody cases. Forty-five states have statutes enabling people to set up trusts to provide for their pets after their death, up from eight states in 2000. Pets are increasingly an issue in divorce proceedings, too, with judges being forced to decide whether to treat pets as property, whereby whoever bought the animal keeps it, or more like children, for whom consideration is given to who can provide the best home.

of gay marriage, which Wise suspects might reflect a sensitivity to equality that would work in his favor.

People have tried previously—and unsuccessfully—to gain legal standing for animals. In 1998, Wise lost a case in which he argued that a dolphin named Kama had legal standing to sue the New England Aquarium to prevent being transferred to a Navy marine mammal facility. In 2004, a district judge in San Francisco ruled that whales, porpoises, and dolphins (represented by a self-appointed attorney) did not have legal standing under federal law to sue the Navy to stop allegedly harmful sonar testing. In both cases, the judges ruled that only "persons" can sue under federal law and that the legislators who wrote the laws did not intend the definition of "person" to include cetaceans.

Wise says he's learned from his mistakes in the Kama case. That's why he's focusing on state common law. "Common law is the law that judges make, so you don't get into this issue of legislative intent," he says. "We're looking for courts that view common law as elastic, as something that changes as morality changes or as new scientific facts come in" about the cognitive capabilities of nonhuman animals.

If he wins, the animal in question will be moved to a better home. But more important from Wise's perspective, a legal door that has been slammed shut will have opened just a crack, enabling him and others to push for more rights for more animals. "Win or lose, we're going to keep going," he says. **–G.M.**

Such cases erode the notion of animals as property and move them closer toward some of the protections and privileges accorded to people—a move that concerns some advocates of biomedical research. But Favre, whose writings on animal law and philosophy are required reading in many animal law courses, finds it long overdue. In a 2010 article in the *Marquette Law Review*, he argues for classifying domestic animals as "living property." This designation would acknowledge that animals have interests—in staying alive, moving freely about, and socializing with other members of their species, for example—that should be weighed against human interests by the legal system.

Favre argues that the law already provides modest rights for animals to protect these interests: Anticruelty laws protect their right not to be harmed, for instance. He advocates expanding such existing rights and creating new ones. Perhaps most provocatively, he argues in a 2005 article in the *Michigan State Law Review* that animals, through self-appointed attorneys, should have the right to sue humans who violate their primary interests. Currently, animals do not have legal standing to sue, and animal welfare advocates have had limited success suing on their behalf. That's because courts will only consider harm done to a human being, leaving animal advocates in the difficult position of arguing that they themselves have been harmed by an animal's suffering. Favre argues that an animal's interests should be part of the legal equation.

Reason for concern?

Although the growth of animal law is undeniable, the implications for animal research are uncertain. There are serious barriers to implementing the kind of theoretical changes to the legal system that Favre and others advocate, says Taimie Bryant, who teaches animal law at the UC Los Angeles School of Law. "How you would take that from academia and put it into a practical setting where most entities that use animals have more lobbying power than academics isn't clear," Bryant says. She thinks changes that affect scientists are more likely to come from societal change and the efforts of organizations like the ALDF and the Humane Society of the United States (HSUS).

Indeed, the HSUS legal team has grown from three full-time lawyers in 2005 to 16 today, and the organization draws from a network of 2000 lawyers who have volunteered to work pro bono, says Jonathan Lovvorn, vice president and chief counsel of animal protection litigation and research. Most litigation and lobbying efforts at HSUS involve pets, livestock, and wildlife, but the group also takes on issues involving research animals when the opportunity arises, including pushing for the Great Ape Protection Act, which would ban invasive research on those animals (*Science*, 13 March 2009, p. 1414).

Some research advocates are wary of all these trends. "Those of us who represent scientists who work with animals don't look on this as a positive development, although a lot of what they're doing we have no objection to," says Deborah Runkle, a senior program associate at the American Association for the Advancement of Science, which supports the use of animals in scientific research (and publishes *Science*). "It's not an immediate threat, but it's something that needs to be watched," says Alice Ra'anan, director of government relations and science policy for the American Physiological Society. "If there's a concern, it's that there are relatively few lawyers who are interested in this who have an understanding and appreciation of animal research and of the laws that already exist to protect animals."

The growth of animal law both reflects and encourages societal change, says Richard Cupp, who writes and teaches about the legal and moral standing of animals at Pepperdine University School of Law in Malibu, California. Cupp applauds legal protections for animal welfare, but in several law review articles he has argued that establishing legal rights for animals would not serve society's best interests. To pick one example, if animals were given the right to sue as Favre proposes, activists suing on behalf of research animals could bog down universities with endless lawsuits. "We could lose a lot of research that might be very helpful," Cupp says.

At a more philosophical level, Cupp argues that talking about rights for animals obscures the fact that at the end of the day any legal case involving animals will be decided by humans. The developing field of animal law should focus on emphasizing and delineating humans' moral responsibility toward other animals rather than on establishing legal rights, Cupp says: "We're stepping toward something, and the fight is over what we should be stepping toward." **–GREG MILLER**

Read more about animal law cases and issues online:

Animal Legal Defense Fund: http://www.aldf.org/

Animal Legal and Historical Center at Michigan State University College of Law: http://www.animallaw.info/

National Association for Biomedical Research, Animal Law Section: http://www.nabranimallaw.org/

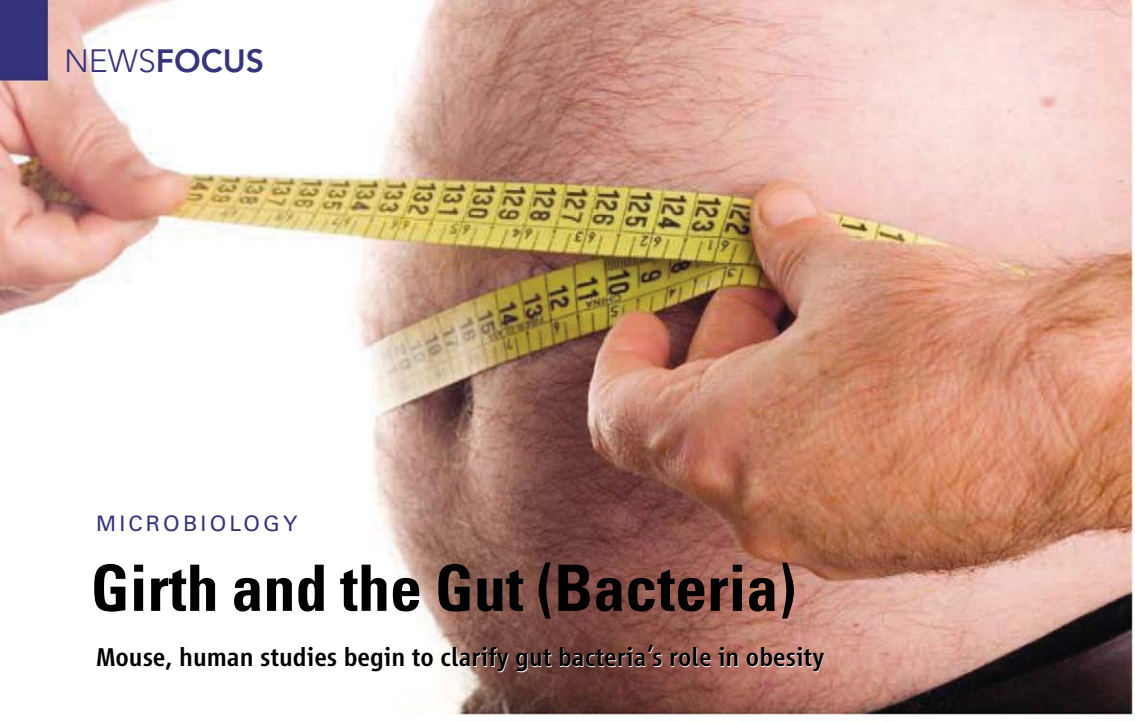

MICROBIOLOGY

Girth and the Gut (Bacteria)

Mouse, human studies begin to clarify gut bacteria's role in obesity

Five years ago, a team headed by Jeffrey Gordon of Washington University in St. Louis (WUSTL) in Missouri made a surprising discovery: The guts of obese mice and people harbor an array of microbes different from that of their lean counterparts. More provocatively, when they gave lean mice certain gut-dwelling microbes, the rodents became fat (*Science*, 29 May 2009, p. 1136). The findings sparked headlines and fueled popular speculation that manipulating gut bacteria might keep weight down in people.

Already, Martin Blaser had been heading down a similar track. Blaser, a microbiologist at New York University in New York City, was struck by how successful farmers are at increasing the growth rates of livestock by adding low doses of antibiotics to their feed. "The earlier in life they start the antibiotic, the more profound the effect," he points out. He began to wonder whether antibiotic use, particularly in children, might affect the long-term establishment of a balanced microbial community in the human gut, eliminating bacteria there that could help ward off obesity. He started conducting mouse studies to examine the hypothesis.

Since then, several other groups have joined in. A raft of intriguing obesity-related findings was presented at a meeting last month on the microbiome, the bacteria that live inside the guts and other tissues of animals. Yet many in the field caution that it remains difficult to determine whether changes in gut microbes drive or contribute to obesity or whether the excess weight itself triggers those changes. "The jury is still out [about] what the role of the gut microbiota may be in obesity in humans," says Claire Fraser-Liggett, a microbiologist at the University of Maryland School of Medicine in Baltimore who has studied gut bacteria and obesity in the Amish.

Case of the missing microbes

The farm animal–antibiotic connection was one clue that led Blaser to wonder about microbial causes of the obesity epidemic. Another was the fact that very few people now harbor the ulcer-causing bacterium *Helicobacter pylori* in their stomachs. *H. pylori*, which has also been linked to stomach cancers, is one of up to 1000 different microbes that call the human body home. Once ubiquitous in the human microbiome and still so in the guts of people from developing countries, it is now found in just 6% of U.S. children. That might seem like good news, as there should be fewer ulcers and cancers. But Blaser suspects that it is also bad news, as studies suggest that *H. pylori*'s presence in the gut helps regulate the stomach's production of the hormone ghrelin, which stimulates food intake.

This bacterium may not be the only species disappearing from our microbiome. After a person takes antibiotics, "it has always been presumed that the microbiota will spring back," Blaser says. But the fate of *H. pylori* suggests otherwise. Its vanishing act and other shifts in the microbiome may contribute to an increased risk for weight gain, Blaser worries.

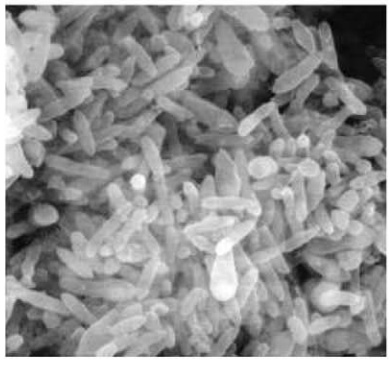

Go with the gut. Antibiotic use may adversely affect the long-term makeup of the intestine's bacterial communities.

He has started to investigate this theory by giving mice either low doses of antibiotics over long periods, akin to what farm animals receive, or short-term, high doses, more like what a sick infant or adult would get. He then compares the physiology and microbiomes of these treated rodents with those of mice raised under similar conditions but given no antibiotics. In one set of studies, the mice fed low doses of antibiotics long-term wound up with 15% more body fat than the control mice, Blaser reported last month at the International Human Microbiome Congress in Vancouver, Canada. The chubbier, antibiotic-fed mice also had about 25% more fat in their livers.

The treated mice also had a different set of bacterial species inhabiting their guts. And several hundred bacterial genes, including ones for fatty acid production, exhibited different levels of activity—some increasing, others decreasing—in these mice compared with the controls. Similar changes occur in the rodents given short pulses of antibiotics, he noted.

Antibiotics "may be driving the gut microbiome to a place where it shouldn't be," Fraser-Liggett says. "We do not know the functional consequences, but with these miracle drugs now 60 years later, we may be seeing effects that change susceptibility to various diseases."

Blaser will examine the gut microbiomes of children to see whether his results are applicable to humans. If so, "that would be a remarkable connection that could have a significant impact on medical care," says genome scientist George Weinstock of WUSTL. But he's cautious: "In a lot of cases, the microbiome in mice doesn't translate into humans."

Patterns in genes

S. Dusko Ehrlich has avoided that issue, bypassing mice and instead directly examining whether patterns in the microbiome of people relate to body mass index and obesity. A microbiologist at the INRA Microbiology and Food Chain Division in Jouy-en-Josas, France, Ehrlich is part of a group, the Meta-

CREDITS (TOP TO BOTTOM): RADE LUKOVIC/THINKSTOCK; JASON HE

HIT consortium, investigating connections between microbial genes in human intestines and human health. By comparing such genes from obese and nonobese individuals, he and his colleagues have found that certain sets of bacterial genes and bacteria correlate with excess weight and insulin resistance.

The researchers first sequenced all the bacterial genes in stool samples of 177 Danes, 55 who were thin and 122 who were either overweight or obese. Although the researchers concluded that most participants in the study had roughly 600,000 distinct bacterial genes in their guts, almost one-third of the obese study participants had only about 360,000 such genes, 30% to 40% fewer. A similar percentage of 36 obese French people had a comparable dearth of gut bacteria genes, Ehrlich reported at the Vancouver meeting. Moreover, the obese people "don't have as great a bacterial diversity" in their guts, Ehrlich reported. One missing microbe in that group was a methane producer, leading Ehrlich to wonder whether "the carbon that does not get out [of the body] as gas could be incorporated as fat."

When they looked at medical histories of all their study subjects, Ehrlich and his colleagues found that the obese people with fewer gut bacteria genes were more likely to be insulin resistant than were the obese people who had a typical tally of intestinal microbial genes. These obese people also tended to have higher than normal white blood cell counts, suggesting that they were in a state of low-level inflammation, Ehrlich said. Some researchers have found evidence of a link between inflammation and obesity (*Science*, 17 December 2010, p. 1621).

Ehrlich and his colleagues have also tested whether the types of bacteria in a person's gut can "diagnose" obesity. Using just six metaspecies, they were able to correctly predict whether a person was lean or obese more than 80% of the time, he reported. When researchers try to make the same predictions by considering all of a person's genetic risk factors for obesity, they are right only 58% of the time, Ehrlich pointed out.

At this point, however, it's unclear whether the differences in intestinal microbes are "the cause, a contribution to, or the consequence" of obesity, notes Ehrlich. "If we can provide evidence that they [at least] provide a contribution, then we can go and find a treatment."

Help from the Amish

Other work presented at the microbiome meeting indicates that sorting out this cause-and-effect puzzle will be tough. Frustrated by the inconsistent results others were getting when they looked for connections between the microbiome and obesity, Fraser-Liggett and her colleagues examined 400 adult Amish living in Pennsylvania. Amish marry within their group and have very similar lifestyles, environment, and eating habits—they even cook in communal kitchens. Thus, Fraser-Liggett hoped to eliminate some of the variables that might have confounded other studies.

The body mass index of Amish ranged from 16 to 51 (30 is obese), and some of the obese ones also had metabolic syndrome. Fraser-Liggett and her colleagues captured a snapshot of the gut microbiome of each Amish by obtaining stool samples, sequencing the DNA in them, and using the 16*S* ribosomal subunit gene often used to tell bacteria apart, identifying any microbial components. Although the scientists did detect some differences in certain bacteria between obese and lean Amish, they didn't find the dramatic shifts that Gordon had documented between lean and obese mice, Fraser-Liggett reported at the meeting.

One problem may be that simply taking a census of the bacteria present in a person's gut may not be enough. "16*S* [analysis] is not very informative," Ehrlich says. "We need to go to more precise measures." Increasingly, microbiome researchers are looking at what bacterial genes are active in a person and not just at which bacteria are there. Scientists have found that although the species mix of the microbiome may vary significantly from one person to the next, those individuals often still have equivalent complements of bacterial genes at work inside them. Through such gene analyses, researchers can begin to better assess what the bacteria in the gut are really doing to, or for, their host, Fraser-Liggett notes.

Gordon suggests that more clarity on the obesity-microbiome issue will also come from using the guts of mice as bioreactors for human microbes. His group has pioneered the study of germ-free mice, which are grown in a sterile environment from birth, and he is now exposing such mice to bacteria from human guts. Once those human microbes have established residence in the guts of the mice, Gordon then feeds the animals a variety of human diets. Using these rodent proxies, he can thus track how different diets affect the "human" microbiomes, assessing the bacteria as often as he needs to to get a dynamic picture. "You can sample many features between the microbial community and the host," he says.

Personalized microbiota. Germ-free mice grown in sterile environments and given human gut microbes provide a way to test links between bacteria and obesity.

CREDIT: LAURA KYRO/CENTER FOR GENOME SCIENCES & SYSTEMS BIOLOGY

Despite his role in igniting the study of obesity and microbiomes, Gordon resists the idea that our gut bacteria are the sole explanation for the growing number of obese people. "It's not the dominant part of the problem; excessive energy intake is," he contends. The simplistic notion of only changing one's gut bacteria to lose weight has been "hyped a lot," he complains.

Others, such as microbial ecologist Liping Zhao of Shanghai Jiao Tong University in China, are more convinced that the microbiome will prove important when it comes to obesity. "Increased abundance of 'bad genes' and [a] decrease of 'good genes' in our diet-disrupted gut microbiome [may] be the primary driving force for this obesity epidemic," Zhao says.

Even if Zhao's prediction proves right, the studies to date make clear that the connection between the microbiome and excess weight is complex, Fraser-Liggett says. For those looking to bacteria to stem the obesity epidemic, she concludes, "there's clearly no magic formula." **–ELIZABETH PENNISI**

“A dream told me to do it.”

Dr. Carl Alving on his inspiration for inventing the vaccine patch.

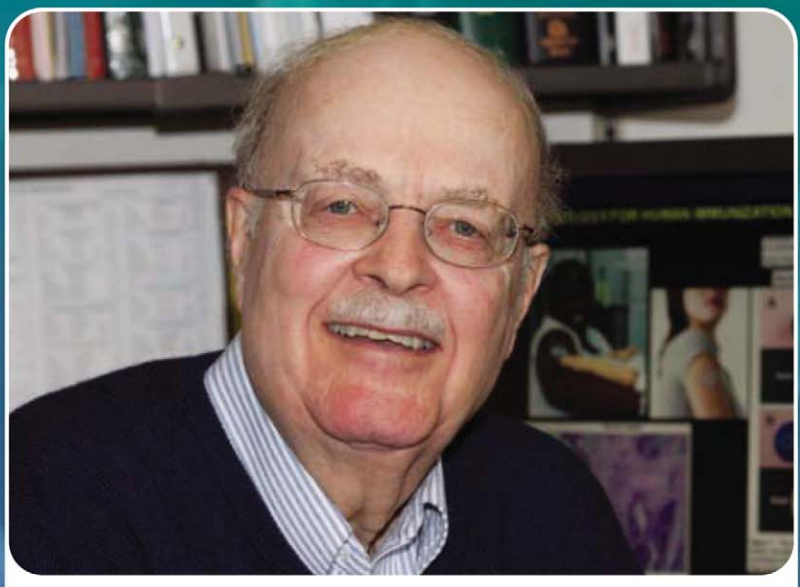

Carl R. Alving, M.D.
Chief of the Department of Adjuvant & Antigen Research, Division of Retrovirology
at the Walter Reed Army Institute of Research
AAAS member

MemberCentral is the new website that looks at science through the eyes of AAAS members. It celebrates their achievements—like Dr. Alving’s vaccine patch—and their shared belief in the transformative power of science. Use **Member**Central to connect with other members, learn about work being done in other fields, and get fresh perspectives on issues ranging from speciation to STEM education.

Visit **Member**Central today and get to know the AAAS member community in a whole new way.

AAAS MEMBERCENTRAL

MemberCentral.aaas.org

Blogs | Videos | Webinars | Discounts | Downloads | Community

LETTERS

edited by Jennifer Sills

Protecting Invaders for Profit

HUMANS HAVE SPREAD SPECIES TO NONNATIVE ENVIRONMENTS FOR generations. In turn, these species can become invasive, threatening native species. There has been much discussion about the best way to control invasive species and protect native species (*1*). However, one point has been overlooked: In some cases, human commercial activity values invasive species more than the native species, and dangerous behavior ensues. For example, trout (e.g., *Salvelinus sp.*) and red deer (*Cervus elaphus*) were introduced to Argentina and Chile from the United States and Europe about 100 years ago for fishing and hunting purposes. Today, these species are invasive, but they represent an economic resource for tourism and sport (*2*, *3*). Because of their commercial value, the Argentinean and Chilean governments maintain healthy populations by setting restrictions on hunting and fishing seasons and the number of fish allowed per day. Similarly, the Argentinean government allows local people to profit by hunting and selling the invasive hare (*Lepus europaeus*) by millions to Europe (*4*). In Patagonia, many farmers hunt or poison native guanacos (*Lama guanicoe*) to avoid competition with nonnative livestock or red deer. Some nonnative species are even advertised as "typical" in the countries where they are introduced. As a result, the citizens of southern South America do not consider invasive species a problem (*5*).

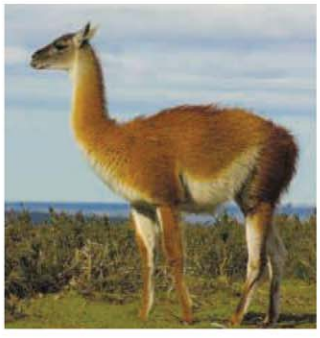

Native species at risk. Farmers in Patagonia hunt guanacos to protect nonnative deer.

It is impractical to eradicate some invasive species. However, by valuing them more than native species, we are promoting their expansion and endangering the native species. The discussion about invasive species must focus on the prevention of their social and commercial overvaluation. We must also educate both local communities and governments about the importance of maintaining and recovering native species populations. In the long run, the negative consequences of species introductions are greater than their short-term commercial benefits (*6*).

SERGIO A. LAMBERTUCCI* AND KARINA L. SPEZIALE

Ecotono Laboratory, INIBIOMA (Comahue National University-CONICET), Bariloche, Argentina.

*To whom correspondence should be addressed. E-mail: slambertucci@comahue-conicet.gob.ar

References

1. D. M. Richardson, Ed., *Fifty Years of Invasion Ecology: The Legacy of Charles Elton* (Wiley-Blackwell, Oxford, 2011).
2. M. A. Pascual *et al*., *Front. Ecol. Environ*. **7**, 533 (2009).
3. T. Veblen *et al*., *Conserv. Biol*. **6**, 71 (1992).
4. S. A. Lambertucci *et al*., *Environ. Sci. Technol*. **44**, 7759 (2010).
5. K. L. Speziale, S. A. Lambertucci, *Nature* **467**, 153 (2010).
6. D. Pimentel *et al*., *Agr. Ecosyst. Environ*. **84**, 1 (2001).

Culturomics: Statistical Traps Muddy the Data

IN THEIR GENERALLY WORTHWHILE DISCUSsion of developments in the English language ("Quantitative analysis of culture using millions of digitized books," Research Article, 14 January, p. 176), J.-B. Michel *et al*. fall into two common traps. First, they assume that the total number of words published in English is a meaningful statistic. Although this figure seems impressive—and has traditionally been used to validate English speakers' belief that their language is exceptional [e.g., (*1*)]—it primarily reflects the large number of English speakers and their relatively high per capita publication rates. The statistic has little to do with the number of words available to an individual English speaker. Second, the authors claim that the English lexicon "is enjoying a period of enormous growth" and that "the size of the language" has grown "by over 70% during the past 50 years." However, they are not measuring the English lexicon directly; they are measuring the written record of the English lexicon. These two concepts should be kept distinct. If the fossil record shows more dinosaur footprints in one period than another, it does not necessarily mean that there were more dinosaurs—it may be that there was more mud.

ELISE E. MORSE-GAGNÉ

Department of English, Tougaloo College, Tougaloo, MS 39174, USA. E-mail: egagne@tougaloo.edu

Reference

1. H. Bradley, *The Making of English* (MacMillan, London, 1904; reprinted by Dover, New York, 2006), p. 78.

Letters to the Editor

Letters (~300 words) discuss material published in *Science* in the past 3 months or matters of general interest. Letters are not acknowledged upon receipt. Whether published in full or in part, Letters are subject to editing for clarity and space. Letters submitted, published, or posted elsewhere, in print or online, will be disqualified. To submit a Letter, go to www.submit2science.org.

Culturomics: Periodicals Gauge Culture's Pulse

FROM THE PERSPECTIVE OF AN ARTIST who mines digital information to understand shifts in temporal culture, the analysis of Google books and the initial description of trends in our culture by J.-B. Michel *et al*. ("Quantitative analysis of culture using

millions of digitized books," Research Article, 14 January, p. 176) is an important step forward in using current digital techniques as a window into history. Although Michel *et al.*'s study was rigorous, the selection of books has certain drawbacks. First, the sample reflects not all published books, but only those that Google or their partners deemed worthy of digital reproduction. Second, and more important, books are inherently more distant from the pulse of a culture than periodicals, in particular newspapers. Book publishing has a substantial lag time to print; periodicals are closer to real-time. Furthermore, as we move further away from news media, we see a shift toward greater analysis, filtering, and a narrowing of subjects. For these reasons, analyses of culture based on the written record should include a wide variety of texts. One of the ultimate challenges to this type of research is representing information in a manner that is effective and relevant to viewers within our culture.

TIM SCHWARTZ

Department of Visual Arts, University of California, San Diego, La Jolla, CA 92093–0327, USA. E-mail: tim.c.schwartz@gmail.com

Response

WE THANK MORSE-GAGNÉ AND SCHWARTZ FOR their Letters, and we are happy to have the opportunity to clarify.

Morse-Gagné questioned whether the size of the English lexicon is a meaningful statistic and points out that such measures are usually associated with rather dubious attempts to prove the superiority of the English language. We share her concern. The concept of a "word" is a fuzzy notion, and ambiguities in how it is defined invariably affect the results of any lexical census. Yet the size of the English lexicon remains a perennial question, and a working definition is needed if we hope to address whether and how our vocabulary is growing. As such, we dealt with the question as best we could: We explicitly defined the notion of "word" as a meaningful string of alphabetic characters that is free of typographical errors and that appears in the text of published books with a frequency greater than one part per billion. Crude though it may be, this approach avoids many of the subjective judgments associated with other attempts to measure the size of the lexicon. We agree with Morse-Gagné that the resulting count of over a million words should not be used to justify anglophilic chauvinism.

We disagree with Morse-Gagné's argument that our measurements of lexical size are consequences of the number of English speakers and their publication rates. Our methods require each word to appear with a frequency of greater than 1 part per billion in the corresponding time period. (Each time period is represented by many billions of words.) Thus, to use Morse-Gagné's analogy, our count of "dinosaur footprints" included careful

CORRECTIONS AND CLARIFICATIONS

Review: "Homoplasy: From detecting pattern to determining process and mechanism of evolution" by D. B. Wake *et al*. (25 February, p. 1032). In the legend to Fig. 1B, the third sentence should have read: "One mode (which has evolved in two independent lineages) elongates individual vertebrae (II); the alternative mode adds vertebrae (III) (*48*)." In the legend to Fig. 3, the fourth sentence should have read: "The phylogeny of Zingiberales indicates the relationships of the eight families with important character transitions (*34*)." The fifth sentence should have read: "For each family, the organs characteristic of each whorl are indicated: green, sepal; orange, petal; yellow, fertile stamen; light orange, petaloid stamen/staminode; blue, carpel." The ninth sentence should have read: "(c and d) Monocostus (Costaceae) flower with distinct sepal and petal whorl organs, fused outer and inner petaloid staminodes forming the labellum, and (d) a single fertile petaloid stamen from the inner stamen whorl."

Perspectives: "Life on low flame in hibernation" by G. Heldmaier (18 February, p. 866). In the fourth paragraph, the basal metabolic rate of bears was incorrect. The correct figure is 0.276 ml O_2 g^{-1} $hour^{-1}$.

Editors' Choice: "Extinction's cause and effect" by N. S. Wigginton (4 February, p. 512). The field heading should have been Paleontology rather than Archaeology.

News Focus: "The Human Genome (patent) Project" by S. Kean (4 February, p. 530). Affymetrix was misidentified. The company does not provide diagnostic services. It provides microarray and clinical application technologies, such as gene chips, for diagnostics work. The story should also have noted that Affymetrix customers, not Affymetrix itself, must clear legal rights for any gene patents when using Affymetrix products.

CREDIT: MAGNUS ELANDER

News Focus: "Going the distance" by E. Pennisi (28 January, p. 395). The researcher in the picture (left) on page 395 was incorrectly identified. He is Anders Kvist, who worked extensively with Blue, the bird who flew 16 hours in a wind tunnel.

News of the Week: "New high-tech screen takes carrier testing to the next level" by J. Couzin-Frankel (14 January, p. 130). A caption incorrectly states that Lesch-Nyhan syndrome, a rare childhood disease, occurs when both parents carry the mutated gene. In fact, the syndrome is an X-linked disorder, so only the mother needs to be a carrier.

controls for the preponderance of mud.

Schwartz notes that our reliance on book data might influence our results. We agree that it will be important to expand our data beyond books, as we emphasized in the final section of our paper. However, digitization at the culturomic scale—all books, all newspapers, all magazines, all manuscripts—remains in its infancy. We chose to study books because they are one of the few types of materials for which comprehensive data is available. If thoughtful scholars like Morse-Gagné and Schwartz continue to lend their voices and pens to the cause, future scholars will have a wider array of options.

EREZ LIEBERMAN AIDEN,[1,2]* JOSEPH P. PICKETT,[3] JEAN-BAPTISTE MICHEL[2,4]*

[1]Harvard Society of Fellows, Cambridge, MA 02138, USA. [2]Visiting Faculty, Google, Inc., Mountain View, CA 94043, USA. [3]American Heritage Dictionary, Houghton Mifflin Harcourt, Boston, MA 02116, USA. [4]Department of Psychology, Harvard University, Cambridge, MA 02138, USA.

*To whom correspondence should be addressed. E-mail: erez@erez.com (E.L.A.); jbmichel@gmail.com (J.-B.M.)

Longer Trips Possible for Human Missions

IN HIS NEWS FOCUS STORY "NASA WEIGHS asteroids: Cheaper than moon, but still not easy" (18 February, p. 841), R. Kerr discusses NASA's search for destination near-Earth asteroids (NEAs) and the hope that a suitably sized candidate NEA, which can serve as a "stepping stone" for humans to continue to explore space, can be found by the mid-2020s.

NASA faces these obstacles because of overly severe mission constraints. For example, longer trip durations should be considered. Four cosmonauts have spent a year or more at a time in Earth orbit, and there are experiments in progress, such as Mars500, to explore the physiological and psychological aspects of long-duration space voyages. Programmatically, Earth-to-NEA round-trip duration times of 12, 18, or 24 months make sense if we are serious about preparing for trips to Mars and beyond.

Of course, it will take hard work and significant new research to generate the confidence required to send humans on such trips and expect them to return intact. Fortunately, we already have two major assets: Russian/Soviet experience in long-duration space flight, and the International Space Station, which was originally conceived for exactly this purpose.

APOSTOLOS CHRISTOU

Armagh Observatory, College Hill, Armagh BT61 9DG, UK. E-mail: aac@arm.ac.uk

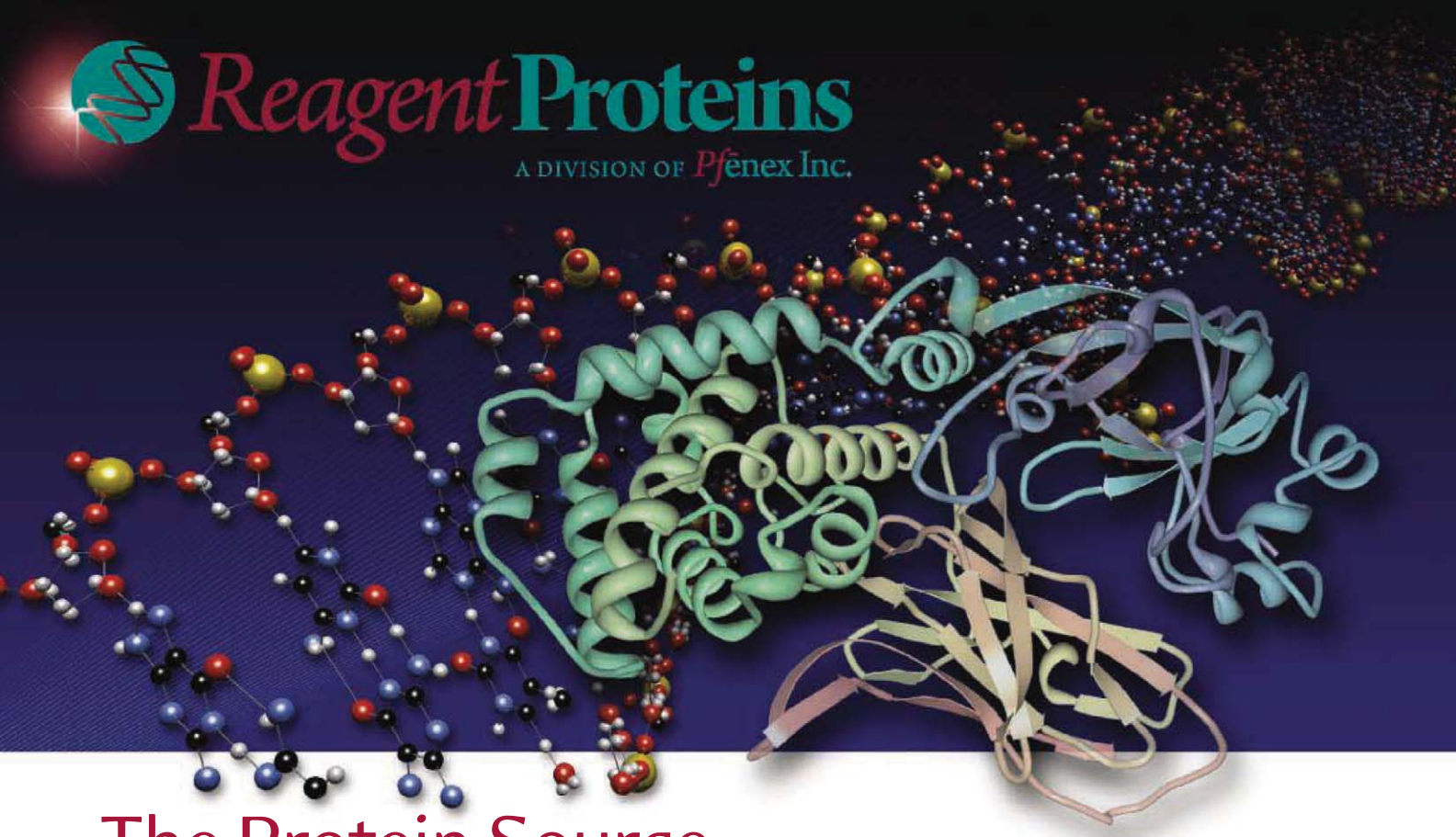

The Protein Source *for Vaccine Development*

Reagent* Proteins** is ***the source for high quality reagent, pre-clinical and cGMP proteins.

Harness the Quality and Power of *Pf*ēnex Expression Technology™

- Recombinant CRM197 and other conjugate vaccine carrier proteins available in pre-clinical and cGMP grade
- Speed your vaccine to the clinic
- Avoid slow, complex and costly production in a pathogenic organism
- Access to Biologic Master File to support IND & BLA filings
- High quality and cost-effective solution for sourcing critical vaccine components

Visit our website for a complete listing of over 2,300 high quality reagent proteins, specialized products and vaccine components.

Reagent Proteins
A DIVISION OF Pfenex Inc.

phone 858 · 352 · 4400 **reagentproteins.com** fax 858 · 352 · 4602

HISTORY OF SCIENCE

The Inquisitive West

Saleem H. Ali

Intellectual Curiosity and the Scientific Revolution
A Global Perspective
by Toby E. Huff
Cambridge University Press, Cambridge, 2011. 368 pp. $90, £60. ISBN 9781107000827. Paper, $27.99, £17.99. ISBN 9780521170529.

Why have some human societies achieved greater scientific accomplishments than others? In *Intellectual Curiosity and the Scientific Revolution*, Toby Huff takes a cultural perspective to explain Western dominance in the sciences. Distinguishing engineering prowess (such as the construction of hydrological systems) from scientific inquiry, he argues that a "curiosity deficit" in the Orient led to scientific stagnation there.

Huff (a sociologist who has turned to the history of science) begins by laying out evidence for Western ascendance in the sciences during the late 16th and 17th centuries. Showing little patience for those who romanticize oriental equivalence in scientific achievement, he convincingly argues how key scientific discoveries (from the laws of planetary motion to anatomical function) were largely products of occidental science. He further challenges the notion of collective learning through colonialism by noting that much of the West's colonial ventures in the East began much later (in the 19th century). Focusing on Chinese and Islamic societies, he argues that most consequential knowledge transfer that occurred was in fact from West to East, particularly by Jesuits in China.

A case study of the invention of the telescope provides the book's core example of Western scientific superiority. Using rigorous historical analysis, Huff carefully traces the knowledge of optics that led to this instrument and the subsequent transfers of the science and telescopes to China, India, and the Ottoman Empire. He offers ample allusions to primary texts and illustrations alongside critical appraisals of secondary commentaries. Huff supplements this core case with considerations of the invention of the microscope, the development of microbiology, and the evolution of early physics (particularly pneumatics and electromagnetism). The knowledge of these discoveries, he argues, was conveyed across the Muslim and Chinese realms but led to little further innovation.

Although Huff gives credit to notable inquisitive researchers in the Islamic tradition (such as Ibn al-Haytham in optics and Ibn Bajja in the science of motion), he takes the inability of such stalwarts to create a larger scientific enterprise in their societies as indicating a systemic cultural problem. The original scientific achievements within the Islamic tradition largely occurred between the 10th and 12th centuries, when there was a willingness for collective learning and a transmission of Greek texts to Western Europe. However, the commendable contributions of the "Arab masters" in areas such as trigonometry were confined. Like earlier Greek discoveries, Muslim contributions to science atrophied and did not lead to historically transformative inventions. Huff also convincingly dismisses specific claims of Arab scientific influence on the West, such as the impact of Nasir al-Din al-Tusi on Copernicus.

One senses a strong undercurrent of Protestant exceptionalism throughout Huff's narrative, in keeping with his earlier work and admiration for Max Weber (*1*). He claims that religious impediments to science were less substantial in Europe than in other parts of the world and that episodes, such as Galileo's conflicts with the Church, have been overplayed by historians. Despite many tensions, Christian Europe had a greater capacity to accept scientific enterprise. Referring to Martin Luther's Wittenberg campaign, Huff comments that "it is extremely difficult to imagine an Islamic scholar" of the 16th or 17th century "posting such a challenge on the door of the Great Mosque in Damascus." In this context, he might also have discussed the role played by clergy such as Gregor Mendel and Thomas Malthus in scientific discovery.

Although Christianity had its set of religious taboos, Huff argues that these were surmounted through a higher literacy rate and the rise of news publications. Perhaps adaptation was also inhibited by greater structural inertia in Islam and Chinese religious traditions. For example, Muslim scientists, despite their potential and intellect for innovation, were prevented from achieving breakthroughs in anatomy because of Islamic prohibitions on dissection and an "aversion to artistic representation of the human body."

In the case of China, Huff highlights the work of Xu Guangqi as a proponent of scientific inquiry after his conversion to Christianity by Jesuit missionaries. The Chinese, however, were reluctant to widely disseminate the new knowledge, and much of the telescope's use was relegated to ratifying cosmological myths. Huff's account falters slightly at this point, because he diminishes the role of Christian evangelism in also hindering scientific knowledge transfer. The ulterior religious motives of the Jesuits may have prompted the reluctance of the Chinese to embrace scientific transmission of knowledge. Had the transmission of science been for purely societal good, its reception may have been different indeed.

Huff does not explore ecological factors, such as those discussed by Jared Diamond (*2*), that might offer further insights into a Western propensity for scientific innovation. Nor does he consider developments in Africa, Mesoamerica, or Oceania.

Despite *Intellectual Curiosity and the Scientific Revolution* being somewhat circumscribed by Huff's sociological and geographic causality, he should be commended for boldly tackling a topic that deserves further historical analysis. While inquisitive impulses are possible in any society, some have been able to embrace this essential scientific attribute more so than others. Instead of feeling threatened by this revelation as a Western idea, all societies should strive for scientific excellence as a fundamentally human quest.

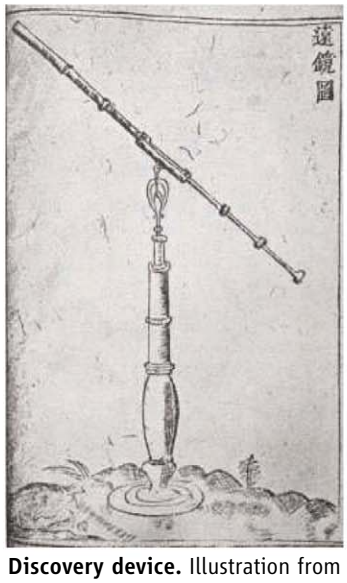

Discovery device. Illustration from Johann Adam Schall von Bell's *Treatise on the Telescope* (1626).

CREDIT: COURTESY TOBY HUFF

The reviewer is at the Rubenstein School of Environment and Natural Resources, University of Vermont, Burlington, VT 05405, USA. E-mail: saleem@alum.mit.edu

References

1. T. E. Huff, *Max Weber and the Methodology of the Social Sciences* (Transaction, New Brunswick, NJ, 1984).
2. J. Diamond, *Guns, Germs, and Steel: The Fate of Human Societies* (Norton, New York, 1997).

10.1126/science.1204095

SCIENCE IN FILM

The Immoralist

Michael Shermer

Beware the prophet who proclaims that the apocalypse, the resurrection, or the biggest thing to happen to humanity ever will arrive in the prophet's own lifetime. It is our natural inclination to assume that we are special and that our generation will witness the new dawn, but the Copernican principle tells us that we are not special. Thus, the chances that even a science-based prophecy such as that proffered by the futurist, inventor, and scientistic visionary extraordinaire Ray Kurzweil—that by 2029 we will have the science and technology to live forever—is unlikely to be fulfilled.

Barry Ptolemy's *Transcendent Man* is a beautifully crafted and artfully edited documentary about Kurzweil and his quest to save humanity. If you enjoy contemplating the big questions in life from a scientific perspective, you will love this film. Accompanied by the eerily haunting music of Philip Glass (who, appropriately enough, also scored Errol Morris's film *The Fog of War*—about another bigger-than-life character who thought he could mold the world through data-driven decisions, Robert McNamara), *Transcendent Man* pulls viewers in through Kurzweil's vision of a future in which we merge with our machines and vastly extend our longevity and intelligence to the point where even death will be defeated. That point is Kurzweil's "singularity," and he arrives at the 2029 date by extrapolating curves based on what he calls the "law of accelerating returns," which is Moore's law (the doubling of computing power every year) on steroids, applied to every conceivable area of science, technology, and economics.

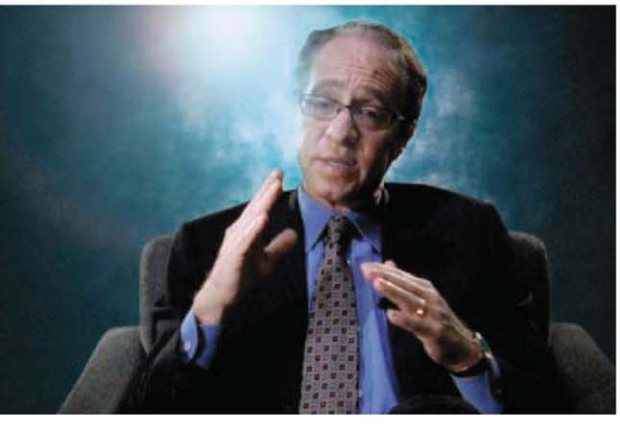

While Ptolemy's portrayal of Kurzweil is unmistakably positive, to his credit he includes several critics from both religion and science. Radio host Chuck Missler, a born-again Christian who heads the Koinonia Institute ("dedicated to training and equipping the serious Christian to sojourn in today's world") proclaims: "We have a scenario laid out that the world is heading for an Armageddon and you and I are going to be the generation that's alive that is going to see all this unfold." Missler seems to be saying that Kurzweil is right about the second coming but wrong about what it is that is coming. Another religiously based admonition comes from the Stanford University neuroscientist William Huribut, who identifies himself as a "practicing Christian." He believes in immortality but not in the way Kurzweil envisions it and pronounces: "Death is conquered spiritually."

Transcendent Man
The Life and Ideas of Ray Kurzweil
Barry Ptolemy, Director
Ptolemaic Productions and Therapy Studios, USA, 2009. 83 minutes.
http://transcendentman.com/

From the science side, Neil Gershenfeld, director of the Massachusetts Institute of Technology's Center for Bits and Atoms, sagely notes: "What Ray does consistently is to take a whole bunch of steps that everybody agrees on and take principles for extrapolating that everybody agrees on and show they lead to things that nobody agrees on." Likewise, the futurist Kevin Kelly, who has painted a much more realistic portrait of what our futures may (or may not) hold (*1*), comments that "the precursors of those technologies that would have to exist simply are not here." Although he find's Kurzweil's expectation "heartwarming," he predicts that "it isn't going to happen." While Kelly agrees that Kurzweil's exponential growth curves are accurate, he holds that the conclusions and especially the inspiration drawn from them are not. He identifies Kurzweil as "a modern-day prophet" for whom "nothing can waiver his absolutely certainty."

The film is clearly intended as an uplifting celebration of all the ways science and technology have enriched and are going to enrich our lives. I don't know if it is the music, the cinematography, or the subject himself, but I found *Transcendent Man* to be a sad film about a genius who has been in agony since the premature death of his father at age 58. Fredric Kurzweil was a professional musician who, Ray's mother says on camera, was never around while his charge was growing up. Like father, like son—Kurzweil's own workaholic tendencies in his creation of over a dozen companies starting when he was 17 meant he never really knew his father. As the film portrays the tormented inventor, Kurzweil's mission in life seems more focused on resurrecting his patriarch than rescuing humanity.

An especially lachrymose moment occurs when Kurzweil is riffling through his father's journals and documents in a storage room dedicated to preserving his memory until the day that all these "data" (including Ray's own fading memories) can be reconfigured into an artificial intelligence simulacrum, thus reuniting father and son. Through heavy sighs and wistful looks, Kurzweil comes off not as a proselytizer on a mission but as a man tormented. It is, in fact, the film's leitmotif. In one scene, Kurzweil wipes away a tear at his father's grave site, in another he pauses over photographs and looks longingly at mementos, and in yet another he recalls when his father, just days before his death, "uncharacteristically" phoned him, as if he'd had a premonition. Although Kurzweil says he is optimistic and cheery about life, he can't seem to stop talking about death: "It's such a profoundly sad, lonely feeling that I really can't bear it," he admits. "So I go back to thinking about how I'm not going to die." One wonders how much of life he is missing by overthinking death and how burdensome it must surely be to imbibe over 200 supplement tablets a day and have your blood tested and cleansed every couple of months, all in an effort to reprogram the body's biochemistry.

There is something almost religious about Kurzweil's scientism. He notes similarities between his goals and those of the world's religions: "the idea of a profound transformation in the future, eternal life, bringing back the dead." Although the film never discloses his religious beliefs (he was raised by Jewish parents as a Unitarian Universalist), in a (presumably) unintentionally humorous moment that ends the film, Kurzweil reflects on the god question and answers it himself: "Does God exist? I would say, 'Not yet.'" Cheeky.

The reviewer, the author of *The Mind of the Market*, is at Claremont Graduate University and *Skeptic* magazine, Post Office Box 338, Altadena, CA 91001, USA. E-mail: mshermer@skeptic.com

References

1. K. Kelly, *What Technology Wants* (Viking, New York, 2010).

10.1126/science.1205601

CREDIT: RAY KURZWEIL/COURTESY TRANSCENDENT MAN

CONSERVATION

Economic Importance of Bats in Agriculture

Insectivorous bat populations, adversely impacted by white-nose syndrome and wind turbines, may be worth billions of dollars to North American agriculture.

Justin G. Boyles,[1]* Paul M. Cryan,[2] Gary F. McCracken,[3] Thomas H. Kunz[4]

White-nose syndrome (WNS) and the increased development of wind-power facilities are threatening populations of insectivorous bats in North America. Bats are voracious predators of nocturnal insects, including many crop and forest pests. We present here analyses suggesting that loss of bats in North America could lead to agricultural losses estimated at more than $3.7 billion/year. Urgent efforts are needed to educate the public and policy-makers about the ecological and economic importance of insectivorous bats and to provide practical conservation solutions.

Infectious Disease and Wind Turbines

Insectivorous bats suppress populations of nocturnal insects (*1*, *2*), but bats in North America are under severe pressure from two major new threats. WNS is an emerging infectious disease affecting populations of hibernating cave-dwelling bats throughout eastern North America (*3*). WNS is likely caused by a newly discovered fungus (*Geomyces destructans*). This fungus infects the skin of bats while they hibernate and is thought to trigger fatal alterations in behavior and/or physiology (e.g., premature depletion of energy reserves) (*3*, *4*). Since February 2006, when WNS was first observed on bats in upstate New York, *G. destructans* has spread west of the Appalachian Mountains and into Canada. To date, over one million bats have probably died, and winter colony declines in the most affected region exceed 70% (*5*). Populations of at least one species (little brown bat, *Myotis lucifugus*) have declined so precipitously that regional extirpation and extinction are expected (*5*).

At the same time, bats of several migratory tree-dwelling species are being killed in unprecedented numbers at wind turbines across the continent (*6*, *7*). Why these species are particularly susceptible to wind turbines remains a mystery, and several types of attraction have been hypothesized (*6*). There are no continental-scale monitoring programs for assessing wildlife fatalities at wind turbines, so the number of bats killed across the entire United States is difficult to assess. However, by 2020 an estimated 33,000 to 111,000 bats will be killed annually by wind turbines in the Mid-Atlantic Highlands alone (*7*). Obviously, mortality from these two factors is substantial and will likely have long-term cumulative impacts on both aquatic and terrestrial ecosystems (*5*, *7*). Because of these combined threats, sudden and simultaneous population declines are being witnessed in assemblages of temperate-zone insectivorous bats on a scale rivaled by few recorded events affecting mammals.

Economic Impact

Although much of the public and some policy-makers may view the precipitous decline of bats in North America as only of academic interest, the economic consequences of losing so many bats could be substantial. For example, a single colony of 150 big brown bats (*Eptesicus fuscus*) in Indiana has been estimated to eat nearly 1.3 million pest insects each year, possibly contributing to the disruption of population cycles of agricultural pests (*8*). Other estimates suggest that a single little brown bat can consume 4 to 8 g of insects each night during the active season (*9*, *10*), and when extrapolated to the one million bats estimated to have died from WNS, between 660 and 1320 metric tons of insects are no longer being consumed each year in WNS-affected areas (*11*).

Estimating the economic importance of bats in agricultural systems is challenging, but published estimates of the value of pest suppression services provided by bats ranges

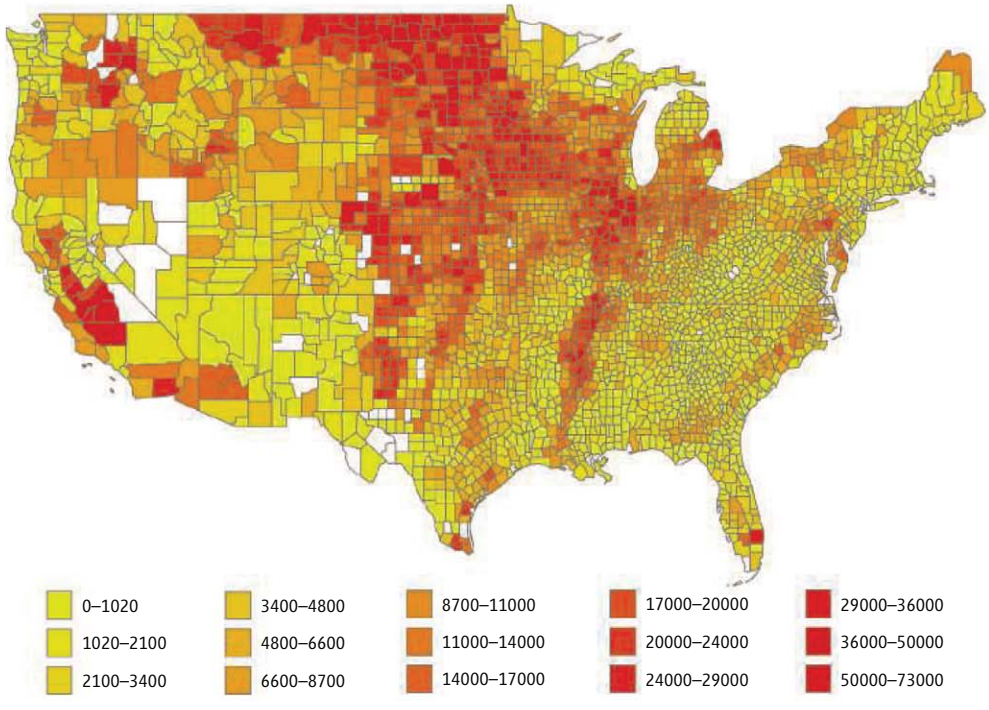

The worth of insectivorous bats. Estimated annual value of insectivorous bats in the agricultural industry at the county level. Values (×$1000 per county) assume bats have an avoided-cost value of ~$74/acre of cropland (*12*). (See SOM for details.)

[1]Department of Zoology and Entomology, University of Pretoria, Pretoria 0002, South Africa. [2]U.S. Geological Survey, Fort Collins Science Center, Fort Collins, CO 80526, USA. [3]Department of Ecology and Evolutionary Biology, University of Tennessee, Knoxville, TN 37996, USA. [4]Center for Ecology and Conservation Biology, Department of Biology, Boston University, Boston, MA 02215, USA.

*Author for correspondence. E-mail: jgboyles@zoology.up.ac.za

from about $12 to $173/acre (with a most likely scenario of $74/acre) in a cotton-dominated agricultural landscape in south-central Texas (*12*). Here, we extrapolate these estimates to the entire United States as a first assessment of how much the disappearance of bats could cost the agricultural industry [see supporting online material (SOM)].

Assuming values obtained from the cotton-dominated agroecosystem in Texas, and the number of acres of harvested cropland across the continental United States in 2007 (*13*), we estimate the value of bats to the agricultural industry is roughly $22.9 billion/year. If we assume values at the extremes of the probable range (*12*), the value of bats may be as low as $3.7 billion/year and as high as $53 billion/year. These estimates include the reduced costs of pesticide applications that are not needed to suppress the insects consumed by bats (*12*). However, they do not include the "downstream" impacts of pesticides on ecosystems, which can be substantial (*14*), or other secondary effects of predation, such as reducing the potential for evolved resistance of insects to pesticides and genetically modified crops (*15*). Moreover, bats can exert top-down suppression of forest insects (*1*, *2*), but our estimated values do not include the benefit of bats that suppress insects in forest ecosystems because economic data on pest-control services provided by bats in forests are lacking. Even if our estimates are halved or quartered, they clearly show how bats have enormous potential to influence the economics of agriculture and forestry.

Although adverse impacts of WNS on bat populations have occurred relatively rapidly, impacts of wind energy development appear to pose a more chronic, long-term concern. WNS has caused rapid and massive declines of hibernating bats in the northeastern United States, where this disease has persisted for at least 4 years (*5*). Thus, the coming growing season may be the first in which the adverse effects of this disease will become noticeable. Because of regional differences in crop production, the agricultural value of bats in the U.S. Northeast may be comparatively small relative to much of the United States (see the figure) (SOM). However, evidence of the fungus associated with WNS was recently detected in the Midwest and Great Plains, where the estimates of the value of bats to agriculture are substantial (see the figure). Additionally, because this region has the highest onshore wind capacity in North America, increased development of wind energy facilities and associated bat fatalities in this region can be expected (*16*). Thus, if mortality of bats associated with WNS and wind turbines continues unabated, we can expect noticeable economic losses to North American agriculture in the next 4 to 5 years.

Policy

A recently stated goal of the United Nations Environment Programme is to demonstrate the value of biodiversity to policy-makers and the public (*17*). In keeping with this goal, we hope that the scale of our estimates and the importance of addressing this issue will resonate both with the general public and policy-makers. Bats provide substantial ecosystem services worldwide, and their benefits to human economies are not limited to North America. For example, pioneering research in tropical ecosystems shows the importance of plant-visiting bats in the pollination of valuable fruit crops (*18*, *19*). Although the economic impacts of mass mortality of bats associated with WNS appear to be confined, at present, to North America, wind turbines are also causing bat fatalities in Europe (*20*), and the potential for WNS to spread to other parts of the world is unknown.

We suggest that a wait-and-see approach to the issue of widespread declines of bat populations is not an option because the life histories of these flying, nocturnal mammals—characterized by long generation times and low reproductive rates—mean that population recovery is unlikely for decades or even centuries, if at all. Currently, there are no adequately validated or generally applicable methods for substantially reducing the impacts of WNS or wind turbines on bat populations. To date, management actions to restrict the spread of WNS have been directed primarily toward limiting anthropogenic spread (e.g., cave and mine closures and fungal decontamination protocols) (*21*). Other proactive solutions for understanding and ameliorating the effects of WNS include developing improved diagnostics to detect early-stage infections and fungal distribution in the environment; defining disease mechanisms; investigating the potential for biological or chemical control of the fungus; and increasing disease resistance through habitat modification, such as creation of artificial or modified hibernacula that are less conducive to disease development and transmission (*11*, *22*). Other approaches, such as culling of infected bats have been widely discussed and dismissed as viable options for control (*23*). New research also shows that altering wind turbine operations during high-risk periods for bats significantly reduces fatalities (*24*, *25*). Specific action on these issues will benefit from scientific research carefully aimed at providing practical conservation solutions for bats in the face of new threats and at assessing their economic and ecological importance. We as scientists should also make concerted efforts to develop and use more effective methods for educating the public and policy-makers about the ecosystem services provided by bats.

Bats are among the most overlooked, yet economically important, nondomesticated animals in North America, and their conservation is important for the integrity of ecosystems and in the best interest of both national and international economies. In our opinion, solutions that will reduce the population impacts of WNS and reduce the mortality from wind-energy facilities are possible in the next few years, but identifying, substantiating, and applying solutions will only be fueled in a substantive manner by increased and widespread awareness of the benefits of insectivorous bats among the public, policy-makers, and scientists.

References

1. M. B. Kalka, A. R. Smith, E. K. V. Kalko, *Science* **320**, 71 (2008).
2. K. Williams-Guillén, I. Perfecto, J. Vandermeer, *Science* **320**, 70 (2008).
3. D. S. Blehert *et al.*, *Science* **323**, 227 (2009).
4. P. M. Cryan, C. U. Meteyer, J. G. Boyles, D. S. Blehert, *BMC Biol.* **8**, 135 (2010).
5. W. F. Frick *et al.*, *Science* **329**, 679 (2010).
6. P. M. Cryan, R. M. R. Barclay, *J. Mammal.* **90**, 1330 (2009).
7. T. H. Kunz *et al.*, *Front. Ecol. Environ* **5**, 315 (2007).
8. J. O. Whitaker, Jr., *Am. Midl. Nat.* **134**, 346 (1995).
9. E. L. P. Anthony, T. H. Kunz, *Ecology* **58**, 775 (1977).
10. A. Kurta, G. P. Bell, K. A. Nagy, T. H. Kunz, *Physiol. Zool.* **62**, 804 (1989).
11. J. G. Boyles, C. K. R. Willis, *Front. Ecol. Environ* **8**, 92 (2010).
12. C. J. Cleveland *et al.*, *Front. Ecol. Environ* **4**, 238 (2006).
13. USDA, *2007 Census of Agriculture: United States Summary and State Data*, vol. 1, *Geographic Area Series* (AC-07-A-51, USDA, Washington, DC, 2009).
14. D. Pimentel, in *Integrated Pest Management: Innovation-Development Process*, R. Peshin and A. K. Dhawan, Eds. (Springer Media, Houten, Netherlands, 2009), pp. 89–111.
15. P. Federico *et al.*, *Ecol. Appl.* **18**, 826 (2008).
16. D. L. Elliot, C. G. Holladay, W. R. Barchet, H. P. Foote, W. F. Sandusky, *Wind Energy Resource Atlas of the United States* (Solar Energy Research Institute, U.S. Department of Energy, Golden, CO, 1986).
17. The Economics of Ecosystems and Biodiversity, www.teebweb.org/.
18. S. Bumrungsri, E. Sripaoraya, T. Chongsiri, K. Sridith, P. A. Racey, *J. Trop. Ecol.* **25**, 85 (2009).
19. S. Bumrungsri *et al.*, *J. Trop. Ecol.* **24**, 467 (2008).
20. J. Rydell *et al.*, *Acta Chiropt.* **12**, 261 (2010).
21. U.S. Fish and Wildlife Service, www.fws.gov/whitenosesyndrome/.
22. J. Foley, D. Clifford, K. Castle, P. Cryan, R. S. Ostfeld, *Conserv. Biol.* **25**, 223 (2011).
23. T. G. Hallam, G. F. McCracken, *Conserv. Biol.* **25**, 189 (2011).
24. E. F. Baerwald, J. Edworthy, M. Holder, R. M. R. Barclay, *J. Wildl. Manage.* **73**, 1077 (2009).
25. E. Arnett *et al.*, *Front. Ecol. Environ* **16**, (2010). 10.1890/100103

Supporting Online Material

www.sciencemag.org/cgi/content/full/332/6025/41/DC1

10.1126/science.1201366

IMMUNOLOGY

Danger, Microbes, and Homeostasis

Hosts may modulate their immune response by measuring a combination of signals from pathogens and damaged tissue.

Brian P. Lazzaro[1] and Jens Rolff[2]

The immune system is conventionally viewed as a means to fight infection. It has become clear, however, that what is considered the "immune" system has also evolved to maintain homeostasis and regulate commensal microbes that normally inhabit the body. Such varied functions demand nuanced and context-appropriate control of immune responses. The thoughts on how immunity becomes activated include two views: by recognition of "nonself" molecules of infectious agents (*1*) or by recognition of "danger" signals—host molecules released by damaged host cells (*2*). Empirical evidence supports both models, but also reveals their limits. Insights from recent studies on insect immune systems, which are generalizable to vertebrates, suggest that the two models may be compatible. That is, a host determines the balance of nonself elicitors and danger signals to decide when to activate the immune system against pathogenic infection while also maintaining healthy relationships with commensals.

Bacterial associations with their hosts can be beneficial, damaging, or benign, depending on the context and the identity of players. It is generally believed that insects recognize bacteria through the presence of conserved molecules in the prokaryotic cell wall called "microbe-associated molecular patterns" (MAMPs). During infection, these molecules are recognized by pattern recognition receptors (PRRs) expressed by host cells, thereby triggering immune system activity and microbial elimination (*1*, *3*). The insect MAMP-PRR model is analogous to the distinction between self- and nonself molecules by the vertebrate immune system. But this concept of immunity poses a puzzle: If the immune system is hardwired to readily recognize and kill bacteria, how are symbiotic bacteria, which have enormous importance to the health and physiology of the host (*4*), maintained? Studies in insect model systems suggest that the joint presence of both MAMPs and danger signals may be required to launch a true defense response (*5*) and that insects have mechanisms for disregarding MAMPs presented in the absence of pathological damage to the host.

The animal gut is constantly exposed to potentially pathogenic bacteria that are ingested along with food. Yet, the gut is also the most important compartment of immune-modulated regulation of beneficial microbial communities that aid in digestion and nutritional assimilation (*4*). Beneficial microbes in both vertebrate and insect guts display MAMPs that are recognized by the immune system, yet immune activity is modulated such that the microbial community is actively regulated but not eliminated (*6*, *7*). Studies in the fruit fly *Drosophila melanogaster* have found that some MAMPs (peptidoglycan molecules) that are shed by bacteria in the gut induce expression of host proteins that degrade these MAMPs to a nonimmunostimulatory form (*6*, *8*). This negative-feedback loop dampens defense activity and allows the host to regulate commensal abundance without entirely eliminating the symbionts. Similar scenarios of the host inhibiting its defense response against mutualist symbionts have been described in bacteriomes, specialized organs where insects harbor mutualistic bacteria (*9*, *10*).

In addition to displaying MAMPs, true pathogens stimulate the release of danger signals by damaging host cells or secreting molecules that interfere with host biology. This combination of MAMPs and danger signals can override the homeostatic negative regulation of the insect immune system in tissues like the gut, resulting in a full-blown defense response that includes high expression of antibiotic proteins and biochemicals (*11*–*13*). Interestingly, the lower level of defense activity triggered even by commensals stimulates gut stem cell activity and epithelial renewal (*13*), providing an unexpected mechanism by which hosts and microbes interact to effect host homeostasis.

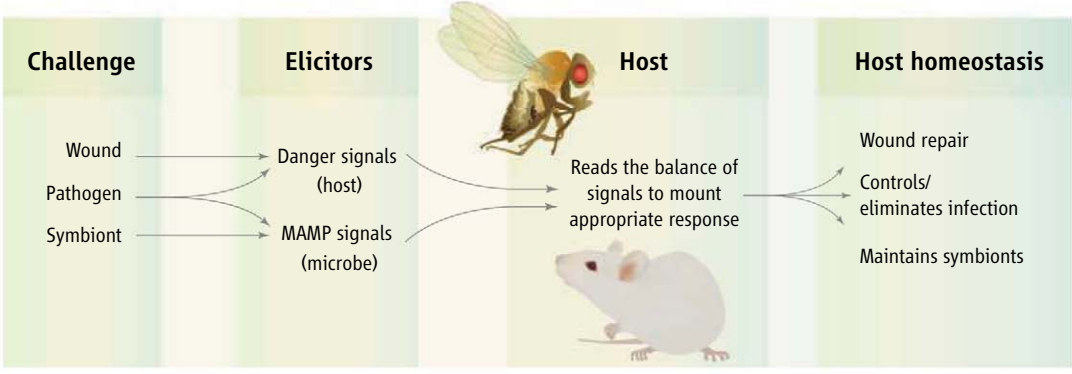

Elicitor ratio. Wounding, pathogen infection, and symbionts challenge the homeostasis of the host. A sterile wound generates exclusively danger signals, whereas symbionts display MAMPs without causing tissue damage that stimulates danger signals. Pathogens both display MAMPs and trigger danger signals, stimulating a robust immune response. The nature and strength of immune defense and homeostasis may be determined by the balance of danger and MAMP signals, combining the core tenets of the danger and infectious nonself models.

The reliance on the combination of danger signals and MAMPS to stimulate immune reactions is not restricted to gut tissues, but is a general property of defense activation. In the waxmoth *Galleria mellonella*, systemic bacterial and fungal infection results in damage to host cells and the release of collagen fragments and nucleic acids that synergize with MAMPs to stimulate an immune response (*14*). Extracellular collagen and nucleic acids are also danger signals in vertebrates (*15*, *16*). The expression of genes that encode antimicrobial peptides is induced by sterile wounding in insects, although this expression is transient in the absence of MAMPs (*17*).

The use of danger signals in combination with MAMPs may stem partly from an

[1]Department of Entomology, Cornell University, Ithaca, NY 14853, USA. [2]Department of Animal and Plant Sciences, University of Sheffield, Sheffield S10 2TN, UK. E-mail: jor@sheffield.ac.uk

economical approach to defense. In infections, the damage caused by pathogenicity must be offset against the costs of deploying an immune response (*18*). Rather than striving to completely eliminate infections, the immune system might manage a persistent infection at a low and nondamaging level (*19*). This is analogous to the concept of "economic injury level" in agricultural pest control, whereby pests are not eradicated but are suppressed to a threshold where the cost of pest-driven damage is lower than the cost of further control. MAMPs indicate the presence of microbes, but if the microbes are doing little or no damage to the host, the cost of immune activity may exceed the benefit of clearing the infection. The presentation of damage-triggered danger signals in conjunction with MAMPs, however, indicates a severe infection that justifies the expense of a defense response.

The immune system cannot afford to be rampantly stimulated by benign foreign molecules, but needs to determine whether a signal indicates microbial nonself or danger. Insights from insect immunity point to the possibility that both types of elicitors may be important in combination. Perhaps neither MAMPs nor danger signals are by themselves a sufficient cue for optimal regulation of host immunity, but together they constitute a reliable indicator for modulating the immune response to yield both effective defense and homeostatic regulation of commensal microbial communities (see the figure). In this scenario, the two models of immune activation (*1*, *2*) as triggered by nonself versus by danger signals need not be considered mutually exclusive, but could be merged into a single model where the host reads the balance of signals to mount an appropriate immunological reaction.This measuring of signals may allow the host to effectively fight an infection, while maintaining healthy relationships with commensals.

References and Notes

1. R. Medzhitov, C. A. Janeway Jr., *Science* **296**, 298 (2002).
2. P. Matzinger, *Science* **296**, 301 (2002).
3. E. Ragan, C. An, H. Jiang, M. Kanost, in *Insect Infection and Immunity*, J. Rolff, S. Reynolds, Eds. (Oxford Univ. Press, Oxford, 2009), pp. 34–48.
4. R. J. Dillon, V. M. Dillon, *Annu. Rev. Entomol.* **49**, 71 (2004).
5. R. E. Vance, R. R. Isberg, D. A. Portnoy, *Cell Host Microbe* **6**, 10 (2009).
6. J. H. Ryu, S. H. Kim, H. Y. Lee, J. Y. Bai, Y. D. Nam, J. W. Bae, D. G. Kee, S. C. Shin, E. M. Ha, W. J. Lee, *Science* **319**, 777 (2008).
7. N. H. Salzman, K. Hung, D. Haribhai, H. Chu, J. Karlsson-Sjöberg, E. Amir, P. Teggatz, M. Barman, M. Hayward, D. Eastwood, M. Stoel, Y. Zhou, E. Sodergren, G. M. Weinstock, C. B. Williams, N. A. Bos, *Nat. Immunol.* **11**, 76 (2010).
8. A. Zaidman-Rémy, M. Hervé, M. Poidevin, S. Pili-Floury, M. S. Kin, D. Blanot, B. H. Oh, R. Ueda, D. Mengin-Lecreulx, B. Lemaitre, *Immunity* **24**, 463 (2006).
9. C. Anselme, V. Pérez-Brocal, A. Vallier, C. Vincent-Monegat, D. Charif, A. Latorre, A. Moya, A. Heddi, *BMC Biol.* **6**, 43 (2008).
10. J. Wang, Y. Wu, G. Yang, S. Aksoy, *Proc. Natl. Acad. Sci. U.S.A.* **106**, 12133 (2009).
11. P. Liehl, M. Blight, N. Vodovar, F. Boccard, B. Lemaitre, *PLoS Pathog.* **2**, e56 (2006).
12. E.-M. Ha, C.-T. Oh, Y. S. Bae, W.-J. Lee, *Science* **310**, 847 (2005).
13. N. Buchon, N. A. Broderick, M. Poidevin, S. Pradervand, B. Lemaitre, *Cell Host Microbe* **5**, 200 (2009).
14. A. Vilcinskas, *Virulence* **1**, 206 (2010).
15. R. Lande, J. Gregorio, V. Facchinetti, B. Chatterjee, Y. H. Wang, B. Homey, W. Cao, Y. H. Wang, B. Su, F. O. Nestle, T. Zal, I. Mellman, J. M. Schröder, Y. J. Liu, M. Gilliet, *Nature* **449**, 564 (2007).
16. S. Gambaryan, A. Kobsar, N. Rukoyatkina, S. Herterich, S. Geiger, A. Smolenski, S. M. Lohmann, U. Walter, *J. Biol. Chem.* **285**,18352 (2010).
17. B. Lemaitre, J. M. Reichhart, J. A. Hoffmann, *Proc. Natl. Acad. Sci. U.S.A.* **94**, 14614 (1997).
18. B. P. Lazzaro, T. J. Little, *Philos. Trans. R. Soc. Lond. B Biol. Sci.* **364**, 15 (2009).
19. E. R. Haine, Y. Moret, M. T. Siva-Jothy, J. Rolff, *Science* **322**, 1257 (2008).

20. We thank O. Otti, A. Dobson, and S. Reynolds for comments on the manuscript.

10.1126/science.1200486

CELL BIOLOGY

Phosphatase Inhibition Delays Translational Recovery

A small molecule, guanabenz, increases survival of cells under stress.

R. Luke Wiseman[1] and Jeffery W. Kelly[1,2,3]

In cells, various signaling pathways help to maintain proteostasis—the proper concentrations, folding, and function of proteins. When a cell is under stress, upstream "stress sensors" within these pathways are activated, initiating a signaling cascade that minimizes the misfolding and aggregation of proteins, which can lead to disease (*1*–*3*). Stress sensors often respond to the accumulation of misfolded proteins within specific cell compartments by activating the transcription of proteostasis components, such as enzymes and "chaperone" proteins that assist with folding or by attenuating new protein synthesis. The propagation of stress-response signaling is often mediated by phosphorylation, or the addition of a phosphate group to the stress sensor and/or downstream signaling components. Because of the central importance of stress signaling pathways in maintaining the integrity of the cellular proteome, manipulating these pathways has become an attractive strategy for preventing the protein misfolding linked to numerous human diseases (*4*, *5*).

On page 91 of this issue, Tsaytler *et al.* take a step toward this goal. They demonstrate that the selective inhibition of a stress-induced phosphatase complex involved in a stress-signaling pathway that controls proteostasis in the endoplasmic reticulum (ER) increases cellular survival (*6*). This novel approach demonstrates the potential for manipulating stress-signaling cascades through direct targeting of a property that emerges from these complex signaling cascades (an emergent property), allowing for specific manipulation of stress signaling that is independent of pathways involved in general cellular homeostasis.

One of the best-characterized stress-responsive signaling pathways is called the unfolded protein response. It maintains proteostasis in the ER, where the secreted proteome is folded (*1*, *7*). The unfolded protein response comprises integrated signaling pathways that emanate from three transmembrane stress sensors localized in the ER: IRE1, ATF6, and PERK. These sensors are activated by the accumulation of misfolded proteins within the ER lumen. Activation of IRE1 and ATF6 enhances protein folding capacity within the ER lumen

[1]Department of Molecular and Experimental Medicine, Scripps Research Institute, La Jolla, CA 92037, USA. [2]Department of Chemistry, Scripps Research Institute, La Jolla, CA 92037, USA. [3]Skaggs Institute for Chemical Biology, Scripps Research Institute, La Jolla, CA 92037, USA. E-mail: wiseman@scripps.edu; jkelly@scripps.edu

through transcriptional up-regulation of ER chaperones, folding enzymes, and components of the ER-associated degradation pathway. Activation of PERK induces the selective phosphorylation of the α subunit of eukaryotic initiation factor 2 (eIF2α), which results in attenuation of ribosomal translation, thus reducing the load on the ER proteostasis network (see the figure). Phosphorylated eIF2α also selectively promotes translation of the transcription factor ATF4, which targets stress-responsive genes, including the transcription factor CHOP. In turn, CHOP induces transcription of the protein phosphatase 1 regulatory subunit GADD34 (also called PPP1R15A), which binds to the catalytic subunit of protein phosphatase 1. A heterodimer consisting of the protein phosphatase 1 catalytic subunit and GADD34 regulatory subunit selectively dephosphorylates eIF2α, thus providing a negative feedback loop in the PERK signaling cascade. This loop turns off signaling and facilitates restoration of ribosomal translation after ER stress.

Through expert detective work, Tsaytler *et al*. correctly suspected that the small molecule guanabenz selectively binds to GADD34. This prevents the assembly of the active protein phosphatase 1–GADD34 heterodimer and delays recovery from stress-induced translational attenuation (see the figure). Although guanabenz binds the stress-induced regulatory subunit GADD34, it does not bind the constitutively expressed eIF2α regulatory subunit CReP (PPP1R15B), which similarly forms a heterodimer with protein phosphatase 1 and catalyzes eIF2α dephosphorylation. Thus, guanabenz only slows eIF2α dephosphorylation during stress. In addition, guanabenz does not induce cytotoxicity on its own, as do other inhibitors of eIF2α phosphatases, such as calyculin A (*8*). Instead, guanabenz provides a boost to the endogenous PERK signaling pathway, extending the duration of translational attenuation and enabling the recovery from ER stress by targeting an emergent property of the PERK signaling cascade.

Research has shown that PERK signaling is critical for maintaining ER proteostasis in pancreatic beta cells expressing high levels of insulin (*9*). Thus, modulation of PERK signaling may alleviate ER stress associated with increased insulin production. Consistent with this hypothesis, Tsaytler *et al*. demonstrated that guanabenz dose-dependently protects cells against ER stress induced by the overexpression of a destabilized mutant insulin protein. Similarly, recent evidence suggests that increased activity of IRE1 and/or PERK signaling enhances mutant enzyme folding capacity within the ER, increasing trafficking and function of destabilized mutant proteins associated with lysosomal storage diseases (*10*). It would be interesting to see whether prolonged PERK signaling, enabled by guanabenz, is sufficient to restore mutant lysosomal enzyme proteostasis. Guanabenz also has the potential to modulate translational attenuation in response to other cellular stresses, such as amino acid deprivation, heme deficiencies, and oxidative insults that activate alternative eIF2α kinases (*11*, *12*). If so, it could potentially enhance cellular survival in a manner analogous to that observed by Tsaytler *et al*.

Multiple groups have sought, or are seeking, small molecules that can activate a specific arm or arms of the unfolded protein response (*4*), and there is optimism that these strategies will lead to the development of drugs targeting numerous maladies. Molecules such as guanabenz could represent an interesting category of these so-called proteostasis regulators, because they might be able to make up for insufficient stress-responsive signaling by prolonging its duration. The regulation of stress-response pathways is only partially understood, and it is likely that other strategies for extending the duration of stress responses exist, such as extending the duration of the cytosolic heat-shock response by modulating histone deacetylase (*13*). These agents could exhibit additive or synergistic properties with other stress-signaling pathway activators (*10*). This strategy, targeting an emergent property of stress-responsive signaling, represents an elegant opportunity for adapting proteostasis to treat human diseases.

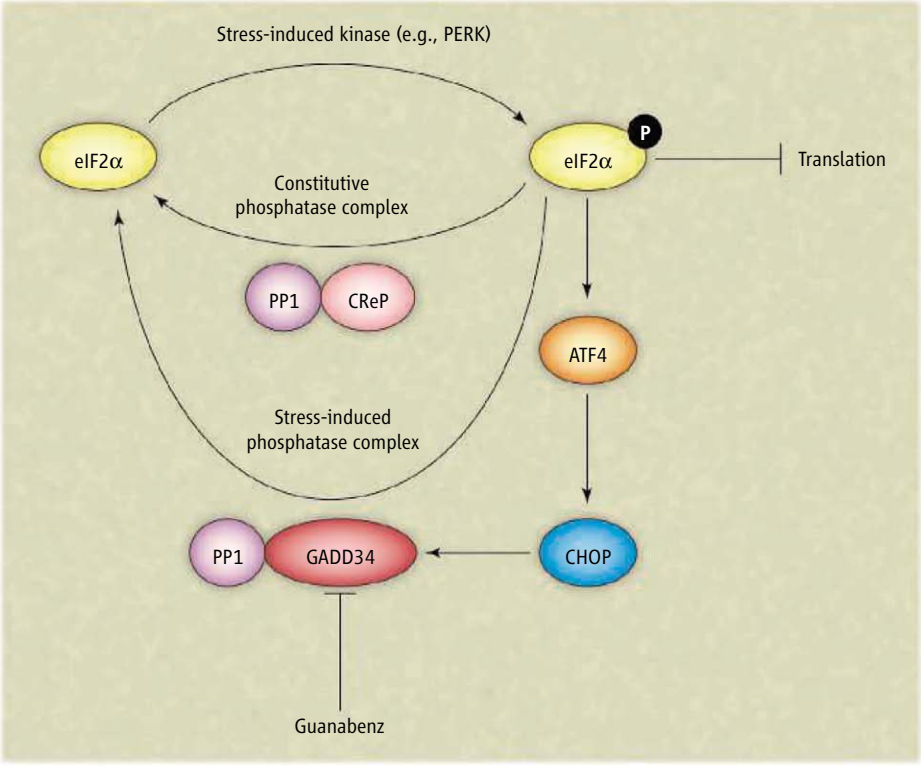

Enhancing proteostasis. Guanabenz selectively inhibits the GADD34-mediated negative feedback loop of PERK signaling through direct binding to GADD34, preventing its association with protein phosphatase 1 (PP1). As a result, guanabenz extends translational attenuation in response to ER stress, increasing chaperone-to-substrate ratios and alleviating protein misfolding within the ER lumen.

References

1. D. Ron, P. Walter, *Nat. Rev. Mol. Cell Biol.* **8**, 519 (2007).
2. R. I. Morimoto, *Genes Dev.* **22**, 1427 (2008).
3. C. M. Haynes, D. Ron, *J. Cell Sci.* **123**, 3849 (2010).
4. W. E. Balch, R. I. Morimoto, A. Dillin, J. W. Kelly, *Science* **319**, 916 (2008).
5. E. T. Powers, R. I. Morimoto, A. Dillin, J. W. Kelly, W. E. Balch, *Annu. Rev. Biochem.* **78**, 959 (2009).
6. P. Tsaytler, H. P. Harding, D. Ron, A. Bertolotti, *Science* **332**, 91 (2011); 10.1126/science/science.1201396.
7. M. Schröder, R. J. Kaufman, *Annu. Rev. Biochem.* **74**, 739 (2005).
8. M. Boyce *et al*., *Science* **307**, 935 (2005).
9. A. Volchuk, D. Ron, *Diabetes Obes. Metab.* **12** (suppl. 2), 48 (2010).
10. T. W. Mu *et al*., *Cell* **134**, 769 (2008).
11. R. C. Wek, H.-Y. Jiang, T. G. Anthony, *Biochem. Soc. Trans.* **34**, 7 (2006).
12. H. P. Harding *et al*., *Mol. Cell* **11**, 619 (2003).
13. S. D. Westerheide, J. Anckar, S. M. Stevens Jr., L. Sistonen, R. I. Morimoto, *Science* **323**, 1063 (2009).

10.1126/science.1204505

A Journal with Impact from AAAS, the publisher of *Science*

Science Translational Medicine

Integrating Medicine and Science

"The 2010 selection for the Nobel Prize in Physiology or Medicine as well as the three Lasker Awards brought welcome opportunities to celebrate truly groundbreaking translational research."*

This quote illuminates the importance of translational medicine discoveries. A recent journal article features the sequencing of fetal DNA from plasma of a pregnant woman to permit prenatal, noninvasive genome-wide screening to diagnose fetal genetic disorders.

Indexed in MEDLINE/PubMed

* Sci Transl Med 22 December 2010:
Vol. 2, Issue 63, p. 63ed9
DOI: 10.1126/scitranslmed.3001816

Recommend an institutional subscription to your library today!

ScienceOnline.org/recommend

Science Translational Medicine
AAAS

ScienceTranslationalMedicine.org

IMMUNOLOGY

An Innate Role for IL-17

Human genetic mutations point to a cytokine as critical for fighting a fungal infection.

Margarita Dominguez-Villar and David A. Hafler

Insight into the functional role of a particular component of the immune system, such as a cell type, cytokine, or constituent of a signaling pathway, can be gleaned from diverse human genetic mutations that have naturally occurred in critical immune system processes. For example, immune dysregulation polyendocrinopathy enteropathy X-linked syndrome is an autoimmune disease that was determined to be secondary to dysregulation of a subset of regulatory immune cells (CD4 subset of T cells) caused by mutations in the *FOXP3* gene. This discovery identified the transcription factor FOXP3 in controlling normal immune responses and raised the issue of defects in regulatory T cells in more common human autoimmune disorders (*1*). On page 65 of this issue, Puel *et al*. (*2*) report tracing an abnormal immune response to infection with the common fungus *Candida albicans* to mutations in components of a signaling pathway involving the cytokine interleukin-17 (IL-17).

Candida is a genus of commensal fungi found in the normal flora of the skin and mucosal surfaces of healthy individuals. Fungal infections (called candidiasis) with short-lived symptoms of oral thrush or vaginitis, though unpleasant, are not life-threatening. However, in some individuals, *Candida* spp. (*C. albicans* primarily) cause a persistent infection either by infecting mucosal and epidermal surfaces (mucocutaneous candidiasis) or by disseminating in the blood (systemic candidiasis). Mucocutaneous candidiasis is typically a chronic syndrome, whereas systemic candidiasis is acute. Chronic mucocutaneous candidiasis is a clinically highly heterogeneous infection, as it is usually associated with other severe infections, particularly in patients with acquired or inherited T cell immunodeficiencies [such as HIV (*3*) and severe combined immunodeficiency (*4*)] and/or autoimmune disorders. In a number of these cases, genetic alterations have been described in patients, such as in autoimmune polyendocrine syndrome type 1 (caused by mutations in the gene encoding the transcription factor autoimmune regulator (*AIRE*) (*5*)] or hyper-immunoglobulin E syndrome [caused by mutations in the gene encoding the transcription factor signal transducer and activator of transcription 3 (*STAT3*) (*6*)]. But *Candida* infection is also found as an isolated syndrome in the absence of other severe infections or autoimmune disorders. In this case, called chronic mucocutaneous candidiasis disease, the underlying etiology is unknown (*7*). Puel *et al*. describe two genetic etiologies of this syndrome: an autosomal dominant mutation in the gene encoding IL-17F, resulting in a deficiency in this cytokine; and an autosomal recessive mutation in the gene encoding interleukin-17 receptor A (IL-17RA), resulting in a deficiency in this receptor for the cytokine. These mutations clearly implicate the IL-17 immune pathway in this disease.

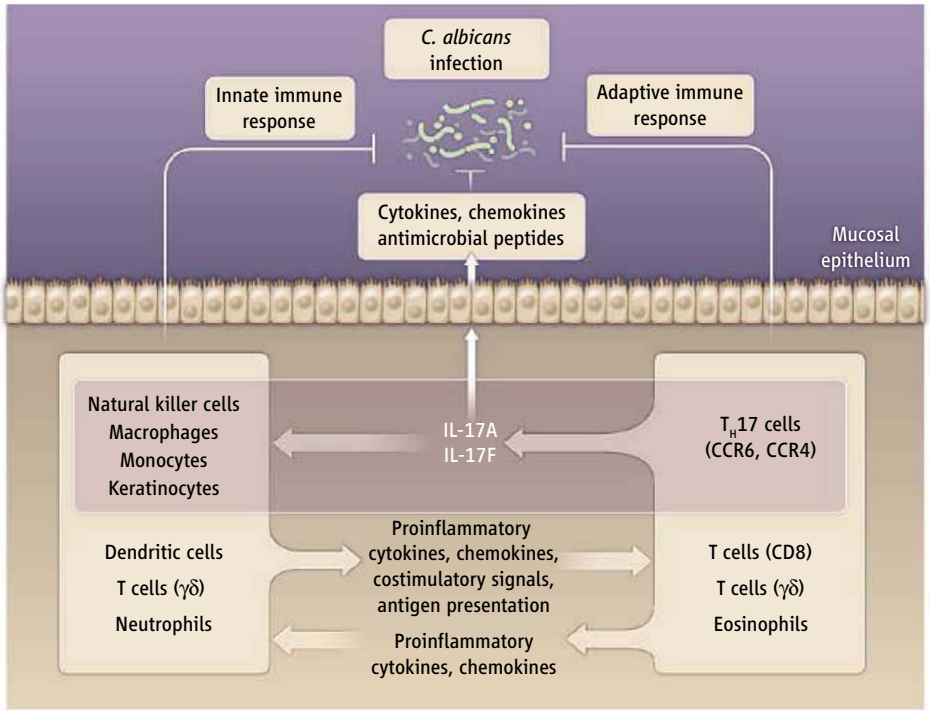

Handling *Candida*. Upon infection with the fungus *C. albicans*, innate immune cells instruct the adaptive arm of the human immune response to secrete IL-17, which acts on different cells that are essential for protection against *Candida*.

Chronic mucocutaneous candidiasis disease is characterized by infections of the nails, skin, and oral and reproductive mucosae in patients infected with *C. albicans* but who have no signs of other infections or autoimmune disorders. In systemic candidiasis, cells of the innate immune system, particularly neutrophils, are essential for protection against the infection (*8*). By contrast, in chronic mucocutaneous candidiasis, cells of the adaptive immune system mediate protection (*9*). The immune response against *Candida* had long been thought to be driven primarily by T helper 1 (T_H1) cells, because patients with chronic mucocutaneous candidiasis produced lower amounts of type 1 cytokines, which are produced by T_H1 cells (*3*) [such as interferon-γ (IFN-γ)], specifically in response to *Candida* spp. (*10*). More recently, with the discovery of the T_H17 cell lineage, studies in mice (*11*, *12*) and humans (*13*) have revealed an important protective role for T_H17 cells in *Candida* infections. T_H17 cells are a subset of T helper cells that secrete the cytokines IL-17A, IL-17F, IL-22, and IL-21, and are important for the host defense against organisms at the mucosal barriers (*14*, *15*).

With *Candida* infection, cells from the innate immune system can inhibit the infection directly themselves through antifungal activities (including secretion of antimicrobial peptides and engulfing microbes by phagocytosis) (see the figure). These cells also produce proinflammatory cytokines and

Department of Neurology and Immunobiology, Yale School of Medicine, New Haven, CT 06520, USA. E-mail: david.hafler@yale.edu

chemokines, and provide costimulatory and antigen processing and presentation signals to instruct the adaptive immune response cells to secrete IL-17. These IL-17–producing cells are predominantly T_H17 cells, but there are other cells from both the innate and adaptive immune system [(T cells (γδ), natural killer cells, neutrophils, T cells (CD8 subtype), and eosinophils] that also produce IL-17. Moreover, T_H17 cells secrete several chemokines (CXCL1, CXCL5, and IL-8) that in turn act on cells of the innate immune system, stimulating their migration to the site of infection. IL-17 stimulates mucosal epithelial cells to secrete proinflammatory cytokines, chemokines, and antimicrobial peptides.

Puel *et al*. describe two case reports with two different genetic etiologies for these chronic *Candida* infections. In one case, a child diagnosed with chronic mucocutaneous candidiasis had an autosomal recessive mutation in the gene encoding IL-17RA. This receptor binds both IL-17A and IL-17F, and is expressed in multiple tissues, such as vascular endothelial cells, peripheral T cells, B cells, fibroblasts, lung, myelomonocytic cells, and bone marrow stromal cells. The authors sequenced genes encoding the key cytokines produced by T_H17 cells from this patient (IL-22, IL-17A, and IL-17F) and their corresponding receptors, and found a homozygotic nonsense mutation in the *IL17RA* gene that abrogated IL-17RA receptor expression in fibroblasts and peripheral blood mononuclear cells. This mutation caused fibroblasts and leukocytes isolated from this patient to be unresponsive to IL-17A and IL-17F (homo- or heterodimers). In the second case report, the authors found a missense mutation in *IL17F* gene in a multiplex family with autosomal dominant inheritance of chronic mucocutaneous candidiasis. This mutation was located in the cavity of the cytokine, a region implicated in receptor binding. Cytokines that were genetically engineered to express the mutated form of the cytokine (in the context of either an IL-17F homodimer or IL-17A–IL-17F heterodimer) did not bind to IL-17RA on fibroblasts. These mutant cytokines also altered the stimulation of cytokine secretion by peripheral blood mononuclear cells, suggesting that the mutation caused a partial loss of *IL17F* gene function.

The discovery of genetic defects in chronic mucocutaneous candidiasis that are related to T_H17 cells supports previous data from mouse models and humans suggesting the importance of this cell type for protection against *Candida* infections. It further indicates that other genetic etiologies related to this lineage could underly chronic mucocutaneous candidiasis in other subjects, opening an important field for developing therapeutic strategies that target T_H17 cells in these patients. Puel *et al*. also demonstrate that the percentage of total T cells (defined by CD3 expression) that secretes IL-17A was not altered in the patients from both case reports compared to healthy individuals. However, it is unknown whether afferent defects in immune responses to *Candida* mediated by defects in IL-17A and IL-17F production by T cells, or loss of the efferent effects of IL-17 on mucosal and epithelial surfaces, underlie the chronic mucocutaneous fungal infection.

Although thrush and vaginitis occur in only a subset of the population, the findings of Puel *et al*. suggest that allelic variations in key components of the IL-17 signaling pathways may predispose to common candidiasis infection. Nevertheless, these data clearly link evolution of the IL-17 pathway with host responses to *Candida*.

References

1. V. Viglietta, C. Baecher-Allan, H. L. Weiner, D. A. Hafler, *J. Exp. Med.* **199**, 971 (2004).
2. A. Puel *et al*., *Science* **332**, 65 (2011); 10.1126/science.1200439.
3. L. de Repentigny, D. Lewandowski, P. Jolicoeur, *Clin. Microbiol. Rev.* **17**, 729 (2004).
4. C. Antachopoulos, *Clin. Microbiol. Infect.* **16**, 1335 (2010).
5. J. Aaltonen *et al*., *Nat. Genet.* **17**, 399 (1997).
6. Y. Minegishi *et al*., *Nature* **448**, 1058 (2007).
7. K. Eyerich, S. Eyerich, J. Hiller, H. Behrendt, C. Traidl-Hoffmann, *Eur. J. Dermatol.* **20**, 260 (2010).
8. L. Romani *et al*., *Res. Immunol.* **147**, 512 (1996).
9. H. R. Conti, S. L. Gaffen, *Microbes Infect.* **12**, 518 (2010).
10. D. De Moraes-Vasconcelos *et al*., *Clin. Exp. Immunol.* **123**, 247 (2001).
11. H. R. Conti *et al*., *J. Exp. Med.* **206**, 299 (2009).
12. L. Lin *et al*., *PLoS Pathog.* **5**, e1000703 (2009).
13. K. Eyerich *et al*., *J. Invest. Dermatol.* **128**, 2640 (2008).
14. S. J. Aujla *et al*., *Semin. Immunol.* **19**, 377 (2007).
15. T. Korn, E. Bettelli, M. Oukka, V. K. Kuchroo, *Annu. Rev. Immunol.* **27**, 485 (2009).

10.1126/science.1205311

MATERIALS SCIENCE

Impurities Enhance Semiconductor Nanocrystal Performance

The electronic properties of free-standing semiconductor nanocrystals can be tuned by diffusing metallic impurities into them.

Y. Charles Cao

Department of Chemistry, University of Florida, Gainesville, FL 32611, USA. E-mail: cao@chem.ufl.edu

The semiconductor industry annually spends billions of dollars deliberately adding atomic impurities, called dopants, into very pure semiconductors. Dopants can make devices run faster by increasing the number of negatively (n) or positively (p) charged mobile carriers. They can also determine the predominant type of charge carrier: electrons in n-type semiconductors, "holes" in p-type semiconductors (the dopant atom accepts an electron, resulting in the formation of a "hole"). Without doping, the fabrication of key transistor components such as p-n junctions would not be possible (*1*). Doping has had less impact on lower-cost devices in which semiconductor nanocrystals may be used, such as solar cells, printable low-power devices, and light-emitting diodes (*2*). Our knowledge of the doping effects on the electronic properties of semiconductor nanocrystals has been incomplete because of a lack of robust synthetic methods for doping free-standing nanocrystals (as opposed to thin films of nanocrystals). On page 77 of this issue, Mocatta *et al*. (*3*) report a solution-phase synthesis of metallically doped, free-standing indium arsenide (InAs) nanocrystals. They present strong evidence that both n- and p-type nanocrystals were formed, as well as insights into the electronic and optical effects of doping small nanocrystals (less than 10 nm in diameter).

The light emission and electronic structures of a semiconductor nanocrystal can differ from those of bulk samples or thin films because of quantum confinement effects created by its small size (*4*). These properties have already led to applications; for example, colloidal semiconductor nanocrystals can be used as fluorescent labels for the long-term monitoring of biological pathways in living cells (*5*). It has been predicted that intentional

addition of impurities in nanocrystals might lead to effects not observed in the bulk. For example, magnetic impurities such as manganese (Mn) can be positioned inside a colloidal nanocrystal with angstrom-scale precision (*6*) to tune optical and magnetic properties. Nanocrystals doped with magnetic impurities are of interest for their potential use in spin-based electronic devices (*7*).

Little progress has been made in the n- or p-type impurity doping of free-standing semiconductor nanocrystals. Instead of using an impurity, Shim and Guyot-Sionnest (*8*) made undoped semiconductor nanocrystals n-type by injecting extra electrons into them. These extra electrons occupy the discrete conduction-band state of the nanocrystals (in bulk semiconductors, energy states of mobile electrons form a conduction band that lies above the states of the bound electrons in the valence band; the energy separation between them is the band gap). In studies of thin films of nanocrystals, Talapin and Murray (*9*) reported a general method to control the carrier type in lead selenide nanocrystals with hydrazine treatments, and Bawendi and co-workers (*10*) switched InAs nanocrystals from n-type to p-type conduction via doping with cadmium ions. However, the carrier type determined in these transport experiments is a collective property of many nanocrystals, and may not necessarily be the same as the carrier type of the individual nanocrystals in the film.

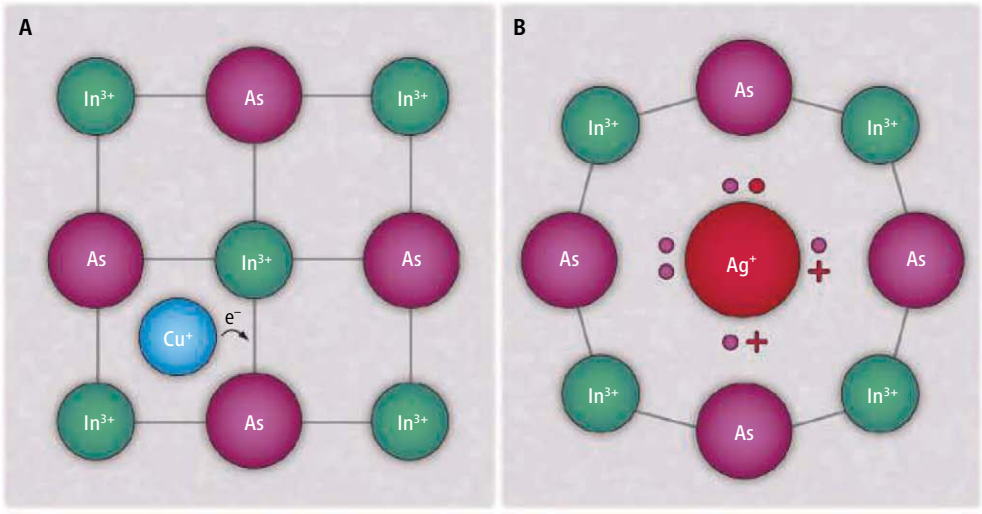

Moving in. Lewis chemical structure diagrams illustrate a simplified two-dimensional view of the bonding in an InAs lattice containing metallic impurities. Mocatta *et al*. introduced metallic dopants, which modify the electronic properties of InAs nanocrystals, through diffusion. Bonding electrons are represented either by black lines or by paired dots, whose color aims to indicate the atom to which it belongs. Plus signs indicate the lack of an electron in a bonding orbital. (**A**) A Cu impurity in an interstitial site in the InAs lattice donates valence electrons to the crystal and causes n-type doping. (**B**) A substitutional Ag impurity occupying an indium site in the InAs lattice. The Ag causes InAs lattice disorder and introduces two electron acceptor sites into the lattice. The resulting deficiency of valence electrons causes p-type doping.

Mocatta *et al*. doped free-standing colloidal InAs nanocrystals with metallic impurities—copper (Cu) or silver (Ag)—by solid-state diffusion (see the figure). Although Cu and Ag impurities show similar diffusion properties inside the InAs crystal lattice, they produce opposite electronic doping effects in bulk InAs. Copper is an n-type interstitial impurity (it squeezes into empty sites between atoms in the crystal) and donates electrons that become the main charge carrier. Silver is a p-type substitutional impurity (it replaces an In ion), and the lower charge of its ion relative to In causes holes to be the main carrier (*11*).

Optical measurements by Mocatta *et al*. suggest that, unlike the n-type nanocrystals made by carrier injection (*8*), new impurity states are formed that increase the density of energy states near the semiconductor band gap. They also used scanning tunneling spectroscopy (STS) to characterize the doped InAs nanocrystals. This method can directly measure the electronic energy levels with respect to the Fermi level, which is the energy of the highest state occupied with electrons (*12*). In general, shifts of the Fermi level up toward the conduction band characterize a semiconductor as n-type, and shifts down toward the valence band characterize it as p-type. The STS measurements show that the Cu-doped InAs nanocrystals are indeed n-type, and that the Ag-doped ones are p-type.

Modeling by Mocatta *et al*. suggests that the electronic doping effects in small semiconductor nanocrystals strongly depend on the low density of states in their conduction band (an effect of quantum confinement) as well as being "heavily doped"—a 4-nm nanocrystal containing just one impurity atom is comparable to the most heavily doped regime for a bulk semiconductor. Their theoretical analysis reveals that the heavy doping modifies the nanocrystal electronic states through the interplay of two fundamental effects. One is the creation of the quantum-confined impurity band, which is partially filled by charge carriers from the impurity. The other is called band-tailing, which is related to disordering of the crystal lattice by the introduction of dopants.

It will be interesting to correlate the electronic nature of these individual n- or p-type semiconductor nanocrystals with the carrier type in the thin films made of these nanocrystals. One open question is whether Stark effects (shifts in energy levels created by internal electrical fields) might also be responsible for the electronic properties of heavily doped semiconductor nanocrystals. A second issue concerns the location of the impurities within the doped InAs nanocrystals, as both copper and silver ions have large room-temperature solid-state diffusion coefficients. Although some impurity atoms may stay on the surface, the work of Mocatta *et al*. strongly argues that only the impurities inside nanocrystals play a major role in determining the electronic properties of these nanocrystals. Despite these issues, the ability to control the position of the Fermi level in semiconductor nanocrystals via impurity doping should enhance their performance in electronic devices that can be prepared by scalable bottom-up manufacturing.

References

1. D. J. Norris, A. L. Efros, S. C. Erwin, *Science* **319**, 1776 (2008).
2. I. Gur, N. A. Fromer, M. L. Geier, A. P. Alivisatos, *Science* **310**, 462 (2005).
3. D. Mocatta *et al*., *Science* **332**, 77 (2011).
4. A. P. Alivisatos, *Science* **271**, 933 (1996).
5. A. P. Alivisatos, W. W. Gu, C. Larabell, *Annu. Rev. Biomed. Eng.* **7**, 55 (2005).
6. Y. A. Yang, O. Chen, A. Angerhofer, Y. C. Cao, *J. Am. Chem. Soc.* **128**, 12428 (2006).
7. R. Beaulac, L. Schneider, P. I. Archer, G. Bacher, D. R. Gamelin, *Science* **325**, 973 (2009).
8. M. Shim, P. Guyot-Sionnest, *Nature* **407**, 981 (2000).
9. D. V. Talapin, C. B. Murray, *Science* **310**, 86 (2005).
10. S. M. Geyer *et al*., *ACS Nano* **4**, 7373 (2010).
11. C. S. Fuller, K. B. Wolfstirn, *J. Electrochem. Soc.* **114**, 856 (1967).
12. U. Banin, Y. W. Cao, D. Katz, O. Millo, *Nature* **400**, 542 (1999).

10.1126/science.1203702

RETROSPECTIVE

George Bugliarello (1927–2011)

Ilan Juran and John Falcocchio

The creative vision of a civil engineer to turn universities into driving forces of innovation spawned new design concepts for inner-city renewal, industrial parks, and sustainable cities.

George Bugliarello, a creative engineer, outstanding researcher, and dedicated educator, died on 18 February at age 83, in New York. His range of interests and expertise transcended many disciplines, including civil engineering, biomedical engineering, urban development, science policy, water resources, and environmental science. His vision of the role of science, innovation, and education, coupled with a passion for turning his vision into reality, is reflected in today's urban communities, forged through academic and industry interactions in ways that spur economic growth and societal well-being, while respecting the quality of human life and the environment.

George was born in Trieste, Italy, in 1927. After graduating from the University of Padua in 1951, he went to the United States and earned master's and Ph.D. doctoral degrees in civil engineering at the University of Minnesota (1954) and the Massachusetts Institute of Technology (1959). His career path included a faculty position at Carnegie Mellon University and dean of engineering at the University of Illinois at Chicago (1969–1973), where he explored the seamless melding of biology, society, and machines, and coined the term "biosoma."

George came to the Polytechnic Institute of New York University (Poly) where he served as president for 21 years (1973–1994). His vision of rescuing the then Polytechnic Institute of Brooklyn from deep financial trouble began with its merger with the engineering school of New York University. He realized that for Poly to grow, it needed to change the poor physical and economic character of its neighborhood. He converted this problem into an opportunity for Poly. By recognizing that cities have historically been the product of technology, George carved a path to revitalize downtown Brooklyn and placed Poly in a leading role to guide its renaissance. Two years after his arrival, he proposed the development of a technology park. His tenacity in developing and marketing this idea finally paid off in 1989, when ground was broken for MetroTech, the first modern university-industry research and technology park in the United States. It grew into a workforce of more than 20,000 employees in financial, utilities, and communication sectors (including the as "911" emergency system of New York City). Among his key decisions was creating the Center for Advanced Technology in Telecommunications in 1982, which continues to receive funding from the state of New York in return for transferring research in technologies to New York companies for new applications. He also created a Center for Technology and Financial Services at Poly in 1994, with teaching and research functions and a strong focus on users of technology in the financial industry. This fostered the first American academic master's degree program in Financial Engineering. The success of MetroTech became the catalyst that George believed would transform downtown Brooklyn into the new vibrant place of today. He was honored by the *Engineering News-Record* as one of "Those Who Made Marks," and in 1994 he was awarded the New York City Mayor's Award for Excellence in Science and Technology.

George's diverse research interests ranged from stochastic simulations of hydrodynamics to sustainable megacities in emerging countries. His 60 years of scientific work is reflected in more than 300 professional publications. He also founded (and was coeditor of) the journal *Technology in Society.* His awards are many and include the Walter L. Huber Civil Engineering Research Prize of the American Society of Civil Engineers in 1967 and the 2009 Marconi Society's Beacon of Light Award.

He served on numerous national boards and committees in the United States, including the Advisory Committee for Science and Engineering Education of the National Science Foundation (NSF), the Board on Infrastructure and the Constructed Environment of the National Research Council, the National Academies committee on Megacities, the National Committee on Science Education Standards and Assessment, and the Lawrence Livermore National Laboratory Engineering Advisory Committee. George was also a member of many science and engineering organizations including The American Society of Civil Engineers, the Biomedical Engineering Society, and the American Society for the Advancement of Science.

George's expertise was also called upon on an international level, where he advised groups on science policy and urban and economic development. These included committees for the U.S. National Academy of Sciences (NAS), the North Atlantic Treaty Organization (NATO), the NSF, and the U.S. National Institutes of Health. He advised the U.S. Department of State in Venezuela and Central Africa, held a Senior Faculty Fellowship for NATO at the Technical University of Berlin, was a member of the U.S.–Egypt Joint Consultative Committee of the NAS, and was on the Science for Peace Steering Committee of NATO. George served as Foreign Secretary of the U.S. National Academy of Engineering (NAE), was a lifetime National Associate of the National Academies, and was chair of the NAE Council's International Affairs Committee.

George was an elite humanistic explorer, whose creative scientific work and educational dedication was often inspired by a holistic quest for understanding the universe of the complex and intertwined relationships among biological, societal, environmental, and technological systems. For him, engineering was the art of creating technology and systems as the processes that human societies devise to modify or preserve nature for their sustainable development, and the capability of their strategic integration in the design of the metropolis to address future societal needs. His fellow faculty and academic community believe that his scientific legacy and academic vision will have a great impact on the next generation of multidisciplinary engineers and nurture a professional culture that will inherently recognize the integration of bioenvironmental risks, societal inspirations, and technological innovation as key elements for the sustainable development of urban society.

10.1126/science.1205706

CREDIT: POLYTECHNIC INSTITUTE OF NEW YORK UNIVERSITY

Urban Infrastructure Institute & Urban Utility Center, Polytechnic Institute of New York University, Brooklyn, NY 11201, USA. E-mail: ijuran@poly.edu

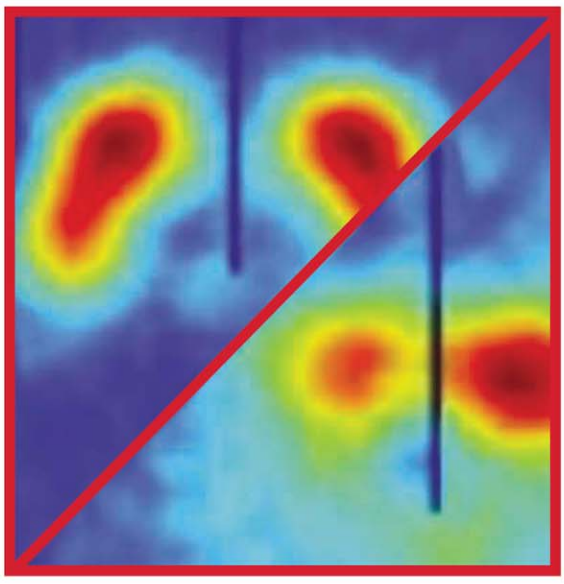

Early Detection of Parkinson's Disease:

The Challenges and Potential of New Biomarkers

WEBINAR

Wednesday, April 27, 2011
12 noon ET, 9 am PT,
4 pm GMT, 5 pm UK

Ten years or more before the classic tremors of Parkinson's disease (PD) appear, the destruction of dopaminergic neurons in the brain's nigrostriatal pathway is well underway. Identifying biological markers (biomarkers) of PD in its earliest stages will be crucial for early intervention with therapeutics to prevent or even reverse loss of dopaminergic neurons. Biomarkers for early PD could be used to identify patients at risk for PD or in the earliest stages of the disease and to assess the efficacy of new drugs or therapies. Biomarkers could also be used to select appropriate patients for clinical trials and to monitor disease progression or drug-induced remission in real time. So far, only one biomarker for PD called DaTscan—SPECT imaging of dopamine transporters at dopaminergic nerve terminals in the nigrostriatal pathway—has been approved by the FDA. Given the number of patients with PD (~1 million in the United States and ~5 million worldwide), developing new biomarkers for detecting the earliest stages of this disease is imperative if new drugs and treatments are to be developed.

During this Webinar our distinguished panelists will:

- Explain the need for biomarkers for detecting early PD and how these biomarkers can be used in drug development and clinical trials
- Provide an overview of promising new biological and neuroimaging markers
- Discuss the challenges and bottlenecks in the development of new biomarkers for PD and the role of the Parkinson's Progression Markers Initiative (PPMI).

Register Now!
Early bird discounts available before 25 March, 2011.
Additional discounts for members and students/postdocs.
Questions can be submitted live during the webinar or in advance by e-mail. To register, visit
www.sciencemag.org/webinar

Moderator:
Todd Sherer, Ph.D.
The Michael J. Fox Foundation for Parkinson's Research, New York, NY

Participants:
Kenneth Marek, M.D.
Institute for Neurodegenerative Disorders, New Haven, CT

Michael G. Schlossmacher, M.D., FRCPC
University of Ottawa, Ottawa, Ontario

Norbert Schuff, Ph.D.
University of California and VA Medical Center, San Francisco, San Francisco, CA

Andrew Siderowf, M.D., MSCE
University of Pennsylvania School of Medicine, Philadelphia, PA

Brought to you by *Science*/AAAS and *Science Translational Medicine*, in association with the Michael J. Fox Foundation.

Science
AAAS

Science Translational Medicine
AAAS

THE MICHAEL J. FOX FOUNDATION FOR PARKINSON'S RESEARCH

Submission deadline August 1

Your name here.

The GE & Science Prize for Young Life Scientists. Because brilliant ideas build better realities.

Imagine standing on the podium at the Grand Hotel in Stockholm, making your acceptance speech for the GE & Science Prize for Young Life Scientists. Imagine having your essay read by your peers around the world. Imagine discussing your work in a seminar with other prize winners and Nobel Laureates. Imagine what you could do with the $25,000 prize money. Now stop imagining. If you were awarded your Ph.D. in molecular biology in 2010, then submit your 1000-word essay by August 1, and you can make it reality.

Want to build a better reality? Go to www.gescienceprize.org

GE & Science Prize for Young Life Scientists

imagination at work

Science AAAS

* For the purpose of this prize, molecular biology is defined as "that part of biology which attempts to interpret biological events in terms of the physico-chemical properties of molecules in a cell".

(McGraw-Hill Dictionary of Scientific and Technical Terms, 4th Edition).

28-9402-06AB

Beyond Predictions: Biodiversity Conservation in a Changing Climate

Terence P. Dawson,[1] Stephen T. Jackson,[2] Joanna I. House,[3] Iain Colin Prentice,[3,4,5] Georgina M. Mace[4,6]*

Climate change is predicted to become a major threat to biodiversity in the 21st century, but accurate predictions and effective solutions have proved difficult to formulate. Alarming predictions have come from a rather narrow methodological base, but a new, integrated science of climate-change biodiversity assessment is emerging, based on multiple sources and approaches. Drawing on evidence from paleoecological observations, recent phenological and microevolutionary responses, experiments, and computational models, we review the insights that different approaches bring to anticipating and managing the biodiversity consequences of climate change, including the extent of species' natural resilience. We introduce a framework that uses information from different sources to identify vulnerability and to support the design of conservation responses. Although much of the information reviewed is on species, our framework and conclusions are also applicable to ecosystems, habitats, ecological communities, and genetic diversity, whether terrestrial, marine, or fresh water.

Alarming predictions about the potential effects of future climate change are prompting policy responses at local to global levels (*1*, *2*). Because greenhouse gas emissions to date commit Earth to substantial climate change in the coming decades (*3*), the potential for loss of biodiversity, termination of evolutionary potential, and disruption of ecological services must be taken seriously. Averting deleterious consequences for biodiversity will require immediate action, as well as strategic conservation planning for the coming years and decades. But how good are our current predictions, and how fit are they for conservation planning purposes?

To date, assessments of climate-change impacts on biodiversity have largely been based on empirical niche (or climate-envelope) models (*4*). For most species, these models indicate large geographic displacements and widespread extinctions. However, niche models are best suited to identifying exposure to climate change, which is only one aspect of vulnerability. Assessing biodiversity consequences of climate change is a multifaceted problem, requiring consideration of all aspects of vulnerability: exposure, sensitivity, and adaptive capacity (*5*) (see Box 1). Additional sources of evidence include observations of responses to climate changes (both past and present), experiments, and mechanistic (process) modeling based on ecophysiology and population biology. These studies show a range of natural coping mechanisms among populations exposed to climate change, with diverse consequences for resilience at local to global scales. The capacity to cope depends on both intrinsic factors (species biology, genetic diversity) and extrinsic factors (rate, magnitude, and nature of climatic change). Integration of multiple approaches and perspectives is needed for more accurate information about which species and habitats, in which places, are likely to be most at risk, as well as how conservation managers can leverage adaptive capacities in natural systems to maximum advantage. There is a wealth of knowledge upon which to draw.

[1]School of the Environment, University of Dundee, Dundee DD1 4HN, Scotland, UK. [2]Department of Botany, Program in Ecology, and Berry Biodiversity Conservation Center, University of Wyoming, Laramie, WY 82071, USA. [3]QUEST, Department of Earth Sciences, University of Bristol, Bristol BS8 1RJ, UK. [4]Grantham Institute for Climate Change and Division of Biology, Imperial College London, London SW7 2AZ, UK. [5]Department of Biological Sciences, Macquarie University, North Ryde, NSW 2109, Australia. [6]Centre for Population Biology, Imperial College London, Ascot SL5 7PY, UK.

*To whom correspondence should be addressed. E-mail: g.mace@imperial.ac.uk

How Reliable Is the Current Generation of Predictions?

Climate-change impacts on biodiversity, both positive and negative, are already manifest in recent widespread shifts in species ranges and phenological responses (*6*, *7*). Although human land use remains the main driver of present-day species extinction and habitat loss (*8*), climate change is projected to become equally or more important in the coming decades (*9*, *10*). Assessing the biodiversity consequences of climate change is complicated by uncertainties about the degree, rate, and nature of projected climate change (*11*), the likelihood of novel and disappearing climates (*12*), the diversity of individual-species responses to a broad suite of interacting climate variables (*6*), and interactions of climate-change effects with other biotic factors (e.g., competition, trophic relationships) and stressors (land use, invasive species, pathogens, pollutants) (*13*, *14*).

Syntheses of climate change and biodiversity for decision-makers, conservation organizations, and governments (*1*, *2*, *15*) have relied heavily on empirical niche (or climate-envelope) modeling and analog scenarios of climate space (*4*). This approach uses statistical relationships between current climate variables and geographic patterns of species distribution and/or abundance to define an "environmental space" associated with a particular species. The models are then applied to climate projections from general circulation models (GCMs), yielding maps of species ranges predicted under future climate scenarios. Application of these models has led to dire warnings of biodiversity loss (*16*). This has led in turn to calls for radical and immediate intervention measures, including the redesign of protected-area systems, development of new areas for restoration and management, and human-assisted migration (*17*, *18*).

Box 1. Vulnerability in the context of climate and biodiversity.

Vulnerability is the extent to which a species or population is threatened with decline, reduced fitness, genetic loss, or extinction owing to climate change. Vulnerability has three components: exposure (which is positively related to vulnerability), sensitivity (positively related), and adaptive capacity (negatively related).

Exposure refers to the extent of climate change likely to be experienced by a species or locale. Exposure depends on the rate and magnitude of climate change (temperature, precipitation, sea level rise, flood frequency, and other hazards) in habitats and regions occupied by the species. Most assessments of future exposure to climate change are based on scenario projections from GCMs often downscaled with regional models and applied in niche models.

Sensitivity is the degree to which the survival, persistence, fitness, performance, or regeneration of a species or population is dependent on the prevailing climate, particularly on climate variables that are likely to undergo change in the near future. More sensitive species are likely to show greater reductions in survival or fecundity with smaller changes to climate variables. Sensitivity depends on a variety of factors, including ecophysiology, life history, and microhabitat preferences. These can be assessed by empirical, observational, and modeling studies.

Adaptive capacity refers to the capacity of a species or constituent populations to cope with climate change by persisting in situ, by shifting to more suitable local microhabitats, or by migrating to more suitable regions. Adaptive capacity depends on a variety of intrinsic factors, including phenotypic plasticity, genetic diversity, evolutionary rates, life history traits, and dispersal and colonization ability. Like sensitivity, these can be assessed by empirical, observational, and modeling studies.

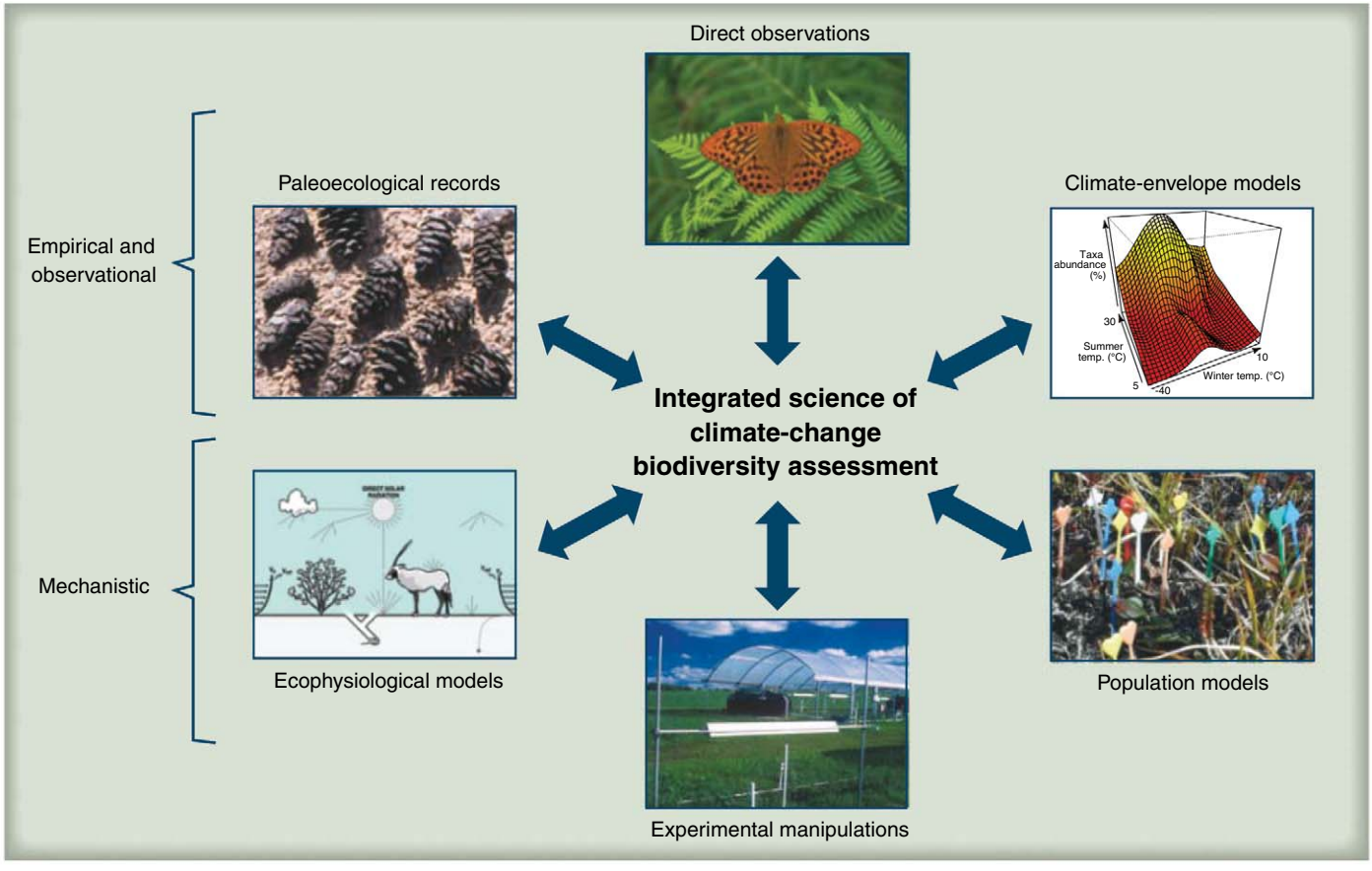

Fig. 1. An integrated science of climate-change biodiversity assessment will draw from multiple sources and approaches. Each provides useful but incomplete information on exposure, sensitivity, and adaptive capacity. Integration of these approaches will provide a more robust basis for vulnerability assessment and allocation of resources for conservation and adaptation. Direct observations, including long-term monitoring, are applicable at a broad range of scales and can be used to assess all aspects of vulnerability. Paleoecological records extend the observational foundation to encompass a broader range of rates, magnitudes, and kinds of climate change. They can reveal adaptive capacity and risks. Climate-envelope (or niche) models are statistical models based on correlations between geographic patterns of species distributions and climate, and are best suited for assessment of exposure. Mechanistic models such as population models and ecophysiological models are diverse, require taxon-specific parameters, and are often coupled. They are particularly effective in assessing sensitivity and adaptive capacity. Experimental manipulations provide information on sensitivity and adaptive capacity, and are valuable in parameterizing mechanistic models. [Photo credits: direct observations (silverwashed fritillary, *Argynnis paphia*), www.learnaboutbutterflies.com; climate-envelope models, S. Brewer; population models, S. T. Jackson; experimental manipulations, A. K. Knapp; ecophysiological models, W. P. Porter; paleoecological records, S. T. Jackson]

The heavy reliance of conservation management and policy on a single scientific approach creates risks of policy or management failures, particularly given that the underlying assumptions of that approach are under debate. Critiques center on the correlative nature of the niche models, scale dependency, the difficulty of reliable extrapolation outside observed climate space, and failure to represent key ecological and evolutionary processes that could allow species to persist in a heterogeneous landscape (*13*, *19*–*23*). Niche models impart ease of use and power in explaining modern distributions (*24*), but their efficacy in assessing extinction risk, delineating suitable future habitats, and predicting ecological outcomes is unproven (*25*).

Niche models provide a tool for assessing exposure to climate change as projected in various GCM scenarios (Box 1). Given the global nature of projected climate changes (*1*), exposure is inevitable for any species that has a finite geographic distribution, although the amount of climate change to be faced varies widely among species. However, exposure is only one of many factors determining the impacts of climate change. Assessment of vulnerability must also include climate sensitivity and adaptive capacity (*5*) (Box 1).

Complementary methodologies are available that tell us much more about natural responses to climate change (Fig. 1). These indicate that biodiversity losses may not be as large as predicted from niche models, although the rate of change and land use (habitat loss or destruction, harvesting) remain barriers to some natural response mechanisms. Approaches based on observations in the present and the past, experiments, and new modeling techniques are developing rapidly. Integration of these approaches should provide the foundation for a robust science of climate-change assessment.

Elements of Integrated Climate-Change Assessment for Biodiversity

Ecological observations in real time. Many species are altering their geographic ranges and adjusting phenological responses in ways consistent with the relatively small climate changes of the past few decades (*6*, *26*). Although some species are undergoing rapid, widespread population declines, in most cases the primary drivers of decline involve land-use change and habitat fragmentation, biotic interactions, pathogens, and invasive species (*8*, *9*). To date, there is more evidence for climate-driven range expansion than for range contraction (*27*). It might appear that many species are coping with climate change. However, range contraction and population extirpation (local extinction) may be more difficult to document than expansion and migration, owing to undersampling of small or isolated populations, long-term local persistence of populations, and extinction lags (*28*). Extirpations already entrained by climate change may take years or decades to run their full course (*29*). Detecting (or forecasting) species decline is challenging because the processes are not well understood, and species decline as well as loss

of ecosystem function may involve threshold transitions (*30*–*32*).

New knowledge emerges from real-time tracking of species responses to climate change, but direct observations are not, on their own, a sufficient method for forecasting risks or the intrinsic capacity of species and populations to adapt. It remains unknown whether the ongoing range expansions and phenological shifts will allow species populations to survive, or whether these are transient responses in populations with reduced fitness in the changed environment. Future environments will display novel combinations of climate variables (*12*). So far there is limited evidence of microevolutionary adaptive change (*33*), perhaps because reliable methods to detect microevolution have rarely been applied (*34*, *35*). Furthermore, recent case studies where the causal processes driving population responses to climate change have been disentangled suggest that the climate variables, and the way they interact with species life history, can be both complex and context-specific (*30*, *31*, *36*–*38*). The use of observational evidence will therefore need to be applied alongside deeper understanding of the biological differences among species that determine their fate under climate change.

Intrinsic adaptive capacity for climate change. Observations, experiments, and mechanistic models indicate that many species populations have the capacity to adjust to climate change in situ via phenotypic plasticity (e.g., acclimation, acclimatization, developmental adjustments) (Fig. 2) (*35*, *39*) and microevolution (*40*, *41*), and that many populations are able to disperse locally to suitable microhabitats (*42*, *43*) or regionally to

Fig. 2. Representative modes of population and species-range response to environmental changes since the last glacial maximum, documented for selected North American conifer trees and Eurasian cervids. Populations of many species have persisted in situ at individual sites since the last glacial maximum (toleration) and many have undergone habitat shifts, moving short distances (1 to 10 km) to sites with different aspects, slopes, elevations, and other attributes as the environment changed. Migrations of 100 to 1000 km are well documented for many species. Both migration and habitat shift are forms of environment tracking, in which species adjust their geographic locations to track suitable environments. At least a few species have undergone universal extinction (e.g., *Megaloceros giganteus*) owing to environmental change; others have experienced loss of genetic diversity, usually associated with severe population bottlenecks (near-extinction episodes) (e.g., *Picea martinezii*). Species' responses to climate change may consist of multiple modes. For example, since the last glacial maximum, populations of *Juniperus osteosperma* and *Alces alces* have persisted at some sites (toleration), undergone habitat shifts (usually elevational or topographic) within some regions, and colonized extensive new territory while disappearing from previously occupied territory (migration). *Alces alces* has also undergone a severe genetic bottleneck. Differences among modes within and among species depend on rates, magnitudes, and geographic patterns of climatic change, the capacity of species populations to adapt (via phenotypic plasticity, evolution, and/or dispersal), and other factors (e.g., geographic barriers, and other stressors and interactions). References, additional examples, and detailed discussion are provided in the supporting online material. [Photo credits: S. T. Jackson (*Juniperus osteosperma*, *Pinus flexilis*, *Picea glauca*, *Picea martinezii*); A. D. Barnosky (*Megaloceros giganteus*); www.grambophoto.com (*Alces alces*, *Cervus elaphus*, *Rangifer tarandus*)]

newly suitable locales (*44*). Each of these adaptive mechanisms has constraints, which may limit the capacity of species and populations to keep pace with high rates and magnitudes of climate change (*35*). These processes are, however, the subject of an extensive ecological and evolutionary literature, which has so far been underexploited for determining adaptive capacity.

Given the number and diversity of species potentially under threat, the synthesis and application of existing evidence on adaptation will provide necessary—but not sufficient—information on adaptive mechanisms and capacities. The environmental controls and absolute limits of phenotypic plasticity, and the environmental dependence of optimum phenotypes (*45*), must be determined empirically for a range of species to predict in situ ecological and evolutionary responses to environmental change (*34*, *35*). Empirical and theoretical studies of relevant ecological processes (propagule dispersal, establishment, population growth, fecundity, mortality, metapopulation dynamics) provide a basis for assessing response times for local, regional, and continental adjustments in distribution and abundance (*46*). This task can be simplified by using existing data and targeted studies of a range of representative taxa with diverse life history patterns and functional traits.

Biodiversity consequences of past climate changes. Increasingly, geohistorical records and paleoecological studies are being integrated with independent paleoclimate records to reveal effects of past climate changes (*47*, *48*), which, in some periods and regions, were as large and rapid as those projected for the future (*49*, *50*). Although possible future climates will be unlike those of the past, paleoecological records offer vital information about how species responded to different rates and degrees of change, with numerous case studies in terrestrial, freshwater, and marine ecosystems. The diverse outcomes for different taxa and life history types emphasize the range of past responses that are likely to be reflected in the present and future (Fig. 2).

Paleoecological observations can be further integrated with modern genetic and ancient DNA studies to assess the genetic consequences of these dynamics (*47*, *51*–*53*). By determining past climate-driven losses in genetic and species diversity at local to regional scales, and by identifying the circumstances under which species have escaped extinction and populations have resisted extirpation, these studies can contribute to assessments of adaptive capacity and vulnerability (Fig. 2).

All species or species groups living on Earth today have persisted through a glacial-to-interglacial transition 20,000 to 12,000 years ago that included rapid, high-magnitude climate changes at all latitudes and in both terrestrial and marine environments. This transition followed immediately upon a series of abrupt, high-magnitude glacial-age climate changes with near-global impact (*50*). The last glacial-interglacial cycle is only the most recent of at least 20 such cycles during the past 2 million years. Ecological and biogeographic responses to these climatic changes are particularly well documented for the past 10,000 to 20,000 years for many regions; such responses included repeated reorganization of terrestrial communities, changes in both the location and overall size of geographic ranges, and often rapid increases and decreases in sizes of local and regional populations (*12*, *49*, *54*–*56*).

The fact that the biodiversity on Earth today passed through these events indicates natural resilience and adaptive responses. Plant and animal species have shown capacity for persistence in small populations and microhabitats (*52*, *55*, *57*, *58*), long-distance migration and dispersal (*59*, *60*), shifts along habitat gradients and mosaics (*49*, *61*), and rapid expansion under favorable conditions (*21*). Many species have also undergone rapid range contraction and widespread population decline (*16*, *49*, *62*). Low genetic diversity indicates that many species have passed through recent genetic bottlenecks (*63*, *64*). But few documented species extinctions can be ascribed solely to climatic change (*65*–*67*). Megafaunal extinctions occurred in North America at a time of rapid climate change during the last deglaciation, but human exploitation is also a possible cause (*66*). Extinction of only one plant species (*Picea critchfieldii*) has been documented during the last deglaciation (*65*).

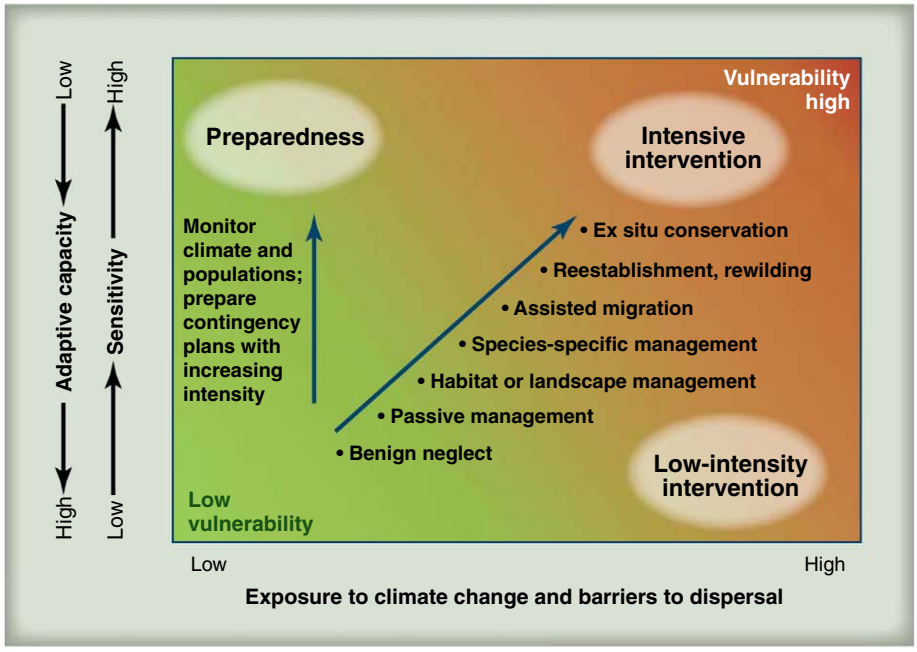

Fig. 3. The vulnerability of a species or ecosystem is based on its exposure to climate change, its sensitivity, and its inherent capacity to adapt to change. The relative balance of these different components of vulnerability would lead to different management interventions. The *x* axis represents the degree of exposure to climate change faced by species and communities (exogenous factors). This axis is largely determined by the species' or population's geographical location, the rate and magnitude of climate change anticipated for that region, and the size, cohesiveness, and connectivity of the species' habitat within and beyond that region. The other two measures from the vulnerability framework, adaptive capacity and sensitivity (see Box 1), are plotted together on the *y* axis. This axis is primarily determined by biological characteristics of species that influence their mobility, specificity, and sensitivity (endogenous factors). These include, for example, physiological constraints, phenotypic plasticity, evolutionary potential, dispersal and growth capacity, and biotic interactions critical to persistence. The relative position of species and ecosystems along the axes can inform decisions on appropriate research, monitoring, and management strategies. Decisions are also likely to be affected by costs and assessments of benefits (e.g., an ecosystems service value or lower cost might shift strategies implemented toward the top right). Circled text denotes generic conservation responses. Specific conservation responses that will be appropriate under the different circumstances are discussed in the text. Species in the upper left corner have high sensitivity to climate change but are expected to face relatively minor challenges. Such species are not a priority for intervention unless there is a change in climate-change pressures or landscape permeability. Their potential vulnerability means that they need to be monitored to ensure that they are thriving and remain unthreatened, with contingency plans that can be deployed in a timely manner in case of change. Species with high exposure but low sensitivity and high adaptive capacity (lower right corner) can presumably cope with change, and therefore need only low-intensity intervention as change becomes more extreme. Species in the upper right corner will have relatively high levels of both exposure and sensitivity; with decreasing adaptability, more intensive and specific management will be required.

Developing an Integrated Science of Climate-Change Biodiversity Assessment

The diverse sources of evidence discussed above can be integrated in a vulnerability framework (*68*). Vulnerability assessment has been suggested for prioritizing species at risk from climate change (*5*) and has been applied to both taxonomic and regional species groups (*69*, *70*). The empirical foundation for trait-based climate-change vulnerability analysis is now starting to appear, including species that were exposed to relatively rapid climate shifts during the Quaternary (*47*, *71*) as well as some recent studies (*44*, *72*–*75*). A combination of expert opinion and expectations from ecological and evolutionary theory has been used to identify vulnerable traits for some groups (*69*, *76*), including, for example, ecological specialists at higher trophic levels, with long generation times, poor dispersal ability, and low reproductive output. Body mass is strongly correlated with extinction risk and is often associated with other risk-promoting traits (e.g., delayed reproductive maturity, small geographic range) (*77*). Large range sizes may imply a large population size and can act to buffer against habitat loss or fragmentation. A broad geographical distribution may not only protect against individual habitat patches becoming climatically unsuitable, but may also foster high genetic variability. However, there are many exceptions to these generalizations, and paleoecological records suggest that they may break down under rapid climate change (*49*, *65*).

Today, many species will be required to disperse rapidly through highly fragmented, human-dominated landscapes in order to keep pace with changing climate. Paleoecological evidence suggests that many plant species have responded to past rapid climate changes with migration rates orders of magnitude higher than predicted by mean observed dispersal distances. This suggests a potential role for rare long-distance dispersal (LDD) through the transportation of seeds in atmospheric updrafts and water courses, oceanic currents, and dispersal by birds and animals. Humans are very effective as LDD vectors and, like natural LDD mechanisms, do not require contiguous habitat to establish or maintain connectivity between populations, perhaps facilitating conservation strategies.

Given the evidence that the responses of species and communities to climate change will be highly variable, we need to move beyond predictions of future range changes, which may overestimate or underestimate risks in particular cases. Because of the variety of vulnerabilities and the factors that contribute to them, a one-size-fits-all strategy risks failure. We advocate a combination of strategies governed by assessment of vulnerability and its three components—exposure, sensitivity, and adaptive capacity—drawn from multiple lines of evidence.

Figure 3 displays species responses to climate change on two axes, based on a vulnerability framework. This approach can inform managers about the relative urgency and the type of conservation action necessary. The diagonal axis in Fig. 3 broadly reflects increasing intensity of conservation interventions. This axis runs from "laissez-faire" (i.e., let natural processes run their course) to direct, targeted, and often intensive "command and control" interventions. The most adaptable and/or insensitive species and those with low exposure will need minimal interventions with low-level monitoring, a strategy we call "benign neglect." For example, in the United States and Africa, vast territories designated as wilderness areas or reserves are "managed" with a laissez-faire approach. Active management is restricted to sporadic rewilding (e.g., top-predator reintroduction), low-impact eradication of invasive species, and removal of individuals dangerous to humans (e.g., rogue grizzly bears). These designations may, of course, change in the future. For example, it is likely that some ecosystems that currently receive minimal management, such as boreal forests, may require more active management under climate change.

As exposure and sensitivity increase and autonomous-response capability decreases, substantial benefits may result from simply designating new protected areas and undertaking low-level habitat management to reinforce species' intrinsic dispersal and migration mechanisms. Analyses based on niche models have prescribed this approach (*15*). Periodic reevaluation of ongoing and planned protected-areas strategies may be needed to maintain potential for species resilience and mobility under climate change. For example, dynamic placing of buffer zones, removal of barriers, and establishment of corridors or "stepping stones" within a wider landscape may be necessary (*78*), although the definition, costs, and benefits of connectivity are under debate (*79*). A complementary strategy is to maintain high within-region habitat heterogeneity (edaphic, topographic, or elevational), which provides more options for both natural populations and conservation managers (*80*).

In any habitat or community, some species may require specific actions for their conservation or to retain critical biological interactions. Intermediate strategies—including intervention to arrest or divert natural succession or ecosystem regime shifts, maintenance of specific habitats or habitat diversity, and targeted interventions to restore disrupted species interactions (e.g., pollinator or plant-herbivore networks)—are now widely used. Species-specific management may be costly and intensive, but it can reverse the fate of endangered species (*8*).

Intensive intervention strategies include assisted migration and translocation of species outside their native range (*18*). Reestablishment and rewilding involve intensive habitat management to restore critical habitat types, with whole communities recreated from populations surviving elsewhere. These are generally considered to be high-risk strategies because of potentially negative ecological, evolutionary, and economic impacts (*81*) and ethical concerns (*82*). Despite these risks, such interventions may be necessary in some circumstances. It is not too early to debate whether, when, and how such strategies should be deployed (*83*). Finally, controlled ex situ conservation, involving captive breeding and genetic manipulation in zoological and botanical gardens and recently developed cryogenic seed banks, may contribute to conserving species or populations with a view to future release or reintroduction.

The particular strategies deployed will depend on the circumstances of the species (Fig. 3) and will also vary in the financial and other resources they require. The perceived conservation value of particular habitats and species will also play a part and may be informed by ecosystem service assessments. Thus, management decisions will depend on judgments of potential risks and benefits balanced against costs and available or anticipated resources. Decisions must balance tradeoffs. For example, creating permeable landscapes to facilitate migration may be more effective under climate change than intensive management in "static" conservation areas as climate change proceeds, but may risk further spread of disease or invasive species. This assessment should aim to maximize the likelihood of the desired management outcome, minimize the financial costs, and assess associated risks.

Outlook

Conservationists are increasingly concerned about biodiversity disruption and loss as climate-change impacts intensify in the coming decades. So far the focus has mostly been on multispecies, place-based predictions with emphasis on exposure to climate change. Our review of the evidence from paleohistory, current observations, experiments, and models emphasizes the extent to which species vary in their vulnerability. This variation represents perhaps our best hope for maintaining biodiversity and its associated ecological goods and services in the future. Developing effective strategies will rely on improved understanding of the nature of the climate threat to species, and the way that it interacts with their natural coping mechanisms. The rich history of ecological, evolutionary, and paleontological field studies, brought together with relevant climate data and with appropriate evolutionary and ecological theory and modeling, has the potential to transform the way that we assess climate-change vulnerability. More appropriate conservation actions will result from taking into account all three aspects of vulnerability—species sensitivity, adaptive capacity, and exposure.

Many orthodox conservation practices, such as the restoration and protection of habitats and the removal of anthropogenic pressures unrelated to climate, will continue to increase species and ecosystem adaptive capacity to climate change. Additional, more informed approaches will require new research, especially to identify and parameterize key ecological and evolutionary

variables, and to develop models that are capable of providing reliable predictions without being unrealistically data-hungry. The evidence is there to build upon. Now is the time for conservation biology to move beyond predictions to analysis, diagnosis, and design and implementation of effective measures to protect biodiversity.

References and Notes

1. IPCC, *Climate Change 2007: Impacts, Adaptation and Vulnerability. Contribution of Working Group II to the Fourth Assessment Report of the Intergovernmental Panel on Climate Change* (Cambridge Univ. Press, Cambridge, 2007).
2. P. Leadley *et al*., *Biodiversity Scenarios: Projections of 21st Century Change in Biodiversity and Associated Ecosystem Services* (Secretariat of the Convention on Biological Diversity, Montreal, 2010).
3. S. Solomon, G. K. Plattner, R. Knutti, P. Friedlingstein, *Proc. Natl. Acad. Sci. U.S.A.* **106**, 1704 (2009).
4. A. Guisan, W. Thuiller, *Ecol. Lett.* **8**, 993 (2005).
5. S. E. Williams, L. P. Shoo, J. L. Isaac, A. A. Hoffmann, G. Langham, *PLoS Biol.* **6**, e325 (2008).
6. C. Parmesan, *Annu. Rev. Ecol. Evol. Syst.* **37**, 637 (2006).
7. R. Hickling *et al*., *Glob. Change Biol.* **12**, 450 (2006).
8. M. Hoffmann *et al*., *Science* **330**, 1503 (2010).
9. W. Jetz, D. S. Wilcove, A. P. Dobson, *PLoS Biol.* **5**, e157 (2007).
10. H. M. Pereira *et al*., *Science* **330**, 1496 (2010).
11. IPCC, *Climate Change 2007: The Physical Science Basis. Contribution of Working Group I to the Fourth Assessment Report of the Intergovernmental Panel on Climate Change* (Cambridge Univ. Press, Cambridge, 2007).
12. J. W. Williams, S. T. Jackson, *Front. Ecol. Environ* **5**, 475 (2007).
13. J. M. Jeschke, D. L. Strayer, *Ann. N.Y. Acad. Sci.* **1134**, 1 (2008).
14. G.-R. Walther, *Philos. Trans. R. Soc. Ser. B* **365**, 2019 (2010).
15. L. Hannah *et al*., *Front. Ecol. Environ* **5**, 131 (2007).
16. C. D. Thomas *et al*., *Nature* **427**, 145 (2004).
17. L. Hannah, *Conserv. Biol.* **24**, 70 (2010).
18. O. Hoegh-Guldberg *et al*., *Science* **321**, 345 (2008).
19. C. M. Beale, J. J. Lennon, A. Gimona, *Proc. Natl. Acad. Sci. U.S.A.* **105**, 14908 (2008).
20. C. F. Dormann, *Basic Appl. Ecol.* **8**, 387 (2007).
21. S. T. Jackson, J. L. Betancourt, R. K. Booth, S. T. Gray, *Proc. Natl. Acad. Sci. U.S.A.* **106** (suppl. 2), 19685 (2009).
22. J. A. Wiens, D. Stralberg, D. Jongsomjit, C. A. Howell, M. A. Snyder, *Proc. Natl. Acad. Sci. U.S.A.* **106** (suppl. 2), 19729 (2009).
23. K. J. Willis, S. A. Bhagwat, *Science* **326**, 806 (2009).
24. J. Elith *et al*., *Ecography* **29**, 129 (2006).
25. D. B. Botkin *et al*., *Bioscience* **57**, 227 (2007).
26. G. R. Walther *et al*., *Nature* **416**, 389 (2002).
27. G.-R. Walther, S. Beißner, C. A. Burga, *J. Veg. Sci.* **16**, 541 (2005).
28. S. T. Jackson, D. F. Sax, *Trends Ecol. Evol.* **25**, 153 (2010).
29. R. Menéndez *et al*., *Proc. Biol. Sci.* **273**, 1465 (2006).
30. D. F. Doak, W. F. Morris, *Nature* **467**, 959 (2010).
31. D. M. Johnson *et al*., *Proc. Natl. Acad. Sci. U.S.A.* **107**, 20576 (2010).
32. T. P. Dawson, M. D. A. Rounsevell, T. Kluvankova-Oravska, V. Chobotova, A. Stirling, *Biodivers. Conserv.* **19**, 2843 (2010).
33. P. Gienapp, C. Teplitsky, J. S. Alho, J. A. Mills, J. Merilä, *Mol. Ecol.* **17**, 167 (2008).
34. L.-M. Chevin, R. Lande, G. M. Mace, *PLoS Biol.* **8**, e1000357 (2010).
35. M. E. Visser, *Proc. Biol. Sci.* **275**, 649 (2008).
36. W. E. Bradshaw, C. M. Holzapfel, *Science* **312**, 1477 (2006).
37. S. Jenouvrier *et al*., *Proc. Natl. Acad. Sci. U.S.A.* **106**, 1844 (2009).
38. A. Ozgul *et al*., *Nature* **466**, 482 (2010).
39. A. C. Baker, C. J. Starger, T. R. McClanahan, P. W. Glynn, *Nature* **430**, 741 (2004).
40. S. J. Franks, S. Sim, A. E. Weis, *Proc. Natl. Acad. Sci. U.S.A.* **104**, 1278 (2007).
41. A. B. Phillimore, J. D. Hadfield, O. R. Jones, R. J. Smithers, *Proc. Natl. Acad. Sci. U.S.A.* **107**, 8292 (2010).
42. Z. G. Davies, R. J. Wilson, S. Coles, C. D. Thomas, *J. Anim. Ecol.* **75**, 247 (2006).
43. C. D. Thomas *et al*., *Nature* **411**, 577 (2001).
44. X. Morin, M. J. Lechowicz, *Biol. Lett.* **4**, 573 (2008).
45. C. A. Deutsch *et al*., *Proc. Natl. Acad. Sci. U.S.A.* **105**, 6668 (2008).
46. D. A. Keith *et al*., *Biol. Lett.* **4**, 560 (2008).
47. G. M. MacDonald *et al*., *Prog. Phys. Geogr.* **32**, 139 (2008).
48. B. Shuman, A. K. Henderson, C. Plank, I. Stefanova, S. S. Ziegler, *Ecology* **90**, 2792 (2009).
49. S. T. Jackson, J. T. Overpeck, *Paleobiology* **26** (suppl.), 194 (2000).
50. S. P. Harrison, M. F. Sanchez Goñi, *Quat. Sci. Rev.* **29**, 2957 (2010).
51. L. Dalén *et al*., *Proc. Natl. Acad. Sci. U.S.A.* **104**, 6726 (2007).
52. D. Magri *et al*., *New Phytol.* **171**, 199 (2006).
53. B. Shapiro *et al*., *Science* **306**, 1561 (2004).
54. J. L. Betancourt, T. R. Van Devender, P. S. Martin, *Packrat Middens: The Last 40,000 Years of Biotic Change* (Univ. of Arizona Press, Tucson, AZ, 1990).
55. J. L. Blois, J. L. McGuire, E. A. Hadly, *Nature* **465**, 771 (2010).
56. K. J. Willis, K. D. Bennett, S. A. Bhagwat, H. J. B. Birks, *Syst. Biodivers.* **8**, 3 (2010).
57. J. S. McLachlan, J. S. Clark, P. S. Manos, *Ecology* **86**, 2088 (2005).
58. K. C. Rowe, E. J. Heske, P. W. Brown, K. N. Paige, *Proc. Natl. Acad. Sci. U.S.A.* **101**, 10355 (2004).
59. L. Kullman, *Glob. Ecol. Biogeogr.* **5**, 94 (1996).
60. M. E. Lyford, S. T. Jackson, J. L. Betancourt, S. T. Gray, *Ecol. Monogr.* **73**, 567 (2003).
61. R. S. Thompson, in *Vegetation History*, B. Huntley, T. Webb III, Eds. (Kluwer Academic, Dordrecht, Netherlands, 1988), pp. 415–458.
62. J. W. Williams, D. M. Post, L. C. Cwynar, A. F. Lotter, A. J. Levesque, *Geology* **30**, 971 (2002).
63. J. Boys, M. Cherry, S. Dayanandan, *Am. J. Bot.* **92**, 833 (2005).
64. M. Kuch *et al*., *Mol. Ecol.* **11**, 913 (2002).
65. S. T. Jackson, C. Weng, *Proc. Natl. Acad. Sci. U.S.A.* **96**, 13847 (1999).
66. P. L. Koch, A. D. Barnosky, *Annu. Rev. Ecol. Evol. Syst.* **37**, 215 (2006).
67. A. M. Lister, A. J. Stuart, *C. R. Geosci.* **340**, 615 (2008).
68. B. L. Turner II *et al*., *Proc. Natl. Acad. Sci. U.S.A.* **100**, 8074 (2003).
69. A. Chin, P. M. Kyne, T. I. Walker, R. B. McAuley, *Glob. Change Biol.* **16**, 1936 (2010).
70. NatureServe Climate Change Vulnerability Index (www.natureserve.org/prodServices/climatechange/ccvi.jsp).
71. C. N. Johnson, *Proc. R. Soc. London Ser. B* **269**, 2221 (2002).
72. F. Altermatt, *Ecol. Lett.* **13**, 1475 (2010).
73. C. Both *et al*., *Proc. R. Soc. Ser. B* **277**, 1259 (2010).
74. F. Jiguet *et al*., *Ecol. Lett.* **9**, 1321 (2006).
75. S. J. Thackeray *et al*., *Glob. Change Biol.* **16**, 3304 (2010).
76. W. Foden *et al*., in *The 2008 Review of the IUCN Red List of Threatened Species*, C. Hilton-Taylor, S. Stuart, J. C. Vie, Eds. (IUCN, Gland, Switzerland, 2008), pp. 1–14.
77. M. Cardillo *et al*., *Science* **309**, 1239 (2005); 10.1126/science.1116030.
78. R. G. Pearson, T. P. Dawson, *Biol. Conserv.* **123**, 389 (2005).
79. A. Hodgson, C. D. Thomas, B. A. Wintle, A. Moilanen, *J. Appl. Ecol.* **46**, 964 (2009).
80. P. Beier, B. Brost, *Conserv. Biol.* **24**, 701 (2010).
81. A. Ricciardi, D. Simberloff, *Trends Ecol. Evol.* **24**, 248 (2009).
82. R. Sandler, *Conserv. Biol.* **24**, 424 (2010).
83. D. M. Richardson *et al*., *Proc. Natl. Acad. Sci. U.S.A.* **106**, 9721 (2009).

84. We thank three anonymous reviewers for helpful comments. Some of the ideas presented here emerged from discussions among the participants at the NERC QUEST (Quantifying and Understanding the Earth System) Working Group on Biodiversity and Climate Change, which was cosponsored by and held at the Royal Botanic Gardens, Kew, in September 2009. Supported by QUEST (J.I.H. and I.C.P.), NSF grant 0949308 (S.T.J.), and the UK Natural Environment Research Council (G.M.M.).

Supporting Online Material

www.sciencemag.org/cgi/content/full/332/6025/53/DC1
SOM Text
References

10.1126/science.1200303

2011 ASPIRE Hemophilia Research Awards

Pfizer is proud to announce the Advancing Science through Pfizer – Investigator Research Exchange (ASPIRE) 2011 Investigator Awards in Hemophilia Research, a competitive, peer-reviewed grants program sponsored by Pfizer for investigators in the United States.

Mission

- To support basic science, translational and clinical research through a competitive grants program that advances medical knowledge in the pathogenesis and treatment of hemophilia.
- To support academic research as well as the career development of promising young and established scientists.

Area of Research Focus

Pfizer will support competitive grant programs which address one of the following areas in Hemophilia A and/or Hemophilia B.

- Epidemiology / burden of disease / Outcomes Research
- Patient adherence to prescribed regimen
- Routine prophylaxis and preventative treatment
- Surgical prophylaxis, dosing
- On Demand dosing
- Treatment of inhibitors: Immune Tolerance Therapy, inhibitor bypass therapy
- Switching experience
- Management of adolescent Hemophilia patients & quality of life
- Management of the aging hemophilia population
- Basic science: Point of differentiation study
- Clinical monitoring of hemophilia treatment
- Recovery experience (hemophilia B patients)

Application & Selection Process

Application is open to US investigators. Selection of research proposals will be performed by an independent, external expert panel comprised of nationally known academic clinicians. Project duration should be 1-3 years and should be approximately $100,000/year, inclusive of overhead costs (capped at 28%).

For more information please visit **www.aspireresearch.org**

ASPIRE
Advancing Science Through Pfizer – Investigator Research Exchange

Pfizer

The World's Technological Capacity to Store, Communicate, and Compute Information

Martin Hilbert[1]* and Priscila López[2]

We estimated the world's technological capacity to store, communicate, and compute information, tracking 60 analog and digital technologies during the period from 1986 to 2007. In 2007, humankind was able to store 2.9×10^{20} optimally compressed bytes, communicate almost 2×10^{21} bytes, and carry out 6.4×10^{18} instructions per second on general-purpose computers. General-purpose computing capacity grew at an annual rate of 58%. The world's capacity for bidirectional telecommunication grew at 28% per year, closely followed by the increase in globally stored information (23%). Humankind's capacity for unidirectional information diffusion through broadcasting channels has experienced comparatively modest annual growth (6%). Telecommunication has been dominated by digital technologies since 1990 (99.9% in digital format in 2007), and the majority of our technological memory has been in digital format since the early 2000s (94% digital in 2007).

Leading social scientists have recognized that we are living through an age in which "the generation of wealth, the exercise of power, and the creation of cultural codes came to depend on the technological capacity of societies and individuals, with information technologies as the core of this capacity" (*1*). Despite this insight, most evaluations of society's technological capacity to handle information are based on either qualitative assessments or indirect approximations, such as the stock of installed devices or the economic value of related products and services (*2*–*9*).

Previous work. Some pioneering studies have taken a more direct approach to quantify the amount of information that society processes with its information and communication technologies (ICTs). After pioneering work in Japan (*10*), Pool (*11*) estimated the growth trends of the "amount of words" transmitted by 17 major communications media in the United States from 1960 to 1977. This study was the first to show empirically the declining relevance of print media with respect to electronic media. In 1997, Lesk (*12*) asked, "How much information is there in the world?" and presented a brief outline on how to go about estimating the global information storage capacity. A group of researchers at the University of California at Berkeley took up the measurement challenge between 2000 and 2003 (*13*). Their focus on "uniquely created" information resulted in the conclusion that "most of the total volume of new information flows is derived from the volume of voice telephone traffic, most of which is unique content" (97%); because broadcasted television and most information storage mainly consists of duplicate information, these omnipresent categories contributed relatively little. A storage company hired a private sector research firm [International Data Corporation (IDC)] to estimate the global hardware capacity of digital ICT for the years 2007–2008 (*14*). For digital storage, IDC estimates that in 2007 "all the empty or usable space on hard drives, tapes, CDs, DVDs, and memory (volatile and nonvolatile) in the market equaled 264 exabytes" (*14*). During 2008, an industry and university collaboration explicitly focused on information consumption (*15*) measured in hardware capacity, words, and hours. The results are highly reliant on media time-budget studies, which estimate how many hours people interact with a media device. The result obtained with this methodology was that computer games and movies represent 99.2% of the total amount of data "consumed."

Scope of our exercise. To reconcile these different results, we focused on the world's technological capacity to handle information. We do not account for uniqueness of information because it is very difficult to differentiate between truly new and merely recombined, duplicate information. Instead, we assume that all information has some relevance for some individual. Aside from the traditional focus on the transmission through space (communication) and time (storage), we also considered the computation of information. We defined storage as the maintenance of information over a considerable amount of time for explicit later retrieval and estimated the installed (available) capacity. We did not consider volatile storage in the respective inventory

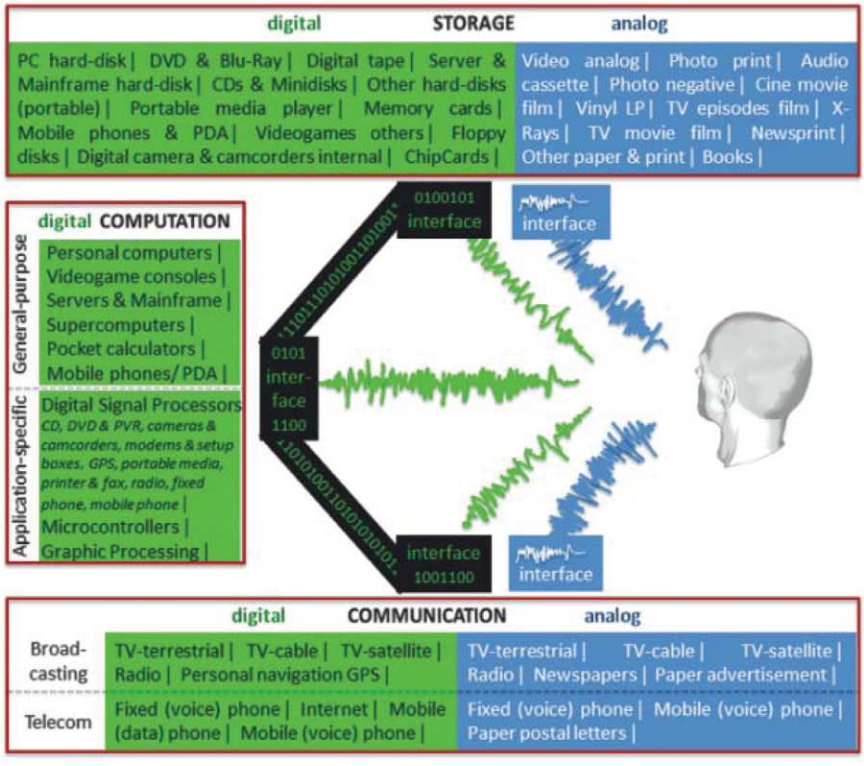

Fig. 1. The three basic information operations and their most prominent technologies.

[1]Annenberg School of Communication, University of Southern California, Los Angeles, CA 90089, USA; United Nations Economic Commission for Latin America and the Caribbean (ECLAC). [2]Information and Communication Sciences Department, Open University of Catalonia, Barcelona 08018, Spain.

*To whom correspondence should be addressed. E-mail: mhilbert@usc.edu

(such as RAM) because the ultimate end of volatile memory is computation, not storage per se. Communication was defined as the amount of information that is effectively received or sent by the user while being transmitted over a considerable distance (outside the local area). This includes those transmissions whose main purpose consists in the overcoming of distances, not the local sharing of information (such as the distribution of copies at a meeting, or communication through private local area networks). We took inventory of the effective communication capacity (the actual amount of bits transmitted). We defined computation as the meaningful transformation of information and estimated the installed (available) capacity.

More precisely, as shown in Fig. 1, we distinguished among storage of information in bits, unidirectional diffusion through broadcasting in bits per second, bidirectional telecommunication in bits per second, computation of information by general purpose computers in instructions per second [or MIPS, million (or mega) instructions per second], and the estimated computational capacity of a selected sample of application-specific devices (MIPS). Whereas previous studies tracked some two or three dozen categories of ICT over three consecutive years at most, our study encompasses worldwide estimates for 60 categories (21 analog and 39 digital) and spans over two decades (1986–2007).

We obtained the technological capacity by multiplying the number of installed technological devices with their respective performances. All estimates are yearly averages, but we adjusted for the fact that the installed technological stock of a given year is the result of an accumulation process of previous years, whereas each year's technologies contribute with different performance rates. We used 1120 sources and explain our assumptions in detail in (*16*). The statistics we rely on include databases from international organizations [such as (*17*–*22*)], historical inventories from individuals for commercial or academic purposes [such as (*23*–*26*)], publicly available statistics from private research firms [such as (*27*, *28*)], as well as a myriad of sales and product specifications from equipment producers. We filled in occasional blanks with either linear or exponential interpolations, depending on the nature of the process in question. Frequently, we compared diverse sources for the same phenomena and strove for reasonable middle grounds in case of contradictions. In cases in which specific country data were not available, we aimed for a globally balanced outlook by creating at least two international profiles, one for the "developed" member countries of the Organisation for Economic Co-operation and Development (OECD) and another one for the rest of the world.

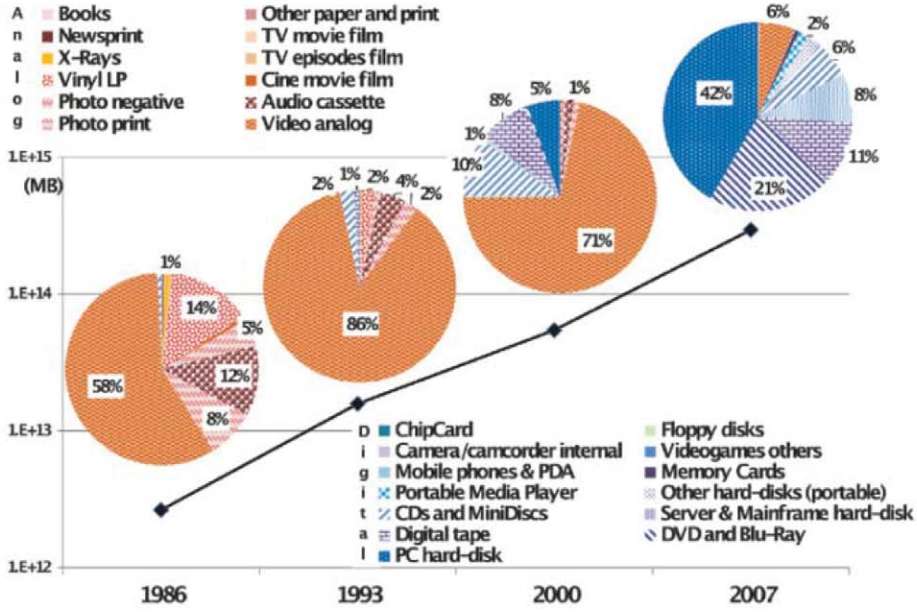

Fig. 2. World's technological installed capacity to store information (table SA1) (*16*).

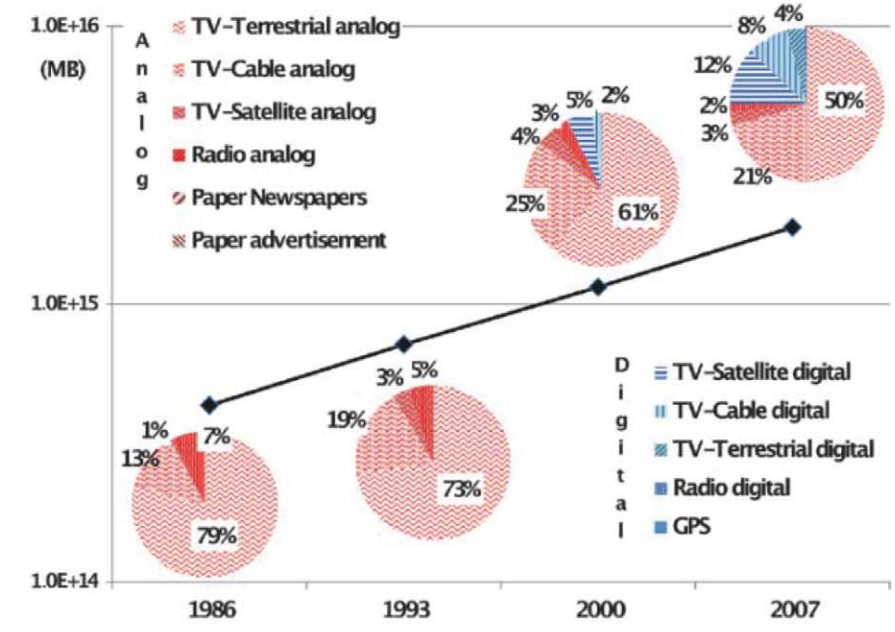

Fig. 3. World's technological effective capacity to broadcast information in optimally compressed megabytes MB per year, for 1986, 1993, 2000, and 2007; semi-logarithmic plot (table SA2) (*16*).

Information, not hardware with redundant data. Although the estimation of the global hardware capacity for information storage and communication is of interest for the ICT industry (*14*), we are more interested in the amount of information that is handled by this hardware. Therefore, we converted the data contained in storage and communication hardware capacity into informational bits by normalizing on compression rates. This addresses the fact that information sources have different degrees of redundancy. The redundancy (or predictability) of the source is primarily determined by the content in question, such as text, images, audio, or video (*29*, *30*). Considering the kind of content, we measured information as if all redundancy were removed with the most efficient compression algorithms available in 2007 (we call this level of compression "optimally compressed"). Shannon (*29*) showed that the uttermost compression of information approximates the entropy of the source, which unambiguously quantifies the amount of information contained in the message. In an information theoretic sense (*30*), information is defined as the opposite of uncertainty. Shannon (*29*) defined one bit as the amount of information that reduces uncertainty by half (regarding a given probability space, such as letters from an alphabet or pixels from a color scale). This definition is independent of the specific task

or content. For example, after normalization on optimally compressed bits we can say things like "a 6-cm^2 newspaper image is worth a 1000 words" because both require the same average number of binary yes/no decisions to resolve the same amount of uncertainty.

Normalization on compression rates is essential for comparing the informational performance of analog and digital technologies. It is also indispensable for obtaining meaningful time series of digital technologies because more efficient compression algorithms enable us to handle more information with the same amount of hardware. For example, we estimated that a hard disk with a hardware performance of 1 MB for video storage was holding the equivalent of 1 optimally compressed MB in 2007 ("optimally compressed" with MPEG-4) but only 0.45 optimally compressed MB in 2000 (compressed with MPEG-1), 0.33 in 1993 (compressed with cinepack), and merely 0.017 optimally compressed MB in 1986 (supposing that no compression algorithms were used). Given that statistics on the most commonly used compression algorithms are scarce, we limited our estimations of information storage and communication to the years 1986, 1993, 2000 and 2007 [(*16*), section B, Compression].

Conventionally, bits are abbreviated with a small "b" (such as in kilobits per second: kbps) and bytes (equal to 8 bits) with a capital "B" (such as in megabyte: MB). Standard decimal prefixes are used: kilo- (10^3), mega- (10^6), giga- (10^9), tera- (10^{12}), peta- (10^{15}), exa- (10^{18}), and zetta- (10^{21}).

Storage. We estimated how much information could possibly have been stored by the 12 most widely used families of analog storage technologies and the 13 most prominent families of digital memory, from paper-based advertisement to the memory chips installed on a credit card (Fig. 2). The total amount of information grew from 2.6 optimally compressed exabytes in 1986 to 15.8 in 1993, over 54.5 in 2000, and to 295 optimally compressed exabytes in 2007. This is equivalent to less than one 730-MB CD-ROM per person in 1986 (539 MB per person), roughly 4 CD-ROM per person of 1993, 12 CD-ROM per person in the year 2000, and almost 61 CD-ROM per person in 2007. Piling up the imagined 404 billion CD-ROM from 2007 would create a stack from the earth to the moon and a quarter of this distance beyond (with 1.2 mm thickness per CD).

Our estimate is larger than the previously cited hardware estimate from IDC for the same year (IDC estimates 264 exabytes of digital hardware, not normalized for compression, whereas we counted 276 optimally compressed exabytes on digital devices, which occupy 363 exabytes of digital hardware) (*14*). Although our study is more comprehensive, we are not in a position to fully analyze all differences because IDC's methodological assumptions and statistics are based on inaccessible and proprietary company sources.

Before the digital revolution, the amount of stored information was dominated by the bits stored in analog videotapes, such as VHS cassettes (Fig. 2). In 1986, vinyl long-play records still made up a considerable part (14%), as did analog audio cassettes (12%) and photography (5% and 8%). It was not until the year 2000 that digital storage made a notable contribution to our technological memory, contributing 25% of the total in 2000. Hard disks make up the lion share of storage in 2007 (52% in total), optical storage contributed more than a quarter (28%), and digital tape roughly 11%. Paper-based storage solutions captured a decreasing share of the total (0.33% in 1986 and 0.007% in 2007), even though their capacity was steadily increasing in absolute terms (from 8.7 to 19.4 optimally compressed petabytes).

Communication. We divided the world's technological communication capacity into two broad groups: One includes technological systems that provide only unidirectional downstream capacity to diffuse information (referred to as broadcasting), and one provides bidirectional upstream and downstream channels (telecommunication). The ongoing technological convergence between broadcasting and telecommunication is blurring this distinction, as exemplified by the case of digital television, which we counted as broadcasting even though it incorporates a small but existent upstream channel (such as video-on-demand).

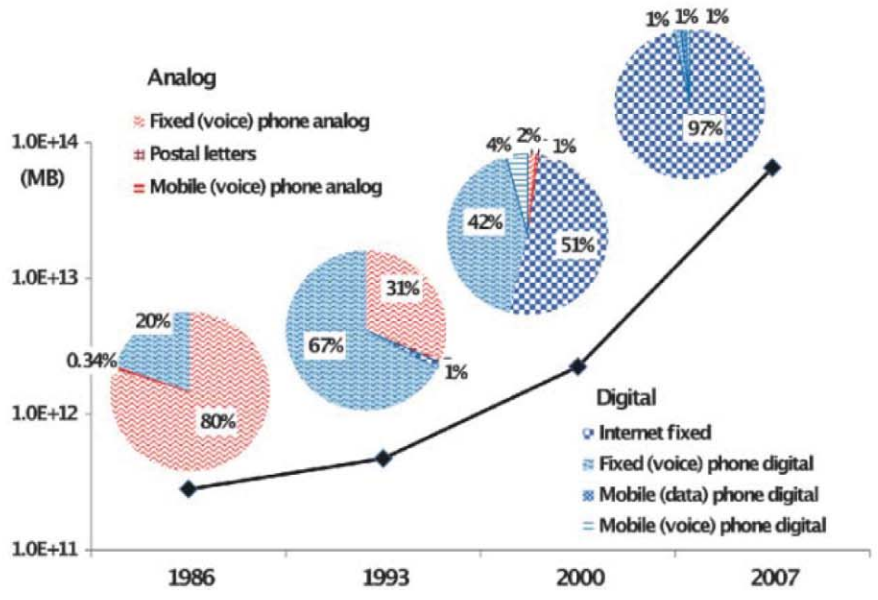

Fig. 4. World's technological effective capacity to telecommunicate information (table SA2) (*16*).

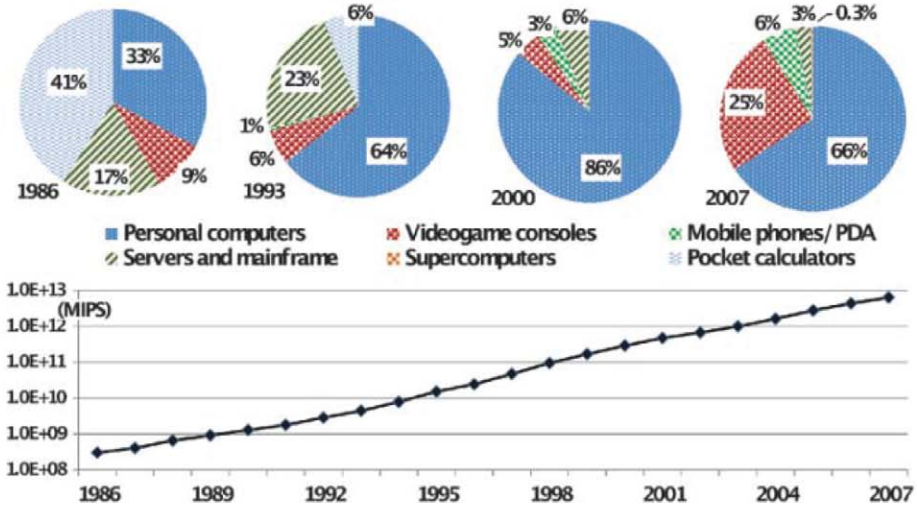

Fig. 5. World's technological installed capacity to compute information on general-purpose computers, in MIPS (table SA3) (*16*).

The inventories of Figs. 3 and 4 account for only those bits that are actually communicated. In the case of telecommunication, the sum of the effective usages of all users is quite similar to the total installed capacity (any difference represents an over- or future investment). This is because most backbone networks are shared and only used sporadically by an individual user. If all users demanded their promised bandwidth simultaneously, the network would collapse. This is not the case for individual broadcast subscribers, who could continuously receive incoming information. To meaningfully compare the carrying capacities of each, we applied effective consumption rates to the installed capacity of broadcasting (calling it the effective capacity). This reduced the installed capacity by a stable factor (by 9 in 1986, 9.1 in 1993, 8.7 in 2000, and 8.4 in 2007), implying an average individual broadcast consumption of roughly 2 hours and 45 min per 24 hours. It did not notably change the relative distribution of the diverse technologies (Fig. 3).

Figure 3 displays the capacity of six analog and five digital broadcast technologies, including newspapers and personal navigation devices [global postioning system (GPS)]. In 1986, the world's technological receivers picked up around 432 exabytes of optimally compressed information, 715 optimally compressed exabytes in 1993, 1.2 optimally compressed zettabytes in 2000, and 1.9 optimally compressed zettabytes in 2007. Cable and satellite TV steadily gained importance, but analog, "over-the-air" terrestrial television still dominated the evolutionary trajectory. Digital satellite television led the pack into the digital age, receiving 50% of all digital broadcast signals in 2007. Only a quarter of all broadcasting information was in digital format in 2007. The share of radio declined gradually from 7.2% in 1986 to 2.2% in 2007.

Figure 4 presents effective capacity of the three most common bidirectional analog telecommunication technologies and their four most prominent digital heirs. The 281 petabytes of optimally compressed information from 1986 were overwhelmingly dominated by fixed line telephony, whereas postal letters contributed only 0.34%. The year 1993 was characterized by the digitization of the fixed phone network (471 optimally compressed petabytes). We estimate the year 1990 to be the turning point from analog to digital supremacy. The Internet revolution began shortly after the year 2000. In only 7 years, the introduction of broadband Internet effectively multiplied the world's telecommunication capacity by a factor of 29, from 2.2 optimally compressed exabytes in 2000 to 65 in 2007. The most widespread telecommunication technology was the mobile phone, with 3.4 billion devices in 2007 (versus 1.2 billion fixed-line phones and 0.6 billion Internet subscriptions). Nevertheless, the fixed-line phone is still the solution of choice for voice communication (1.5% of the total). The mobile phone network became increasingly dominated by data traffic in 2007 (1.1% for mobile data versus 0.8% for mobile voice).

When compared with broadcasting, telecommunications makes up a modest but rapidly growing part of the global communications landscape (3.3% of the sum in 2007, up from 0.07% in 1986). Although there are only 8% more broadcast devices in the world than telecommunication equipment (6.66 billion versus 6.15 billion in 2007), the average broadcasting device communicates 27 times more information per day than the average telecommunications gadget. This result might be unexpected, especially considering the omnipresence of the Internet, but can be understood when considering that an average Internet subscription effectively uses its full bandwidth for only around 9 min per day (during an average 1 hour and 36 min daily session).

Computation. From a theoretical standpoint, a "computation" is the repeated transmission of information through space (communication) and time (storage), guided by an algorithmic procedure (*31*). The problem is that the applied algorithmic procedure influences the overall performance of a computer, both in terms of hardware design and in terms of the contributions of software. As a result, the theoretical, methodological, and statistical bases for our estimates for computation are less solid than the ones for storage and communication. In contrast to Shannon's bit (*29*, *30*), there is no generally accepted theory that provides us with an ultimate performance measure for computers. There are several ways to measure computational hardware performance. We chose MIPS as our hardware performance metric, which was imposed on us by the reality of available statistics. Regarding the contributions of software, it would theoretically be possible to normalize the resulting hardware capacity for algorithmic efficiency (such as measured with O-notation) (*32*). This would recognize the constant progress of algorithms, which continuously make more efficient use of existing hardware. However, the weighted contribution of each algorithm would require statistics on respective execution intensities of diverse algorithms on different computational devices. We are not aware of such statistics. As a result of these limitations, our estimates refer to the installed hardware capacity of computers.

We distinguished between two broad groups of computers. The first group includes all computers whose functionality is directly guided by their human users. We call this group "general-purpose computers" and include six technological families (Fig. 5). The second group carries out automated computations that are incidental to the primary task, such as in electronic appliances or visual interfaces. The user may have a range of predefined choices regarding their functionality but cannot change the automated logic of these

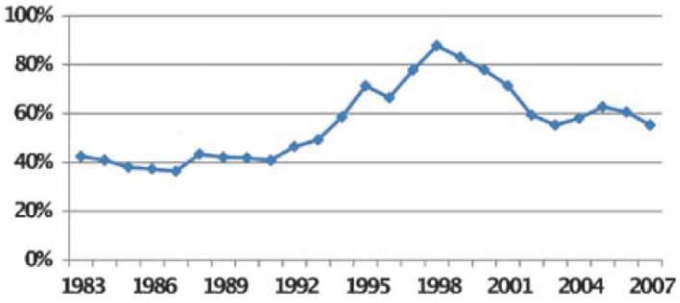

Fig. 6. Annual growth of installed general-purpose computational capacity as percentage of all previous computations since 1977 (year t / Σ[1977, year $t-1$]) (table SA2) (*16*).

Table 1. Evolution of the world's capacity to store, communicate, and compute information, absolute per capita, CARG, and percentage in digital format (tables SA1 to SA3 and SA5) (*16*).

		1986	1993	2000	2007	CAGR 1986–2007
Storage	MB optimal compression per capita (installed capacity)	539	2,866	8,988	44,716	23%
	Percent digital	0.8%	3%	25%	94%	
Broadcast	MB optimal compression per capita per day (effective capacity)	241	356	520	784	6%
	Percent digital	0.0%	0.0%	7.3%	25%	
Telecom	MB optimal compression per capita per day (effective capacity)	0.16	0.23	1.01	27	28%
	Percent digital	19.8%	68.5%	97.7%	99.9%	
General-purpose computation	MIPS per capita (installed capacity)	0.06	0.8	48	968	58%
Sample of application-specific computation	MIPS per capita (installed capacity)	0.09	3.3	239	28,620	83%

embedded systems. We call this group "application-specific computers."

Although general-purpose computers are also equipped with application-specific parts (for example, mobile phones come with digital signal processors, and PCs contain microcontroller units), we only include the capacity of humanly guidable microprocessors in the respective inventory. The calculator laid the cornerstone for modern microprocessors and was still the dominant way to compute information in 1986 (41% of 3.0×10^8 general-purpose MIPS). The landscape changed quickly during the early 1990s as personal computers and servers and mainframe computers pushed the evolutionary trajectory to 4.4×10^9 MIPS. The personal computer extended its dominance during the year 2000 (86% of a total of 2.9 10^{11} MIPS), to be rivaled in 2007 by videogame consoles (1.6×10^{12} MIPS, or 25% of the total of 6.4×10^{12} MIPS) and increasingly relevant mobile phones (3.7×10^{11} MIPS, or 6% of the 2007 total). Nowadays, clusters of videogame consoles are occasionally used as supercomputer substitutes for scientific purposes and other data-intensive computational tasks (*33*). The relatively small role of supercomputers (less than 0.5% throughout) and professional servers and mainframes might come as a surprise. It can partially be explained by the fact that the inventory of Fig. 5 presents the installed capacity, independent of effective usage rates. We also carried out some estimations on the basis of the effective gross usage of the computers, which considers the time users interact with computers (not the net computational time). As a result, we get between 5.8 and 9.1% of the installed capacity (table SA4) (*16*). With this setup, the share of servers and mainframes grew to 89% in 1986 and 11% in 2007, and supercomputers contributed 4% to the effective capacity in 2007.

The data also allows us to look at respective growth rates. Until the early 1990s, the annual growth rate was quite stable at roughly 40% (Fig. 6). The 1990s show outstanding growth, reaching a peak of 88% in 1998. Since then, the technological progress has slowed. In recent times, every new year allows humankind to carry out roughly 60% of the computations that could have possibly been executed by all existing general-purpose computers before that year.

Our inventory of application-specific computations is the least complete one. The entire group of application-specific computers is very large and diverse (for example, dice cups and roulette wheels are application-specific, analog, random-number generators), and it is often not straightforward to translate their performance into MIPS. The main goal of our inventory of this group was to show that the computational hardware capacity of application-specific computers is larger than the computational capacity of general-purpose computers (table SA3) (*16*). To achieve this, we focused on a sample that includes three prominent groups: digital signal processors (DSPs), which translate between analog and digital signals (including CD, DVD, and PVR devices; cameras and camcorders; modems and setup boxes; GPS; portable media; printer and fax; radio; and fixed-line and mobile phones); microcontrollers (MCUs) (which regulate electronics and appliances); and graphic processing units (GPUs) (an increasingly powerful microprocessor for visual displays). Although microcontrollers dominated our sample of application-specific computing support in 1986 (90% of the 4.3×10^8 application-specific MIPS from our sample), graphic processing units clearly made up the lion's share in 2007 (97% of 1.9×10^{14} MIPS).

Comparisons and growth rates. The world's technological capacity to compute information has by far experienced the highest growth (Table 1). The per capita capacity of our sample of application-specific machine mediators grew with a compound annual growth rate (CAGR) of 83% between 1986 and 2007, and humanly guided general-purpose computers grew at 58% per year. The world's technological capacity to telecommunicate only grew half as fast (CAGR of 28%). This might seem a little surprising because the advancement of telecommunications, and especially the Internet, is often celebrated as the epitome of the digital revolution. The results from Table 1 challenge this idea and move the world's ability to compute information into the spotlight. The storage of information in vast technological memories has experienced a growth rate almost similar to telecommunication (CAGR of 23% per capita over two decades). The lower growth rate results from the relatively high base level provided by prevalent analog storage devices. The main characteristic of the storage trajectory is the digitalization of previously analog information (from 0.8% digital in 1986 to 94% in 2007). The global capacity to broadcast information has experienced the least progress at 6% CAGR per capita. Broadcasting is also the only information operation that is still dominated by analog ICT. As a result, the capacity to store information has grown at a much faster rate than that of the combined growth rate of tele- and broadcast communication. In 1986, it would have been possible to fill the global storage capacity with the help of all effectively used communication technologies in roughly 2.2 days (539/241.16). In 1993, it would have taken almost 8 days; in the year 2000, it would take roughly 2.5 weeks; and in 2007, almost 8 weeks would be required.

The CAGRs represent the temporal average of periods that were experiencing different patterns of technological change. General-purpose computation had its peak growth around the turn of the millennia (Fig. 6). Storage capacity slowed down around the year 2000, but accelerated growth has been occurring in recent years (CAGR of 27% for 1986–1993, 18% for 1993–2000, and 26% for 2000–2007) (Table 1). The introduction of broadband has led to a continuous acceleration of telecommunication (CAGR of 6% for 1986–1993, 23% for 1993–2000, and 60% for 2000–2007) (Table 1), whereas broadcasting had a relatively stable rate of change (CAGRs of 5.7%, 5.6%, and 6.1% for 1986–1993, 1993–2000, and 2000–2007, respectively) (Table 1).

The growth rates also allow us to look at the application of Moore's laws (*34*) for the technological information processing capacity of humankind. Machines' application-specific capacity to compute information per capita has roughly doubled every 14 months over the past decades in our sample, whereas the per capita capacity of the world's general-purpose computers has doubled every 18 months. The global telecommunication capacity per capita doubled every 34 months, whereas the world's storage capacity per capita required roughly 40 months. Per capita broadcast information has doubled roughly every 12.3 years. Of course, such averages disguise the varying nature of technological innovation avenues (*35*).

Perspectives. To put our findings in perspective, the 6.4×10^{18} instructions per second that humankind can carry out on its general-purpose computers in 2007 are in the same ballpark area as the maximum number of nerve impulses executed by one human brain per second (10^{17}) (*36*). The 2.4×10^{21} bits stored by humanity in all of its technological devices in 2007 is approaching an order of magnitude of the roughly 10^{23} bits stored in the DNA of a human adult (*37*), but it is still minuscule as compared with the 10^{90} bits stored in the observable universe (*38*). However, in contrast to natural information processing, the world's technological information processing capacities are quickly growing at clearly exponential rates.

References and Notes

1. M. Castells, *End of Millennium, The Information Age: Economy, Society and Culture,* vol. III (Wiley-Blackwell, Malden, MA, 2000).
2. D. Bell, *The Coming of Post-Industrial Society: A Venture in Social Forecasting* (Basic Books, New York, NY, 1973).
3. M. U. Porat, "The Information Economy: Definition and Measurement" (1977); available at www.eric.ed.gov/ERICWebPortal/contentdelivery/servlet/ERICServlet?accno=ED142205.
4. Y. Masuda, *The Information Society as Post-Industrial Society* (Transaction Publishers, Piscataway, NJ, 1980).
5. C. Perez, *Futures* **15**, 357 (1983).
6. T. Forester, *The Information Technology Revolution* (MIT Press, Cambridge, MA, 1985).
7. C. Freeman, F. Louçã, *As Time Goes By: From the Industrial Revolutions to the Information Revolution* (Oxford Univ. Press, New York, 2002).
8. M. Castells, *The Rise of the Network Society: The Information Age: Economy, Society, and Culture*, vol. I (Wiley-Blackwell, Malden, MA, 2009).
9. E. Brynjolfsson, A. Saunders, *Wired for Innovation: How Information Technology is Reshaping the Economy* (MIT Press, Cambridge, MA, 2009).
10. Y. Ito, *Mass Commun. Rev. Yearbook* **2**, 671 (1981).
11. I. D. S. Pool, *Science* **221**, 609 (1983).
12. M. Lesk, "How Much Information Is There In the World?" (1997); available at www.lesk.com/mlesk/ksg97/ksg.html.
13. P. Lyman *et al.*, "How Much Information? 2003" (Univ. California at Berkeley, Berkeley, CA, 2003); available at www2.sims.berkeley.edu/research/projects/how-much-info-2003/.
14. J. Gantz *et al.*, "The Diverse and Exploding Digital Universe: An Updated Forecast of Worldwide Information Growth Through 2011" (IDC sponsored by EMC, Framingham, 2008); available at www.emc.com/leadership/digital-universe/expanding-digital-universe.htm.

15. R. Bohn, J. Short, "How Much Information? 2009 Report on American Consumers" (Global Information Industry Center of University of California, San Diego, San Diego, CA, 2009); available at http://hmi.ucsd.edu/howmuchinfo.php.
16. Materials and methods are available as supporting material on *Science* Online.
17. International Telecommunications Union (ITU), "World Telecommunication/ICT Indicators Database" (ITU, Geneva, 2010); available at www.itu.int/ITU-D/ict/statistics/.
18. Faostat, *ForesSTAT* (Food and Agriculture Organization of the United Nations, 2010); available at http://faostat.fao.org/.
19. Universal Postal Union (UPU), *Postal Statistics* (UPU, Berne, Switzerland, 2007); available at www.upu.int/en/resources/postal-statistics/.
20. International Federation of the Phonographic Industry (IFPI), "The Recording Industry World Sales 1995–2004"; available at www.ifpi.org/content/section_statistics/index.html.
21. Japanese Recording-Media Industries Association, "Press Releases" (2007); available at www.jria.org/english.html.
22. TOP500, "TOP500 List Releases" (TOP500 Supercomputer sites, 2009); available at www.top500.org/lists.
23. J. Porter, "Disk/Trend Reports 1977–1999" (California, 2005); available at www.disktrend.com/.
24. R. Longbottom, "Computer Speed Claims 1980 to 1996" (Roy Longbottom's PC Benchmark collection, 2006); available at www.roylongbottom.org.uk/mips.htm.
25. J. McCallum, in "The Computer Engineering Handbook," V. G. Oklobdzija, Ed. (CRC, Boca Raton, FL, 2002), pp. 136–153.
26. T. Coughlin, "Digital Storage Technology Newsletters" (Coughlin Associates, Atascadero, CA, 2007); available at www.tomcoughlin.com/.
27. Global Technology Team, "Technology Q1 2006 Global Technology Data Book" (Morgan Stanley, New York, 2006); available at www.morganstanley.com/institutional/techresearch/pdfs/global_techdatabook0306.pdf.
28. International Data Corporation (IDC), IDC Media Center (2008); available at www.idc.com/about/press.jsp.
29. C. Shannon, *Bell Syst. Tech. J.* **27**, 379–423 and 623–656 (1948).
30. T. M. Cover, J. A. Thomas, *Elements of Information Theory* (Wiley-Interscience, Hoboken, NJ, 2006).
31. A. M. Turing, *Proc. London Math. Soc.* **s2**, 230 (1937).
32. T. Cormen, C. Leiserson, R. Rivest, C. Stein, *Introduction to Algorithms* (McGraw-Hill, Boston, 2003).
33. B. Gardiner, *Wired Mag.* "Astrophysicist Replaces Supercomputer with Eight PlayStation 3s"; available at www.wired.com/techbiz/it/news/2007/10/ps3_supercomputer (2007).
34. Moore's law measures technological progress of computer performance by counting the numbers of transistors on an integrated circuit, which has approximately doubled every 2 years since the 1960s (*39*).
35. D. Sahal, *Res. Policy* **14**, 61 (1985).
36. This is assuming 100 billion neurons × 1000 connections per neuron × maximum 1000 nerve impulses per second.
37. This is considering a quaternary DNA alphabet, in which each base pair can store 4 bits × 3 billion DNA base pairs per human cell × 60 trillion cells per adult human. Because base pair couples are determined, the 4 bits can be compressed to 2 bits, which can optimally be compressed to 1.73 inside one cell (*40*).
38. S. Lloyd, *Phys. Rev. Lett.* **88**, 237901 (2002).
39. G. E. Moore, *Proc. SPIE* **2439**, 2 (1995).
40. X. Chen, M. Li, B. Ma, J. Tromp, *Bioinformatics* **18**, 1696 (2002).
41. We thank the Information Society Program of United Nations ECLAC (in Chile) for its support; T. Coughlin, J. McCallum, D. Franz, M. Gonzalez, C. Vasquez, L. Adleman, M. Castells, and the statisticians from UPU (Universal Post Union) and ITU (International Telecommunications Union); as well as numerous colleagues who motivated us by doubting the feasibility of this undertaking.

Supporting Online Material

www.sciencemag.org/cgi/content/full/science.1200970/DC1
Materials and Methods
Figs. A1 to E12
Tables SA1 to SE24
References and Notes

29 November 2010; accepted 1 February 2011
Published online 10 February 2011;
10.1126/science.1200970

Chronic Mucocutaneous Candidiasis in Humans with Inborn Errors of Interleukin-17 Immunity

Anne Puel,[1]*‡ Sophie Cypowyj,[2]* Jacinta Bustamante,[1] Jill F. Wright,[3] Luyan Liu,[1] Hye Kyung Lim,[2] Mélanie Migaud,[1] Laura Israel,[1] Maya Chrabieh,[1] Magali Audry,[2] Matthew Gumbleton,[4] Antoine Toulon,[5] Christine Bodemer,[5] Jamila El-Baghdadi,[6] Matthew Whitters,[3] Theresa Paradis,[3] Jonathan Brooks,[3] Mary Collins,[3] Neil M. Wolfman,[3] Saleh Al-Muhsen,[7] Miguel Galicchio,[8] Laurent Abel,[1,2]† Capucine Picard,[1,9,10]† Jean-Laurent Casanova[1,2,7,10]‡

Chronic mucocutaneous candidiasis disease (CMCD) is characterized by recurrent or persistent infections of the skin, nails, and oral and genital mucosae caused by *Candida albicans* and, to a lesser extent, *Staphylococcus aureus*, in patients with no other infectious or autoimmune manifestations. We report two genetic etiologies of CMCD: autosomal recessive deficiency in the cytokine receptor, interleukin-17 receptor A (IL-17RA), and autosomal dominant deficiency of the cytokine interleukin-17F (IL-17F). IL-17RA deficiency is complete, abolishing cellular responses to IL-17A and IL-17F homo- and heterodimers. By contrast, IL-17F deficiency is partial, with mutant IL-17F–containing homo- and heterodimers displaying impaired, but not abolished, activity. These experiments of nature indicate that human IL-17A and IL-17F are essential for mucocutaneous immunity against *C. albicans*, but otherwise largely redundant.

Chronic mucocutaneous candidiasis (CMC) is characterized by infections of the skin, nails, and oral and genital mucosae with *Candida albicans*, which is commensal in healthy individuals (*1*). In patients with inherited or acquired T cell immunodeficiencies, CMC is associated with various infectious diseases (*1*). In patients with STAT3 deficiency and a lack of interleukin-17A (IL-17A)– and IL-22–producing T cells (*2*–*5*), CMC is associated with severe cutaneous and pulmonary staphylococcal infections (*1*). In some patients with IL-12p40 or interleukin-12 receptor β1 (IL-12Rβ1) deficiency and mycobacterial disease (*2*) and in a family with caspase recruitment domain 9 (CARD9) deficiency with systemic candidiasis and peripheral dermatophytosis (*6*), CMC and low proportions of IL-17A–producing T cells were also documented. Finally, CMC is the only infection of patients with autoimmune regulator (AIRE) deficiency, who have neutralizing autoantibodies against IL-17A, IL-17F, and/or IL-22 (*7*, *8*). These data suggest that human IL-17A, IL-17F, and/or IL-22 are involved in mucocutaneous immunity to *C. albicans* (*1*). CMC disease (CMCD), the molecular and cellular basis of which is unknown, consists of CMC in the absence of other overt infectious or autoimmune signs (*1*). CMCD was initially thought to be benign, until squamous cell carcinoma (*9*) and cerebral aneurysms (*10*) were reported. First described in 1967 in sporadic cases (*11*), familial CMC segregating as autosomal dominant (AD) (*12*) and autosomal recessive (AR) traits (*13*) was soon reported. We thus searched for the genetic basis of CMCD, testing the hypothesis that CMCD may be caused by inborn errors of IL-17A, IL-17F, or IL-22 immunity (*1*, *14*).

Autosomal recessive IL-17RA deficiency. We first investigated a French child born to first-cousin parents of Moroccan descent (Fig. 1A) [report S1 (*15*)]. He presented with *C. albicans* dermatitis during the neonatal period and dis-

[1]Laboratory of Human Genetics of Infectious Diseases, Necker Branch, Institut National de la Santé et de la Recherche Médicale, U980, and University Paris Descartes, Necker Medical School, 75015 Paris, France. [2]St. Giles Laboratory of Human Genetics of Infectious Diseases, Rockefeller Branch, The Rockefeller University, New York, NY 10065, USA. [3]Inflammation and Immunology, Pfizer Research, Cambridge, MA 02140, USA. [4]SUNY Upstate Medical University, Syracuse, NY 13210, USA. [5]Dermatology Unit, Necker Hospital, 75015 Paris, France. [6]Unit of Genetics, Military Hospital of Instruction Mohamed V, Rabat 10000, Morocco. [7]Prince Naif Center for Immunology Research, Department of Pediatrics, College of Medicine, King Saud University, Riyadh 11461, Saudi Arabia. [8]Victor J. Vilela Children's Hospital, Rosario, Santa Fe 2000, Argentina. [9]Center for the Study of Primary Immunodeficiencies, Necker Hospital, 75015 Paris, France. [10]Pediatric Hematology-Immunology Unit, Necker Hospital, Paris 75015, France.

*These authors contributed equally to this work.
†These authors contributed equally to this work.
‡To whom correspondence should be addressed. E-mail: jean-laurent.casanova@rockefeller.edu (J.-L.C.); anne.puel@inserm.fr (A.P.)

played *Staphylococcus aureus* dermatitis at 5 months of age. Known causes of CMC were excluded clinically and genetically, and the lack of any phenotype other than CMC led to a diagnosis of AR CMCD. We sequenced the candidate genes encoding IL-22, IL-22RA1, IL-10RB, IL-17A, IL-17F, IL-17RA, and IL-17RC (*16*–*18*). IL-22 binds as a monomer to its receptor, composed of IL-22RA1 and IL-10RB, whereas IL-17A and IL-17F can form homo- or heterodimers that signal via a receptor comprising IL-17RA and IL-17RC chains. The child was found to be homozygous for the c.850C>T nonsense mutation (c.850C>T/c.850C>T), which replaces the glutamine codon in position 284 with a stop codon (Q284X/Q284X) in the *IL17RA* gene (*19*) (Fig. 1B). This premature stop codon is located in the part of the gene encoding the extracellular domain of IL-17RA, upstream from the transmembrane domain sequence (Fig. 1C). No mutations were found elsewhere in *IL17RA* or in any of the other six genes sequenced. The parents and siblings of this child are healthy and heterozygous for the mutant allele, consistent with AR inheritance for this trait. The mutant allele was not found in 1065 healthy controls from 52 ethnic groups from the Centre d'Etude du Polymorphisme Humain–Human Genome Diversity Cell Line Panel CEPH-HGDP, 100 French controls, and 70 Moroccan controls of Berber descent, which ruled out an irrelevant polymorphism and suggested that the mutation may define a rare AR CMCD-causing allele.

The IL-17RA protein was not detected on the surface of fibroblasts, peripheral blood mononuclear cells (PBMCs), or, more specifically, CD4+ T cells, CD8+ T cells, and monocytes from the patient, as shown by flow cytometry with two specific antibodies against the extracellular domain (Fig. 2A and fig. S1). The absence of IL-17RA had no impact on the expression of IL-17RC, which was normal on the patient's monocytes (the only leukocyte subset expressing IL-17RC in controls) and fibroblasts (figs. S1 and S2). Likewise, IL-22RA1 was normally expressed on the patient's fibroblasts (fig. S2). The patient also had a normal proportion of circulating IL-17A– and IL-22–producing T cells (fig. S3). We investigated whether the lack of IL-17RA expression had any functional consequences for the response to IL-17 cytokines, by testing the responses of the patient's fibroblasts to various concentrations of recombinant IL-17A and IL-17F homodimers and to IL-17A–IL-17F heterodimers (*17*, *18*). Like nuclear factor-κB essential modulator (NEMO)–deficient fibroblasts, which have impaired NF-κB activity, and unlike fibroblasts from a healthy control, the patient's fibroblasts did not respond to any of the three IL-17 cytokines, in terms of IL-6 and growth-regulated oncogene-α (GRO-α) induction (*20*), as assessed by enzyme-linked immunosorbent assay (ELISA) on supernatants (Fig. 2, B and C). Moreover, the patient's PBMCs did not respond above baseline to IL-17A or IL-17F for any of the cytokines tested (fig. S4A). Transfection of the patient's fibroblasts with wild-type (WT) *IL17RA*, but not with a mock vector, restored IL-17RA expression and the response to IL-17 cytokines (Fig. 2, D to F). By contrast, IL-6 production by NEMO-deficient cells was not rescued by transfection with *IL17RA* (fig. S4B). Thus, the patient with CMCD that we studied displayed AR, complete IL-17RA deficiency, and a lack of cellular responses to at least three IL-17 cytokine dimers—IL-17A, IL-17F, and IL-17A–IL-17F—in fibroblasts and leukocytes.

Autosomal dominant IL-17F deficiency. We then investigated a multiplex family from Argentina, with AD inheritance of CMCD (Fig. 3A) [report S2 (*15*)]. The *IL22*, *IL22RA*, *IL10RB*, *IL17RA*, *IL17RC*, and *IL17A* genes contained no mutations, but a heterozygous missense mutation was found in the *IL17F* gene of the index case. This mutation, c.284C>T, replaced the serine residue in position 65 of the mature protein with a leucine residue (S65L) (Fig. 3, B and C). The Ser^{65} residue is conserved across mammalian species (fig. S5). Moreover, the sequencing of 1074 control individuals from the CEPH-HGD panel ruled out the possibility that this mutation was an irrelevant polymorphism. Computational analysis showed that Ser^{65} lies in the cavity of the protein, which is thought to be involved in cytokine-to-receptor binding (Fig. 3C) (*21*). No other *IL17F* variations were found in the index case, including the *IL17F* g.7488T>C (rs763780) polymorphism, in which an arginine residue replaced a histidine in position 161 of the protein (H161R), a mutation previously thought to be loss-of-function (*22*). By contrast, we found that the H161R allele encoded an IL-17F protein able to stimulate murine lung epithelial cells (MLEs) (fig. S6). Heterozygosity for the S65L allele was found in all tested members of the kindred with CMCD; we were unable to genotype the fifth patient (III.1 in Fig. 3A), who died at 6 years of age from complications of the disease. The mutant allele was found in only two apparently healthy family members, aged 9 months (III.3 in Fig. 3A) and 21 years (II.8 in Fig. 3A), which suggested incomplete clinical penetrance. We did not detect IL-17F–expressing T cells in controls by flow cytometry, but the patients tested displayed normal proportions of IL-17A– and IL-22–expressing T cells, and their PBMCs secreted normal amounts of cytokines, as measured by Bioplex (fig. S7, A and B).

We investigated the possible deleterious effects of the S65L mutation by producing the mutant IL-17F protein in human embryonic kidney (HEK) 293 cells. The mutation did not seem to affect production of the monomeric protein or the formation of IL-17F homodimers (mutant-mutant and wild-type–mutant) or heterodimers with IL-17A (fig. S8). The mutant-containing dimers seemed to bind normally to homodimeric IL-17 receptors (IL-17RA and IL-17RC), as shown by surface plasmon resonance (table S1 and fig. S9). However, the mutant proteins did not bind IL-17RA on fibroblasts, as shown by flow cytometry, with IL-17RA–deficient cells as controls (confirming that their lack of IL-17RA expression prevented cytokine binding) (figs. S10 and S11). Accordingly, when control fibroblasts (Fig. 4, A and B) and keratinocytes (fig. S12, A and B) were stimulated with mutant S65L IL-17F homodimers, they displayed much weaker IL-6 and GRO-α induction than observed with WT IL-17F homodimers (IL-17WT), IL-17A homodimers, or IL-17A–IL-17FWT heterodimers (*20*). Moreover, control PBMCs showed impaired induction of several cytokines when stimulated with S65L IL-17F homodimers compared with

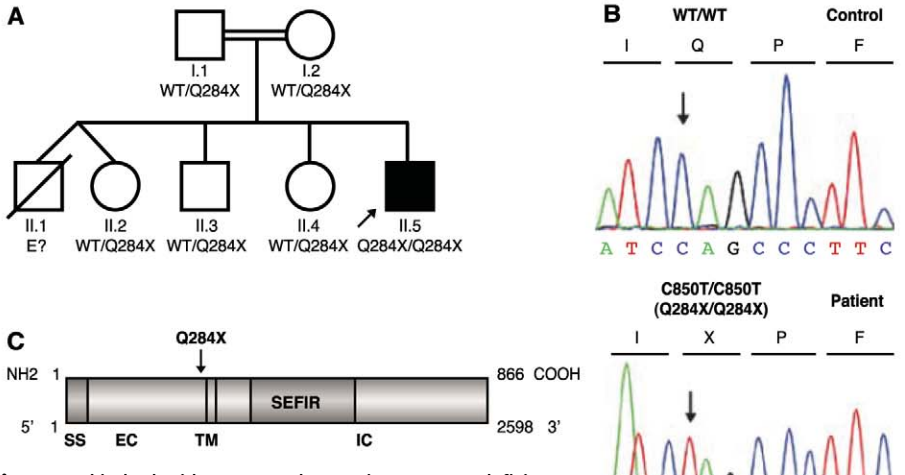

Fig. 1. A kindred with autosomal recessive IL-17RA deficiency. (**A**) Pedigree of the family established by IL-17RA genotyping. The proband is indicated by an arrow. E? indicates individuals whose genetic status could not be evaluated. (**B**) *IL17RA* DNA sequence electrophoregrams for a control and the patient. (**C**) Schematic diagram of the IL-17RA protein with the signal sequence (SS), extracellular (EC), transmembrane (TM), intracellular (IC), and SEFIR (expression similar to fibroblast growth factor–IL-17R) domains and the position within the extracellular domain affected by the mutation.

WT IL-17F homodimers (fig. S12C). These data suggest that the *IL17F* S65L allele is severely hypomorphic (Fig. 4, A and B, and fig. S12, A and B). Furthermore, when the S65L mutant IL-17F formed a heterodimer with either IL-17FWT or IL-17A, the induction of IL-6 and GRO-α was severely impaired in control fibroblasts (Fig. 4, A and B) and keratinocytes (fig. S12, A and B), which indicated a dominant-negative effect of this allele. Finally, as predicted by the lack of binding of mutant cytokine dimers to their receptor (fig. S11), these dimers did not compete with WT dimers (fig. S13, A to D). Thus, the AD CMCD in this kindred results from a hypomorphic, dominant-negative *IL17F* allele, which impairs the receptor binding and bioactivity of both IL-17F homodimers and IL-17A–IL-17F heterodimers.

Concluding remarks. IL-17RA and IL-17F deficiencies underlying mucocutaneous disease caused by *C. albicans* and, to a lesser extent, *S. aureus* are consistent with the mouse model (*23*). IL-17RA– and IL-17RC–deficient mice were more susceptible to oropharyngeal candidiasis (*24*, *25*) and IL-17RA–deficient mice to cutaneous staphylococcal disease (*26*). IL-17A–deficient mice also display impaired clearance of *C. albicans* skin infection (*27*). IL-17F–deficient mice have not yet been tested, but IL-23–deficient mice with impaired expression of IL-17A and IL-17F are also vulnerable (*27*). IL-17A or IL-17F alone are not required for peripheral immunity to *S. aureus*, but mice deficient for both IL-17A and IL-17F display an impaired peripheral immunity to *S. aureus* (*28*). Somewhat at odds with our observations, IL-17A is also required for systemic immunity to *C. albicans* (*29*) and *S. aureus* (*30*). Moreover, mice with IL-17RA, IL-17RC, IL-17A, or IL-17F deficiency are vulnerable to multiple infections at various anatomical sites (*17*, *23*). Overall, our report indicates that human IL-17A and IL-17F are essential for protective immunity to *C. albicans* and, to a lesser extent, *S. aureus* in the nails, skin, and oral and genital mucosae, but otherwise redundant. We

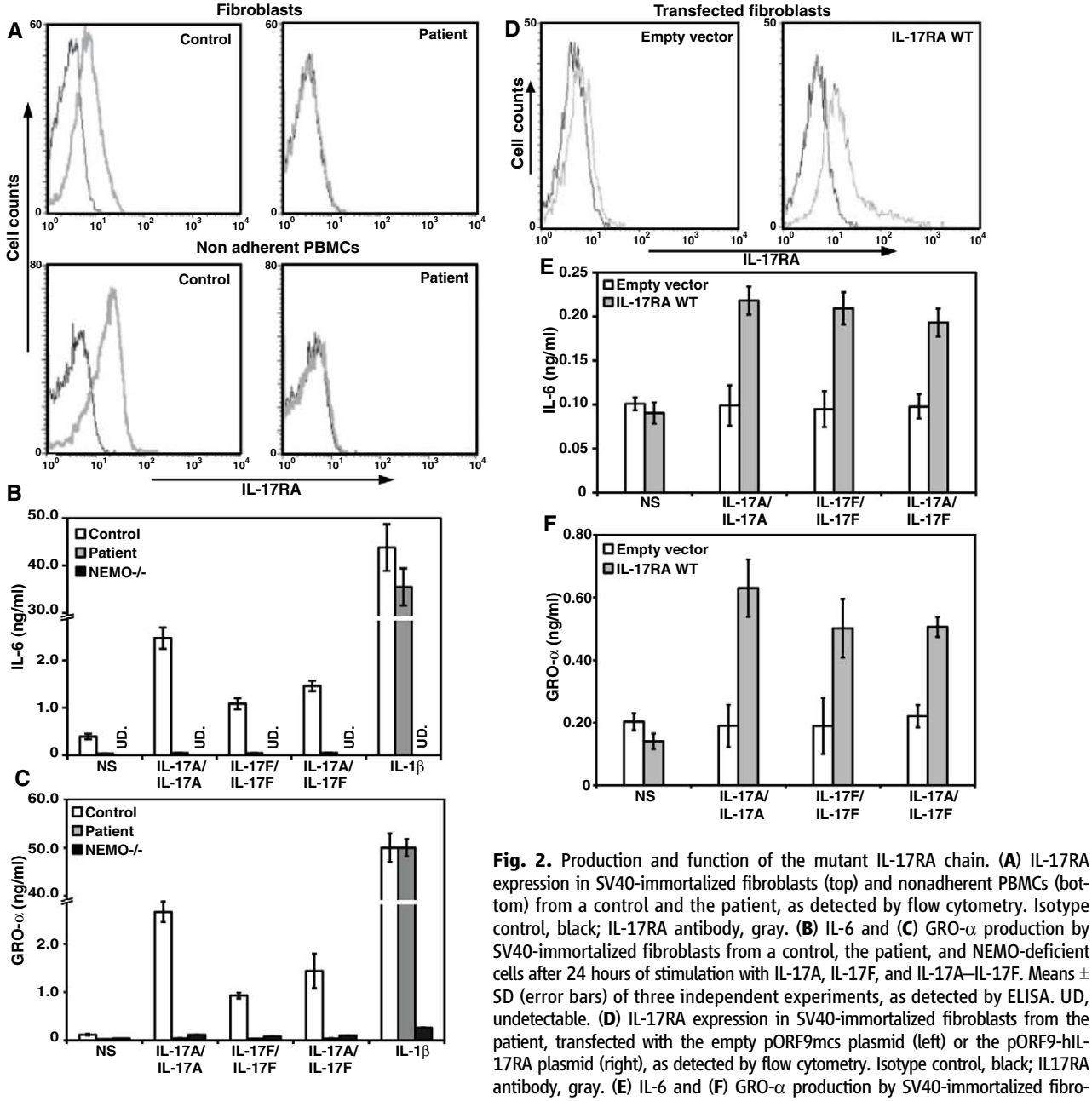

Fig. 2. Production and function of the mutant IL-17RA chain. (**A**) IL-17RA expression in SV40-immortalized fibroblasts (top) and nonadherent PBMCs (bottom) from a control and the patient, as detected by flow cytometry. Isotype control, black; IL-17RA antibody, gray. (**B**) IL-6 and (**C**) GRO-α production by SV40-immortalized fibroblasts from a control, the patient, and NEMO-deficient cells after 24 hours of stimulation with IL-17A, IL-17F, and IL-17A–IL-17F. Means ± SD (error bars) of three independent experiments, as detected by ELISA. UD, undetectable. (**D**) IL-17RA expression in SV40-immortalized fibroblasts from the patient, transfected with the empty pORF9mcs plasmid (left) or the pORF9-hIL-17RA plasmid (right), as detected by flow cytometry. Isotype control, black; IL17RA antibody, gray. (**E**) IL-6 and (**F**) GRO-α production by SV40-immortalized fibroblasts from the patient, transfected with the empty pORF9mcs plasmid (white) or the pORF9-hIL17RA plasmid (gray), after 24 hours of stimulation with IL-17A, IL-17F, and IL-17A–IL-17F. Means ± SD (error bars) of three independent experiments, as detected by ELISA.

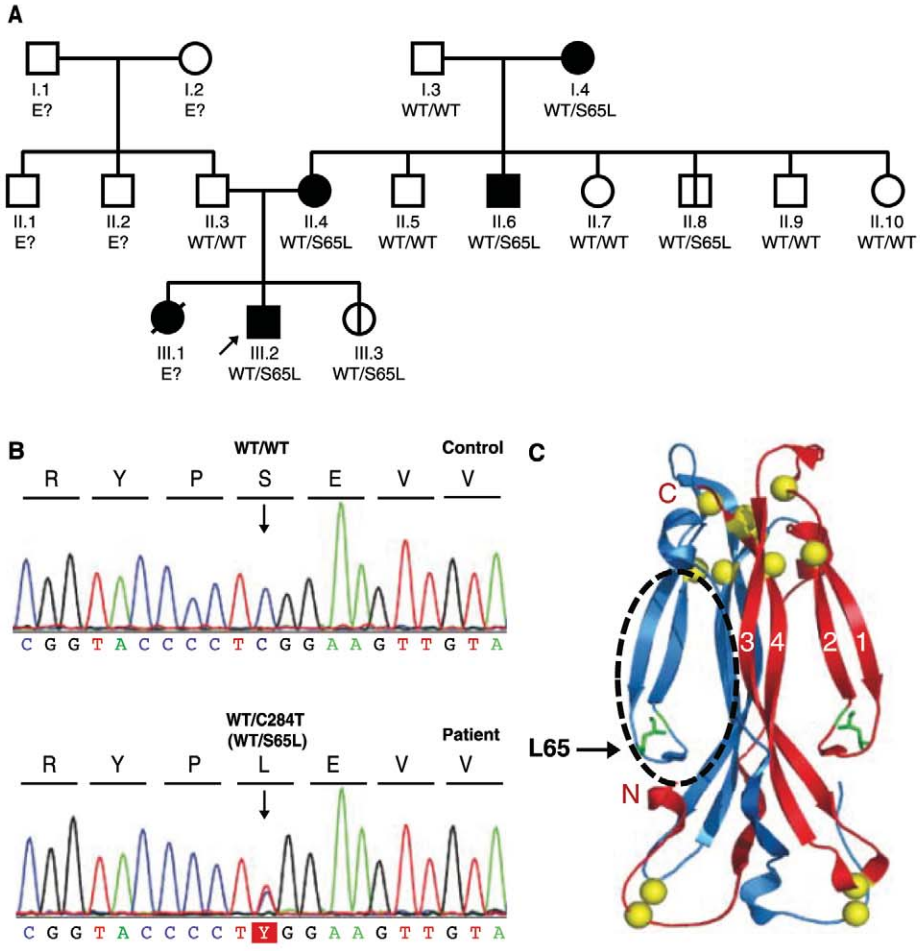

Fig. 3. A kindred with autosomal dominant IL-17F deficiency. (**A**) Family pedigree, with allele segregation. The patients, shown in black, are all heterozygous for the mutation, as is II.8, who is asymptomatic. The proband is indicated by an arrow. E? indicates individuals whose genetic status could not be evaluated. III.3 is a 9-month-old baby, also heterozygous for the mutation and currently asymptomatic. All other family members are healthy and WT for *IL17F* and are shown in white. (**B**) Heterozygous c.284C>T mutation in the patients. *IL17F* DNA sequence electrophoregrams of a control and the patient III.2. (**C**) Ribbon trace of the IL-17F dimer. Beta strands are labeled. Sulfur atoms are shown in yellow. The position of the cavity that binds to the receptor is indicated by a black circle.

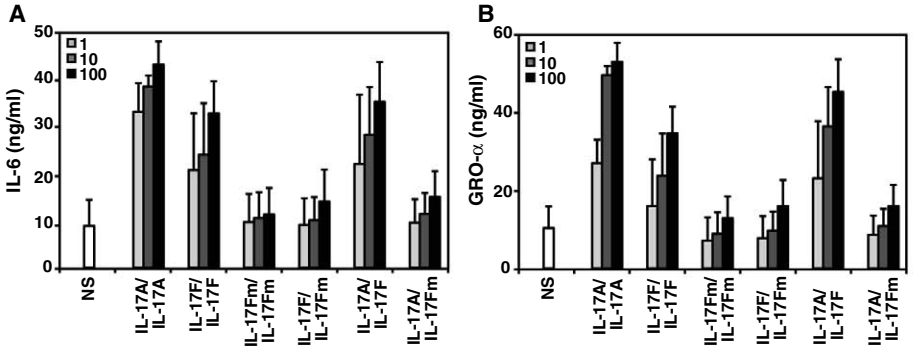

Fig. 4. Function of the mutant IL-17F protein. (**A**) Production of IL-6 and (**B**) GRO-α by control SV40 fibroblasts in response to increasing doses (ng/ml) of IL-17A, IL-17FWT, mutant IL-17F (IL-17FS65L), IL-17FWT–IL-17FS65L homodimers and of IL-17A–IL-17FWT and IL-17A–IL-17FS65L heterodimers for 24 hours. Means ± SD (error bars) of three independent experiments, as detected by ELISA.

cannot exclude the possibility that other infections may occur in patients with inborn errors of IL-17 immunity. In any event, in natura, inborn errors of IL-17 immunity clearly impair mucocutaneous immunity to *C. albicans* (*14*, *31*). Patients receiving IL-17–blocking agents should be carefully monitored, at least for mucocutaneous infections (*32*).

References and Notes

1. A. Puel *et al.*, *Curr. Opin. Immunol.* **22**, 467 (2010).
2. L. de Beaucoudrey *et al.*, *J. Exp. Med.* **205**, 1543 (2008).
3. C. S. Ma *et al.*, *J. Exp. Med.* **205**, 1551 (2008).
4. Y. Minegishi *et al.*, *J. Exp. Med.* **206**, 1291 (2009).
5. J. D. Milner *et al.*, *Nature* **452**, 773 (2008).
6. E. O. Glocker *et al.*, *N. Engl. J. Med.* **361**, 1727 (2009).
7. K. Kisand *et al.*, *J. Exp. Med.* **207**, 299 (2010).
8. A. Puel *et al.*, *J. Exp. Med.* **207**, 291 (2010).
9. D. M. Williamson, *Br. J. Dermatol.* **81**, 125 (1969).
10. D. Leroy, A. Dompmartin, J. P. Houtteville, J. Theron, *Dermatologica* **178**, 43 (1989).
11. R. A. Chilgren, P. G. Quie, H. J. Meuwissen, R. Hong, *Lancet* **290**, 688 (1967).
12. L. Canales, R. O. Middlemas 3rd, J. M. Louro, M. A. South, *Lancet* **294**, 567 (1969).
13. R. S. Wells, J. M. Higgs, A. Macdonald, H. Valdimarsson, P. J. Holt, *J. Med. Genet.* **9**, 302 (1972).
14. J. L. Casanova, L. Abel, *Science* **317**, 617 (2007).
15. Materials and methods are available as supporting material on *Science* Online.
16. K. Wolk, E. Witte, K. Witte, K. Warszawska, R. Sabat, *Semin. Immunopathol.* **32**, 17 (2010).
17. T. Korn, E. Bettelli, M. Oukka, V. K. Kuchroo, *Annu. Rev. Immunol.* **27**, 485 (2009).
18. S. L. Gaffen, *Nat. Rev. Immunol.* **9**, 556 (2009).
19. Single-letter abbreviations for the amino acid residues are as follows: A, Ala; C, Cys; D, Asp; E, Glu; F, Phe; G, Gly; H, His; I, Ile; K, Lys; L, Leu; M, Met; N, Asn; P, Pro; Q, Gln; R, Arg; S, Ser; T, Thr; V, Val; W, Trp; Y, Tyr; and X, stop.
20. J. F. Wright *et al.*, *J. Immunol.* **181**, 2799 (2008).
21. S. G. Hymowitz *et al.*, *EMBO J.* **20**, 5332 (2001).
22. M. Kawaguchi *et al.*, *J. Allergy Clin. Immunol.* **117**, 795 (2006).
23. S. A. Khader, S. L. Gaffen, J. K. Kolls, *Mucosal Immunol.* **2**, 403 (2009).
24. H. R. Conti *et al.*, *J. Exp. Med.* **206**, 299 (2009).
25. A. W. Ho *et al.*, *J. Immunol.* **185**, 1063 (2010).
26. J. S. Cho *et al.*, *J. Clin. Invest.* **120**, 1762 (2010).
27. S. Kagami, H. L. Rizzo, S. E. Kurtz, L. S. Miller, A. Blauvelt, *J. Immunol.* **185**, 5453 (2010).
28. H. Ishigame *et al.*, *Immunity* **30**, 108 (2009).
29. S. Saijo *et al.*, *Immunity* **32**, 681 (2010).
30. L. Henningsson *et al.*, *Infect. Immun.* **78**, 3783 (2010).
31. A. Alcaïs *et al.*, *Ann. N. Y. Acad. Sci.* **1214**, 18 (2010).
32. W. Hueber *et al.*; Psoriasis Study Group; Rheumatoid Arthritis Study Group; Uveitis Study Group, *Sci. Transl. Med.* **2**, 52ra72 (2010).

33. We thank the patients, their families, and their clinicians. We also thank all members of the laboratory for helpful discussions and T. Kochetkov for keratinocyte culture. This work was supported by institutional funding from INSERM, University Paris Descartes, the Rockefeller University, the Rockefeller University CTSA grant number 5UL1RR024143-04, the St. Giles Foundation, and the Candidoser association awarded to J.-L.C. Genomic DNA sequences of the mutations IL-17RA (JF305973) and IL-17F (JF305974) can be found in GenBank. The following reagents are available under a Materials Transfer Agreement: human IL-17A homodimer (– mutation) purified protein, human IL-17F homodimer (+/– mutation) purified protein, human IL-17A–IL-17F heterodimer (+/– mutation) purified protein, and antibody against human IL-17F.

Supporting Online Material

www.sciencemag.org/cgi/content/full/science.1200439/DC1
Materials and Methods
Figs. S1 to S13
Table S1
References

15 November 2010; accepted 7 February 2011
Published online 24 February 2011;
10.1126/science.1200439

PAMELA Measurements of Cosmic-Ray Proton and Helium Spectra

O. Adriani,[1,2] G. C. Barbarino,[3,4] G. A. Bazilevskaya,[5] R. Bellotti,[6,7] M. Boezio,[8] E. A. Bogomolov,[9] L. Bonechi,[1,2] M. Bongi,[2] V. Bonvicini,[8] S. Borisov,[10,11,12] S. Bottai,[2] A. Bruno,[6,7] F. Cafagna,[7] D. Campana,[4] R. Carbone,[4,11] P. Carlson,[13] M. Casolino,[10] G. Castellini,[14] L. Consiglio,[4] M. P. De Pascale,[10,11] C. De Santis,[10,11] N. De Simone,[10,11] V. Di Felice,[10] A. M. Galper,[12] W. Gillard,[13] L. Grishantseva,[12] G. Jerse,[8,15] A. V. Karelin,[12] S. V. Koldashov,[12] S. Y. Krutkov,[9] A. N. Kvashnin,[5] A. Leonov,[12] V. Malakhov,[12] V. Malvezzi,[10] L. Marcelli,[10] A. G. Mayorov,[12] W. Menn,[16] V. V. Mikhailov,[12] E. Mocchiutti,[8] A. Monaco,[6,7] N. Mori,[1,2] N. Nikonov,[9,10,11] G. Osteria,[4] F. Palma,[10,11] P. Papini,[2] M. Pearce,[13] P. Picozza,[10,11]* C. Pizzolotto,[8] M. Ricci,[17] S. B. Ricciarini,[2] L. Rossetto,[13] R. Sarkar,[8] M. Simon,[16] R. Sparvoli,[10,11] P. Spillantini,[1,2] Y. I. Stozhkov,[5] A. Vacchi,[8] E. Vannuccini,[2] G. Vasilyev,[9] S. A. Voronov,[12] Y. T. Yurkin,[12] J. Wu,[13]† G. Zampa,[8] N. Zampa,[8] V. G. Zverev[12]

Protons and helium nuclei are the most abundant components of the cosmic radiation. Precise measurements of their fluxes are needed to understand the acceleration and subsequent propagation of cosmic rays in our Galaxy. We report precision measurements of the proton and helium spectra in the rigidity range 1 gigavolt to 1.2 teravolts performed by the satellite-borne experiment PAMELA (payload for antimatter matter exploration and light-nuclei astrophysics). We find that the spectral shapes of these two species are different and cannot be described well by a single power law. These data challenge the current paradigm of cosmic-ray acceleration in supernova remnants followed by diffusive propagation in the Galaxy. More complex processes of acceleration and propagation of cosmic rays are required to explain the spectral structures observed in our data.

Since the discovery of cosmic rays, various mechanisms have been proposed to explain the acceleration of particles to relativistic energies and their subsequent propagation in our Galaxy. It was pointed out long ago (*1*, *2*) that supernovae fulfill the power requirement to energize Galactic cosmic rays. Subsequently, models were put forward explaining the acceleration of cosmic-ray particles via diffusive shock acceleration produced by supernova shock waves propagating in the interstellar medium [see (*3*) for a review].

At the end of the acceleration phase, particles are injected into the interstellar medium where they propagate, diffusing through the turbulent Galactic magnetic fields. Nowadays, this propagation is well described by solving, numerically (*4*) or analytically (*5*, *6*), the transport equations for particle diffusion in the Galaxy. The Galactic magnetic fields mask the arrival direction of charged particles, making the cosmic-ray flux isotropic, although there are hints of anisotropy in the 10- to 100-TeV range (*7*).

Recent PAMELA (payload for antimatter matter exploration and light-nuclei astrophysics) measurements of the antiparticle component of the cosmic radiation (*8*–*10*) have prompted a reevaluation of possible contributions from additional Galactic sources, either of astrophysical [e.g., pulsars (*11*)] or exotic [e.g., dark matter (*12*, *13*)] origin. Detailed knowledge of cosmic-ray spectra is needed to: (i) identify sources and acceleration/propagation mechanisms of cosmic rays; (ii) estimate the production of secondary particles, such as positrons and antiprotons, to disentangle the secondary-particle component from possible exotic sources; and (iii) estimate the particle flux in the geomagnetic field and in Earth's atmosphere for in-orbit dose estimations and to derive the atmospheric muon and neutrino flux, respectively.

We present absolute cosmic-ray proton and helium spectra in the rigidity interval between 1 GV and 1.2 TV (Fig. 1 and tables S1 and S2), based on data gathered between 2006 and 2008 with PAMELA, a detector orbiting Earth in a 350- to 610-km, 70°-inclination orbit as part of the Russian Resurs-DK1 spacecraft (*14*).

Our results are consistent with those of other experiments (Fig. 1), considering the statistical and systematic uncertainties of the various experiments. There are differences at low energies (< 30 GeV) caused by solar-modulation effects [PAMELA was operating during a period of minimum solar activity with a solar-modulation parameter (Φ) of 450 to 550 MV in the spherical force-field approximation (*15*)]. PAMELA results overlap with Advanced Thin Ionization Calorimeter (ATIC)–2 data (*16*) between ~200 and ~1200 GV, but differ both in shape and absolute normalization at lower energies. The extrapolation to higher energy of the PAMELA fluxes suggests a broad agreement with the results of CREAM (Cosmic Ray Energetics and Mass Experiment) (*17*) and JACEE (Japanese-American Collaborative Emulsion Experiment) (*18*); the extrapolation of PAMELA helium flux is higher than the helium flux measured by RUNJOB (Russia-Nipon Joint Balloon) experiment (*19*).

To gain a better understanding of the spectra, we have analyzed our results in terms of rigidity instead of kinetic energy per nucleon (Fig. 2 and tables S3 and S4). Two important conclusions can be drawn from the PAMELA data.

First, the proton and helium spectra [$J(R)$] have different spectral shapes. If a single power law, $J(R) = AR^{-\gamma^R}$ (where A is the normalization constant, R is rigidity, and γ is the spectral index), is fit to the data between 30 GV (above the influence of solar modulation) and 1.2 TV, the resulting spectral indices are $\gamma^R_{30-1000\ \mathrm{GV,p}} = 2.820 \pm 0.003(stat) \pm 0.005(syst)$ and $\gamma^R_{30-1000\ \mathrm{GV,He}} = 2.732 \pm 0.005(stat)^{+0.008}_{-0.003}(syst)$, which establishes that there is a significant difference between the two spectral indices in this rigidity region (stat, statistical errors; syst, systematic errors; p, proton; He, helium). These effects are also seen in Fig. 3 (and in table S5), where the proton-to-helium flux ratio is shown as a function of rigidity. Presenting the results as a ratio reduces the possible impact of systematic errors, because a number of instrumental effects cancel in the ratio (for example, the estimation of live time and the error associated with the alignment of the tracker and the track-reconstruction algorithm). The proton-to-helium flux ratio shows a continuous and smooth decrease as the rigidity increases. The same ratio cast in terms of kinetic energy per nucleon or total kinetic energy exhibits more irregular behavior (fig. S1). By applying a power-law approximation to the two spectra, the ratio can be used to determine the difference between the two spectral indices with a smaller associated systematic error $\Delta_{\gamma^R} = \gamma^R_{\mathrm{p}} - \gamma^R_{\mathrm{He}} = 0.101 \pm 0.0014\,(stat) \pm 0.0001(sys)$. The ratio is well described by a power law down to rigidities as low as 5 GV (green line in Fig. 3). For rigidities $R >> \Phi$, the ratio of the two species is independent of the solar-modulation parameter and allows Δ_γ for the interstellar spectrum to be measured in the

[1]Department of Physics, University of Florence, I-50019 Sesto Fiorentino, Florence, Italy. [2]Istituto Nazionale di Fisica Nucleare (INFN), Sezione di Florence, I-50019 Sesto Fiorentino, Florence, Italy. [3]Department of Physics, University of Naples "Federico II," I-80126 Naples, Italy. [4]INFN, Sezione di Naples, I-80126 Naples, Italy. [5]Lebedev Physical Institute, RU-119991, Moscow, Russia. [6]Department of Physics, University of Bari, I-70126 Bari, Italy. [7]INFN, Sezione di Bari, I-70126 Bari, Italy. [8]INFN, Sezione di Trieste, I-34149 Trieste, Italy. [9]Ioffe Physical Technical Institute, RU-194021 St. Petersburg, Russia. [10]INFN, Sezione di Rome "Tor Vergata," I-00133 Rome, Italy. [11]Department of Physics, University of Rome "Tor Vergata," I-00133 Rome, Italy. [12]Moscow Engineering and Physics Institute, RU-11540 Moscow, Russia. [13]Department of Physics, Kungliga Tekniska Högskolan, and the Oskar Klein Centre for Cosmoparticle Physics, AlbaNova University Centre, SE-10691 Stockholm, Sweden. [14]Istituto di Fisica Applicata Nello Carrara, I-50019 Sesto Fiorentino, Florence, Italy. [15]Department of Physics, University of Trieste, I-34147 Trieste, Italy. [16]Department of Physics, Universität Siegen, D-57068 Siegen, Germany. [17]INFN, Laboratori Nazionali di Frascati, Via Enrico Fermi 40, I-00044 Frascati, Italy.

*To whom correspondence should be addressed. E-mail: picozza@roma2.infn.it

†On leave from School of Mathematics and Physics, China University of Geosciences, CN-430074 Wuhan, China.

rigidity range of 5 to 30 GV, where solar-modulation effects dominate. Previous measurements (*20*–*24*) did not have the statistical and systematic precision to demonstrate this decrease in the ratio.

Secondly, as seen in Fig. 4, the PAMELA data show clear deviations from a single–power-law model. The spectrum of protons gradually softens in the rigidity range 30 to 230 GV. In the rigidity range 30 to 80 GV, $\gamma^{R}_{30-80\mathrm{GV,p}} = 2.801 \pm 0.007(stat) \pm 0.002(syst)$, which is lower than the value fitted between 80 to 230 GV: $\gamma^{R}_{80-230\mathrm{GV,p}} = 2.850 \pm 0.015(stat) \pm 0.004(syst)$. In the case of helium, $\gamma^{R}_{30-80\mathrm{GV,He}} = 2.71 \pm 0.01(stat) \pm 0.002(syst)$, which is lower than $\gamma^{R}_{80-230\mathrm{GV,He}} =$

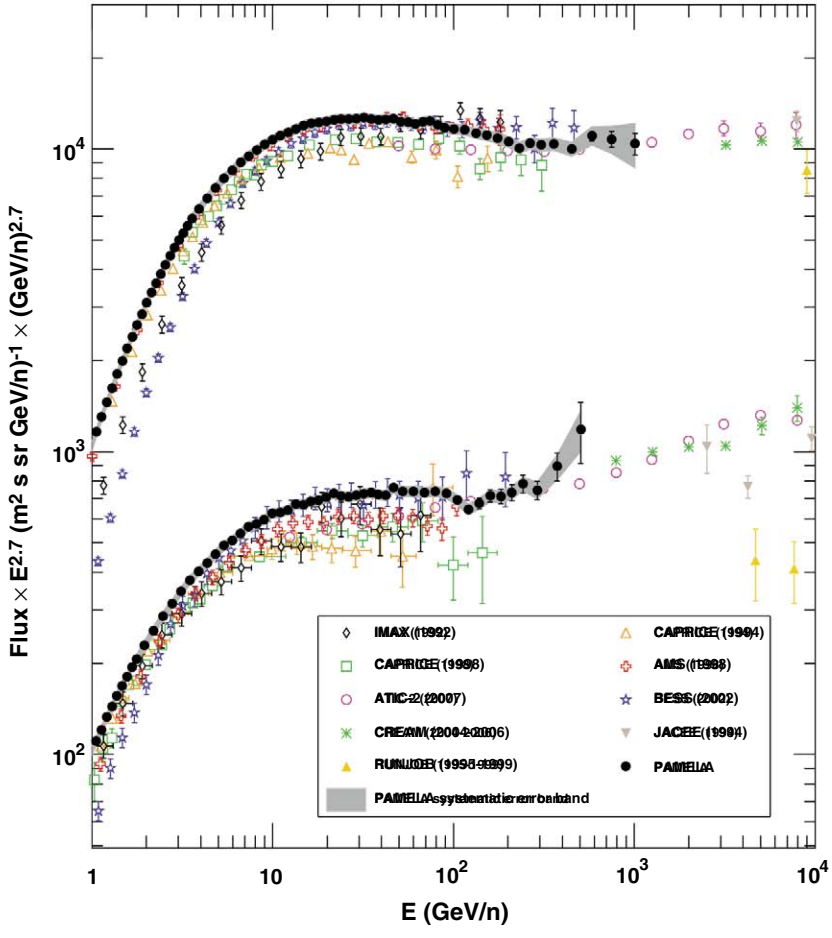

Fig. 1. Proton and helium absolute fluxes measured by PAMELA above 1 GeV per nucleon, compared with a few of the previous measurements (*16*–*24*). All but one of the previous measurements (*24*) come from balloon-borne experiments. Previous data up to few hundred billion electron volts per nucleon were collected by magnetic spectrometer experiments (*20*–*24*), whereas higher-energy data come from calorimetric measurements. PAMELA data cover the energy range 1 GeV to 1.2 TeV (1 to 600 GeV per nucleon for He). The fluxes are expressed in terms of kinetic energy per nucleon, converted from the rigidity measured in the tracker and neglecting any contribution from less abundant deuterium ($d/p \simeq 1\%$) (where d is deuterium) and ^{3}He (^{3}He/^{4}He $\simeq$ 10%). Therefore, pure proton and ^{4}He samples are assumed. Error bars are statistical and indicate 1 SD; the gray shaded areas represent the estimated systematic uncertainty. E, kinetic energy per nucleon.

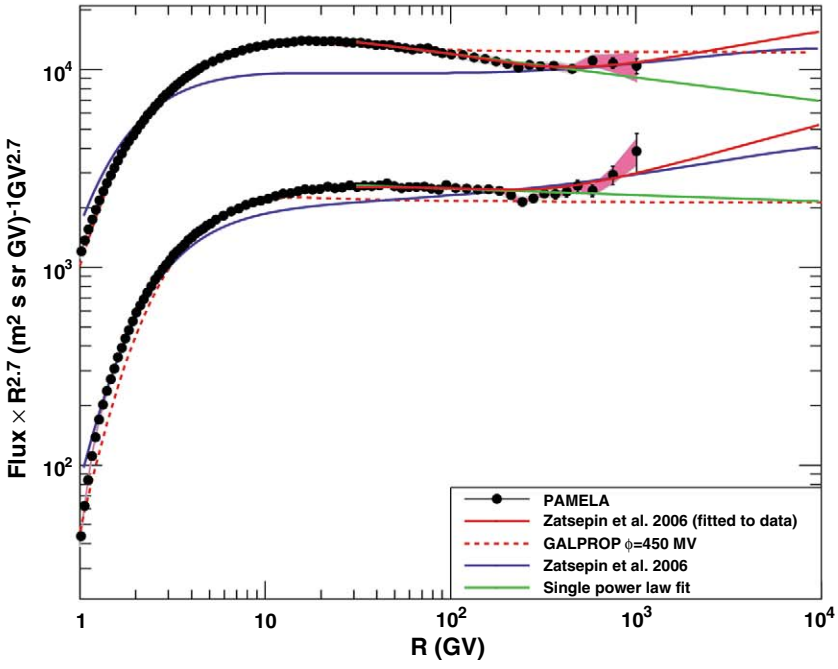

Fig. 2. Proton (top data set) and helium (bottom data set) fluxes measured by PAMELA in the rigidity range 1 GV to 1.2 TV. The pink shaded areas represent the estimated systematic uncertainty. The lines represent the fit with a single power law and the GALPROP (*36*) and Zatsepin (*29*) models. Details of the models are presented in tables S1 and S2.

2.77 ± 0.03(*stat*) ± 0.004(*syst*). We applied Fisher's and Student's *t* tests to the single–power-law hypothesis in the range 30 to 230 GV for both protons and helium [see section 5 of the supporting online material (SOM) for details]. This hypothesis is rejected at the 95% confidence level (CL). Considering the same rigidity interval in terms of kinetic energy per nucleon, the Fisher's and Student's *t* tests reject a single–power-law hypothesis at 99.7% CL.

At 230 to 240 GV, the proton and helium data exhibit an abrupt spectral hardening. Applying Fisher's test and Student's *t* test to the proton spectrum above 80 GV, the single–power-law hypothesis is rejected at 99.7% CL if only statistical errors are considered. A similar result is obtained if the fluxes are increased in line with the systematic uncertainties. If the fluxes are instead decreased, the single–power-law hypothesis is rejected at 95% CL. The hardening of the proton spectrum occurs at 232^{+35}_{-30} GV with change of spectral index from $\gamma^{R}_{80-232\mathrm{GV,p}} = 2.85 \pm 0.015(stat) \pm 0.004(syst)$ to $\gamma^{R}_{>232\mathrm{GV,p}} = 2.67 \pm 0.03 \pm 0.05$. For the helium data, the single–power-law hypothesis is rejected at 95% CL with spectral hardening setting in at 243^{+27}_{-31} GV and a corresponding change of spectral index of $\gamma^{R}_{80-240\mathrm{GV,He}} = 2.766 \pm 0.01 \pm 0.027$ and $\gamma^{R}_{>243\mathrm{GV,He}} = 2.477 \pm 0.06 \pm 0.03$. As a consistency check, we repeated this analysis with the three highest-energy data points excluded; no changes in the proton and helium results were observed. We obtained similar results when we used alternative statistical methods such as the cumulative sum test (see section 5.4 in the SOM).

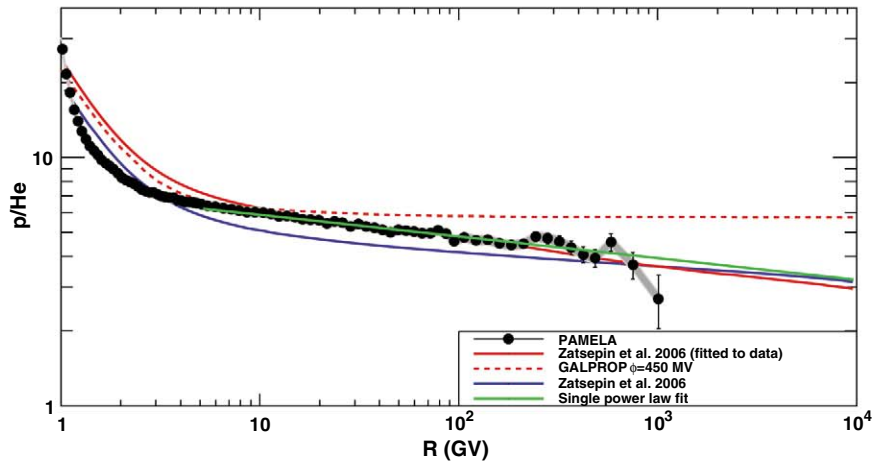

Fig. 3. Ratio of the flux between proton and helium data of PAMELA versus rigidity. The gray shaded area represents the estimated systematic uncertainty. Lines show the fit using a single power law (describing the difference of the two spectral indices) and the GALPROP (*36*) and Zatsepin models with the original values of the paper (*29*) fitted to the data. Details of the models are presented in tables S1 and S2.

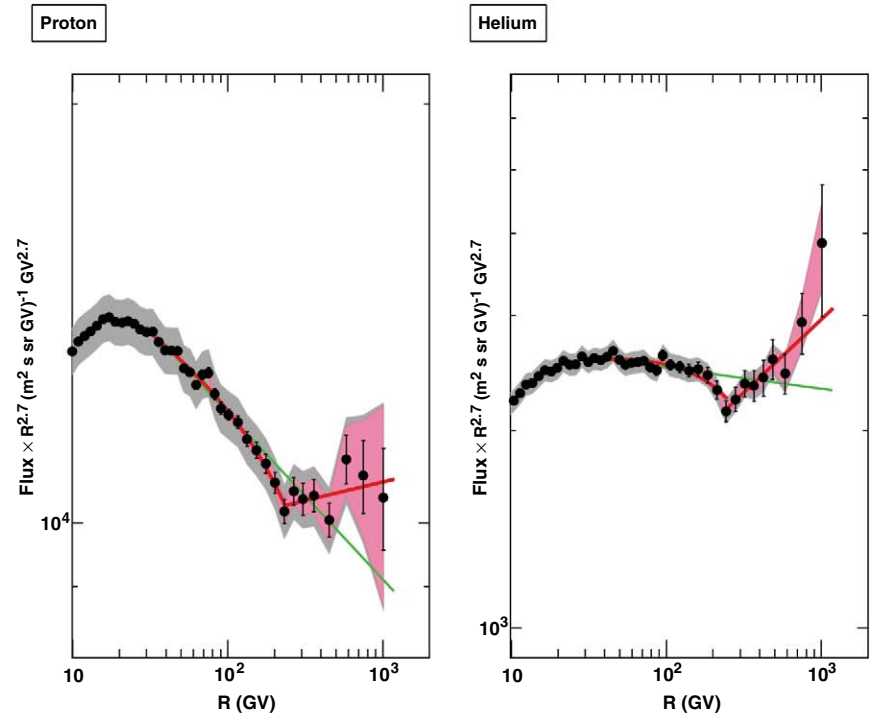

Fig. 4. Proton (**left**) and helium (**right**) spectra in the range 10 GV to 1.2 TV. The gray shaded area represents the estimated systematic uncertainty, and the pink shaded area represents the contribution due to tracker alignment. The green lines represent fits with a single power law in the rigidity range 30 to 240 GV. The red curves represent the fit with a rigidity-dependent power law (30 to 240 GV) and with a single power law above 240 GV.

One of the most notable features of the cosmic rays before PAMELA observations was their apparently featureless energy spectra. Until now, single power laws, as predicted by the shock diffusion acceleration model and diffusive propagation in the Galaxy [see (*25*) for a recent review], could reproduce spectra using similar spectral indices (a fit to the experimental data yields $\gamma \simeq 2.7$) for protons and heavier nuclei up to energies of about $\approx 10^{15}$ eV (the so-called "knee" region). Such assumptions are routinely incorporated into commonly used propagation models such as GALPROP (*4*), which is widely considered to be the standard model of cosmic-ray acceleration and propagation. Our results challenge this scenario (*26*). As can be seen in Figs. 2 and 3, the GALPROP calculation does not reproduce PAMELA data across the full-rigidity region. Moreover, it is difficult, even with recent models of nonlinear shock acceleration (*27*, *28*), to produce significant differences in the proton and helium spectra as low as a few tens of gigavolts.

The hardening in the spectra observed by PAMELA around 200 GV could be interpreted as an indication of different populations of cosmic-ray sources. As an example of a multisource model, Fig. 2 shows a comparison with a calculation by Zatsepin and Sokolskaya (*29*) (blue curves), which was put forward to explain ATIC-2 data (*16*) and considered novae stars and explosions in superbubbles as additional cosmic-ray sources. The parameters of the model were fitted to match ATIC-2 data and, consequently, are in disagreement with PAMELA data in absolute fluxes and the ratio. If the parameters of this model are fitted to the PAMELA data, the agreement can be greatly improved (red curves in Figs. 2 and 3). CREAM also reported a direct measurement, albeit with a low statistical and systematic significance, of a change of the slope for nuclei ($Z \geq 3$) at 200 GeV per nucleon; that is, at a higher rigidity ($\simeq$ 400 GV) than our observed break in the helium spectrum.

An indication that proton and helium have different spectral indices at high energy (~10 TeV) was reported by JACEE (*18*). More recently, CREAM (*17*)—also using AMS (alpha magnetic spectrometer) (*24*) and BESS (balloon-borne experiments with a superconducting spectrometer) (*30*) data—indirectly inferred that spectral defor-

mation should occur at ~200 GeV per nucleon for both species. This is similar to our results for protons but higher (400 GV) than our results for helium. Results from ATIC-2 (*16*) implied that protons and helium nuclei have different energy spectra, although the results suffered from unclear systematic uncertainties, and there were differences with respect to previously reported ATIC-1 (*31*) data.

References and Notes

1. P. O. Lagage, C. J. Cesarsky, *Astron. Astrophys.* **118**, 223 (1983).
2. V. L. Ginzburg, S. I. Syrovatskii, *The Origin of Cosmic Rays* (Macmillan, New York, 1964).
3. M. A. Malkov, L. O.'C. Drury, *Rep. Prog. Phys.* **64**, 429 (2001).
4. A. W. Strong, I. V. Moskalenko, *Astrophys. J.* **509**, 212 (1998).
5. F. C. Jones, A. Lukasiak, V. Ptuskin, W. Webber, *Astrophys. J.* **547**, 264 (2001).
6. F. Donato *et al.*, *Astrophys. J.* **563**, 172 (2001).
7. M. Amenomori *et al.*, *Science* **314**, 439 (2006).
8. O. Adriani *et al.*, *Nature* **458**, 607 (2009).
9. O. Adriani *et al.*, *Phys. Rev. Lett.* **102**, 051101 (2009).
10. O. Adriani *et al.*, *Phys. Rev. Lett.* **105**, 121101 (2010).
11. C. Grimani, *Class. Quantum Gravity* **26**, 235009 (2009).
12. N. Arkani-Hamed, D. P. Finkbeiner, T. R. Slatyer, N. Weiner, *Phys. Rev. D* **79**, 015014 (2009).
13. G. Kane, R. Lu, S. Watson, *Phys. Lett. B* **681**, 151 (2009).
14. PAMELA comprises a number of high-performance detectors, capable of identifying particles through the determination of charge (Z), rigidity ($R = pc/|Z|e$, where p is the momentum of a particle of charge Ze, c is the speed of light, and e is the electron charge), and velocity ($\beta = v/c$, where v is the velocity) over a wide energy range. The device is built around a permanent magnet with a six-plane double-sided silicon microstrip tracker, providing absolute charge information and track-deflection ($\eta = \pm 1/R$, with the sign depending on the sign of the charge derived from the curvature direction) information. A scintillator system, composed of three double layers of scintillators (S1, S2, S3 in fig. S2) provides the trigger, a time-of-flight measurement, and an additional estimation of absolute charge. A silicon-tungsten tracking calorimeter, a bottom scintillator (S4), and a neutron detector are used to perform lepton-hadron discrimination. An anticoincidence system is used off-line to reject spurious event triggers generated by particles interacting in the apparatus. Respect to balloon-borne experiments, PAMELA has the advantage of a substantially longer period of uninterrupted observing time. Furthermore, taking data in space is not affected by environmental systematics such as those due to correction for secondary particles produced in the residual atmosphere that affects balloon-borne experiments. A more detailed description of PAMELA and the analysis methodology can be found in (*32*, *33*) and in the SOM.
15. L. J. Gleeson, W. I. Axford, *Astrophys. J.* **154**, 1011 (1968).
16. J. P. Wefel *et al.*, in *Proceedings of the 30th International Cosmic Ray Conference*, R. Caballero *et al.*, Eds. (Universidad Nacional Autónoma de México, Mexico City, 2008), vol. 2, pp. 31–34.
17. H. S. Ahn *et al.*, *Astrophys. J. Lett.* **714**, L89 (2010).
18. K. Asakimori *et al.*, *Astrophys. J.* **502**, 278 (1998).
19. M. Hareyama, RUNJOB collaboration, *J. Phys. Conf. Ser.* **31**, 159 (2006).
20. W. Menn *et al.*, *Astrophys. J.* **533**, 281 (2000).
21. M. Boezio *et al.*, *Astrophys. J.* **518**, 457 (1999).
22. M. Boezio *et al.*, *Astropart. Phys.* **19**, 583 (2003).
23. S. Haino *et al.*, *Phys. Lett. B* **594**, 35 (2004).
24. AMS Collaboration, *Phys. Lett. B* **490**, 27 (2000).
25. A. W. Strong, I. V. Moskalenko, V. S. Ptuskin, *Annu. Rev. Nucl. Part. Sci.* **57**, 285 (2007).
26. The changing spectral characteristics of the proton spectrum between 30 and 230 GV may be partly due to heliospheric effects. Although solar-modulation effects are considered negligible above 30 GV in the spherical force-field approximation (*15*), more detailed models, which use the full Parker equation to describe the propagation of cosmic rays in a two- or three-dimensional heliosphere (*34*, *35*), may be needed to fully understand the impact of this effect.
27. D. Caprioli, P. Blasi, E. Amato, *Astroparticle Phys.*; preprint available at http://arxiv.org/abs/1007.1925.v2 (2010).
28. D. C. Ellison, D. J. Patnaude, P. Slane, P. Blasi, S. Gabici, *Astrophys. J.* **661**, 879 (2007).
29. V. I. Zatsepin, N. V. Sokolskaya, *Astron. Astrophys.* **458**, 1 (2006).
30. T. Sanuki *et al.*, *Adv. Space Res.* **27**, 761 (2001).
31. H. S. Ahn *et al.*, *Adv. Space Res.* **37**, 1950 (2006).
32. P. Picozza *et al.*, *Astropart. Phys.* **27**, 296 (2007).
33. M. Casolino *et al.*, *Adv. Space Res.* **42**, 455 (2008).
34. J. R. Jokipii, E. H. Levy, W. B. Hubbard, *Astrophys. J.* **213**, 861 (1977).
35. M. S. Potgieter, *J. Atmos. Sol. Terr. Phys.* **70**, 207 (2008).
36. A. E. Vladimirov *et al.*, preprint available at http://arxiv.org/abs/1008.3642v1 (2010).

37. We thank P. Blasi, F. Donato, P. Lipari, and I. Moskalenko for helpful discussions concerning the interpretation of our results and D. Marinucci for helpful discussions on statistical methods. We acknowledge support from the Italian Space Agency, Deutsches Zentrum für Luft- und Raumfahrt, the Swedish National Space Board, the Swedish Research Council, the Russian Space Agency (Roscosmos), and the Russian Foundation for Basic Research.

Supporting Online Material

www.sciencemag.org/cgi/content/full/science.1199172/DC1
SOM Text
Figs. S1 to S6
Tables S1 to S7
References

18 October 2010; accepted 9 February 2011
Published online 3 March 2011;
10.1126/science.1199172

Spontaneous Ferroelectric Order in a Bent-Core Smectic Liquid Crystal of Fluid Orthorhombic Layers

R. Amaranatha Reddy,[1] Chenhui Zhu,[2] Renfan Shao,[2] Eva Korblova,[1] Tao Gong,[1] Yongqiang Shen,[2] Edgardo Garcia,[1,3] Matthew A. Glaser,[2] Joseph E. Maclennan,[2] David M. Walba,[1] Noel A. Clark[2]*

Macroscopic polarization density, characteristic of ferroelectric phases, is stabilized by dipolar intermolecular interactions. These are weakened as materials become more fluid and of higher symmetry, limiting ferroelectricity to crystals and to smectic liquid crystal stackings of fluid layers. We report the $SmAP_F$, the smectic of fluid polar orthorhombic layers that order into a three-dimensional ferroelectric state, the highest-symmetry layered ferroelectric possible and the highest-symmetry ferroelectric material found to date. Its bent-core molecular design employs a single flexible tail that stabilizes layers with untilted molecules and in-plane polar ordering, evident in monolayer-thick freely suspended films. Electro-optic response reveals the three-dimensional orthorhombic ferroelectric structure, stabilized by silane molecular terminations that promote parallel alignment of the molecular dipoles in adjacent layers.

The first theoretical description of the orientational ordering of liquid crystals was by Born, who in 1916 formulated an electric analog of the Curie-Weiss mean-field model of ferromagnetism [see, for example, (*1*)] to describe a fluid with spontaneous macroscopic ordering of its molecular electric dipoles (*2*). Such a liquid crystal would be the highest symmetry ferroelectric phase, with only a fluid macroscopic polarization and its required uniaxial optical anisotropy as broken symmetries. This phase, in which the polarization would be fluid (energetically free to adopt any orientation), has not yet been realized because known molecular architectures do not have interactions that are strong enough to stabilize polar order in the translationally symmetric milieu of a three-dimensional (3D) liquid. The more recent discoveries of spontaneous polar ordering (*3*) and macroscopic chirality (*4*) in fluid smectic liquid crystals (LCs) of achiral bent-core molecules, phases of stacked 2D fluid layers, has opened a new path for making materials with polar fluid degrees of freedom, exploiting the much stronger intermolecular interaction afforded by their polar steric molecular shape, the exploration of which has generated a rich new class of soft materials (*5*, *6*).

The bent-core fluid lamellar LCs can be grouped according to whether the constituent 2D layers have an optical dielectric tensor principal axis (OPA) along the layer normal (SmA, orthogonal) or not (SmC, monoclinic). The orthogonal achiral

[1]Department of Chemistry and Biochemistry, Liquid Crystal Materials Research Center, University of Colorado, Boulder, CO 80309–0215, USA. [2]Department of Physics, Liquid Crystal Materials Research Center, University of Colorado, Boulder, CO 80309–0390, USA. [3]Laboratório de Química Computacional, Instituto de Química, Universidade de Brasilia, Brasilia DF 70910-900, Brasil.

*To whom correspondence should be addressed. E-mail: noel.clark@colorado.edu

smectic phases of interest here consist of layers of one of the symmetries sketched in Fig. 1A: (i) uniaxial ($C_{\infty h}$), the SmA phase (*7*), some examples of which have high susceptibility for field-induced in-plane polar order (*8*); (ii) uniaxial polar $C_{\infty v}$, the polar smectic A phase, not yet found in bent-core materials; (iii) nonpolar orthorhombic (D_{2h}), the biaxial SmAb phase (*9*–*11*); and (iv) polar orthorhombic (C_{2v}), the SmAP phases, with fluid in-plane layer polarization and macroscopic antiferroelectric ordering of adjacent layers ($SmAP_A$) (*12*–*17*). Here, we report a fluid smectic ferroelectric phase with orthorhombic symmetry, the highest symmetry polar fluid possible in a layered system, leaving only the fully 3D liquid uniaxial or biaxial polar nematics among higher symmetry polar fluid phases to be realized.

The approach to the design of W586 (Fig. 1B) is to start with the bow-shaped structural theme exemplified by the mesogen cores shown in Fig. 2, B and E, known to form spontaneously polar fluid smectic layers, typically with a tilted principal axis as in the SmCP of Fig. 2A and antiferroelectric 3D interlayer order [compound **1** (*4*)]. Molecules that favor untilted layers and ferroelectric interlayer order are then obtained respectively by (*18*) (i) reducing the tendency for tilt by employing molecules with only a single alkyl tail to provide more space for the tails and thus lower their in-plane entropic pressure (Fig. 2D) (*12*) and (ii) reducing the tendency for antiferroelectric layer ordering by terminating the tail with a carbosilane group to suppress the interpenetration of tails in adjacent layers (ellipse, Fig. 2C) (*19*).

X-ray, optical, and calorimetric studies of W586 provide compelling evidence for the target $SmAP_F$ phase. W586 melts upon heating at T = 110°C and exhibits the following phase sequence on cooling: isotropic (I) – 155°C – SmA – 136°C – $SmAP_F$ – 80°C – crystal (X). In both the SmA and $SmAP_F$ phases, synchrotron x-ray diffraction exhibited a resolution-limited, first-order reflection in the small-angle region due to the smectic layering (Fig. 1) and diffuse scattering with a peak at a spacing of $D \sim 4.6$ Å, indicating liquid-like in-plane order (*18*). The layer spacing $L \sim 61$ Å is much larger than the calculated extended (all trans) molecular length $L_m \sim 52$ Å (*18*), implying a structure in which each layer is nonpolar along the layer normal ***z***, with the cores strongly overlapping but having half the molecules in each layer with tails along $+z$ and half with tails along $-z$, in both the SmA and $SmAP_F$ phases (Fig. 1B, inset, and fig. S7) (*18*).

The optical textures of samples of W586 were studied using four distinct preparation methods: (i) freely suspended films (Fig. 3, F and G, and fig. S2) (*18*); and, with the LC in few-micron-thick gaps between glass plates: (ii) homeotropic cells, made using clean glass plates, yielding homeotropic alignment, i.e., smectic layers parallel to the plates (Fig. 3, A and E); (iii) random-planar cells, made using nylon films on clean glass or indium/tin oxide (ITO) coated glass plates, yielding random planar focal-conic textures with the smectic layers locally normal to the plates (Fig. 3B); and (iv) aligned planar cells, made using rubbed Teflon films on glass or ITO, yielding planar alignment of oriented smectic layers normal to both the rubbing direction and the plates (Fig. 3, C and D).

The phase identified as SmA gives excellent extinction between crossed polarizer and analyzer in the homeotropic geometry (Fig. 3A, left), evidence for an optical uniaxis normal to the layers and plates. In contrast, upon cooling to the phase identified as $SmAP_F$, a distinct Schlieren texture of in-layer birefringence appeared (Fig. 3A, right, and 3E), characterized by smooth brush patterns indicative of slowly varying optical anisotropy and thus revealing in-layer orientational ordering of the molecular bow planes. Point defects in the texture exhibited four-brush patterns when viewed between crossed polarizer and analyzer, indicating a 2π reorientation of a principal optic axis about each defect core, and thus polar ordering (Fig. 3E). Additionally, a quasiperiodic pattern of stripes can appear (Fig. 3A, right), each of which marks the termination of a single smectic layer accommodating the spatial variation of the gap between the glass plates. The appearance of these stripes is analogous to that found due to single-layer edge dislocations in homeotropic samples of rodlike molecules as one passes through the SmA to SmC transition (*20*). Conoscopy of the homeotropic W586 samples confirmed uniaxial order in the SmA phase and locally biaxial ordering with an optic axis normal to the layers and increasing in-plane birefringence Δn with decreasing temperature T in the $SmAP_F$ phase.

The random-planar samples exhibited focal conic textures, which showed a strong increase of effective birefringence when an electric field of either sign was applied normal to the plates but no accompanying optic axis rotation about the applied field direction (Fig. 3B), as is observed with tilted chiral ferroelectric LCs. This and the

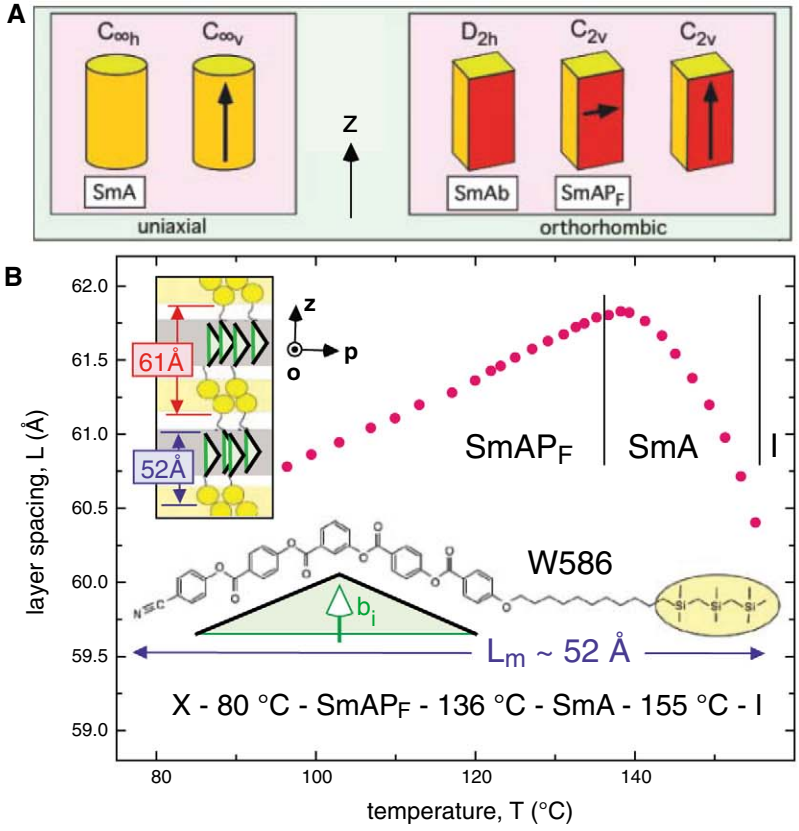

Fig. 1. (**A**) Symmetries of achiral smectic layers (layer normal, ***z***), where the solid figure represents the optical dielectric tensor of the layer and the arrow its polarization. We report the $SmAP_F$ bent-core phase, having macroscopic, in-plane ferroelectric ordering of orthorhombic layers with in-plane polarity (C_{2v}). (**B**) Molecular structure, phase diagram, and layer spacing versus T of W586. The layer spacing obtained from high-resolution synchrotron x-ray diffraction ($\delta q \sim 0.0004$ Å^{-1}) is about 61Å (*18*), much larger than the calculated extended molecular length, L_m = 52 Å (fig. S7), implying a structure in which each layer is nonpolar along ***z***, with the cores overlapping but with half the molecules in each layer with tails along $+z$ and half with tails along $-z$, in both SmA and $SmAP_F$ phases (inset). The $L(T)$ of W586 exhibits the typical SmA layer expansion with decreasing T as the tails elongate, but in the $SmAP_F$ the layers contract. The silane termination of W586 suppresses out-of-layer fluctuations to promote ferroelectric coupling of adjacent layers.

observed homeotropic Schlieren texture indicates that one OPA is along the layer normal z and that the other two, p and o, are in the layer plane. In this frame, the optical dielectric tensor ε is diagonal, with respective principal optical dielectric constants $\varepsilon_z = n_z^2$, $\varepsilon_p = n_p^2$, and $\varepsilon_o = n_o^2$, where we choose the p axis to have the higher in-plane index ($n_p > n_o$). This orientation of the OPAs, together with the sign of birefringence in the planar geometry that indicates that ε_z is the largest diagonal term of ε, provides direct evidence that this polar smectic phase has the mean molecular long axis normal to the layers, indicating either the $SmAP_F$, the monolayer phase of on-average untilted molecules, or possibly a phase of tilted molecules having a multilayer unit cell, such as the bilayer SmC_AP_F structure shown in Fig. 2F. Remarkably, a well-aligned planar texture with z parallel to the glass plates and along the rubbing direction was obtained for both the smectic A phases in rubbed Teflon cells, as shown in Fig. 3C, a rare case in which a smectic phase of banana molecules has been successfully aligned by rubbing.

Freely suspended films (FSFs), drawn in air with an integer number of smectic layers, N, and imaged with depolarized reflected light microscopy (DRLM) (*21*) with oblique laser illumination, have been used to probe coupled in-layer-plane molecular orientation and electric polarization fields in smectic liquid crystal phases of rodlike (*22*) and bent-core molecules (*4*). Here, we apply the DRLM-film technique to W586 to probe the ground-state structure of the observed smectic phase. Films of uniform thickness with N in the range $1 < N < 10$, as well as films with layer steps, were prepared for study by drawing them over a 5-mm-diameter hole in a glass cover slip. Film thickness was determined by laser reflectivity (*21*).

DRLM observations of W586 films with oblique incidence (angle of incidence ≈ 7°) reveal textures of brush patterns and topological defects similar to those found in SmC films (*21*) (Fig. 3, F and G). Uncrossing the analyzer enables determination of the local high-index, in-plane orientation, distinguishing p from o and enabling the local azimuthal orientation, $\psi(x,y)$, of $p(x,y)$ to be mapped, as indicated in Fig. 3F. The topological defects (vortices) revealed by the four-brush patterns seen with decrossed polarizer and analyzer in Fig. 3F show that, as with the homeotropic cells, the films only have defects with $+2\pi$ or -2π reorientation of p. The absence of $+\pi$ or $-\pi$ defects is a distinctive signature that locally this in-plane structure is polar, with macroscopic polar order within each layer. The $+2\pi$ (+1, blue) and -2π (–1, red) defects are distinct in that while the in-plane polarization $P(x,y)$ rotates smoothly in a bend deformation around the core of the $+2\pi$ defect, it is broken into four domains, each of nearly uniform orientation, about the -2π defect (Fig. 3F). This fracturing of the polarization field, to date observed in polar films in which the magnitude of P is at least several hundred nC/cm^2, is a consequence of the space charge and associated electrostatic energy accompanying splay distortion of P required around the –1 defect (*23*) (Fig. 3F). Uncrossing the analyzer shows that $P(x,y)$ is parallel to $p(x,y)$, the optical fast axis, i.e., $P(x,y) = Pp(x,y)$, where P is the polarization magnitude. Another consequence of the large energy cost of splay of P is the thready nature of the fluctuations of the film textures, a characteristic of the suppression of splay fluctuations by space charge, leaving predominately bend fluctuations (green circle, Fig. 3G).

Application of an in-plane electric field $E \sim 10$ V/mm provided additional evidence of macroscopic polarization, with the films exhibiting a π rotation of p on field reversal and field stabilization of 2π walls terminating on the topological defects, as is typical of ferroelectric films (*21*), and direct confirmation that P is parallel to p. Observations of both the defect structure and field response were carried out as a function of N. Antiferroelectric FSFs always exhibit distinctive odd-even polarization effects in such experiments, as the net P normal to the tilt plane cancels for even-N antiferroelectric films (*22*, *24*). In W586 films, no discernible odd-even effects of P were found. The fracturing mentioned above about –1 defects was found for all film thicknesses, indicating large P for all thicknesses and confirming that the intralayer ordering of P is ferroelectric in the SmAP phase of W586, i.e., that it is P_F.

The optical and x-ray observations showing the bulk phase to have macroscopic polarity and an OPA along the layer normal indicate that the molecular long axis is on average untilted, i.e., oriented along the layer normal, a constraint consistent with either a bulk $SmAP_F$ where the molecules in every layer are untilted (orthorhombic layers, Fig. 2G), or with the SmC_AP_F where the layers have alternating molecular tilts (monoclinic layers, Fig. 2F) (*25*). DRLM of freely suspended films at oblique incidence (*22*) is an effective way

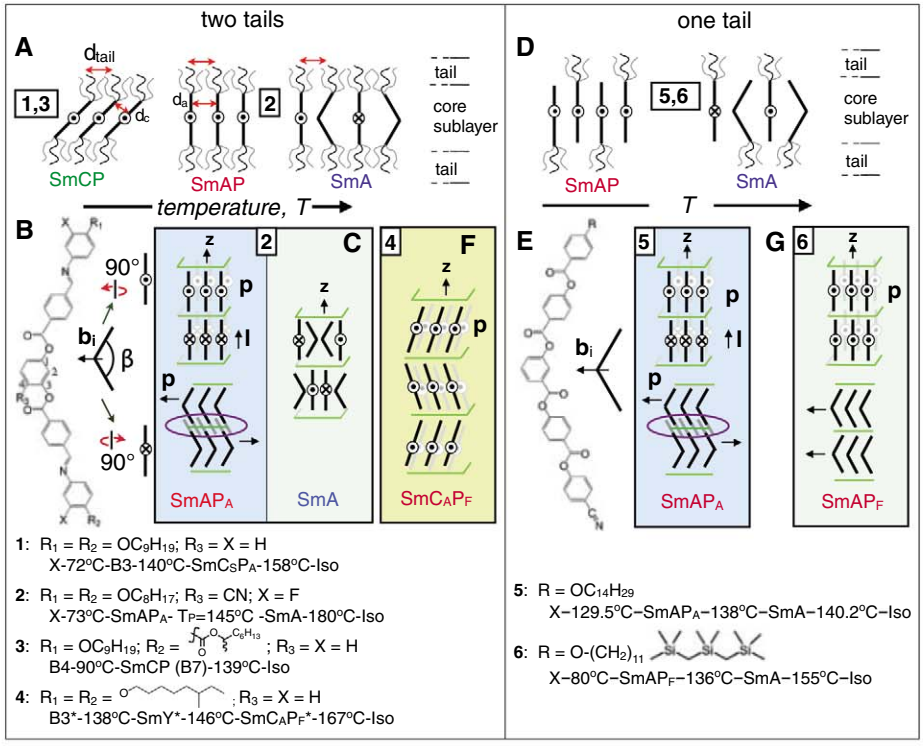

Fig. 2. (**A**) Sketches of the layer structure of the SmA and SmAP phases, found in compound **2** (*13*), and the SmCP phases, found in compounds **1** (*4*) and **3** (*29*). (**B**) Core structures, showing the opening angle β, which is larger in **2** due to the CN substitution at R3. (**C**) Supermolecular structure of the SmA and $SmAP_A$ phase observed in **2**, showing the average molecular long axis layer, l, parallel to the layer normal z, and the average molecular polar axis p, normal to z. The $SmAP_A$ is stabilized by the synclinic ordering and interpenetration of the molecular tails at the layer interfaces, indicated by the gray lines in the ellipse. The SmA phase appears in **2** at higher T. (**D**) Reducing the number of tails from two to one per molecule creates more space for the tails, promoting orthogonal phases. The layer spacing larger than the molecular length can be understood on the basis of the structure in fig. S7 (*18*). Steric interaction between the cores is enhanced at low T, giving the SmAP phases. (**E**) Bent-core structure of **5** (*12*) and **6** (W586). (**F**) In bulk optical experiments, the $SmAP_F$ is indistinguishable from the SmC_AP_F exemplified by compound **4** (*25*), both having an optic axis along the layer normal. However the $SmAP_F$ can be identified in freely suspended films by the absence of odd/even effects versus layer number, N. (**G**) Out-of-layer fluctuations (ellipse) enable penetration of tails into the adjacent layers favoring synclinic tail tilt at the layer interfaces and thus macroscopic antiferroelectric ($SmAP_A$) order. Introducing carbosilane into the tail suppresses out-of-layer fluctuations, favoring anticlinic tail orientation and thus the $SmAP_F$ structure.

of probing the tilt of the OPA with respect to the layer normal. Our observations, for example, the equal intensity of the four brushes in the DRLM images of $N = 1$ films (Fig. 3G), show no evidence for a tilted OPA in W586 films, eliminating the the SmC_AP_F as a possible structure (*18*).

In films, the SmA to SmAP phase transition was observed at 150°C, slightly elevated relative to the bulk, as often found in smectic films. Both the response to applied electric field and the in-plane birefringence decrease substantially with increasing temperature in the $SmAP_F$ phase but do not disappear completely even in the SmA phase. Fine-texture birefringence patterns persist into the SmA phase and only gradually disappear with increasing temperature, suggestive of remnant biaxial ordering on the surfaces of internally uniaxial films.

The electrical and optical responses of W586 to an applied electric field, $\boldsymbol{E}$, and surface interactions in planar-aligned ITO-on-glass cells were used to probe the azimuthal orientation and ordering of the molecules about the layer normal, z, at different temperatures. Application of a triangle wave voltage $v(t)$ across the cell plates induces peaks in the optical transmission between crossed polarizers and a polarization current (inset, Fig. 4B) in the $SmAP_F$ phase, indicating a Goldstone-like response of macroscopic ferroelectric ordering, which we have analyzed in detail. The field couples to $\boldsymbol{P}$, tending to minimize the electrostatic potential energy density $-\boldsymbol{P}\cdot\boldsymbol{E} = -PE\cos\psi$, by varying the azimuthal orientation ψ of $\boldsymbol{P}$, where we take $\psi = 0$ when $\boldsymbol{P}$ is parallel to $\boldsymbol{E}$ (Fig. 4A) . In molecular terms, $\boldsymbol{P} = P\boldsymbol{p} = P_m\langle\boldsymbol{p}\cdot\boldsymbol{b}_i\rangle\boldsymbol{p} = \boldsymbol{p}P_m\langle\cos\phi_i\rangle$, where ϕ_i gives the azimuthal orientation of the bow plane $\boldsymbol{b}_i$ of molecule i relative to the mean orientation $\boldsymbol{p}$ (Fig. 1B), P_m is the molecular polarization density, and $\langle\cos\phi_i\rangle$ is the polarization orientation order parameter, the first moment of fluctuations of orientations of individual molecular bow planes $\boldsymbol{b}_i$ about the mean orientation $\boldsymbol{p}(\psi)$. Similarly, the in-plane dielectric anisotropy is $\Delta\varepsilon = \varepsilon_p - \varepsilon_o = \Delta\varepsilon_{max}Q$, where the in-plane quadrupolar order parameter, $Q = (\langle\cos^2\phi_i\rangle - \langle\sin^2\phi_i\rangle)$, is the second moment of fluctuations of $\boldsymbol{b}_i$ about $\boldsymbol{p}$. Because $\varepsilon = n^2$ and Δn is small, the in-plane refractive index anisotropy is $\Delta n = \Delta\varepsilon/2\,\bar{n} = (\varepsilon_p - \varepsilon_o)/2\,\bar{n}$, where the mean in-plane refractive index is given by $\bar{n} = \sqrt{(n_p^2 + n_o^2)/2} \approx (n_p + n_o)/2$. Both P and Q will depend on temperature T.

We consider planar alignment so that z is parallel to the glass, giving an index $n_z = \varepsilon_z^{1/2}$ for light polarized along z and incident normally on the cell. The effective in-plane index, $n_{eff}(\psi)$, for light polarized normal to z is given by $1/n_{eff}(\psi)^2 = \sin^2\psi/{n_p}^2 + \cos^2\psi/{n_o}^2$, and the planar cell transmission, for crossed polarizer and analyzer at 45° to z, by $T(\psi) = \sin^2[\pi\delta n(\psi)d/\lambda]$, determined by the resulting effective birefringence $\delta n(\psi) \equiv n_z - n_{eff}(\psi)$, cell thickness d, and wavelength λ. The peaks in the $T(\psi)$ data were used to extract the dependence of ψ on applied voltage, $\psi(v)$, under the assumption that $n_p - n_o$ is independent of ψ

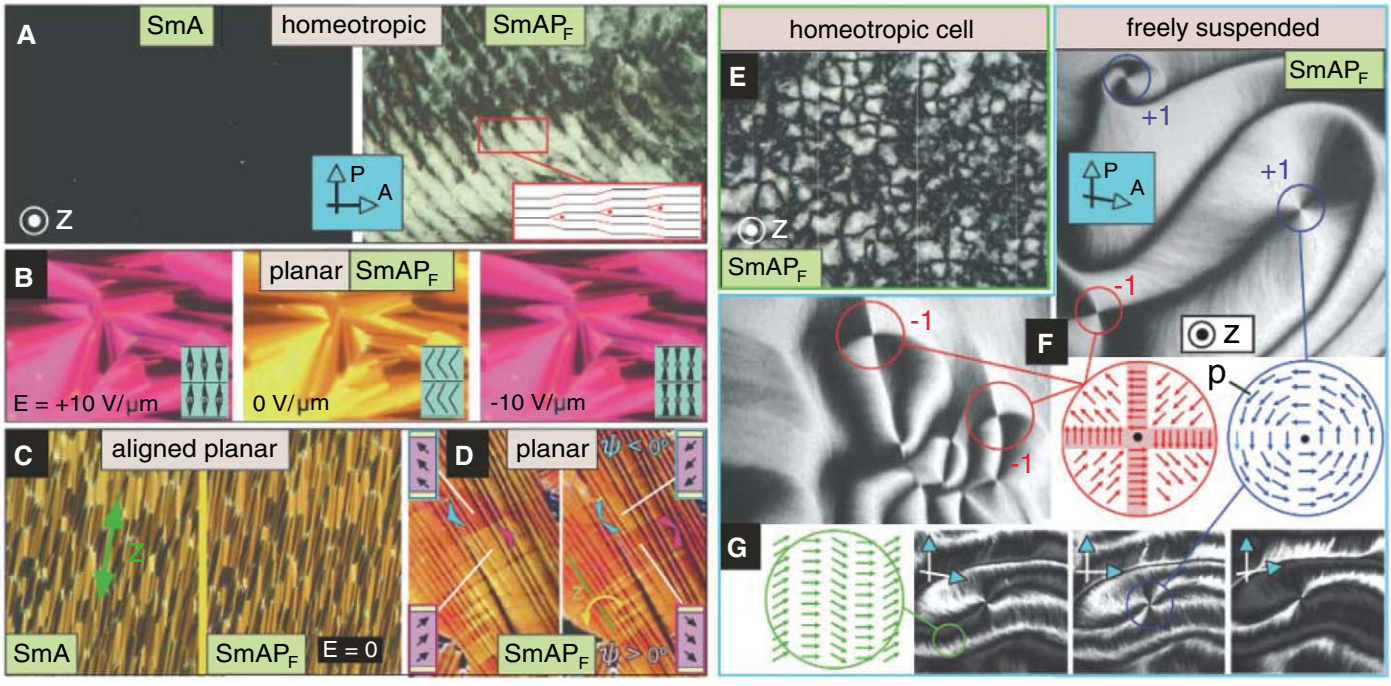

Fig. 3. Transmitted light optical textures in white light of W586 between treated glass plates viewed between crossed polarizer and analyzer, oriented as indicated for all images. (**A**) Clean glass preparation with layers parallel to the plates and LC layer ~1μm thick. Extinction indicates the uniaxial symmetry of the SmA phase, and the optical biaxiality of the $SmAP_F$ phase generates a Schlieren texture, periodically influenced by single smectic layer edge dislocations. (**B**) Nylon films on glass give random-planar focal conics with the layers normal to the plates in a 5.0-μm-thick cell. At zero field, the bow-plane director is nearly parallel to the glass plates, exhibiting smaller apparent birefringence $n_z - n_p$, whereas at $E = \pm 10$ V/μm the bow-plane director is nearly perpendicular to the glass plates, exhibiting larger apparent birefringence $n_z - n_o$. Brushes aligned along analyzer/polarizer with or without field indicates the SmA-like structures in both cases. (**C**) Teflon-rubbed films on glass give uniform planar alignment with the layer normal $\boldsymbol{z}$ along the rubbing direction (arrow) in both SmA and $SmAP_F$ phases in a 3.6-μm-thick cell. (**D**) Tilting the cell about $\boldsymbol{z}$ enables visualization of domains of opposite sign of ψ, shown schematically in cross sections of the cell in the insets (glass plates shown in yellow). (**E**) Clean glass preparation with the LC sample ~1 μm thick and layers parallel to the plates. Defects exhibit four-brush patterns between crossed analyzer and polarizer, indicating a 2π reorientation of an optic axis about each defect core, and thus polar ordering in the $SmAP_F$ phase. (**F**) Freely suspended films with layers parallel to the image plane. DRLM images in the $SmAP_F$ phase with oblique incidence and slightly uncrossed polarizers reveal a texture of brush patterns, confirming the biaxiality of the $SmAP_F$ phase. The absence of $+\pi$ or $-\pi$ defects indicates that the in-plane order is locally polar. The -2π defect is broken into four domains of nearly uniform in-plane polarization about the defect core, a consequence of the space charge and associated electrostatic energy accompanying splay distortion of $\boldsymbol{P}$. The $+2\pi$ defect avoids splay of $\boldsymbol{P}$ by adopting the indicated bend-only orientation. This suppression of splay of P also produces the thready texture of largely bend fluctuations in (F) and (G) (green circle). (**G**) Single-layer ($N = 1$) freely suspended film exhibiting equal intensity bright brushes emanating from a $+2\pi$ defect viewed with crossed polarizer and analyzer, indicating an OPA normal to the film.

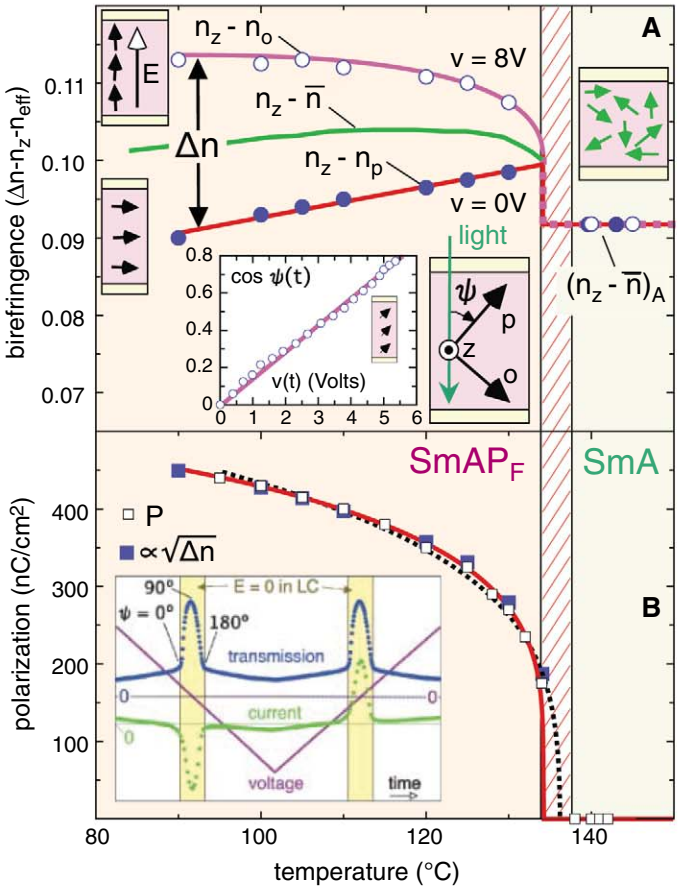

Fig. 4. (**A**) Birefringence of planar-aligned cells measured using a Berek compensator with normally incident white light. On cooling the $SmAP_F$ phase, the birefringence with field on, $n_z - n_o$, increases and the birefringence without field, $n_z - n_p$, decreases, indicating a reduced fluctuation in ψ, where ψ is the azimuthal orientation of the ***p-l*** plane. The insets show schematically the polarization orientation in the cell (glass plates shown in yellow). The plot shows cosψ versus the cell voltage $v(t)$ in the $SmAP_F$ phase. The linear dependence of $v(t)$ on cosψ suggests a typical "V-shaped" reorientation of ***P*** (*26*, *27*), a consequence of the total screening of the applied voltage in the LC by the component of ***P*** normal to the cell plates. (**B**) The current associated with field-induced polarization reorientation in the $SmAP_F$ phase (inset) exhibits a peak due to the analog reorientation of ***P***, which was integrated to give the macroscopic polarization P. The MMF model gives the red and magenta curves for Δn in (A) and the red curve for P in (B) (*18*), and the dashed black curve is the LdG prediction (*18*). Comparison of the dependence of $\Delta n(T)$ (blue squares) and $P(T)$ (white squares) shows that $P \propto \sqrt{\Delta n} \propto \sqrt{Q}$ is rather well satisfied, a relationship shown by the models to indicate that P drives Q (*18*).

and that ψ is uniform through the cell thickness. This analysis shows that $v(t) \propto \cos\psi(t)$ (inset of Fig. 4A), just the result first obtained in the "V-shaped" reorientation of **P** in high-polarization chiral SmC materials, shown to be a consequence of the total screening of the applied voltage in the LC by the component of ***P*** normal to the cell plates (*26*) and recently demonstrated in a SmC_AP_F bent-core phase (*27*). In this model, $\varepsilon vt = 2dP\cos\psi[v(t)]$, where ε and d are respectively the dielectric constant and the thickness of the insulating alignment layers on the electrode plates. The ~12 V width of the $0° < \psi < 180°$ peaks is consistent with estimates of ε and d and the measured P (*26*). These observations provide a self-consistent confirmation of the "block polarization" mode of field-induced reorientation of ψ (reorientation with ψ spatially uniform) and enables the measurement of $n_z - n_o$ (at $\psi = 0°$) and $n_z - n_p$ (at $\psi = 90°$), shown in Fig. 4A. The magnitude $P(T)$ is determined by integrating the polarization current peak in Fig. 4B. Behavior in the vicinity of the SmA to $SmAP_F$ transition (red crosshatched area, Fig. 4) is difficult to assess because the field required to measure P itself induces a substantial polarization (fig. S5) (*18*). Differential scanning calorimetry of the SmA to $SmAP_F$ transition shows a weak anomaly, indicating a second-order or weakly first-order transition (fig. S9).

The mean in-plane refractive index is shown as $n_z - \bar{n}$ (green line) in Fig. 4A. These data indicate a difference in $n_z - \bar{n}$ and in $n_p - n_o = \Delta n(T) \propto Q(T)$ across the cross-hatched SmA–$SmAP_F$ transition region, interestingly with no corresponding detectable discontinuity in $L(T)$ there, even with high x-ray diffraction resolution ($\delta d = 0.02$ Å, Fig. 1B), although $L(T)$ does go through a maximum in the vicinity. Comparison of the T-dependence of $\Delta n(T)$ and $P(T)$ shows that the relationship $P(T) \propto \sqrt{\Delta n}$ and thus $P(T) \propto \sqrt{Q}$ is rather well satisfied (Fig. 4B, blue and white squares, and fig. S3).

Several theoretical approaches were pursued to understand these data and to guide exploration of other novel phase behavior (*18*), for example, the SmAb and polarization splay modulated phases: (i) Variational molecular mean-field (MMF) XY Model. The $P(T)$ and $Q(T)$ data were fit to a generalized 3D XY lattice model with a nearest-neighbor interaction potential $U(\phi_{ij})$ expressed as an expansion in circular harmonics in $\phi_{ij} = \phi_j - \phi_i$ (*18*). Keeping only the first- and third-harmonic amplitudes in $U(\phi_{ij})$ is enough to describe $P(T)$ and $Q(T)$ versus T very well, the resulting $U(\phi_{ij})$ exhibiting a sharp minimum at $\phi_{ij} = 0$ and a maximum at $\phi_{ij} = \pi$. These features respectively give the correct saturation behavior of $P(T)$ and yield the observed $Q(T) \propto P(T)^2$. (ii) SmA/SmAB/$SmAP_F$ phase diagram. Using a mean-field Hamiltonian, Radzihovsky, Weichman, and Park have calculated the phase behavior of Bose-Einstein condensates (BECs) across a Feshbach resonance, showing that they can exhibit distinct normal fluid (NF), atomic superfluid (ASF), and molecular superfluid (MSF) phases (*28*). We argue that this Hamiltonian is the same as that for our smectic system and use the NF/ASF/MSF phase diagram to map that of the SmA/SmAb/$SmAP_F$ phases, respectively (*18*). (iii) Landau-deGennes (LdG) Model. The BEC Hamiltonian reduces to a LdG expansion in the scalar order parameters P and Q (*18*). Application of this expansion to the $SmAP_F$ phase describes the $SmAP_F$ well, giving the dotted black curve in Fig. 4B for $P(T)$ as well as the required $Q(T) \propto P(T)^2$.

The MMF and LdG models agree well except in the transition regime, where the LdG gives a second-order transition and the MMF a first-order transition. As mentioned above, we cannot distinguish these cases experimentally because, in the cells studied, the measurement of P requires an applied field large enough to induce significant polarization near the transition (fig. S6).

References and Notes

1. N. W. Ashcroft, N. D. Mermin, *Solid State Physics* (Holt, Rinehart Winston, New York, 1978).
2. M. Born, *Sitzungsber. Konigl. Preuss. Akad. Wiss.* **1916** (Jan.–July), 614 (1916).
3. T. Niori, T. Sekine, J. Watanabe, T. Furukawa, H. Takezoe, *J. Mater. Chem.* **6**, 1231 (1996).
4. D. R. Link *et al.*, *Science* **278**, 1924 (1997).
5. H. Takezoe, Y. Takanishi, *Jpn. J. Appl. Phys.* **45**, (2A), 597 (2006).
6. R. A. Reddy, C. Tschierske, *J. Mater. Chem.* **16**, 907 (2006).
7. I. Wirth *et al.*, *J. Mater. Chem.* **11**, 1642 (2001).
8. Y. Shimbo *et al.*, *Phys. Rev. Lett.* **97**, 113901 (2006).
9. H. R. Brand, P. E. Cladis, H. Pleiner, *Int. J. Eng. Sci.* **38**, 1099 (2000).
10. T. Hegmann, J. Kain, S. Diele, G. Pelzl, C. Tschierske, *Angew. Chem. Int. Ed.* **40**, 887 (2001).
11. R. Pratibha, N. V. Madhusudana, B. K. Sadashiva, *Science* **288**, 2184 (2000).
12. B. K. Sadashiva, R. A. Reddy, R. Pratibha, N. V. Madhusudana, *J. Mater. Chem.* **12**, 943 (2002).
13. A. Eremin *et al.*, *Phys. Rev. E Stat. Nonlin. Soft Matter Phys.* **64**, 051707 (2001).
14. R. A. Reddy, B. K. Sadashiva, *J. Mater. Chem.* **14**, 310 (2004).
15. S. T. Wang *et al.*, *Phys. Rev. E Stat. Nonlin. Soft Matter Phys.* **70**, 061705 (2004).
16. B. Glettner, S. Hein, R. A. Reddy, U. Baumeister, C. Tschierske, *Chem. Commun. (Camb.)* **25**, 2596 (2007).
17. C. Keith, M. Prehm, Y. P. Panarin, J. K. Vij, C. Tschierske, *Chem. Commun. (Camb.)* **46**, 3702 (2010).
18. Materials and methods are available as supporting material on *Science* Online.
19. W. K. Robinson, C. Carboni, P. Kloess, S. P. Perkins, H. J. Coles, *Liq. Cryst.* **25**, 301 (1998).
20. R. B. Meyer, B. Stebler, S. T. Lagerwall, *Phys. Rev. Lett.* **41**, 1393 (1978).
21. R. Pindak, C. Y. Young, R. B. Meyer, N. A. Clark, *Phys. Rev. Lett.* **45**, 1193 (1980).
22. D. R. Link, J. E. Maclennan, N. A. Clark, *Phys. Rev. Lett.* **77**, 2237 (1996).

23. D. R. Link, N. Chattham, J. E. Maclennan, N. A. Clark, *Phys. Rev. E Stat. Nonlin. Soft Matter Phys.* **71**, 021704 (2005).
24. P. M. Johnson, S. Pankratz, P. Mach, H. T. Nguyen, C. C. Huang, *Phys. Rev. Lett.* **83**, 4073 (1999).
25. M. Nakata *et al.*, *Liq. Cryst.* **28**, 1301 (2001).
26. N. A. Clark, D. Coleman, J. E. Maclennan, *Liq. Cryst.* **27**, 985 (2000).
27. M. J. O'Callaghan, M. D. Wand, C. M. Walker, M. Nakata, *Appl. Phys. Lett.* **85**, 6344 (2004).
28. L. Radzihovsky, P. B. Weichman, J. I. Park, *Ann. Phys.* **323**, 2376 (2008).
29. D. M. Walba *et al.*, *Science* **288**, 2181 (2000).

30. This work was supported by NSF Materials Research Science and Engineering Center grant DMR 0820579, NSF grant DMR 0606528, NSF grant DMR 0603223, and NASA grant NAG-NNC04GA50G. Use of the National Synchrotron Light Source was supported by the U.S. Department of Energy, Divisions of Materials and Chemical Sciences.

Supporting Online Material
www.sciencemag.org/cgi/content/full/332/6025/72/DC1
Materials and Methods
SOM Text
Figs. S1 to S9
References

2 September 2010; accepted 15 February 2011
10.1126/science.1197248

Heavily Doped Semiconductor Nanocrystal Quantum Dots

David Mocatta,[1,2] Guy Cohen,[3] Jonathan Schattner,[2,4] Oded Millo,[2,4]* Eran Rabani,[3]* Uri Banin[1,2]*

Doping of semiconductors by impurity atoms enabled their widespread technological application in microelectronics and optoelectronics. However, doping has proven elusive for strongly confined colloidal semiconductor nanocrystals because of the synthetic challenge of how to introduce single impurities, as well as a lack of fundamental understanding of this heavily doped limit under strong quantum confinement. We developed a method to dope semiconductor nanocrystals with metal impurities, enabling control of the band gap and Fermi energy. A combination of optical measurements, scanning tunneling spectroscopy, and theory revealed the emergence of a confined impurity band and band-tailing. Our method yields n- and p-doped semiconductor nanocrystals, which have potential applications in solar cells, thin-film transistors, and optoelectronic devices.

Doping of bulk semiconductors, the process of intentional insertion of impurity atoms into a crystal, was introduced in the 1940s and is the basis for the widespread application of semiconductors in electronic and electro-optic components (*1*). Controlling the size and dimensionality of semiconductor structures is an additional way to tune their properties via quantum confinement effects. In this respect, colloidal semiconductor nanocrystals (NCs) have emerged as a family of materials with size-dependent optical and electronic properties. Combined with their capability for wet-chemical processing, this has led to NC-based light-emitting diodes (*2*), solar cells, (*3*) and transistor devices (*4*) prepared via facile and scalable bottom-up approaches. Impurity doping in such colloidal NCs still remains a challenge (*5*). From the synthesis side, the introduction of a few impurity atoms into a NC that contains only a few hundred atoms may lead to their expulsion to the surface (*6*–*8*) or compromise the crystal structure. This will inherently create a heavily doped NC under strong quantum confinement. The electronic and optical properties in such circumstances are still unresolved.

Several strategies for NC doping have been used. Remote doping, through the use of binding ligands on the nanoparticle surface (which can donate carriers) or electrochemical carrier injection, has been shown to yield n-type doping in semiconductor NC superlattices (*4*, *9*–*11*). Substitutional doping has been studied mainly for color center impurities (*12*) and magnetic impurities, notably Mn atoms (*13*, *14*), thereby providing insight into the challenging chemistry (*15*). The introduction of dopant precursors at specific stages of nanoparticle growth has been effective in controlling the impurity location (*16*). More recently, some progress has been made toward producing n-type CdSe quantum dots (QDs) through the use of tin and indium impurities (*17*, *18*), and Cu impurities have been used to produce p-type InP NCs (*19*).

Here, we describe a simple room-temperature method for doping semiconductor NCs with metal impurities. By changing the dopant type and concentration, we achieved exquisite control of the electronic properties, including the band gap and Fermi energy. We conducted experimental and theoretical studies of the role of strong quantum confinement leading to localization of the impurity wave functions as well as disorder effects

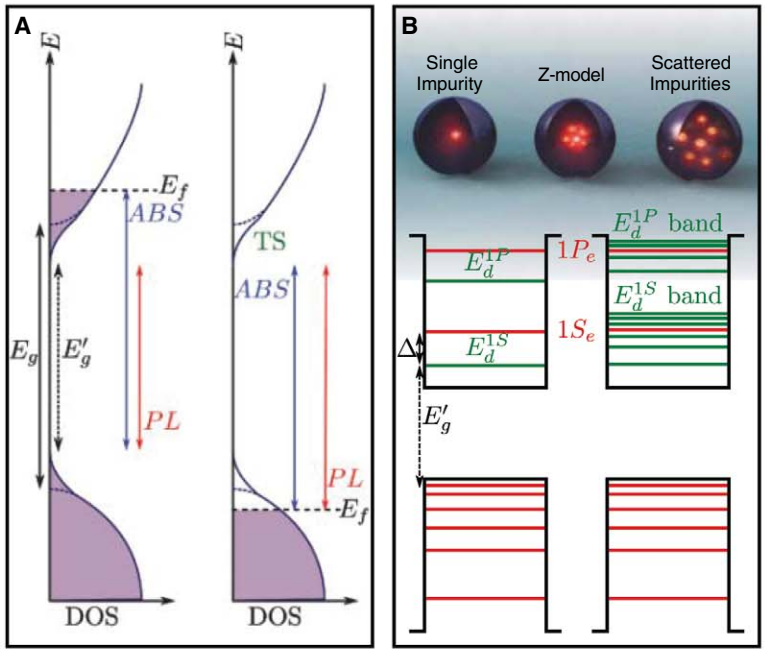

Fig. 1. Diagrams describing the effects of heavy doping in bulk and nanocrystal semiconductors. (**A**) Scheme of the different influences of doping a bulk semiconductor for n-type (left) and p-type (right) dopants. ABS, absorption onset; PL, photoluminescence onset; TS, tail states; E_f, Fermi energy; E'_g, modified band gap; E_g, unperturbed band gap. The purple shading shows state filling up to the Fermi energy. (**B**) Sketch for n-doped nanocrystal QD with confined energy levels. Red and green lines correspond to the QD and impurity levels, respectively. Left panel: The level diagram for a single impurity effective mass model, where E'_g is the quasi-particle gap in the doped QD, $1S_e$ and $1P_e$ are the QD electron levels, and E_d^{1S} and E_d^{1P} are the impurity levels shifted below the corresponding QD levels by a shift Δ. Right panel: Impurity levels develop into impurity bands as the number of impurities increases. Upper panel: Sketch of the different impurity models.

[1]Institute of Chemistry, Hebrew University, Jerusalem 91904, Israel. [2]Center for Nanoscience and Nanotechnology, Hebrew University, Jerusalem 91904, Israel. [3]School of Chemistry, Sackler Faculty of Exact Sciences, Tel Aviv University, Tel Aviv 69978, Israel. [4]Racah Institute of Physics, Hebrew University, Jerusalem 91904, Israel.

*To whom correspondence should be addressed. E-mail: uri.banin@huji.ac.il (U.B.); rabani@tau.ac.il (E.R.); milode@vms.huji.ac.il (O.M.)

leading to band-tailing in small NCs. The method yields n- and p-doped semiconductor NCs that greatly enhance the usefulness of such materials in solar cells, thin-film transistors, and optoelectronic devices.

Adding even a single impurity atom to a semiconductor NC with a diameter of 4 nm, which contains about 1000 atoms, leads to a nominal doping level of 7×10^{19} cm^{-3}. In a bulk semiconductor this is already well within the heavily doped limit, where metallic ("degenerate") behavior is expected (*20*). Heavy doping in bulk semiconductors leads to several effects summarized in Fig. 1A. The impurities interact with each other and an impurity subband emerges near the edge of the respective band (conduction or valence for n- or p-type, respectively). Indeed, this is the criterion that defines the heavily doped regime. Often, tail states (Urbach tails) also develop as a result of distortions in the crystal structure (*21*). In effect, the band gap E_g is narrowed. This may be probed by optical means, where for heavily doped n-type semiconductors (Fig. 1A, left frame) the absorption is blue-shifted as a result of conduction band-filling by the donated electrons (Moss-Burstein effect) (*20*), and the emission emanating from the bottom of the conduction band is red-shifted. For heavy p-type doping, both absorption and emission are typically seen to be red-shifted. This is due to the high density of states (DOS) near the valence band edge, leading to a small Moss-Burstein effect that is often overcome by the red shift due to band-tailing (*20*).

A markedly different situation arises for impurity doping of NCs because of the discrete nature of the quantum-confined states (shown for n-type doping in Fig. 1B). In this case the addition of a single dopant (left frame) introduces impurity levels that significantly alter the DOS—a situation that is not expected for prior remote surface doping strategies. This has been described by a hydrogenic model under spherical confinement, leading to *S*- and *P*-like impurity states denoted by E_d^{1S} and E_d^{2P} that are several tens of meVs below the corresponding dot levels, effectively doubling the DOS near those energies (*22*–*24*). Even more intriguing is the case introduced here, of multiple impurities in a single dot, which are inherently interacting because of the small volume and experience the effect of the confining potential (Fig. 1B, right frame). In this heavily doped regime, the nature of delocalization and interaction of the impurity charge carriers may be greatly modified relative to the bulk case. In addition, multiple impurities in a small confined NC can enhance disorder effects, altering the electronic structure via a quantum-confined Urbach tail mechanism.

To dope InAs NCs with different impurity atoms, we modified a reaction used for gold growth onto semiconductor nanoparticles, which demonstrated the ability to introduce Au into InAs NCs by diffusion (*25*). In a typical metal atom–doping synthesis, the metal salt ($CuCl_2$, $AgNO_3$, AgCl, or $AuCl_3$) is dissolved in a toluene solution with appropriate surfactant and gradually added to a solution of preformed InAs NCs in toluene at room temperature (*26*). The use of preformed NCs allows changes to the properties of the NCs to be assigned wholly to the introduction of the impurity atoms. In general, previous doping methods are based on impurity introduction during NC synthesis, and hence assigning changes to the NC properties are complicated by the inability to differentiate between the influence of the impurity on the NC and the influence of the impurity precursor on the synthesis. This well-controlled approach allows us to follow the intricate changes in the NC properties upon introduction of dopants.

Figure 2A shows a transmission electron microscope (TEM) image of Ag-doped NCs. At the impurity levels reported below, it was not possible to identify the presence of metal regions, indicating that the impurity atoms are dispersed (fig. S8). This was not the case for very high metal atom concentrations (>3000 atoms per NC in the reaction solution), where TEM analysis clearly showed phase separation between InAs and impurity metal regions (*25*). Further support for the dispersion of impurities is provided by x-ray diffraction (fig. S10), where no fingerprints of metal domains were detected while the InAs crystal structure was generally maintained. Some broadening of the peaks is seen, ascribed to a small degree of structural disorder. X-ray photoelectron spectroscopy (XPS) measurements of these samples were also performed, indicating the presence of Ag, Au, and Cu in the respective samples (figs. S11 and S12). This suggests successful addition of these atoms to the InAs NCs, consistent with our previous report of Au growth on InAs NCs, which exhibited the room-temperature solid-state diffusion of Au into the NC (*25*). Indeed, extrapolating the diffusion parameter values to room temperature gives a diffusion length scale of ~10^4 nm per 24 hours, far greater than the NC diameter; large values are also extrapolated for Ag and Cu (table S1).

Figure 2B shows the absorption and emission (inset) spectra of undoped and doped InAs NCs. The addition of Ag atoms results in a red shift of both the first exciton absorption and the emission peaks. The addition of Cu results in a blue shift of the first exciton absorption peak, whereas the emission is not shifted. Addition of Au at similar concentrations does not considerably alter the observed optical gap either in absorption or in emission. The addition of any of these impurity atoms results in the gradual quenching of the emission from the NCs, yet the three impurities lead to qualitatively different effects on the optical spectra and hence on the electronic properties of the doped NCs. The effect of varying amounts of impurities on the first absorption peak and on the emission is shown in Fig. 2, C to E, for InAs NCs with different diameters (see figs.

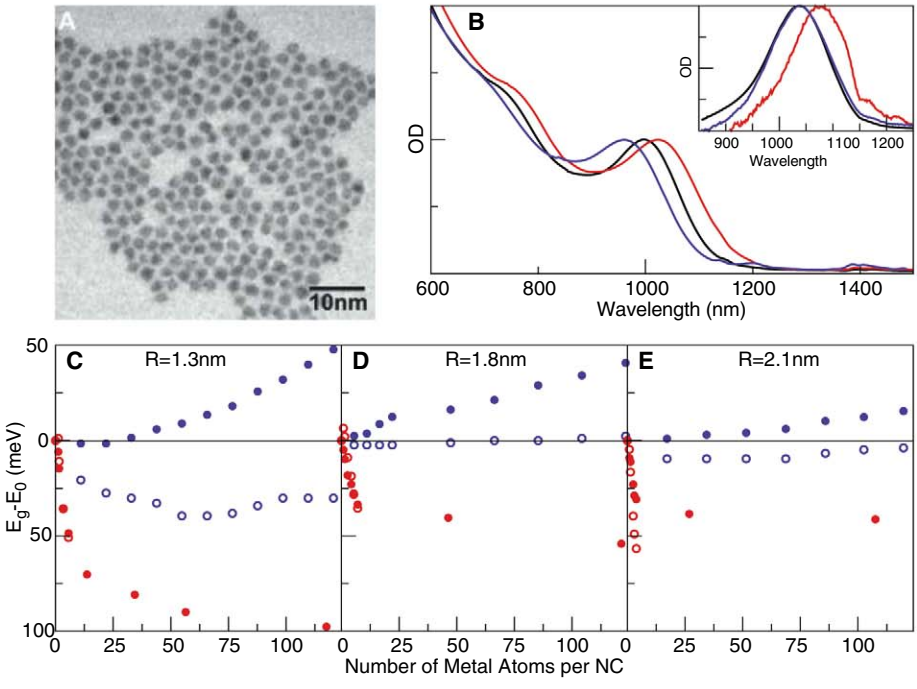

Fig. 2. Optical properties of doped InAs NCs. (**A**) TEM image of Ag-doped 3.3-nm InAs NCs. (**B**) Normalized absorption spectra of three 3.3-nm InAs NC samples. Two of the samples had Cu (blue) and Ag (red) solutions added to them resulting in metal/NC solution ratios of 540 and 264, respectively. These amounts correspond to 73 Cu atoms and 9 Ag atoms per NC. The third sample had a control solution (without metal salt) added to it (black). The inset shows the normalized emission spectra of these samples. (**C** to **E**) The energetic shift of the first exciton peak (solid symbols) and the emission energy (open symbols) against the number of impurity atoms per QD for InAs NCs with radii of 1.3 nm (C), 1.8 nm (D), and 2.1 nm (E). Red symbols correspond to Ag doping, blue symbols to Cu.

S1 and S2 for individual spectra). No considerable bleaching effects were observed in the absorption. The amount of impurities on the NCs was estimated by the analytical method of inductively coupled plasma atomic emission spectroscopy (ICP-AES, figs. S3 to S7).

A first possible source of spectral shifts in such quantum confined particles may be related to size changes upon doping, but this was excluded by detailed sizing analysis (fig. S9). An alternative source of the spectral shifts can be associated with electronic doping by the impurities. In Fig. 3 we show tunneling spectra measured by a scanning tunneling microscope (STM) at T = 4.2 K for undoped, Au-doped, Cu-doped, and Ag-doped InAs QDs 4.2 nm in diameter (see figs. S13 to S15 for additional spectra). Starting from the reference case of the undoped QD shown in the lower panel, the *dI/dV* curves, which are proportional to the DOS, match earlier studies of InAs QDs (*27*). The gap region is clearly identified, whereas on the positive-bias side a doublet of peaks associated with tunneling through the doubly degenerate $1S_e$ state is seen at the onset of the current, followed by a higher-order multiplet at higher bias corresponding to tunneling through the $1P_e$ conduction band state. A more complex peak structure is seen on the negative-bias side, resulting from tunneling through the closely spaced and intricate valence band states.

Several changes are seen upon doping the QDs. Starting with the case of Au, the gap is similar to the undoped QD, consistent with the optical measurements. However, the features in the scanning tunneling spectroscopy (STS) spectra are washed out, suggesting that indeed Au has entered the QD, perturbing the pristine level structure. More notable changes are seen for both the Cu and Ag cases (Fig. 3, upper panel), where band-tailing into the gap and the emergence of in-gap states in regions covering nearly 40% of the gap region are observed. In particular, in the Cu case, a shoulder on a tail-state structure is seen at bias values just below the $1S_e$ doublet (which is remarkably preserved). Additionally, the doublet is superimposed on a notable rising background that increases to the region of the $1P_e$ peaks that are not well resolved (fig. S13). For the Ag-doped QDs, there is pronounced broadening and merging of features on the positive-bias side, and on the negative-bias side a background signal develops.

A clear result of doping in bulk semiconductors is the shift of the Fermi level, which for n-type doping is close to the conduction band, and conversely shifts to a lower energy close to the valence band for p-type impurities. Remarkably, such shifts are clearly identified in the STS of the Cu- and Ag-doped QDs, as measured by the positions of the band edges relative to zero bias. Whereas the Fermi energy for the undoped case, as well as the Au-doped case, is nearly centered, in the Cu-doped case the onset of the conduction band states nearly merges with the Fermi energy, consistent with n-type doping. In contrast, for the Ag-doped case, the Fermi level is much closer to the onset of the valence band states, signifying p-type doping in this case. Considering that the only difference between the samples is the type of impurity atoms, and that the measurements are carried out under the same conditions, surface ligand effects or environmental influences on the Fermi energy shifts (*4*, *9*, *11*, *28*) can be ruled out.

Chemical considerations for the doping of InAs with the different metal atom impurities can help to clarify these observations (fig. S17). Cu can have a formal oxidation state of either +1 or +2. Moreover, its ionic radius is the smallest of the three impurities and therefore may be accommodated in interstitial sites within the InAs lattice (*29*). In such a case, one can expect that the Cu will partly donate its valence electrons to the QD, leading to n-type doping, consistent with the shift in the Fermi energy observed by STS. The incorporation of multiple impurities is expected to lead to the development of closely spaced impurity states, akin to the impurity band formed in the bulk (*20*). This band forms asymmetrically because of the disordered arrangement of the impurities in the QD, surpassing the energy of the $1S_e$ QD state. The observed rising background in the STS curve signifies the presence of such an impurity band. This is a direct indication of the substantial modification of the DOS induced by the impurities in small, heavily doped QDs. Revisiting the observed blue shift in the absorption, this is in line with the filling of the conduction and impurity-band levels in heavily n-type doped QDs, leading to a Moss-Burstein blue shift in the absorption spectrum and minor shifts in the emission (Fig. 2). Furthermore, the addition of impurity levels explains the negligible bleach in the absorption with doping, in contrast to remote surface doping in which QD state filling by the contributed charges leads to a bleach (*9*–*11*).

Ag has a large radius and is considered to be a substitutional impurity in III-V semiconductors (*30*). The replacement of an In atom, which possesses three valence electrons, with a Ag atom, which has only one valence electron, leads to an electron deficiency in the bonding orbitals, causing p-type doping. This is reflected in the shift of the Fermi level, as seen in the STS data (Fig. 3, red trace). In this case, the rising background in the spectrum at negative bias indicates the formation of an impurity band near the valence band. Because Ag has the largest ionic radius of the three impurities, it distorts the crystal structure more than the others; this results in band-tailing analogous to the Urbach tail known for heavily doped bulk semiconductors, and leads to the red shifts observed in the absorption onset as well as the emission (Fig. 2). Au may adopt a +3 valence state, which makes it isovalent with In, and hence doping is not expected to lead to the introduction of charge carriers. Moreover, its size is comparable to that of In (table S1), allowing for substitutional doping without substantial

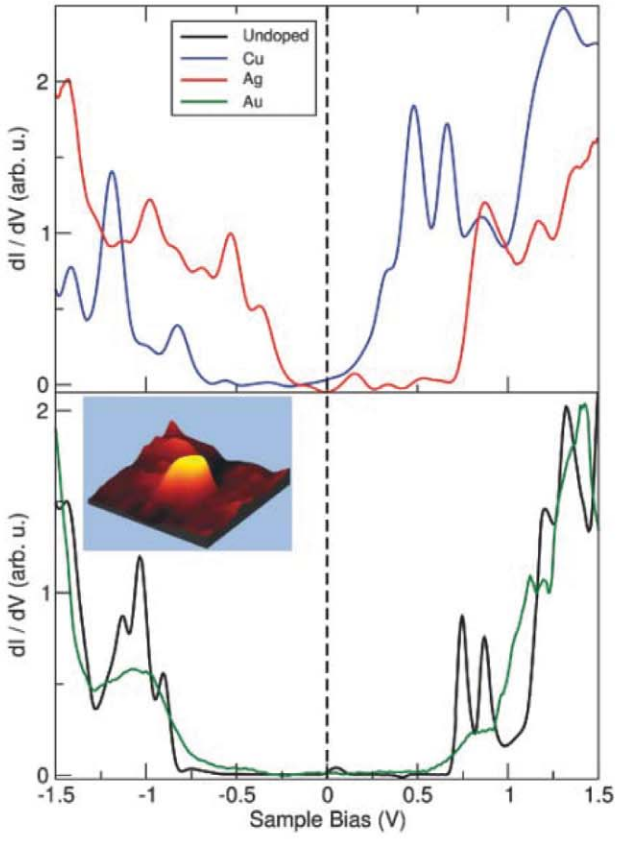

Fig. 3. The effect of doping on the STM tunneling spectra. Four *dI/dV* versus *V* tunneling spectra at 4.2 K, of undoped (black trace), Au-doped (green trace), Cu-doped (blue trace), and Ag-doped (red trace) InAs nanocrystals, nominally 4 nm in diameter. The doped QDs were taken from samples that had Ag, Cu, and Au atom/QD ratios corresponding to 15, 160, and 77, respectively. The vertical (V = 0) dashed line is a guide to the eye, highlighting the relative shifts of the band edges in the doped samples in manner typical of p-doped and n-doped semiconductors for the Ag-doped and Cu-doped nanocrystals, respectively. The inset shows an STM image of a single (Ag-doped) QD on which STS data were measured.

lattice distortions. These features of Au are consistent with the absence of large shifts in absorption, emission, and Fermi energy, as observed in both optical and tunneling spectra.

We also modeled the effects of electronic doping and structural disorder on the electronic properties of strongly confined impurity dopants in QDs. Starting with electronic effects, two models representing two limiting cases of doping were developed (*26*). The starting point for both models is based on the hydrogenic-like impurity model (*22*–*24*). In the first limit ("Z-model," Fig. 1B), we assume weak localization of the impurity states represented as a single central multivalent impurity. In the other limit, impurity electrons are sufficiently localized, to an extent much greater than in bulk (*8*), such that a single-electron tight binding (TB) treatment where each impurity contributes a single electron was applied. In Fig. 4A, we show the impurity DOS for n-type doping of two QD sizes for the TB model. For small number of impurities (e.g., $N = 5$), a peak in the DOS is observed below the QD level ($1S_e$). As the number of impurities increases, an impurity band develops asymmetrically around the QD level, pushing the Fermi energy toward the conduction band. The emerging impurity band develops a tail that extends into the gap, consistent with the STS data for the Cu case.

In Fig. 4B we show TB estimations for the shifts in the absorption spectrum as a function of the QD radius for various doping levels. The single impurity limit is the solution of a finite-barrier confined hydrogenic impurity, and nearly scales as R^{-1}. In this case, for both types of doping, a red shift is calculated. Although the confined energy levels of the impurity and the QD depend strongly on the effective mass ($m^*_{e,h}$), the spectral shifts, which depend on the differences between the impurity and electron/hole levels, only depend weakly on $m^*_{e,h}$ (Fig. 4B). Indeed, to lowest order in the Coulomb interaction, these differences are given by the expectation value of the electrostatic energy. As the number of impurity atoms increases, we find a nonmonotonic dependence of the spectral shifts with QD size. This reflects the transition of the impurity DOS from the gap region into the conduction band.

The onset of the blue shift and its magnitude depend on the model parameters (Fig. 4C). At low impurity concentrations, a red shift is always observed, consistent with the single hydrogenic impurity limit. A turnover from negative to positive shift is observed with increasing impurity density, depending on the degree of impurity carrier localization, which is determined by the ratio of the range of impurity interactions a and QD size R. The regime at which a blue shift is observed sets in earlier as a/R increases. Density functional theory calculations (*31*) for single impurities in QDs suggest $a/R \approx 1/3$, implying a narrow regime of red shift before a blue shift sets in. This is qualitatively consistent with the experimental observations shown in Fig. 4D for Cu, where a red shift is absent, suggesting that $a < R$. Moreover, the size dependence of the blue shift, which decreases with increasing R, is consistent with the R-dependence shown in Fig. 4C for the theory. The theory predicts that the shift will eventually reach a plateau, which is not observed experimentally.

The asymmetry in the shift (Fig. 4C) is directly correlated with the magnitude of the hopping term, γ. The case shown in Fig. 4C is for $\gamma = 5\varepsilon$ (where ε is the single-impurity energy taken from the hydrogenic model), where the blue shift is noticeably larger. When $\gamma = \varepsilon$, one observes a symmetric shift around the QD level (fig. S22). Also shown in Fig. 4C are the results of the Z-model, yielding an opposite behavior (inconsistent with the experiments), where a blue shift is observed for low doping levels, turning to a red shift as the doping level increases. These fundamental differences between the Z- and TB-models suggest that confinement leads to localization, consistent with previous theoretical work on single dopants (*8*).

An additional important mechanism of electronic level modification in the regime of heavily

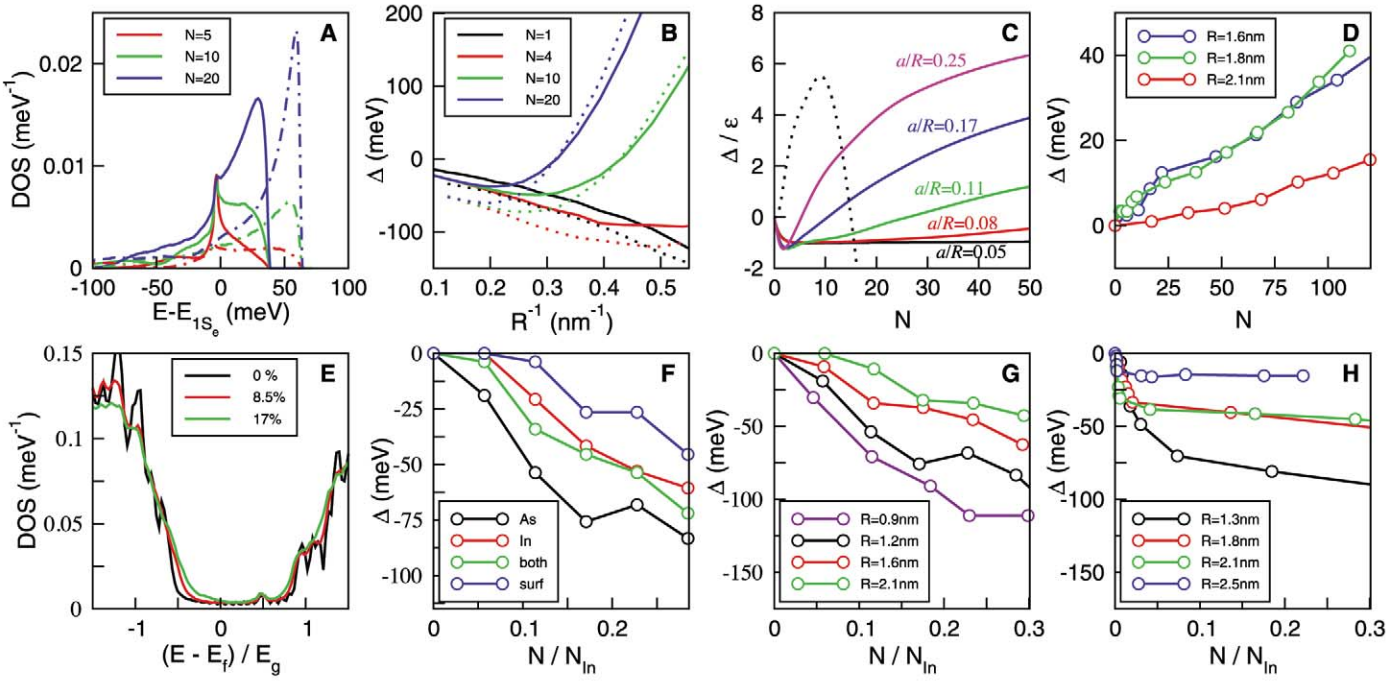

Fig. 4. The effect of doping on the electronic structure of nanocrystals. (A-D) Impurity band formation. (**A**) The impurity DOS from the TB model ($a = 0.4$ nm) for different levels of n-type doping for $R = 2$ nm (solid curves) and $R = 1.3$ nm (dotted-dashed curves). (**B**) The spectral shifts as a function of the inverse QD size for n-type (solid curves) and p-type (dotted curves) doping for different numbers of impurities. The InAs levels were calculated from an effective mass model. The impurity levels were calculated from the TB model with $a = 0.4$ nm. (**C**) Spectral shifts for n-type doping, as a function of the number of impurities N in units of the onsite energy in the tight binding model, ε, for several levels of localization (a/R). Dashed curve is the result of the Z-model. (**D**) Experimental spectral shifts for Cu doping as a function of N for several QD sizes. (**E** to **H**) Band tailing in doped nanocrystals. (E) DOS of an $In_{140}As_{141}$ QD for three levels of doping, expressed as a percentage of displaced In atoms. (F) Shifts in gap as a function of N relative to the number of In atoms (N_{In}) in the NC for different ways of introducing structural disorder. (G) Calculated shifts induced by band-tailing for several QD sizes. (H) Measured spectral shifts for Ag-doped QDs for several QD sizes. We used a normal distribution to induce disorder with a width that is 10% the In-As bond length [see (*26*) for more details on the calculations].

doped semiconductors relates to distortions of the crystal structure by the dopants leading to band-tailing and a red shift of the gap. To address the role of band-tailing we employed an atomistic treatment of the electronic structure of the QD, where disorder was introduced by randomly displacing In or As atoms (*26*). Band-tailing occurs mainly for the valence band edge as evident from the DOS shown in Fig. 4E for different impurity numbers. This results from the heavier effective mass and the denser level structure of the valence band, compared to the light effective mass of the highly delocalized electron. From the DOS we estimate the shifts in the band gaps induced by disorder as shown in Fig. 4F. Tailing occurs for distortions to the In atoms, As atoms, both atoms or only surface atoms. The band gap decreases for higher dopant concentrations. Note that the As distortions lead to larger shifts, consistent with its larger ionic radii.

In Fig. 4, G and H, we show the calculated and measured shifts (for Ag impurities) for several QD sizes as a function of the dopant concentration, respectively. The striking similarities between the theory and experiments suggest that the spectral shifts observed in Ag, unlike the case of Cu, are dominated by band-tailing, although clearly in both cases there is an interplay between band tailing and the impurity band formation. Both theory and experiments show a rapid increase in the magnitude of the shift, reaching a plateau at high dopant concentrations. The increase in the shift depends on the level of disorder induced by each dopant. Furthermore, the shifts decrease with increasing QD size in both cases. We note that in Cu, although a contribution of band-tailing is also possible, the band-filling effect discussed above dominates, leading to the blue shift in that case.

Doping semiconductor NCs with metal impurities provides further means to control their optical and electronic properties. We developed a synthesis for n- and p-type doped InAs NCs by introducing Cu and Ag impurities, respectively. Cu-doped particles showed a blue shift in the absorption with only small bleaching. This is in line with the increased DOS, which results from the addition of new impurity levels that develop into an impurity band, and their partial filling with electrons from interstitial Cu impurities. Correspondingly, the STS measurements show a shift in the Fermi energy to near the conduction band edge, and the development of a confined impurity band. This behavior was rationalized by a TB model, and its size dependence indicates that the confinement leads to localization of the impurity states in small NCs. Conversely, STS measurements of Ag-doped NCs led to a shift of the Fermi energy toward the valence band, proving p-type doping. This was accompanied by a red shift of both absorption and emission peaks, attributed to band-tailing effects analogous to the Urbach tail, in line with Ag adopting substitutional sites. The magnitude and size dependence of the band narrowing agree with atomistic electronic structure calculations incorporating structural disorder induced by the dopants. Interestingly, introduction of Au impurities as a substitutional dopant, although broadening the STS spectra, maintains the position of the Fermi level and does not lead to spectral shifts, in line with its isovalent nature with In. The controlled ability to synthesize n- and p-type doped NCs, along with better understanding of the heavily doped impurity regime in colloidal QDs, opens avenues for diverse electronic and optoelectronic devices.

References and Notes

1. S. M. Sze, *Physics of Semiconductor Devices* (Wiley-Interscience, New York, ed. 2, 1981).
2. S. Coe, W.-K. Woo, M. Bawendi, V. Bulović, *Nature* **420**, 800 (2002).
3. I. Gur, N. A. Fromer, M. L. Geier, A. P. Alivisatos, *Science* **310**, 462 (2005).
4. D. V. Talapin, C. B. Murray, *Science* **310**, 86 (2005).
5. D. J. Norris, A. L. Efros, S. C. Erwin, *Science* **319**, 1776 (2008).
6. D. Turnbull, *J. Appl. Phys.* **21**, 1022 (1950).
7. G. M. Dalpian, J. R. Chelikowsky, *Phys. Rev. Lett.* **96**, 226802 (2006).
8. T. L. Chan, M. L. Tiago, E. Kaxiras, J. R. Chelikowsky, *Nano Lett.* **8**, 596 (2008).
9. M. Shim, P. Guyot-Sionnest, *Nature* **407**, 981 (2000).
10. C. Wang, M. Shim, P. Guyot-Sionnest, *Science* **291**, 2390 (2001).
11. D. Yu, C. J. Wang, P. Guyot-Sionnest, *Science* **300**, 1277 (2003).
12. N. Pradhan, D. Goorskey, J. Thessing, X. Peng, *J. Am. Chem. Soc.* **127**, 17586 (2005).
13. R. N. Bhargava, D. Gallagher, X. Hong, A. Nurmikko, *Phys. Rev. Lett.* **72**, 416 (1994).
14. C. A. Stowell, R. J. Wiacek, A. E. Saunders, B. A. Korgel, *Nano Lett.* **3**, 1441 (2003).
15. S. C. Erwin *et al.*, *Nature* **436**, 91 (2005).
16. Y. Yang, O. Chen, A. Angerhofer, Y. C. Cao, *J. Am. Chem. Soc.* **128**, 12428 (2006).
17. C. Tuinenga, J. Jasinski, T. Iwamoto, V. Chikan, *ACS Nano* **2**, 1411 (2008).
18. S. Roy *et al.*, *J. Phys. Chem. C* **113**, 13008 (2009).
19. R. Xie, X. Peng, *J. Am. Chem. Soc.* **131**, 10645 (2009).
20. R. A. Abram, G. J. Rees, B. L. H. Wilson, *Adv. Phys.* **27**, 799 (1978).
21. J. Tauc, Ed., *Amorphous and Liquid Semiconductors* (Plenum, London, 1976).
22. N. Porras-Montenegro, S. T. Perez-Merchancano, A. Latge, *J. Appl. Phys.* **74**, 7624 (1993).
23. S.-S. Li, J.-B. Xia, *J. Appl. Phys.* **101**, 093716 (2007).
24. M. Barati, G. Rezaei, M. R. K. Vahdani, *Phys. Status Solidi* **244**, 2605 (2007) (b).
25. T. Mokari, A. Aharoni, I. Popov, U. Banin, *Angew. Chem. Int. Ed.* **45**, 8001 (2006).
26. See supporting material on *Science* Online.
27. U. Banin, O. Millo, *Annu. Rev. Phys. Chem.* **54**, 465 (2003).
28. K. S. Leschkies, M. S. Kang, E. S. Aydil, D. J. Norris, *J. Phys. Chem. C* **114**, 9988 (2010).
29. J. Dixon, D. Enright, *J. Appl. Phys.* **30**, 753 (1959).
30. B. Tuck, P. R. Jay, *J. Phys. D* **11**, 1413 (1978).
31. D. V. Melnikov, J. R. Chelikowsky, *Phys. Rev. Lett.* **92**, 046802 (2004).

32. We thank the staff of the Unit for Nanocharacterization of the Center for Nanoscience and Nanotechnology in the Hebrew University, Jerusalem, headed by I. Popov, as well as V. Gutkin for help in the XPS studies. Supported by a grant from the European Research Council under the European Community's Seventh Framework Programme (FP7/2007-2013)/ERC grant agreement 203413 (U.B.); the Israel Science Foundation (O.M.); Seventh Framework Programme Marie Curie International Outgoing Fellowships for Career Development project Hierarchical Junction Solar Cells (E.R.); the Harry de Jur Chair in Applied Science (O.M.); the Alfred and Erica Larisch Memorial Chair (U.B.); an Azrieli Foundation fellowship (G.C.); and the Centre for Scientific Absorption, Ministry of Absorption, State of Israel (D.M.).

Supporting Online Material

www.sciencemag.org/cgi/content/full/332/6025/77/DC1
Materials and Methods
Figs. S1 to S24
Table S1
References

10 August 2010; accepted 10 February 2011
10.1126/science.1196321

Electrochemically Mediated Atom Transfer Radical Polymerization

Andrew J. D. Magenau,[1] Nicholas C. Strandwitz,[2] Armando Gennaro,[3] Krzysztof Matyjaszewski[1]*

Atom transfer radical polymerization is a versatile technique for exerting precise control over polymer molecular weights, molecular weight distributions, and complex architectures. Here, we show that an externally applied electrochemical potential can reversibly activate the copper catalyst for this process by a one-electron reduction of an initially added air-stable cupric species (Cu^{II}/Ligand). Modulation of polymerization kinetics is thereby tunable in real time by varying the magnitude of applied potential. Application of multistep intermittent potentials successfully triggers initiation of polymerization and subsequently toggles the polymerization between dormant and active states in a living manner. Catalyst concentrations down to 50 parts per million are demonstrated to maintain polymerization control manifested in linear first-order kinetics, a linear increase in polymer molecular weight with monomer conversion, and narrow polymer molecular weight distributions over a range of applied potentials.

Living polymerizations, introduced in 1956 by Szwarc (*1*), proceed in the absence of chain termination and chain transfer events, while concurrently maintaining instantaneous initiation and uniform growth of each propagating species (*2*). Processes of this nature allow

macromolecules to be prepared with precisely controlled molecular weights (M_n) and narrow molecular weight distributions (M_w/M_n). Polymerizations with living characteristics grant access to complex polymeric architectures and associated functionalities traditionally accessible only through ionic mechanisms. Relative to ionic polymerizations, radical pathways provide improved tolerance to functional groups and impurities, an expanded range of polymerizable monomers, and an efficient means of copolymerizing a variety of monomers (*3*, *4*). Controlled/living radical polymerizations (CRP), once thought unobtainable (*5*), have now been realized through many remarkable breakthroughs providing characteristics inherent to living polymerizations (*6*–*10*). Control is established in CRP by dynamic equilibria, either through dormant/active chain ends or degenerative transfer, essentially minimizing the concentration of propagating centers and concomitantly reducing bimolecular termination reactions occurring at diffusion-controlled reaction rates (*5*).

Real-time dynamic modulation of polymerization processes offers intermittent regulation of system variables that may include, but are not limited to, alterations of stereoselectivity (*11*), reactivity (*12*), and reaction rates (*13*–*16*). Variable polymerization rates have been demonstrated in only a few accounts using allosteric supramolecular catalysis (*13*), redox controlled catalysts (*14*), and temporal photoirradiation (*15*, *16*). These strategies require complex catalytic systems or are limited in their available tunable parameters. Furthermore, among the stimuli (e.g., light, pressure, and pH) available to externally influence polymerization behavior (*12*, *15*, *17*), application of an electrochemical stimulus (i.e., electrolysis) can be conveniently paired with atom transfer radical polymerization (ATRP), owing to the inherent redox-active nature of the ATRP catalytic system (*18*, *19*).

ATRP, one of the most powerful CRP techniques, proceeds through a concerted atom transfer mechanism via an inner-sphere electron-transfer process (*20*, *21*). The versatility of this process is exemplified by the vast array of suitable polymerization media, encompassing homogenous, heterogeneous, and aqueous systems (*3*, *22*–*25*), and attainable complex polymeric architectures (*3*, *26*). ATRP is dictated by an active/dormant equilibrium, shown in part by Fig. 1A, between lower oxidation state activators {i.e., $Cu^{I}Br$/tris[2-(dimethylamino)ethyl]amine ($Cu^{I}Br/Me_6TREN$)} and alkyl halides (P_n-Br), and their corresponding higher oxidation state deactivators (i.e., $Cu^{II}Br_2$/Me_6TREN) and radicals ($P_n^{\bullet}$), which are capable of monomer (M) addition (*3*, *4*, *6*, *10*). Establishing this dynamic equilibrium ($K_{ATRP} = k_a/k_{da}$), which strongly favors the dormant state, effectively decreases the concentration of propagating species and mediates the polymerization, allowing simultaneous growth of each polymeric chain.

In recent years, the ATRP process has been expanded via activators generated by electron transfer (AGET), a catalytic activation technique that reduces air-stable deactivators to their respective activators in situ by means of reducing agents (e.g., ascorbic acid, tin (II) 2-ethylhexanoate, and Cu^0) (*23*). AGET ATRP led to further process refinements by providing protocols with diminished $Cu^{II}X_2$ catalyst concentrations down to 10 parts per million (ppm) and simplified reaction setups in the presence of oxygen through activators regenerated by electron transfer (ARGET) and initiators for continuous activator regeneration (ICAR) ATRP (*27*–*29*). These systems are conducted in the presence of excess reducing agent where $Cu^{I}X$ activators are continuously regenerated from the $Cu^{II}X_2$ deactivators, a by-product of unavoidable termination events. Notably, the absolute concentration of copper catalyst can be decreased tremendously without affecting the polymerization rate, provided that an adequate $[Cu^{I}X/L]/[Cu^{II}X_2/L]$ ratio is sustained.

This report demonstrates the dynamic modulation of polymerization rates through electrochemical means, fostering precise temporal control over initiation, cessation, and rejuvenation of a CRP process. Electrochemical methods offer adjustable parameters (e.g., current, potential, and total charge passed) to manipulate polymerization rates and selective targeting of redox-active catalytic species. Moreover, advantages of ARGET ATRP such as ppm concentrations of catalyst (*27*, *30*) and tolerance to limited O_2 (*28*) are maintained and bolstered by elimination of environmentally less friendly chemical reducing agents and catalyst removal through electrodeposition (*31*). The proposed mechanism of ATRP mediated electrochemically (*e*ATRP) by (re)generation of activators is shown in Fig. 1A. Air-stable $Cu^{II}Br_2/Me_6TREN$ deactivator is reduced to $Cu^{I}Br/Me_6TREN$ activator electrochemically to invoke or trigger polymerization. In the absence of mass transport limitations, the extent of reduction is dictated by the applied potential (E_{app}), allowing a predefined $[Cu^{I}X/L]/[Cu^{II}X_2/L]$ ratio and fine-tuning of the polymerization rate. Further to this point, electrochemical methods allow a lower oxidation state catalyst ($Cu^{I}Br/Me_6TREN$) to be reverted back to its original higher oxidation deactivator state by simply shifting E_{app} to more positive values, thus providing a means to deactivate an ongoing polymerization.

Reduction of the $Cu^{II}Br_2/Me_6TREN$ complex was accomplished by application of a cathodic current (*32*). A similar methodology, although for generation of acutely air-sensitive click chemistry catalysts, was previously implemented for bioconjugation reactions with an isosahedral virus, resulting in high-efficiency reactions in the presence of ambient O_2 without chemical reducing agents (*33*). Before our electrolysis experiments, cyclic voltammograms (CVs) of methyl acrylate (MA) and acetonitrile (MeCN) over a potential range of 1.5 volts, from 0.0 to –1.5 V versus Ag^{+}/Ag were acquired to ensure the absence

[1]Center for Macromolecular Engineering, Department of Chemistry, Carnegie Mellon University, 4400 Fifth Avenue, Pittsburgh, PA 15213, USA. [2]Kavli Nanoscience Institute and Beckman Institute, and Division of Chemistry and Chemical Engineering, 210 Noyes Laboratory 127-72, California Institute of Technology, Pasadena, CA 91125, USA. [3]Department of Chemical Sciences, University of Padova, via Marzolo 1, 35131 Padova, Italy.

*To whom correspondence should be addressed. E-mail: km3b@andrew.cmu.edu

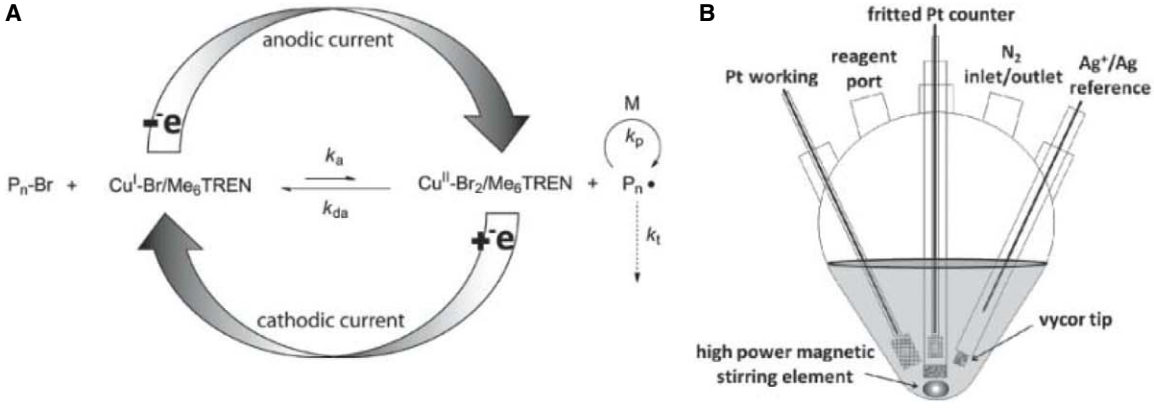

Fig. 1. (A) Mechanism of electrochemically mediated ATRP (*e*ATRP) under a cathodic current to (re)generate the $Cu^{I}Br_2/Me_6TREN$ complex and optional anodic current to revert to the $Cu^{II}Br_2/Me_6TREN$ complex for cessation of polymerization. **(B)** Electrolysis cell configured with platinum mesh working and counter electrodes. The two-compartment cell with a frit-separated counter electrode was maintained under an N_2 atmosphere at 25°C. Redox reactions of Cu^{II}/Cu^{I} couple were performed with applied potentials varied between –0.72 and –0.40 V versus an Ag^{+}/Ag reference electrode.

of any redox process that might interfere with the catalyst reduction (fig. S1A). After confirming the stability of the reaction medium, we acquired an additional CV in the presence of added $Cu^{II}Br_2$/Me_6TREN to identify the potential window appropriate for accurate manipulation of the oxidation states of our redox-active catalyst in electrolysis experiments. The copper catalyst couple (Cu^{II}/Cu^{I}) was observed to have an $E_{1/2}$ = –0.69 V versus Ag^+/Ag (–0.77 V versus Fc^+/Fc) (fig. S1B). Upon addition of the alkyl halide initiator, the CV changed due to regeneration of $Cu^{II}Br_2$/Me_6TREN by reaction of the electro-generated $Cu^{I}Br_2$/Me_6TREN complex with ethyl 2-bromopropionate (EBP) (fig. S1B). This process is similar to homogeneous redox catalysis (*34*): The $Cu^{I}Br_2$/Me_6TREN generated at the electrode reacts in solution to reduce EBP; a portion of the $Cu^{II}Br_2$/Me_6TREN thus regenerated returns to the electrode to be reduced again. The cathodic current is thereby enhanced, because reduction involves more than one-electron/molecule, whereas the anodic current decreases, because $Cu^{I}Br_2$/Me_6TREN is partially oxidized in solution.

Electrolysis of $Cu^{II}Br_2$/Me_6TREN was then carried out over a range of 60 mV, between –0.66 and –0.72 V, designed to probe the influence of applied potential (E_{app}). The cell was filled with ~12 mL of a 1:1 MA/MeCN (v/v) mixture containing 0.1 M electrolyte formulated with the following molar ratios $[MA]_0$:$[EBP]_0$:$[Me_6TREN]_0$:$[Cu^{II}Br_2]_0$ = 500:1:0.025:0.025. Electrolysis studies were carried out in a two-compartment cell fitted with platinum mesh working and counter electrodes, and a silver ion/silver (Ag^+/Ag) reference electrode, as illustrated in Fig. 1B. The counter electrode was always separated by a glass frit from the working electrode compartment, where polymerization occurs, to avoid oxidation of Cu^{I} and/or contamination of the working solution by oxidation products arising from the anodic process. An inert atmosphere and rapid stirring were maintained for the reaction duration to ensure stability of the $Cu^{I}Br$/Me_6TREN catalyst and adequate mass transport to the working electrode. Upon application of a –0.69 V potential, which corresponds to the $E_{1/2}$ of the Cu^{II}/Cu^{I} couple, rapid consumption of monomer occurred, reaching nearly 80% conversion within 2 hours (Fig. 2A). Linear first-order kinetic behavior was observed during the polymerization, indicating a constant concentration of propagating species (fig. S2), and an excellent correlation persisted between theoretical and experimental molecular weight values as the polymerization progressed (Fig. 2B). Molecular weight values increased linearly with conversion, and molecular weight distributions decreased gradually with increasing monomer conversion, reaching a minimum value of approximately M_w/M_n = 1.06. Furthermore, gel permeation chromatography (GPC) depicted monomodal distributions of polymeric species and a clear shift to larger molecular weight values with increasing conversion (Fig. 3).

The rate of ATRP is defined by the ratio of [$Cu^{I}Br_2$/Me_6TREN] and [$Cu^{II}Br_2$/Me_6TREN] and therefore depends on the extent to which $Cu^{II}Br_2$/Me_6TREN is reduced and consequently the E_{app} (*3*). Two additional and separate polymerizations were conducted with a 30-mV increase or decrease of the E_{app} to –0.72 and –0.66 V, respectively. An enhanced polymerization rate was observed at more negative potentials, whereas more positive potentials provided a slower rate of polymerization (Fig. 2A). Initial slopes in the first-order kinetic plots revealed an approximate rate enhancement by a factor of 2.4 by adjusting the E_{app} from –0.66 V to –0.72 V (fig. S2). In all cases, similar correlations between theoretical and experimental molecular weights were observed, and narrow molecular weight distributions were maintained even with enhanced polymerization rates (Fig. 2B and figs. S3 and S4).

Feasibility of an electrochemical switch to modulate copper oxidation states in situ, and thereby activate or deactivate polymerization, was demonstrated by repetitive stepping of the E_{app} from –0.69 V to –0.40 V. The first of these potentials favors formation of Cu^{I} at the electrode and hence triggers an active state, whereas the second potential, being more positive than $E_{1/2}$, favors Cu^{II} and leads to a dormant state. In the first hour of polymerization, no potential was applied and as a result no monomer conversion occurred, confirming the necessity of an E_{app} to trigger polymerization (Fig. 4A). Upon switching the potential to –0.69 V, 10% monomer conversion was observed after ~24 min, at which point the potential was switched to –0.40 V. Once this potential change occurred, the polymerization slowed and then halted, achieving ~2% monomer conversion in the first 25 min and a negligible amount over the following 20 min. The response time for deactivation was on average ≤20 min, whereas a polymerization could be revived in less than 15 min in the early stage of polymerization. This potential cycle was then repeated for three additional cycles, resulting in an increased monomer conversion to 28, 44, and then to 62% during active periods. This behavior manifests characteristics of a living polymerization with regard to efficient reinitiation of chain ends, owing to the preserved chain-end functionality. Throughout the cycling process, molecular weight values correlated strongly with their theoretically predetermined values, and low M_w/M_n values were maintained (Fig. 4B). Clustering of data points in the dormant periods is visible in Fig. 4B, whereas the molecular weight was shown to increase progressively with conversion during active periods when a sufficient E_{app} was imposed. Clear shifts to higher molecular weight were observed by GPC (fig. S5) without any substantial lower molecular weight fraction, confirming near quantitative reinitiation of poly(methyl acrylate) halogen chain ends.

Thus, we demonstrated a successful and well-controlled *e*ATRP of MA in MeCN. The *e*ATRP system is currently being extended to a larger range of monomers, media, and synthesis of various copolymers with complex architectures.

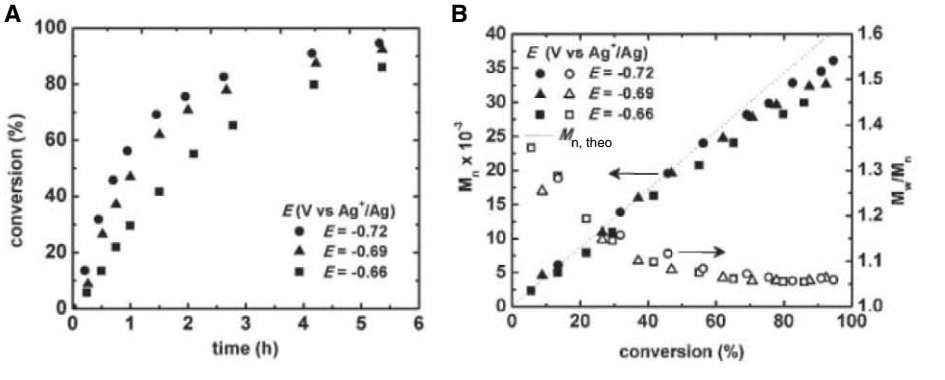

Fig. 2. (**A**) Monomer conversion with respect to time and (**B**) number average molecular weight (M_n) and M_w/M_n (where M_w is weight average molecular weight) with respect to conversion as a function of applied potential. Polymerizations were conducted in 50% (v/v) MA in MeCN at 25°C, with a total reaction volume of ~12 mL. $[MA]_0$ = 5.55 M; $[MA]_0$:$[EBP]_0$:$[Me_6TREN]_0$:$[Cu^{II}Br_2]_0$ = 500:1:0.025:0.025.

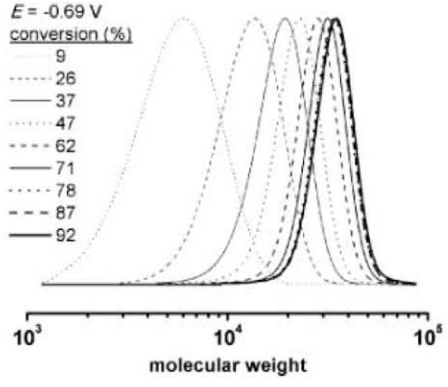

Fig. 3. Evolution of molecular weight with monomer conversion at –0.69 V versus Ag^+/Ag, measured by gel permeation chromatography.

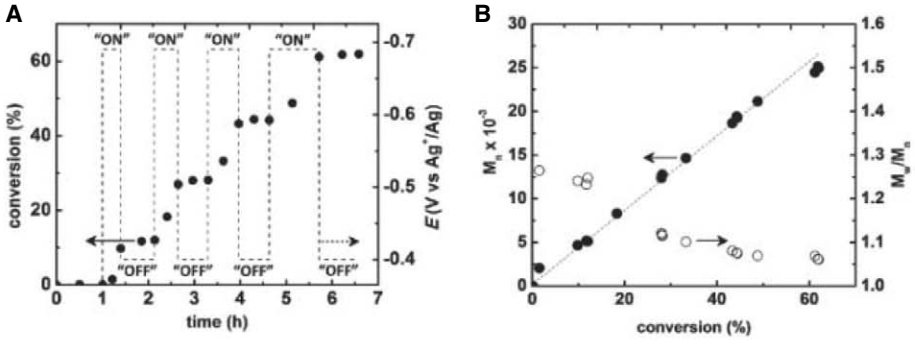

Fig. 4. (**A**) Conversion (solid circles) and applied potential (dashed line) with respect to time and (**B**) M_n and M_w/M_n with respect to conversion. Toggling between active and dormant states is represented by changes of the E_{app} values between −0.69V and −0.40 V versus Ag^+/Ag, respectively. Reaction conditions are identical to those stated in Fig. 2.

References and Notes

1. M. Szwarc, *Nature* **178**, 1168 (1956).
2. A. H. E. Müller, K. Matyjaszewski, *Controlled and Living Polymerizations: Methods and Materials* (Wiley-VCH, Weinheim, Germany, 2009).
3. K. Matyjaszewski, J. Xia, *Chem. Rev.* **101**, 2921 (2001).
4. M. Kamigaito, T. Ando, M. Sawamoto, *Chem. Rev.* **101**, 3689 (2001).
5. K. Matyjaszewski, T. P. Davis, *Handbook of Radical Polymerization*. (Wiley-Interscience, Hoboken, NJ, 2002).
6. T. E. Patten, J. Xia, T. Abernathy, K. Matyjaszewski, *Science* **272**, 866 (1996).
7. M. K. Georges, R. P. N. Veregin, P. M. Kazmaier, G. K. Hamer, *Macromolecules* **26**, 2987 (1993).
8. M. Kato, M. Kamigaito, M. Sawamoto, T. Higashimura, *Macromolecules* **28**, 1721 (1995).
9. J. Chiefari *et al*., *Macromolecules* **31**, 5559 (1998).
10. J.-S. Wang, K. Matyjaszewski, *J. Am. Chem. Soc.* **117**, 5614 (1995).
11. L. H. Peeck, S. Leuthausser, H. Plenio, *Organometallics* **29**, 4339 (2010).
12. M. Benaglia *et al*., *J. Am. Chem. Soc.* **131**, 6914 (2009).
13. H. J. Yoon, J. Kuwabara, J.-H. Kim, C. A. Mirkin, *Science* **330**, 66 (2010).
14. C. K. A. Gregson *et al*., *J. Am. Chem. Soc.* **128**, 7410 (2006).
15. Y. Kwak, K. Matyjaszewski, *Macromolecules* **43**, 5180 (2010).
16. M. Tanabe *et al*., *Nat. Mater.* **5**, 467 (2006).
17. J. Rzayev, J. Penelle, *Angew. Chem. Int. Ed.* **43**, 1691 (2004).
18. V. Bonometti, E. Labbé, O. Buriez, P. Mussini, C. Amatore, *J. Electroanal. Chem.* **633**, 99 (2009).
19. J. Qiu, K. Matyjaszewski, L. Thouin, C. Amatore, *Macromol. Chem. Phys.* **201**, 1625 (2000).
20. C. Y. Lin, M. L. Coote, A. Gennaro, K. Matyjaszewski, *J. Am. Chem. Soc.* **130**, 12762 (2008).
21. A. A. Isse *et al., J. Am. Chem. Soc.*, ASAP (2011); doi: 10.1021/ja110538b.
22. W. A. Braunecker, K. Matyjaszewski, *Prog. Polym. Sci.* **32**, 93 (2007).
23. K. Min, H. Gao, K. Matyjaszewski, *J. Am. Chem. Soc.* **127**, 3825 (2005).
24. M. F. Cunningham, *Prog. Polym. Sci.* **33**, 365 (2008).
25. K. Min, K. Matyjaszewski, *Cent. Eur. J. Chem.* **7**, 657 (2009).
26. K. Matyjaszewski, N. V. Tsarevsky, *Nat. Chem.* **1**, 276 (2009).
27. K. Matyjaszewski *et al*., *Proc. Natl. Acad. Sci. U.S.A.* **103**, 15309 (2006).
28. K. Matyjaszewski, H. Dong, W. Jakubowski, J. Pietrasik, A. Kusumo, *Langmuir* **23**, 4528 (2007).
29. W. Jakubowski, K. Matyjaszewski, *Angew. Chem.* **118**, 4594 (2006).
30. T. Pintauer, K. Matyjaszewski, *Chem. Soc. Rev.* **37**, 1087 (2008).
31. M. Nasser-Eddine, C. Delaite, P. Dumas, R. Vataj, A. Louati, *Macromol. Mater. Eng.* **289**, 204 (2004).
32. Materials and methods are available as supporting material on *Science* Online.
33. V. Hong, A. K. Udit, R. A. Evans, M. G. Finn, *ChemBioChem* **9**, 1481 (2008).
34. A. A. Isse, A. Gennaro, *J. Phys. Chem. A* **108**, 4180 (2004).

35. We acknowledge the U.S. National Science Foundation (grants DMR 09-69301 and CHE 10-26060) and the members of the CRP Consortium at Carnegie Mellon University for financial support. N.C.S. acknowledges the U.S. National Science Foundation for an American Competitiveness in Chemistry postdoctoral fellowship (CHE-1042006). A.J.D.M. and K.M. filed a U.S. provisional patent application (61/459,724) related to this work.

Supporting Online Material

www.sciencemag.org/cgi/content/full/332/6025/81/DC1
Materials and Methods
Figs. S1 to S5
References

30 December 2010; accepted 2 March 2011
10.1126/science.1202357

Thermochronometry Reveals Headward Propagation of Erosion in an Alpine Landscape

David L. Shuster,[1,2]*‡ Kurt M. Cuffey,[3,2]‡ Johnny W. Sanders,[2] Greg Balco[1]

Glacial erosion of mountain ranges produces spectacular alpine landscapes and, by linking climate with tectonics, influences a broad array of geophysical phenomena. Although the resultant landforms are easily identified, the timing and spatial pattern of topographic adjustment to Pleistocene glaciations remain poorly known. We investigated topographic evolution in the archetypal glacial landscape of Fiordland, New Zealand, using (U-Th)/He thermochronometry. We find that erosion during the past 2 million years removed the entire pre-Pleistocene landscape and fundamentally reshaped the topography. Erosion focused on steep valley segments and propagated from trunk valleys toward the heads of drainage basins, a behavior expected if subglacial erosion rate depends on ice sliding velocity. The Fiordland landscape illustrates complex effects of climate on Earth's surface morphology.

The characteristic landforms and large relief of many alpine landscapes indicate that the effect of glacial erosion over the past ~2.5 million years (My) has been profound (*1*, *2*). Understanding how this erosion progressed at the landscape scale over millions of years is essential for analyzing the connections between climate change, topography, and tectonic processes. Most quantitative studies of glacial landscape evolution rely on model simulations that calculate glacial erosion from poorly validated parameterizations [e.g., (*3*, *4*)]. Alternatively, direct observational constraints could reveal the evolution of topography and so guide model development [e.g., (*5*–*7*)]. Such constraints are difficult to obtain, however, because erosion itself effaces evidence of past topography.

We used the isotopic legacy of evolving crustal temperature conditions to constrain the history of relief development in a mountain landscape. We collected low-temperature thermochronometric measurements of 33 bedrock samples from along valley axes and up valley walls in high-relief drainage networks near Milford Sound in Fiordland, New Zealand (*8*). In this setting, patterns of topographic evolution over the past ~2 My are clearly decipherable because of a fortuitous correspondence between the temperature sensitivity of He isotopic techniques and the overall magnitude of Pleistocene exhumation. All samples were taken from a ~21-km–by–38-km region (Fig. 1). The valleys exhibit classic glacial forms, including U-shaped cross sections, concave longitudinal profiles dominated by low slopes, and deeply incised valley-head cirques with exception-

[1]Berkeley Geochronology Center, 2455 Ridge Road, Berkeley, CA 94709, USA. [2]Department of Earth and Planetary Science, University of California, Berkeley, CA 94720, USA. [3]Department of Geography, University of California, Berkeley, CA 94720, USA.

*To whom correspondence should be addressed. E-mail: dshuster@bgc.org
‡These authors contributed equally to this manuscript.

ally steep walls. The examined valleys are incised into strong plutonic rocks, primarily of the Arthur River and Darran complexes (*9*). Mean slopes of valley sides and cirque headwalls commonly exceed ~45° over horizontal and vertical scales of ~1.5 km. The dominant wavelength and relief of the regional surface topography are ~4 km and ~2 km, respectively (Fig. 1). This region currently receives abundant precipitation (>6 m/year) and lies along a tectonically active plate boundary. Oblique convergence of the Australian and Pacific plates, the source of mountain uplift, began about 6 My ago (*10*). Convergence has been accommodated primarily by deformation of weaker crust east of the Fiordland block.

Comparing measured apatite (U-Th)/He ages (*8*) to elevations for all sample sites reveals a broadly crescentic pattern (Fig. 2A); the youngest ages, ~1 My, generally occur at cirque floor elevations (~500 to 700 m), whereas older ages occur both at sea level (where ages approach ~2 My) and on summits (~2.5 My). This crescent-shaped age/elevation relationship appears in multiple valley systems, some of which drain NW from the main divide (to Milford Sound) and others to the SE (inland to Lake Te Anau). With one exception, all median (U-Th)/He ages are <2.5 My. Thus, these data primarily reflect processes active in the Pleistocene. The similarity between longitudinal age/elevation relationships of individual valleys (Fig. 2, B to D) and the regional age/elevation relationship (Fig. 2A) suggests both a consistent pattern of valley development across the region and an absence of localized tectonic influences on the age patterns (*8*).

We also analyzed samples using ^{4}He/^{3}He thermochronometry (*8*). Unlike (U-Th)/He ages, which are calculated from the total abundance of radiogenic ^{4}He relative to U and Th, the ^{4}He/^{3}He method constrains the spatial distribution of ^{4}He within an apatite crystal via controlled stepwise degassing of samples containing synthetic proton-induced ^{3}He (*11*). Such information delimits a sample's continuous cooling history through the temperature range ~80° to ~20°C (*12*). The cooling history, in turn, reveals aspects of topographic development not captured by the He ages alone.

Thermal histories derived from ^{4}He/^{3}He thermochronometry differ greatly across the landscape, even over small distances (Fig. 1). At the head of the North Branch Cleddeau valley, for example, rocks at the floor of an 1100-m-deep cirque cooled continuously over the past ~1 My, from temperatures of ~75° to 110°C to the present surface temperature (Fig. 1D). In contrast, rocks currently at the ridge crest resided at temperatures <25°C throughout this time interval. Superficially, these results suggest that much of the cirque relief developed over the past ~1 My. In this landscape of closely spaced valleys and high relief, however, the geothermal gradient depends strongly on position in the landscape; different thermal histories are expected at different sites, even if topography and mean exhumation rate were steady. To disentangle these factors, and to account for the effects of both surface erosion and rock uplift, we interpreted our data in the context of a three-dimensional thermokinematic finite-element model for subsurface temperature evolution (*13*).

This model allowed us to prescribe both the surface topography and the rock uplift as arbitrary functions of time and space. The sum of surface lowering and rock uplift then determined exhumation, the primary control on thermal histories. Uplift was assumed to be spatially uniform and steady, although we explored the effect of time-varying uplift rate in some sensitivity tests (*8*).

Using a variety of topographic histories, designed to represent idealized styles of morphological change, we calculated evolving temperatures over the past 4.0 My for the three regions delimited by white boxes in Fig. 1. Each calculation began at a steady state. We recorded the time series of temperatures along the particle paths leading to our sample sites on the modern surface. From such cooling histories, we calculated model (U-Th)/He ages and model ^{4}He/^{3}He release spectra as a function of sample characteristics (*14*); these results were compared to observations (*8*). We sought models that could simultaneously reproduce the key features of the data: the minimum of ages at cirque-floor elevations and the very steep age-elevation gradients on the sides of trunk valleys and at some valley heads.

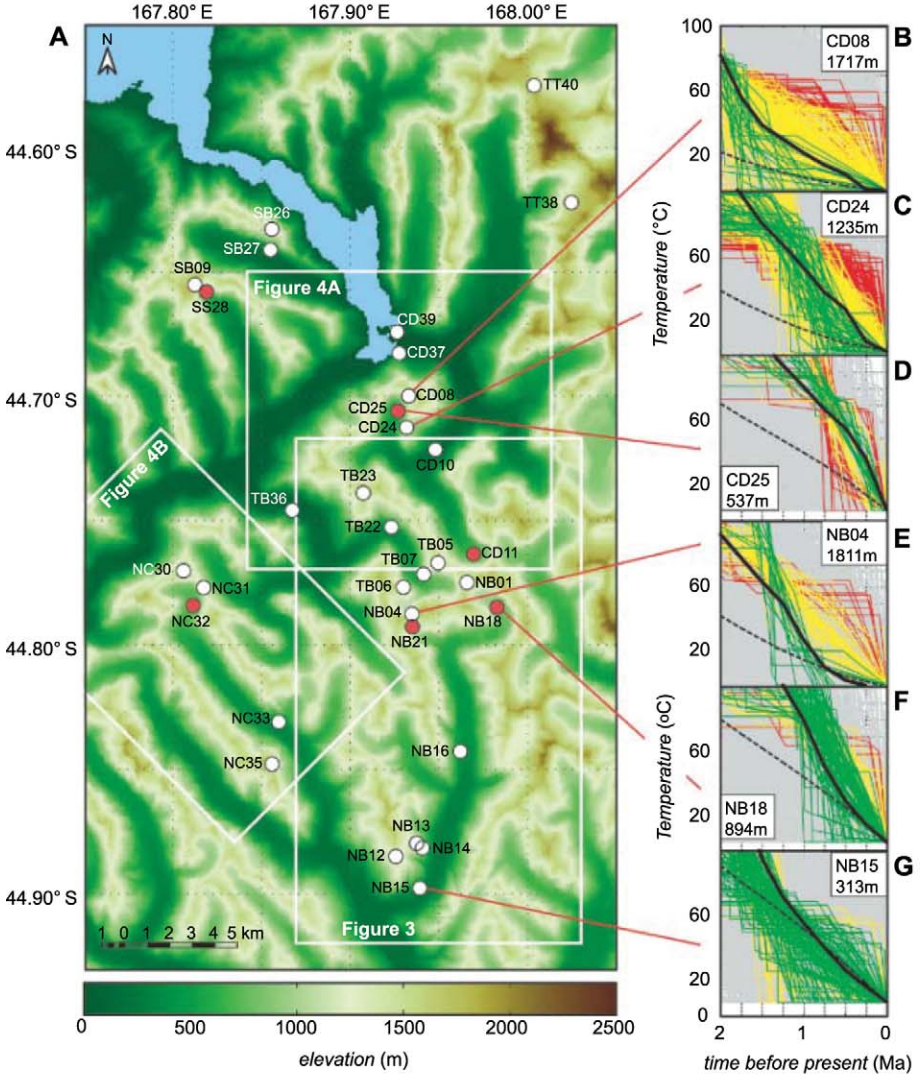

Fig. 1. Modern Fiordland topography and sample locations, together with cooling constraints from apatite ^{4}He/^{3}He thermochronometry. (**A**) Topography and bedrock sample locations; red denotes cirque-floor samples. White rectangles outline model domains (see Figs. 3 and 4). (**B** to **G**) Cooling paths from ^{4}He/^{3}He thermochronometry of select samples from the North Branch Cleddeau [(B) to (D)] and the Neale Burn drainages [(E) to (G)]. The colored sets of randomly generated cooling paths predict each observed (U-Th)/He age to within analytical uncertainty (±1σ); the gray paths do not. Yellow and red paths are progressively inconsistent, respectively, with the ^{4}He/^{3}He data (figs. S1 and S2), whereas green paths are most consistent (*12*). Cooling paths shown as solid black curves were predicted from the topographic evolution models shown in Figs. 3 and 4; the dashed black curves are predictions for steady-state topography, from models calibrated to match lowest-elevation samples (Fig. 2).

We attempted first to predict the observed (U-Th)/He ages by assuming steady topography and exhumation. These models predict a monotonic age/elevation relationship and can never reproduce the key features of the observations (Fig. 2). We then sought to fit the data with progressively more complex models (Fig. 2, E and F, and fig. S3). Rejected model classes include decreasing relief without changes of landform shape (i.e., exhumation proportional to present elevation); transition from an initially flat landscape to the present form (i.e., exhumation inversely related to present elevation); and deepening of valleys as their longitudinal profiles change from linear to concave.

The only class of models capable of matching the observations involves headward progression of erosion, so that deep exhumation of headwater regions (including cirques and drainage divides) occurred roughly 1 My after deep exhumation of the downstream segments of trunk valleys (Figs. 2 to 4). In the best-fitting models, prominent kilometer-scale topographic steps migrated upvalley (Figs. 3 and 4). Although idealized, this morphology resembles modern analogs in Norway and Antarctica, where steep valley ramps descend to level floors (*8*). Best-fitting models of this class imply basin-wide exhumation rates of 0.76 mm/year, partitioned between background exhumation and rock uplift of about 0.6 mm/year and maximum local bedrock lowering rates of ~4 mm/year (Fig. 3, D to F, and table S3). These models also succeed in predicting the local cooling paths constrained by $^{4}He/^{3}He$ data (Fig. 1, B to G).

In all cases, headward progression implies rapid erosion of steep valley segments as compared to adjacent flat segments downstream. Such behavior occurs in river systems, because boundary shear stress and the rate of energy expenditure increase with the slope (*15*). In Fiordland, however, the erosion pattern almost certainly arose from glacial action. Currently, glaciers survive on high slopes in this region of abundant snowfall. For most of the past 2 My, landscapes worldwide were considerably colder and icier than in the present interglacial period (*16*, *17*), and New Zealand glaciations generally followed world trends (*18*). In Fiordland, moreover, elevations upstream of the erosion fronts would have been substantially higher than at present (≥1.5 km according to our estimates; Figs. 3 and 4), placing a large portion of the drainage basins above the snow line even during interglacial periods. Furthermore, fluvial modification of glacial forms

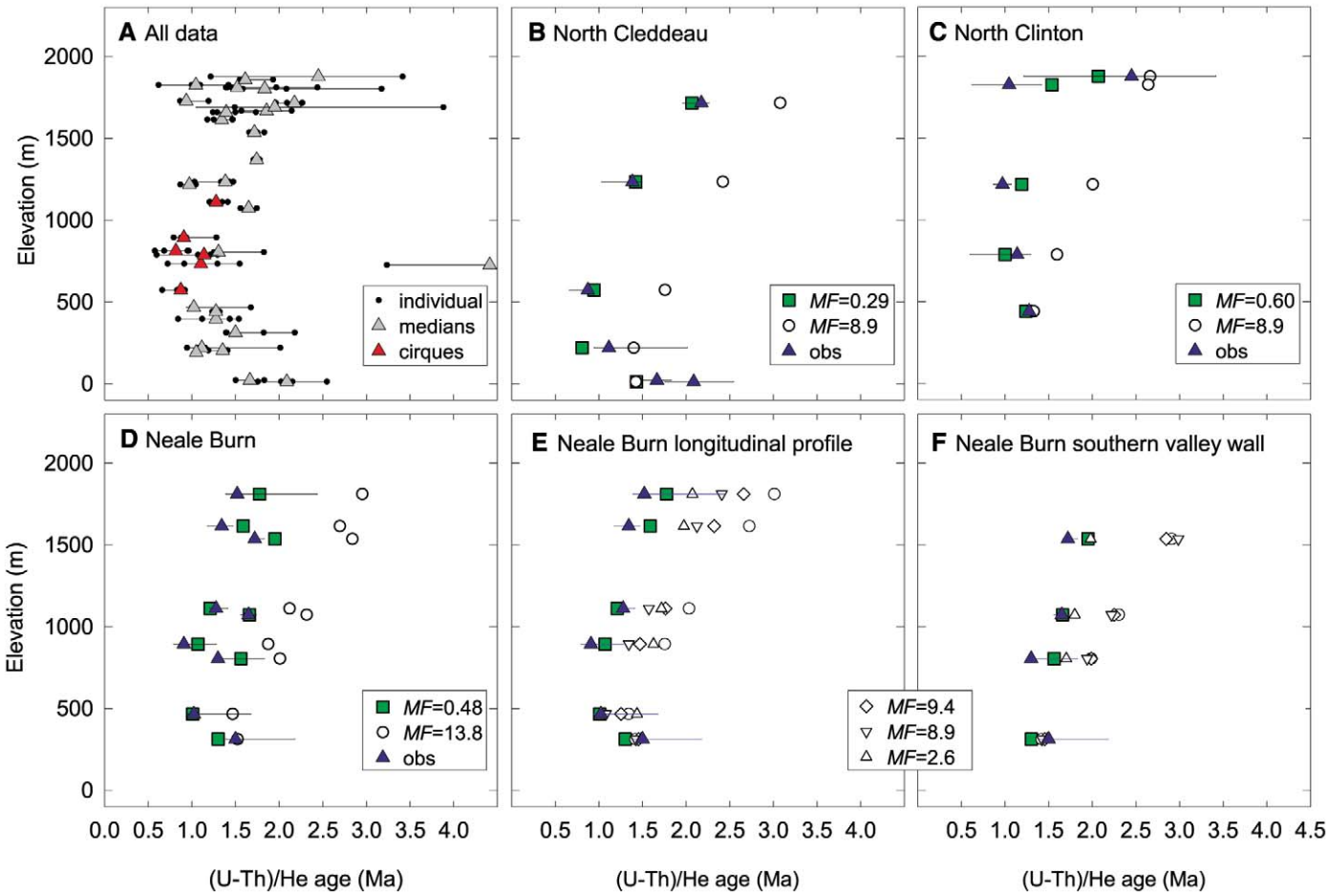

Fig. 2. Observed and modeled apatite (U-Th)/He ages and elevation relationships. (**A**) Observations for all Fiordland sample sites (Fig. 1). Both observations and modeled values are shown within (**B**) the North Branch Cleddeau, (**C**) the North Clinton, and (**D** to **F**) the Neale Burn drainages. Small black points are individual crystal ages; triangles and horizontal lines are the median age and range, respectively, observed for each sample. Squares are model ages predicted for the transient topographies illustrated in Figs. 3 and 4, calculated following (*13*) and (*14*), using each sample's crystal dimensions and U and Th concentrations. Open circles are model ages calculated instead with steady-state (modern) topography. By adjusting free parameters, steady-state models can match a subset of samples (the lowest-elevation ones in this case) but not all. Predicted ages from three alternative model classes are shown in (E) for samples along the axis of the Neale Burn drainage (NB15, NB16, NB18, NB21, NB04, and NB01), and (F) from its southern valley-wall transect (NB15, NB14, NB13, and NB12). To illustrate patterns, all models were calibrated to match the lowest-elevation sample; relative performance of the models is not sensitive to this choice (*8*). Open diamonds represent a proportional decrease in relief from 2.5 My ago to the present; fig. S3A shows the corresponding longitudinal profile evolution. The open downward triangles represent a continuous transition from a linear longitudinal profile (2.5 My ago) to the modern form; fig. S3B shows the profile evolution. The open upward triangles represent an extreme transition, between 1.75 and 0.75 My ago, from a 3-km plateau to the modern form; fig. S3C shows the profile evolution. MF is a misfit statistic calculated from the error-weighted differences between predicted and observed (U-Th)/He ages (*8*).

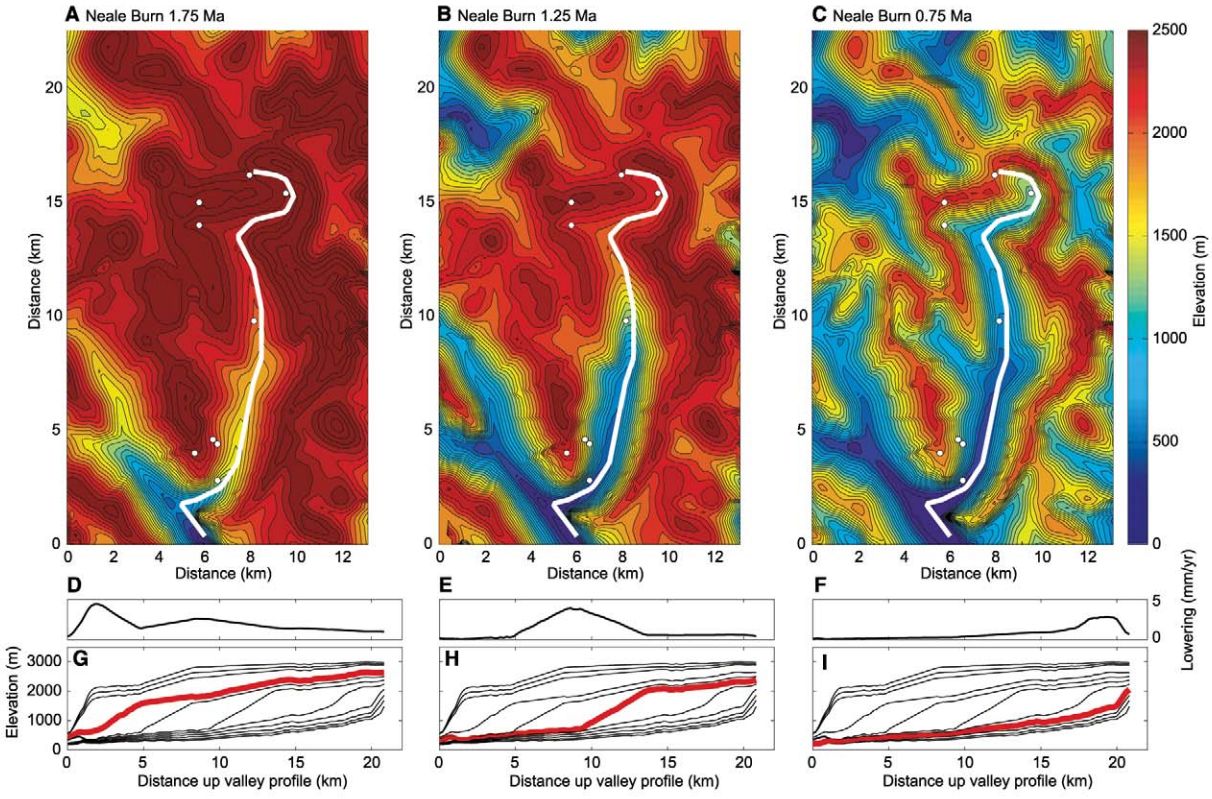

Fig. 3. Best-fit transient topographic scenario of headward erosion propagation along the Neale Burn drainage (domain outlined in Fig. 1). (**A** to **C**) The input topography at three representative model times (1.75, 1.25 and 0.75 My before the present, respectively). White points indicate sample locations, and white curves locate the longitudinal profiles shown in (**D** to **I**). (D) to (F) The local lowering rate (erosion rate minus uplift rate) along the profile, calculated for the preceding 250,000 years of each model time frame. (G) to (I) Model longitudinal profile evolution from 2.5 My ago to the present in 250,000-year intervals; red profiles correspond to time frames shown in (A) to (C). The high-elevation surfaces may represent the level of valley bottoms beneath a nearly isothermal relief.

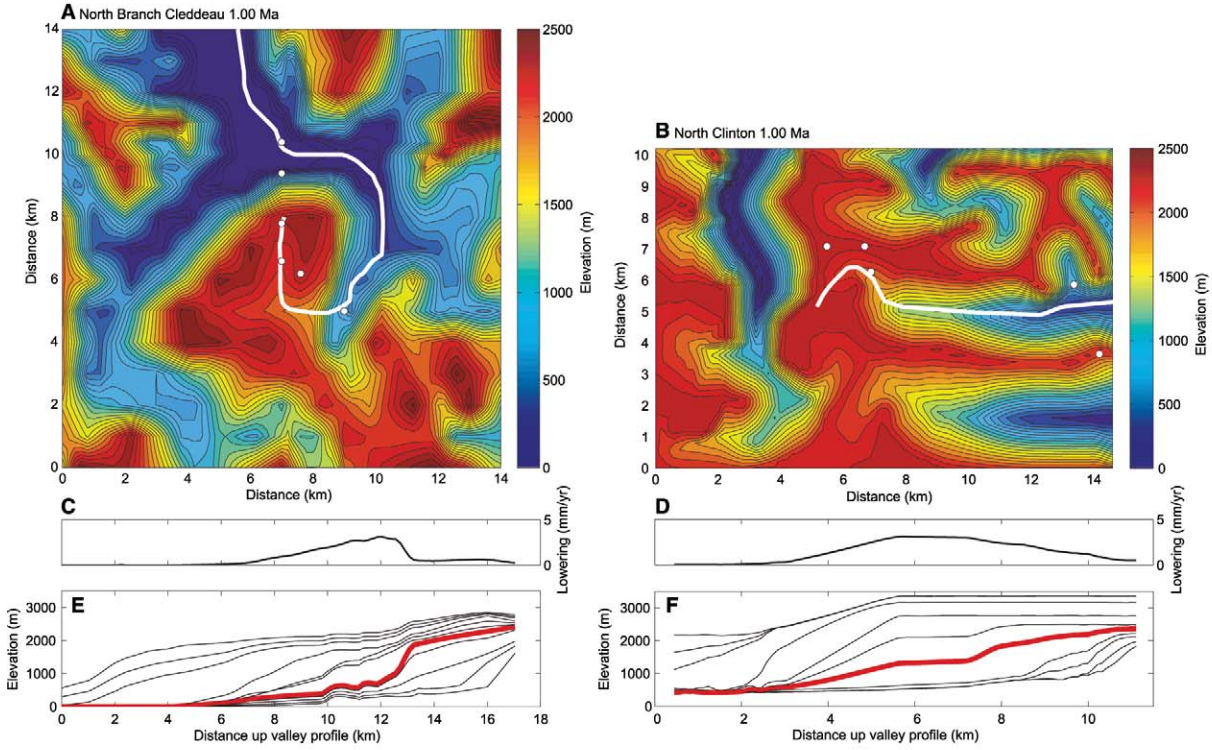

Fig. 4. Best-fit transient topographic scenarios of the North Branch Cleddeau and the North Clinton drainages. (**A** and **B**) The input topography shown at 1.00 My before the present for the model domains outlined in Fig. 1. As in Fig. 3, these models involve headward propagation of erosion along the longitudinal profile of each valley: the North Cleddeau (**C** and **E**) and the North Clinton (**D** and **F**). Panels and curve colors are as in Fig. 3.

during the Holocene has been minimal; features such as the abrupt step where the ~20-km^2 Bowen River basin joins Milford Sound indicate that rivers, even with large discharges and steep slopes, lack the capacity to incise the hard crystalline bedrock at high rates.

Glacial erosion by abrasion and quarrying occurs only if the ice slides along its bed. Theoretical treatments (*19*, *20*) indicate that erosion rate $\dot{e}$ increases with sliding velocity u_b; most simply, take $\dot{e} \propto u_b^r$, with r an unknown positive number. This suggests one origin for headward-propagating erosion in glacial valleys: Compared to more gently sloped sections upstream and downstream, a glacier flowing down a steep incline is thinner and faster, and hence more erosive. Simple calculations (*8*) imply that 10-fold contrasts in $\dot{e}$ along valley profiles (Figs. 3 and 4) most likely correspond to a parameter r value in the range ~1 to ~3. Others have proposed that feedbacks between quarrying, water pressure variability, and glacier geometry should cause up-valley propagation of subglacial bedrock steps with dimensions on the order of 10 to 100 m (*21*, *22*). The steep reaches associated with headward trending of erosion in Fiordland valleys are an order of magnitude larger. Valleys in our study region do display many steep bedrock facets with heights on the order of 100 m, but these features are too small to leave a record of propagation in the (U-Th)/He system.

Our thermochronometric data imply that large spatial variations of erosion rate determined the development of the Fiordland landscape. Our interpretation suggests that such variations arise from a glaciologically governed correlation between topography and sliding rate, together with a sliding-rate dependence of glacial erosion. A simple alternative approach to modeling glacial erosion—to use ice discharge as a proxy for erosion rate (*23*)—would not predict our observations because it precludes large contrasts of erosion rate over distances that are small compared to a glacier's length (except at special places such as tributary junctions).

Our results also suggest a landscape-scale target for model simulations. In Fiordland, the transition to Pleistocene climate initiated a massive reconfiguration of mountain range topography. Trunk valleys eroded rapidly at the outset, but their downstream portions have changed little in the past 1.5 My. By the mid-Pleistocene, erosion focused largely on drainage divides and valley heads, with decreasing area of high-elevation catchments. By 0.5 My ago, fundamental change had ceased, and average exhumation rates were the lowest in the Pleistocene. In essence, after the onset of glaciation, the mountain range was denuded from its flanks into its core and now changes only gradually. Thus, glaciation not only sculpted distinctive landforms but also systematically reshaped broad features of the range. Concerning debates about the response of mountain relief to glacial conditions (*24*), our study suggests that range-scale relief decreased during the Pleistocene, while local peak–to–valley floor relief increased transiently as erosion shifted headward.

References and Notes

1. A. Penck, *J. Geol.* **13**, 1 (1905).
2. D. E. Sugden, B. S. John, *Glaciers and Landscape* (Edward Arnold Publishers, London, 1976).
3. D. L. Egholm, S. B. Nielsen, V. K. Pedersen, J. E. Lesemann, *Nature* **460**, 884 (2009).
4. J. H. Tomkin, *Geomorphology* **103**, 180 (2009).
5. T. A. Ehlers, K. A. Farley, M. E. Rusmore, G. J. Woodsworth, *Geology* **34**, 765 (2006).
6. F. Herman, S. C. Cox, P. J. J. Kamp, *Tectonics* **28**, TC5011 (2009).
7. P. G. Valla, F. Herman, P. A. van der Beek, J. Braun, *Earth Planet. Sci. Lett.* **295**, 511 (2010).
8. Materials and methods are available as supporting material on *Science* Online.
9. A. L. Claypool *et al.*, *Tectonophysics* **359**, 329 (2002).
10. R. I. Walcott, *Rev. Geophys.* **36**, 1 (1998).
11. D. L. Shuster, K. A. Farley, J. M. Sisterson, D. S. Burnett, *Earth Planet. Sci. Lett.* **217**, 19 (2004).
12. T. F. Schildgen, G. Balco, D. L. Shuster, *Earth Planet. Sci. Lett.* **293**, 377 (2010).
13. J. Braun, *Comput. Geosci.* **29**, 787 (2003).
14. R. M. Flowers, R. A. Ketcham, D. L. Shuster, K. A. Farley, *Geochim. Cosmochim. Acta* **73**, 2347 (2009).
15. K. X. Whipple, *Annu. Rev. Earth Planet. Sci.* **32**, 151 (2004).
16. R. Bintanja, R. S. W. van de Wal, *Nature* **454**, 869 (2008).
17. S. C. Porter, *Quat. Res.* **32**, 245 (1989).
18. R. P. Suggate, *Quat. Sci. Rev.* **9**, 175 (1990).
19. B. Hallet, *Ann. Glaciol.* **2**, 23 (1981).
20. B. Hallet, *Ann. Glaciol.* **22**, 1 (1996).
21. R. B. Alley, *Geol. Soc. Am. Spec. Pap. 337* (1999), p. 1.
22. R. L. Hooke, *Geol. Soc. Am. Bull.* **103**, 1104 (1991).
23. R. S. Anderson, P. Molnar, M. A. Kessler, *J. Geophys. Res.* **111**, F01004 (2006).
24. K. X. Whipple, E. Kirby, S. H. Brocklehurst, *Nature* **401**, 39 (1999).

25. We thank Milford Helicopters, B. Lum, and the Caltech Noble Gas Lab for field and laboratory support; J. Braun and F. Herman for modeling guidance; and three anonymous referees for constructive comments. This work was supported by NSF grants EAR-0642869 (to D.L.S.) and EAR-0642830 (to K.M.C.) and by the Ann and Gordon Getty Foundation.

Supporting Online Material

www.sciencemag.org/cgi/content/full/332/6025/84/DC1
Materials and Methods
Figs. S1 to S7
Tables S1 to S3
References

28 September 2010; accepted 14 February 2011
10.1126/science.1198401

Microtomography of Partially Molten Rocks: Three-Dimensional Melt Distribution in Mantle Peridotite

Wenlu Zhu,[1]* Glenn A. Gaetani,[2] Florian Fusseis,[3] Laurent G. J. Montési,[1] Francesco De Carlo[4]

The permeability of the upper mantle controls melt segregation beneath spreading centers. Reconciling contradictory geochemical and geophysical observations at ocean ridges requires a better understanding of transport properties in partially molten rocks. Using x-ray synchrotron microtomography, we obtained three-dimensional data on melt distribution for mantle peridotite with various melt fractions. At melt fractions as low as 0.02, triple junctions along grain edges dominated the melt network; there was no evidence of an abrupt change in the fundamental character of melt extraction as melt fraction increased to 0.2. The porosity of the partially molten region beneath ocean ridges is therefore controlled by a balance between viscous compaction and melting rate, not by a change in melt topology.

The divergence of tectonic plates at oceanic spreading centers induces upwelling and melting of underlying mantle peridotite. The buoyant magmas rise through the mantle and are focused toward the ridge axis, forming new oceanic crust (*1*, *2*). Although up to 20% of the original peridotite may melt in this manner (*3*), melt extraction is efficient enough that only 1 to 3% porosity is observed in geophysical data sets (*4*, *5*). Broad regions of low seismic velocity detected under ridges imply that the mantle is relatively impermeable with a porosity of ~0.02 (*4*). However, geochemical data on mid-ocean ridge basalts (MORBs) indicate that once magma is formed, it segregates very efficiently from the residual peridotite (*6*, *7*). In particular, U-series disequilibria in MORB (*8*–*11*) imply a well-connected permeable mantle that allows efficient extraction of melt fractions lower than 0.01.

Although thermodynamic models of textural equilibrium predict that melt resides in channels along grain edges (i.e., triple junctions) (*12*, *13*), observations of synthetic olivine-basalt aggregates suggest that melt is present both in grain edge channels and as grain boundary films (*14*, *15*). If grain edge melt channels are few at melt fractions $\phi < 0.02$ and they are connected via grain boundary melt films (*15*), the less permeable films may limit the overall permeability at low porosity (*14*). At $\phi > 0.02$, channels become directly interconnected and permeability increases by several orders of magnitude (*14*). However, this model is based on two-dimensional

[1]Department of Geology, University of Maryland, College Park, MD 20742, USA. [2]Department of Geology and Geophysics, Woods Hole Oceanographic Institution, Woods Hole, MA 02543, USA. [3]Western Australian Geothermal Centre of Excellence, The University of Western Australia, Crawley, Australia. [4]Advanced Photon Source, Argonne National Laboratory, Argonne, 60439, USA.

*To whom correspondence should be addressed. E-mail: wzhu@umd.edu

(2D) images of melt distribution. Relying on 2D microstructure to infer quantitative information on 3D melt connectivity inevitably introduces ambiguity (*14*–*17*), especially at low melt fractions. Several studies, based on 2D microstructure, indicate the existence of interconnected triple junctions of melt down to 1% (*16*, *17*). Melt connectivity can also be determined experimentally on analog systems (*18*, *19*) but with the caveat that the applicability to olivine-basalt systems is unknown.

To overcome the limitations of 2D data, we characterized the 3D melt distribution in experimentally produced olivine-basalt aggregates (*20*) using x-ray synchrotron microtomography. This nondestructive imaging technique has a spatial resolution of 0.7 μm, allowing us to image melt distribution at low melt fractions and to characterize melt distribution over a large representative volume.

The 3D reconstructions reveal that melt channels form an interconnected network along grain edges at all melt fractions from 0.02 to 0.20 (Fig. 1 and movie S1), in good agreement with theoretical predictions for isotropic systems (*12*, *13*). However, melt distribution in olivine-basalt aggregates is more complex than expected in that the interconnected melt network is nonuniform. At $\phi = 0.10$ and 0.20, melt wets both grain edges and a large proportion of the grain boundaries (Fig. 1, C and D). At $\phi = 0.05$, melt recedes from grain boundaries and resides primarily along triple junctions (Fig. 1B). At $\phi = 0.02$, while melt films are observed along a small number of grain boundaries, consistent with previous 2D melt distribution studies (*15*), a network of directly interconnected melt channels is evident (Fig. 1A). Although our imaging techniques cannot resolve melt films down to nanometer thickness (*15*), the existence of an interconnected network of melt channels in all our samples implies that permeability of the olivine-basalt system is unlikely to deviate considerably from the power-law permeability-porosity relationships (*13*, *19*), even at $\phi = 0.02$.

The connectivity of the melt network was analyzed with a skeletonization algorithm that systematically reduces cross sections orthogonal to melt channels to their center points. The lines at the center of melt channels and the nodes where these lines meet define the skeleton (*21*). Skeletons from all four samples demonstrate that melt in triple junctions forms an interconnected network (Fig. 2).

The coordination number—number of connections to neighboring nodes—of each node quantifies network connectivity (Fig. 3). At $\phi = 0.05$, nodes with coordination numbers of 4 are most abundant, in agreement with theoretical predictions (*12*, *13*); the melt network is dominated by channels along triple junctions at the edge of grains, which terminate at the junction between four grains. At $\phi = 0.02$, nodes with coordination numbers of 1 or 3 are more abundant than nodes with coordination 4, which is likely an artifact of resolution limits; a detailed examination of the melt network reveals that a large number of melt channels are identified only intermittently by the skeletonization algorithm and appear broken. The abundance of nodes with coordination numbers of 3 in samples with $\phi = 0.10$ and 0.20 represents the limitation of the skeletonization algorithm in separating melt channels within the large melt pool at grain corners (*21*). Notwithstanding these artifacts, our data show little evidence for isolated triple junctions where melt films dictate the melt connectivity from 0.02 to 0.20.

Because percolation through melt channels along grain edges is more effective than through melt films along grain boundaries (*22*), the power-law relation between melt fraction and permeability (*13*, *19*) remains a good approximation for olivine-basalt systems down to $\phi = 0.02$ and perhaps lower. In this model, the permeability (k) of olivine-basalt systems depends on melt fraction (ϕ) and grain size (d):

$$k = \frac{\phi^n d^2}{C} \quad (1)$$

where C is a geometrical factor (*13*). For an isotropic system, $n = 2$ and $C \sim 1600$ to 3000 have been derived numerically (*13*, *23*). Empirical relationships with values of $n \approx 3$ and $C \approx 10$ to 270 were inferred from experimental data (*19*, *24*). The heterogeneous melt distribution observed in this study implies that $n = 3$ provides a better permeability estimate (*22*, *24*). For $d = 3$ mm and $\phi = 0.02$, $k \sim 10^{-12}$ m^2 (*13*, *22*).

Melt ascent velocity (v) beneath a mid-ocean ridge is given by

$$v = \frac{k\,\Delta\rho\,g}{\phi\,\eta} \quad (2)$$

where $\Delta\rho \sim 300$ kg m^{-3} is the density contrast between melt and solid mantle, $g \sim 10$ m s^{-2} is the acceleration of gravity, and $\eta \sim 10$ Pa s is the viscosity of basaltic melts at their liquidus. As a result, $v \sim 50$ cm/year. Thorium disequilibrium in MORB (*9*, *10*) can only be preserved if melt velocities are one or two orders of magnitude greater than this estimate, which can be explained by a lower C (*24*), larger grain size, reduced pyroxene content (*22*), or $\phi > 0.05$. Accurate assessments of the transport properties of the upper mantle require better understanding of 3D melt distribution in systems more complex than the simple olivine-basalt aggregates. For such systems, no simple permeability relationships could account for the grain scale compexity. The lattice Boltzmann method that incorporates high-resolution 3D microstructural data provides an effective numerical approach for simulating fluid flow (*25*, *26*).

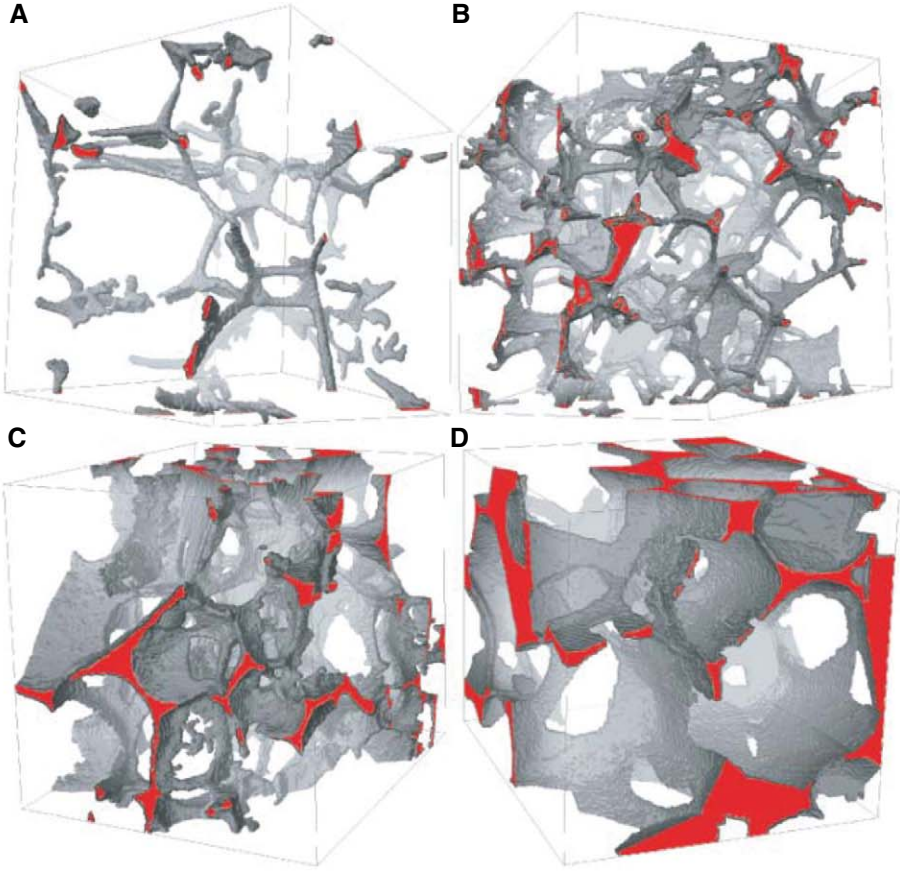

Fig. 1. Three-dimensional melt distribution of olivine-basalt aggregates. The size of each cube is 140 μm by 140 μm by 140 μm. The melt volume fractions are (**A**) 0.02, (**B**) 0.05, (**C**) 0.10, and (**D**) 0.20. Gray represents the interfaces between melt and olivine crystals; red represents the interior of melt channels. The hollow space is where olivine crystals reside. Interconnected melt channels along grain edges are observed in all four samples.

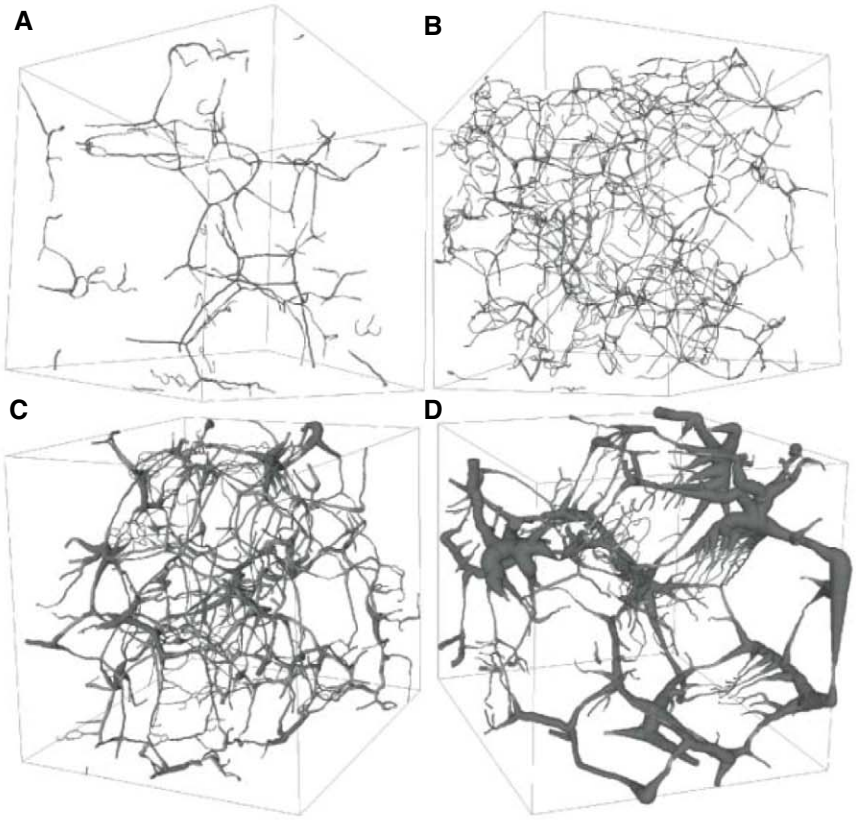

Fig. 2. Interconnectivity of melt channels in olivine-basalt aggregates with melt fractions of (**A**) 0.02, (**B**) 0.05, (**C**) 0.10, and (**D**) 0.20. The thickness of the channels is scaled to the actual size of the melt channel width. The multifurcation of channels along grain boundaries is an indication that the AVIZO skeletonization program (*21*) breaks down at grain boundary residing melt.

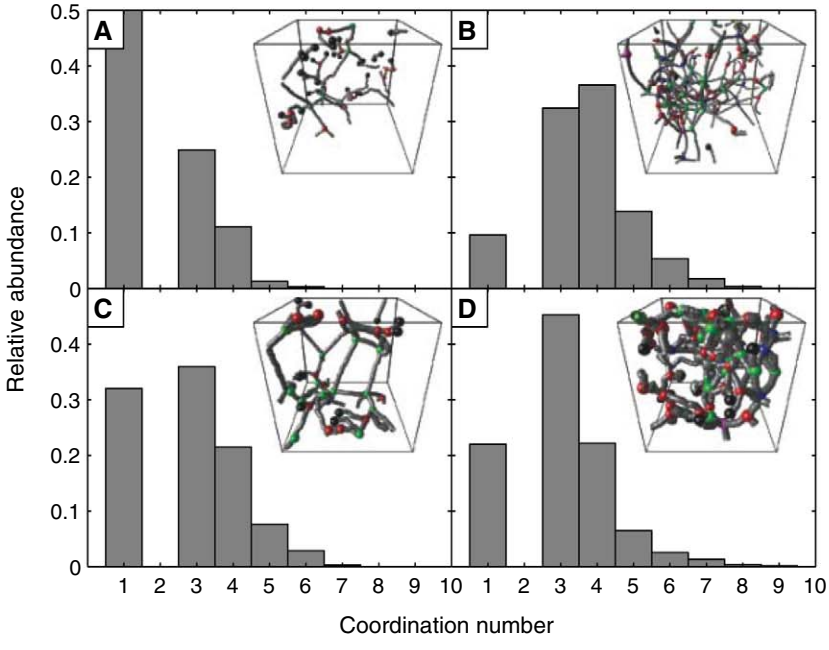

Fig. 3. Histogram of connectivity for samples with melt fraction of (**A**) 0.02 (m = 731), (**B**) 0.05 (m = 2622), (**C**) 0.10 (m = 1211), and (**D**) 0.20 (m = 875), where m is the number of nodes present in the simplified skeleton. The insets display a representative volume of the idealized network (bounding box is 100 μm by 100 μm by 100 μm) with melt channels shown as gray tubes and nodes as spheres color-coded for connectivity: 1, black; 3, red; 4, green; 5, blue; 6, magenta; 7 and above, yellow.

Regardless, no homogeneous permeability model can explain the observed negative correlation between the (^{230}Th/^{238}U) and (^{226}Ra/^{230}Th) activity ratios (*11*). Thus, it is likely that melt transport in the partially molten mantle features strong channelization (*27*–*29*). The existence of two simultaneous melt extraction networks makes it possible to reconcile geochemical and geophysical constraints on melt extraction at mid-ocean ridges. Trace-element depletions (*6*, *27*, *28*) and (^{230}Th/^{238}U) activity ratios (*7*) reflect transport in high-permeability channels, whereas (^{226}Ra/^{230}Th) activity ratios (*30*), seismic data (*4*), and electromagnetic (*5*) data are sensitive to a slower, diffuse, low-porosity mode of transport. Even with ϕ as low as 0.01, melt extraction velocities far exceed mantle upwelling velocity. Thus, the mantle is efficiently drained and its porosity is controlled by a balance between compaction viscosity (*24*) and melting rate (*31*), not by a transition in permeability-porosity relationship.

References and Notes

1. D. W. Sparks, E. M. Parmentier, *Geophys. J. Int.* **112**, 81 (1993).
2. L. B. Hebert, L. G. J. Montési, *Geochem. Geophys. Geosyst.* **11**, Q12008 (2010).
3. P. D. Asimow, M. M. Hirschmann, M. S. Ghiorso, M. J. O'Hara, E. M. Stolper, *Geochim. Cosmochim. Acta* **59**, 4489 (1995).
4. T. M. S. Team; The MELT Seismic Team, *Science* **280**, 1215 (1998).
5. R. L. Evans *et al.*, *Science* **286**, 752 (1999).
6. E. M. Klein, C. H. Langmuir, *J. Geophys. Res.* **92** (B8), 8089 (1987).
7. A. V. Sobolev, N. Shimizu, *Nature* **363**, 151 (1993).
8. M. Spiegelman, T. Elliott, *Earth Planet. Sci. Lett.* **118**, 1 (1993).
9. C. C. Lundstrom, J. B. Gill, Q. Williams, M. R. Perfit, *Science* **270**, 1958 (1995).
10. D. P. McKenzie, *Chem. Geol.* **162**, 81 (2000).
11. K. W. W. Sims *et al.*, *Geochim. Cosmochim. Acta* **66**, 3481 (2002).
12. C. S. Smith, *Metall. Rev.* **9**, 1 (1964).
13. N. von Bargen, H. S. Waff, *J. Geophys. Res.* **91** (B9), 9261 (1986).
14. U. H. Faul, *Nature* **410**, 920 (2001).
15. M. Cmíral, J. D. Fitz Gerald, U. H. Faul, D. H. Green, *Contrib. Mineral. Petrol.* **130**, 336 (1998).
16. D. A. Wark, C. A. Williams, E. B. Watson, J. D. Price, *J. Geophys. Res.* **108**, 2050 (2003).
17. M. J. Daines, F. M. Richter, *Geophys. Res. Lett.* **15**, 1459 (1988).
18. D. Laporte, E. B. Watson, *J. Geol.* **99**, 873 (1991).
19. D. A. Wark, E. B. Watson, *Earth Planet. Sci. Lett.* **164**, 591 (1998).
20. Synthetic olivine-basalt aggregates with melt fractions of 0.02, 0.05, 0.10, and 0.20 were equilibrated at 1.5 GPa and 1350°C (*21*).
21. Materials and methods are available as supporting material on *Science* Online.
22. W. Zhu, G. Hirth, *Earth Planet. Sci. Lett.* **212**, 407 (2003).
23. M. J. Cheadle, M. T. Elliott, D. P. McKenzie, *Geology* **32**, 757 (2004).
24. J. A. D. Connolly, M. W. Schmidt, G. Solferino, N. Bagdassarov, *Nature* **462**, 209 (2009).
25. O. van Genabeek, D. H. Rothman, *Annu. Rev. Earth Planet. Sci.* **24**, 63 (1996).
26. J. T. Fredrich, A. A. DiGiovanni, D. R. Noble, *J. Geophys. Res.* **111** (B3), B03201 (2006).
27. S. R. Hart, *Proc. Natl. Acad. Sci. U.S.A.* **90**, 11914 (1993).
28. P. B. Kelemen, N. Shimizu, V. J. M. Salters, *Nature* **375**, 747 (1995).
29. B. K. Holtzman *et al.*, *Science* **301**, 1227 (2003).

30. M. Jull, P. B. Kelemen, K. W. W. Sims, *Geochim. Cosmochim. Acta* **66**, 4133 (2002).
31. M. Spiegelman, D. McKenzie, *Earth Planet. Sci. Lett.* **83**, 137 (1987).
32. This work is supported by NSF-EAR 0753505 (W.Z. and G.A.G.) and NSF-OCE 0937277 (L.G.J.M.). F.F. was supported by the Western Australian State Government through the Premier's Fellowship Program and the Australian Synchrotron Research Program, funded by the Commonwealth of Australia under the Major National Research Facilities Program. Use of the Advanced Photon Source was supported by the U.S. Department of Energy, Office of Science, Office of Basic Energy Sciences, under contract DE-AC02-06CH11357. We thank X. Xiao and J. Liu for their assistance. We furthermore acknowledge the Centre for Microscopy, Characterisation and Analysis for use of an electron microprobe and iVEC for use of their data storage and visualization facilities.

Supporting Online Material
www.sciencemag.org/cgi/content/full/332/6025/88/DC1
Materials and Methods
Figs. S1 to S3
References
Movie S1

27 December 2010; accepted 16 February 2011
10.1126/science.1202221

Selective Inhibition of a Regulatory Subunit of Protein Phosphatase 1 Restores Proteostasis

Pavel Tsaytler,[1] Heather P. Harding,[2] David Ron,[2] Anne Bertolotti[1]*

Many biological processes are regulated through the selective dephosphorylation of proteins. Protein serine-threonine phosphatases are assembled from catalytic subunits bound to diverse regulatory subunits that provide substrate specificity and subcellular localization. We describe a small molecule, guanabenz, that bound to a regulatory subunit of protein phosphatase 1, PPP1R15A/GADD34, selectively disrupting the stress-induced dephosphorylation of the α subunit of translation initiation factor 2 (eIF2α). Without affecting the related PPP1R15B-phosphatase complex and constitutive protein synthesis, guanabenz prolonged eIF2α phosphorylation in human stressed cells, adjusting the protein production rates to levels manageable by available chaperones. This favored protein folding and thereby rescued cells from protein misfolding stress. Thus, regulatory subunits of phosphatases are drug targets, a property used here to restore proteostasis in stressed cells.

The unfolded protein response (UPR) (*1*–*3*) is a component of the proteostasis network (*4*) that adapts folding in the endoplasmic reticulum (ER) to changing conditions. Upstream components of the UPR are the ER-resident transmembrane proteins IRE1, ATF6, and PERK, which sense folding defects to reprogram transcription and translation in a concerted manner and restore proteostasis. Activated IRE1 and ATF6 increase the transcription of genes involved in ER folding, such as those encoding the chaperones BiP and GRP94. Activated PERK attenuates global protein synthesis by phosphorylating the α subunit of translation initiation factor 2 (eIF2α) on Ser^{51} while promoting translation of the transcription factor ATF4. The latter controls expression of CHOP, another transcription factor, which in turn promotes expression of *Ppp1r15a/Gadd34* (*2*, *3*). PPP1R15A, an effector of a negative feedback loop that terminates UPR signaling, recruits a catalytic subunit of protein phosphatase 1 (PP1c) to dephosphorylate eIF2α, allowing protein synthesis to resume (*5*). UPR failure contributes to many pathological conditions (*6*) that might be corrected by adequate boost of this adaptive response.

Guanabenz, an α_2-adrenergic receptor agonist used in the treatment of hypertension (*7*), shows anti-prion activity (*8*). We decided to assess whether guanabenz had broader activity in protecting against detrimental accumulation of misfolded proteins. Indeed, guanabenz protected against the lethal effects of expression of misfolding-prone $insulin^{Akita}$ (*9*, *10*) in the ER of mouse Min6 and rat INS-1 pancreatic beta cells (Fig. 1, A and B). Guanabenz also promoted the survival of HeLa cells exposed to cytotoxic ER stress induced by tunicamycin in a dose-dependent manner (Fig. 1C), with a median effective concentration of ~0.4 μM (Fig. 1D). Unlike guanabenz, the α_2-adrenergic receptor agonist clonidine and the receptor antagonist efaroxan were without effect on the survival of tunicamycin-stressed cells (fig. S1). Thus, guanabenz rescued cells from lethal ER stress by a mechanism independent of the α_2-adrenergic receptor.

We next measured the effect of guanabenz on the different branches of the UPR. Unlike tunicamycin, 50 μM guanabenz did not increase the levels of the UPR targets GRP94, BiP, ATF4, and CHOP (Fig. 2A), nor did it decrease protein synthesis (Fig. 2B). Thus, guanabenz on its own did not induce the UPR or inhibit the translation machinery. Next, we examined the effect of guanabenz in stressed cells. Attenuation of translation and increased eIF2α phosphorylation, observed 2 hours after addition of tunicamycin,

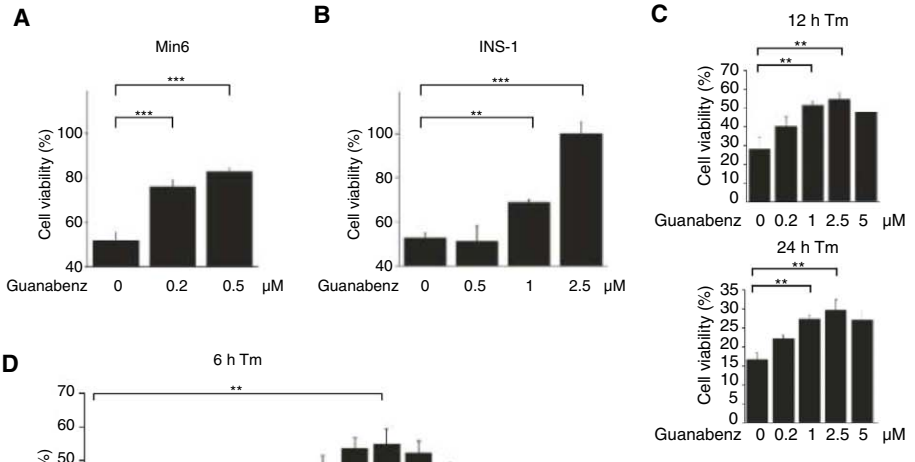

Fig. 1. Guanabenz protects cells from deleterious accumulation of misfolded proteins in the endoplasmic reticulum. (**A**) Assessment of the number of viable, blasticidin-resistant Min6 cells, after transduction with blasticidin resistance (blst)–tagged lentiviruses encoding a misfolding-prone fusion of $insulin^{Akita}$ with green fluorescent protein (GFP) (*10*), treated with the indicated concentrations of guanabenz. Values, corresponding to the cells' ability to reduce WST-8 into formazan, were normalized to those of cells transduced with blst-tagged lentiviruses encoding cytoplasmic GFP. (**B**) Same as (A) with INS-1 cells. (**C**) Viability of HeLa cells assessed by the reduction of WST-8 [2-(2-methoxy-4-nitrophenyl)-3-(4-nitrophenyl)-5-(2,4-disulfophenyl)-2*H*-tetrazolium] into formazan, after treatments with tunicamycin (2.5 μg/ml; Tm) for 12 or 24 hours, with or without the indicated concentrations of guanabenz. (**D**) Dose-dependent protection of HeLa cells by guanabenz, from ER stress induced by 6 hours of exposure to tunicamycin. Data are means ± SD ($n = 4$). $^{**}P \leq 0.001$; $^{***}P \leq 0.0001$.

[1]MRC Laboratory of Molecular Biology, Hills Road, Cambridge CB2 0QH, UK. [2]Institute of Metabolic Sciences, University of Cambridge, Cambridge CB2 0QQ, UK.

*To whom correspondence should be addressed. E-mail: aberto@mrc-lmb.cam.ac.uk

were not altered by guanabenz (Fig. 2, C and D); this result shows that guanabenz did not directly antagonize tunicamycin. As previously reported (*11*), recovery of translation was evident 5 hours after addition of tunicamycin (Fig. 2, B and C). Guanabenz markedly delayed this translational recovery (Fig. 2C and fig. S2), sustained eIF2α phosphorylation in stressed cells, and attenuated tunicamycin-induced expression of the ER stress markers analyzed, including the pro-apoptotic protein CHOP (Fig. 2D).

Sustained translation attenuation caused by guanabenz during ER stress is likely to increase the ratio of chaperones to substrates and favor protein folding. Indeed, the abundance of tunicamycin-induced high–molecular weight complexes, containing the ER chaperone BiP engaged with misfolded proteins (*12*), was markedly reduced by guanabenz (Fig. 2E). Thus, guanabenz acted like a proteostasis regulator (*4*) by lowering protein misfolding in stressed cells.

Two related regulatory proteins, the stress-inducible PPP1R15A/GADD34 (*11*) and the constitutively expressed PPP1R15B/CReP (*13*), recruit PP1c to form heterodimeric phosphatases that dephosphorylate eIF2α. The effects of guanabenz on stressed cells were reminiscent of those observed after ablation of *Ppp1r15a* (*11*). Analysis of the PPP1R15A-PP1c phosphatase complex revealed that PP1c was recovered in PPP1R15A immunoprecipitates from lysates of tunicamycin-treated cells, but not when cells had also been treated with guanabenz (Fig. 3A). Guanabenz similarly disrupted the complex between endogenous PP1c and overexpressed tagged PPP1R15A, whereas the related complex containing the constitutive regulatory subunit PPP1R15B remained intact (Fig. 3B). This explains why guanabenz delayed recovery of protein synthesis in stressed cells without inhibiting translation in unstressed cells not expressing PPP1R15A (Fig. 2, B and C). Guanabenz also disrupted the isolated PPP1R15A-PP1c phosphatase complex in a dose-dependent manner (Fig. 3C). Complete dissociation of all PPP1R15A-PP1c complexes in vitro occurred at higher concentrations of guanabenz than those required for cytoprotection (Figs. 1C and 3C). Thus, it appears likely that cytoprotection by guanabenz required dissociation of only a fraction of the PPP1R15A-PP1c complexes. Unlike calyculin A, which inhibits the catalytic activity of PP1c and is toxic to cells (*14*), guanabenz had no effect on the phosphatase activity of the isolated catalytic subunit (fig. S3) and was not toxic at the concentrations required to protect cells from protein misfolding (Fig. 1C). Thus, guanabenz did not inhibit PP1c directly.

To identify the target of guanabenz, we synthesized a biotinylated form (fig. S4A) with cytoprotective activity similar to that of the non-biotinylated form (fig. S4B). When immobilized on neutravidin agarose beads, biotinylated guanabenz captured PPP1R15A but not PPP1R15B (Fig. 3, D and E), thus establishing that it selectively targeted PPP1R15A. Biotinylated guanabenz bound to a C-terminal fragment of $PPP1R15A^{230–674}$ containing the PP1c binding site (Fig. 3F). A recombinant $PPP1R15A^{230–674}$ fragment also bound to guanabenz, demonstrating a direct interaction between guanabenz and PPP1R15A (Fig. 3F).

The lack of both inducible and constitutive eIF2α phosphatases encoded by *Ppp1r15a* and *Ppp1r15b* is lethal in mice (*15*). Thus, inhibiting PPP1R15A in cells lacking *Ppp1r15b* should eliminate all eIF2α phosphatase activity and also be lethal. Indeed, guanabenz compromised survival of mouse embryonic fibroblasts (MEFs) lacking *Ppp1r15b* (Fig. 4A). However, exposure to

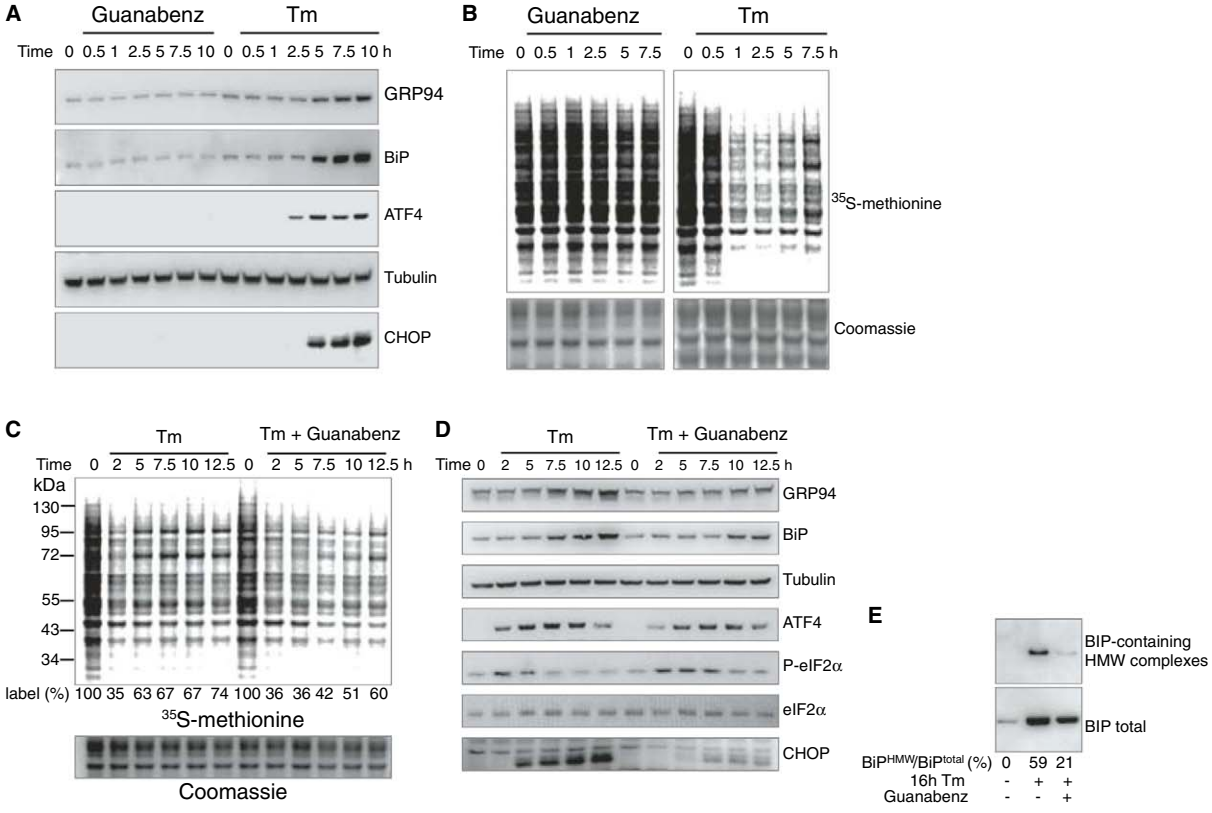

Fig. 2. Guanabenz increases chaperone availability by attenuating translation recovery after ER stress. (**A**) Immunoblot of the indicated proteins in lysates of HeLa cells treated with guanabenz (50 μM) or Tm (2.5 μg/ml; Tm) for the indicated times. (**B**) Autoradiogram of [^{35}S]methionine-labeled proteins in cell lysates resolved by NuPage after a 10-min labeling pulse of HeLa cells exposed to guanabenz (50 μM) or Tm (2.5 μg/ml) for the indicated times. Lower panel is a photomicrograph of the Coomassie-stained gel. (**C**) Same as (B) except that cells were treated with Tm in the presence or absence of guanabenz. (**D**) Immunoblots of HeLa cell lysates from cells treated with tunicamycin (2.5 μg/ml) in the presence or absence of guanabenz (50 μM) for the indicated times. (**E**) Immunoblots of BiP recovered in SDS-resistant high–molecular weight (HMW) complexes (*12*) or in the total cell lysates from HeLa cells left untreated or treated with tunicamycin in the presence or absence of guanabenz. Representative results of three independent experiments are shown.

guanabenz had no measurable effect on the viability of wild-type MEFs, or MEFs lacking a functional allele of *Ppp1r15a*, at concentrations that protected against protein misfolding. To further validate that guanabenz rescued cells from misfolding stress by targeting PPP1R15A, we assessed whether guanabenz could protect cells lacking PPP1R15A activity from lethal ER stress (*11*). Although it protected wild-type MEFs from ER stress, guanabenz had no protective effect in MEFs lacking PPP1R15A activity (Fig. 4B). Thus, all the measurable cytoprotective activity of guanabenz in ER stressed cells resulted from its inhibition of PPP1R15A.

Our results show that specific phosphatases can be inhibited by targeting their regulatory subunits and that selective inhibition of PPP1R15A protects cells from the otherwise lethal accumu-

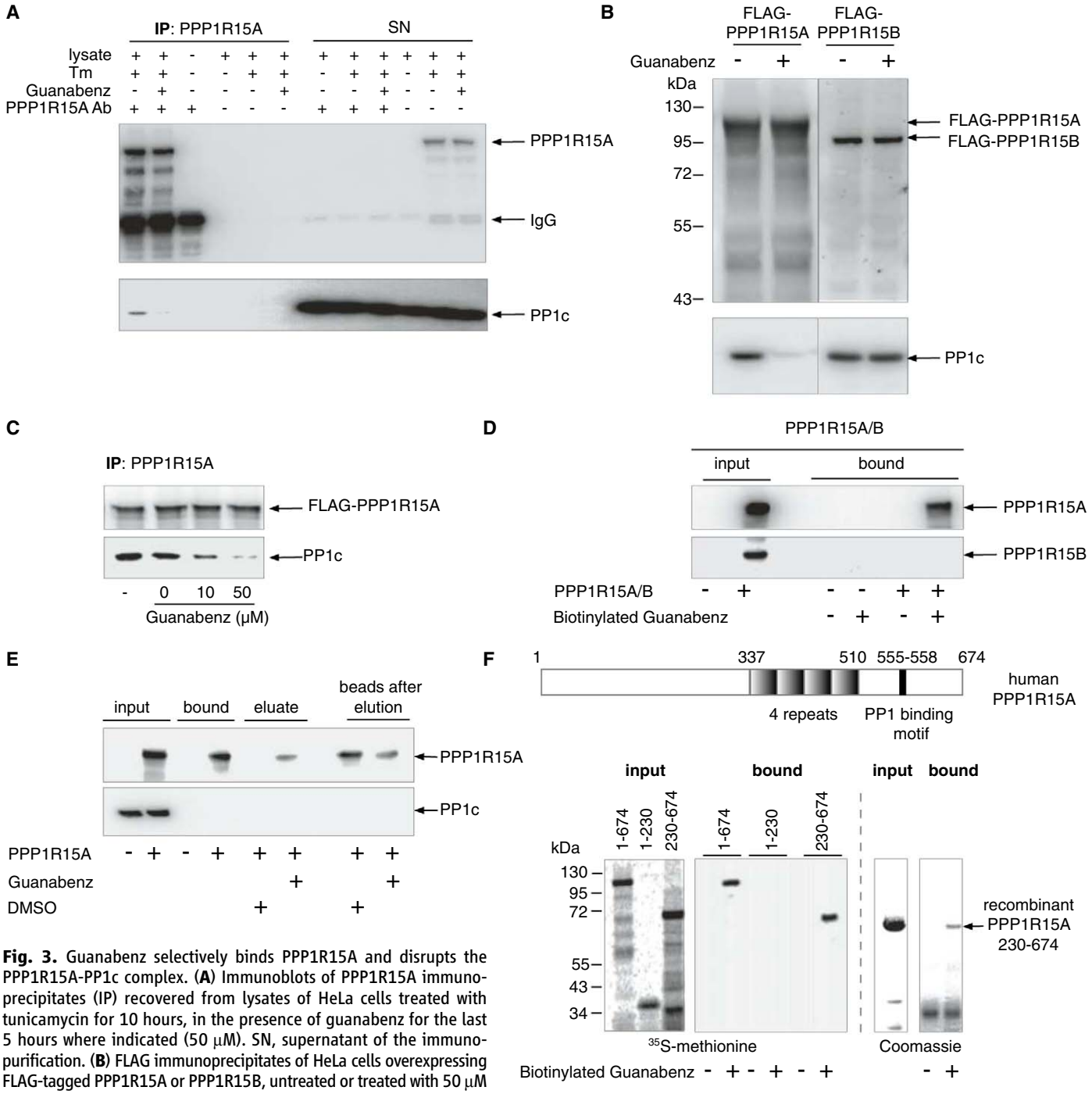

Fig. 3. Guanabenz selectively binds PPP1R15A and disrupts the PPP1R15A-PP1c complex. (**A**) Immunoblots of PPP1R15A immunoprecipitates (IP) recovered from lysates of HeLa cells treated with tunicamycin for 10 hours, in the presence of guanabenz for the last 5 hours where indicated (50 μM). SN, supernatant of the immunopurification. (**B**) FLAG immunoprecipitates of HeLa cells overexpressing FLAG-tagged PPP1R15A or PPP1R15B, untreated or treated with 50 μM guanabenz for 6 hours, analyzed by immunoblotting. (**C**) FLAG-PPP1R15A immunoprecipitates from unstressed HeLa cells, washed with indicated concentrations of guanabenz and analyzed by immunoblotting. (**D**) Immunoblots showing that PPP1R15A but not PPP1R15B, expressed in rabbit reticulocyte lysate (input), selectively bound to biotinylated guanabenz immobilized on neutravidin beads. (**E**) In vitro translated PPP1R15A bound biotinylated guanabenz immobilized on neutravidin beads eluted with 1 mM guanabenz. Immunoblots show inputs, eluates, and beads before and after elution. Note that PP1c did not bind to the biotinylated guanabenz. (**F**) Top: Schematics of human PPP1R15A. Lower left: Same as (D) except that proteins were in vitro translated in the presence of [^{35}S]methionine and revealed by phosphorimaging. Lower right: Coomassie-stained gel showing bacterially expressed and purified PPP1R15A$^{230–674}$ fragment (input) selectively retained on neutravidin beads in the presence of biotinylated guanabenz (bound). Representative results of at least three independent experiments are shown in each panel.

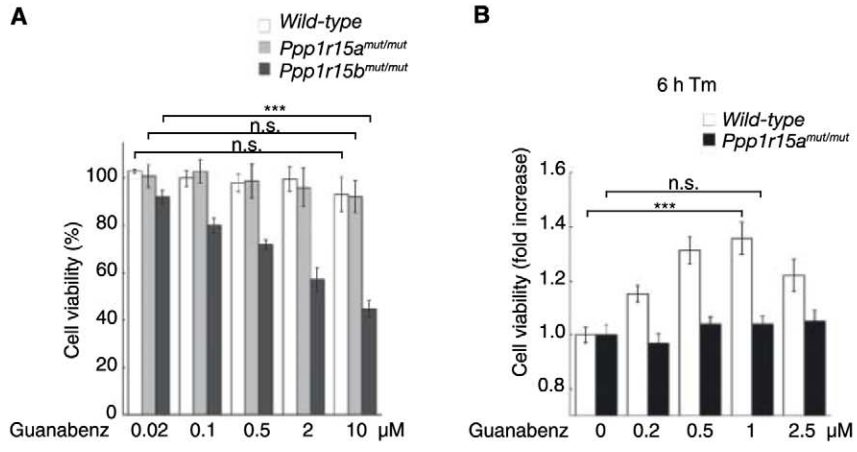

Fig. 4. The ER stress–cytoprotective activity of guanabenz is mediated by inhibition of PPP1R15A. (**A**) Viability of wild-type MEFs or mutant cells (*mut/mut*) lacking PPP1R15A or PPP1R15B activity after exposure to the indicated concentrations of guanabenz for 48 hours. Data are means ± SD ($n = 4$). ***$P \leq 0.0001$; n.s., not significant. (**B**) Viability of wild-type or *Ppp1r15a* mutant (*mut/mut*) MEFs exposed to tunicamycin (1 μg/ml; Tm) for 6 hours with the indicated concentrations of guanabenz, assessed by the ability to reduce WST-8 into formazan. The reducing activity of cells of either genotype exposed to tunicamycin without guanabenz was normalized to 1.

lation of misfolded proteins in the ER. Guanabenz inhibits PPP1R15A and tunes translation in stressed cells to levels manageable by the available chaperones, while sparing PPP1R15B, thereby avoiding intolerable levels of eIF2α phosphorylation (*15*) and deleteriously low levels of protein synthesis (fig. S5). This approach to correcting proteostasis defects by inhibition of PPP1R15A could benefit many conditions characterized by the accumulation of misfolded proteins.

References and Notes

1. D. Ron, P. Walter, *Nat. Rev. Mol. Cell Biol.* **8**, 519 (2007).
2. D. T. Rutkowski, R. J. Kaufman, *Trends Cell Biol.* **14**, 20 (2004).
3. K. Mori, *J. Biochem.* **146**, 743 (2009).
4. W. E. Balch, R. I. Morimoto, A. Dillin, J. W. Kelly, *Science* **319**, 916 (2008).
5. I. Novoa, H. Zeng, H. P. Harding, D. Ron, *J. Cell Biol.* **153**, 1011 (2001).
6. I. Kim, W. Xu, J. C. Reed, *Nat. Rev. Drug Discov.* **7**, 1013 (2008).
7. B. Holmes, R. N. Brogden, R. C. Heel, T. M. Speight, G. S. Avery, *Drugs* **26**, 212 (1983).
8. D. Tribouillard-Tanvier *et al.*, *PLoS One* **3**, e1981 (2008).
9. J. Wang *et al.*, *J. Clin. Invest.* **103**, 27 (1999).
10. M. Liu, I. Hodish, C. J. Rhodes, P. Arvan, *Proc. Natl. Acad. Sci. U.S.A.* **104**, 15841 (2007).
11. I. Novoa *et al.*, *EMBO J.* **22**, 1180 (2003).
12. S. J. Marciniak *et al.*, *Genes Dev.* **18**, 3066 (2004).
13. C. Jousse *et al.*, *J. Cell Biol.* **163**, 767 (2003).
14. A. McCluskey, A. T. Sim, J. A. Sakoff, *J. Med. Chem.* **45**, 1151 (2002).
15. H. P. Harding *et al.*, *Proc. Natl. Acad. Sci. U.S.A.* **106**, 1832 (2009).
16. We thank A. Merritt and C. Wallace for biotinylated guanabenz, J. Hastie for purified recombinant PP1c, anonymous reviewers for suggestions, and M. Goedert for advice on the manuscript. Supported by the UK Medical Research Council. D.R. is a Wellcome Trust Principal Research Fellow. A.B. is a co-inventor on patent WO/2008/041133.

Supporting Online Material
www.sciencemag.org/cgi/content/full/science.1201396/DC1
Materials and Methods
Figs. S1 to S5
References

8 December 2010; accepted 11 February 2011
Published online 3 March 2011;
10.1126/science.1201396

Directional Switching of the Kinesin Cin8 Through Motor Coupling

Johanna Roostalu,[1] Christian Hentrich,[2]* Peter Bieling,[2]† Ivo A. Telley,[2] Elmar Schiebel,[1]‡ Thomas Surrey[2]‡§

Kinesin motor proteins are thought to move exclusively in either one or the other direction along microtubules. Proteins of the kinesin-5 family are tetrameric microtubule cross-linking motors important for cell division and differentiation in various organisms. Kinesin-5 motors are considered to be plus-end–directed. However, here we found that purified kinesin-5 Cin8 from budding yeast could behave as a bidirectional kinesin. On individual microtubules, single Cin8 motors were minus-end–directed motors, whereas they switched to plus-end–directed motility when working in a team of motors sliding antiparallel microtubules apart. This kinesin can thus change directionality of movement depending on whether it acts alone or in an ensemble.

Kinesins are microtubule-binding motor proteins required for essential intracellular movements (*1*). They are known to be unidirectional, and their directionality depends on how the motor domain is linked to the remainder of the molecule (*2*, *3*). Kinesins with an N-terminal motor domain move toward the plus end of microtubules, whereas C-terminal kinesins are minus-end–directed (*4*). The directionality of intracellular transport processes is thought to be regulated by selective recruitment or activation of different sets of motors with characteristic, built-in directionalities (*1*).

Kinesin-5 is an N-terminal homotetrameric kinesin that cross-links microtubules (*5*, *6*). Purified vertebrate kinesin-5 is plus-end–directed and slides antiparallel microtubules apart in vitro (*7*), which is consistent with its role in the mitotic spindle. Budding yeast possesses two largely redundant kinesin-5 proteins, with Cin8 being the more prominent one (*8*, *9*). Apart from its role in spindle assembly (*8*, *9*), Cin8 is required for kinetochore positioning in metaphase (*10*, *11*) and for spindle elongation during anaphase, when it localizes to overlapping antiparallel microtubules in the spindle midzone (*11*–*13*).

We purified recombinant full-length Cin8 fused to monomeric green fluorescent protein (mGFP) (Fig. 1A) (*14*). Cin8-mGFP was a tetramer (table S1 and fig. S1), as expected (*5*). Using total internal reflection fluorescence (TIRF) microscopy, we examined the behavior of single Cin8 tetramers on individual immobilized microtubules in vitro (Fig. 1, B and C, fig. S2, and movie S1). Cin8 motility displayed a combination of directional and diffusive modes as revealed by means of kymographs (time-space plots) (Fig. 1D) and confirmed through mean square displacement (MSD) analysis (Fig. 1E) (*14*). The one-dimensional diffusion coefficient was 0.03 $\mu m^2/s$, and the directional drift speed was 101.7 nm/s. This composite motility is similar to the single-motor behavior of vertebrate kinesin-5 (*15*). However, in contrast to other kinesin-5 family members and all other natural N-terminal kinesins, single

[1]Zentrum für Molekulare Biologie der Universität Heidelberg, DKFZ-ZMBH Allianz, Im Neuenheimer Feld 282, Heidelberg 69120, Germany. [2]Cell Biology and Biophysics Unit, European Molecular Biology Laboratory, Meyerhofstrasse 1, 69117 Heidelberg, Germany.

*Present address: Howard Hughes Medical Institute, Department of Molecular Biology and Center for Computational and Integrative Biology, Massachusetts General Hospital, Boston, MA 02114, USA.

†Present address: Department of Cellular and Molecular Pharmacology, University of California, San Francisco, San Francisco, CA 94158, USA.

‡To whom correspondence should be addressed. E-mail: e.schiebel@zmbh.uni-heidelberg.de (E.S.); thomas.surrey@cancer.org.uk (T.S.)

§Present address: Cancer Research UK London Research Institute, Lincoln's Inn Fields Laboratories, 44 Lincoln's Inn Fields, London WC2A 3LY, UK.

Cin8 motors clearly moved on average toward microtubule minus ends (Fig. 1, C and D, and fig. S2). Mean displacement (MD) analysis (Fig. 1F) revealed that individual Cin8 motors were minus-end–directed, with an average speed of 58 nm/s (Fig. 1F). This difference in speed obtained from either MSD or MD analysis was due to the broad displacement distribution (fig. S2D) (*14*). Minus-end–directed motility of single Cin8 tetramers was an inherent feature of adenosine 5′-triphosphate (ATP)–dependent motor activity because in the presence of ADP, Cin8 displayed only diffusive motion without any directional bias (fig. S3) with reduced dwell times (Fig. 1G). Thus, Cin8 represents an N-terminal kinesin that moves toward the microtubule minus end.

In vivo Cin8 extends the yeast anaphase spindle through plus-end–directed antiparallel microtubule sliding (*13*, *16*). To test whether Cin8 might switch directionality of movement when cross-linking two microtubules, we generated antiparallel microtubule pairs of differently fluorescently labeled and polarity-marked microtubules (*17*). One of the microtubules in a pair

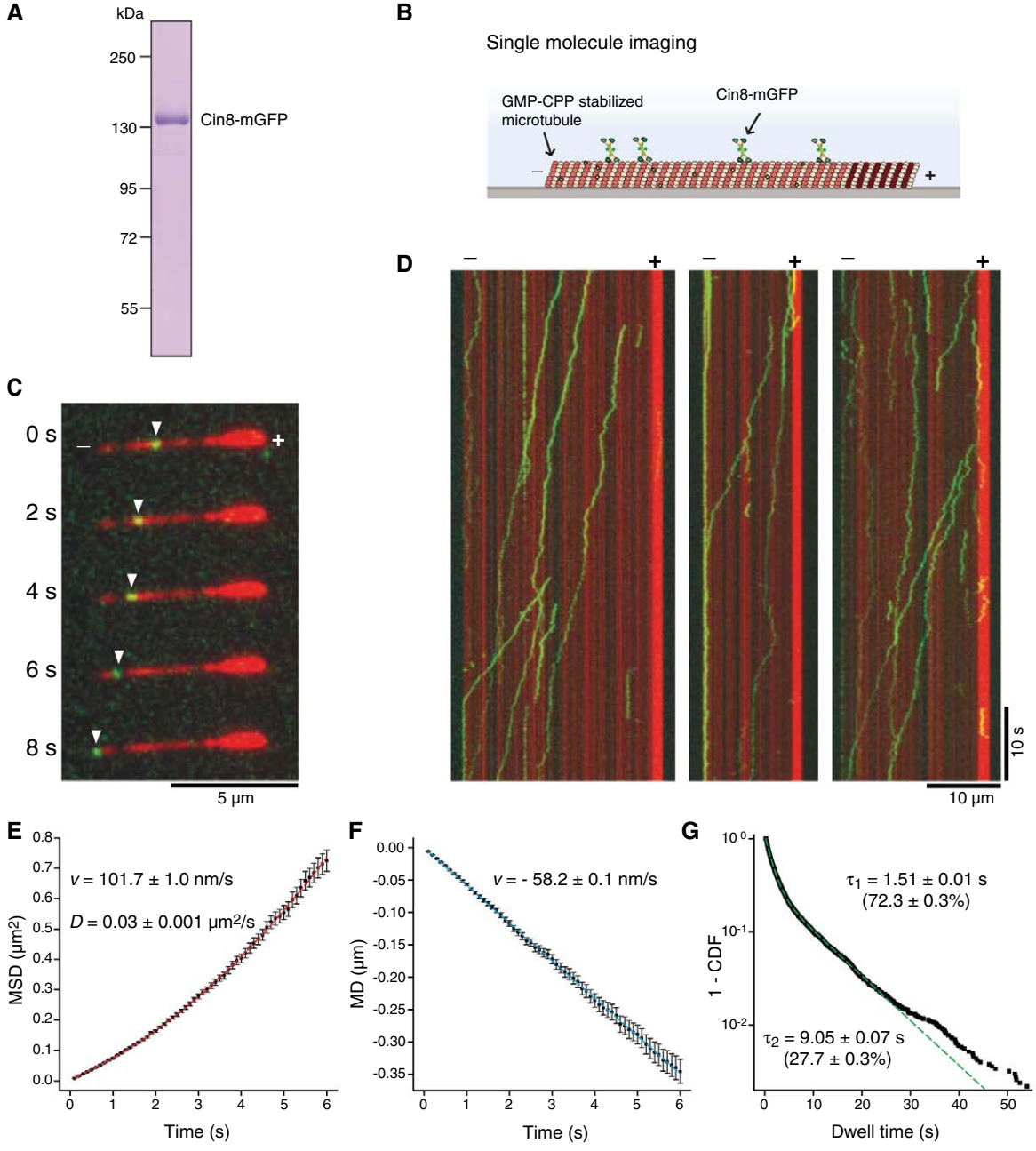

Fig. 1. Single Cin8 motors on individual microtubules are minus-end–directed. (**A**) Coomassie-stained SDS–polyacrylamide gel electrophoresis (SDS-PAGE) of purified recombinant Cin8-mGFP. (**B**) Scheme of the single-molecule assay. (**C**) Example frames of a TIRF microscopy time-lapse movie showing (green; white arrowheads) Cin8-mGFP movement on (red) a surface-immobilized Alexa568-labeled polarity-marked microtubule with a bright plus end and a dim minus end. (**D**) Representative kymographs of (green) Cin8-mGFP movement on (red) Alexa568-labeled polarity-marked microtubules. (**E** to **G**) Quantification of 5000 individual Cin8-mGFP binding events on polarity-marked microtubules. Mean velocities (*v*) and the diffusion constant (*D*) were derived by fitting the following functions to (E) MSD and (F) MD data: (dashed red line) $MSD = v^2t^2 + 2Dt + offset$ and (dashed blue line) $MD = vt$. (G) Mean dwell times (τ) and relative amplitudes (in brackets) were obtained from fitting a bi-exponential function (dashed green line) to the measured dwell time distribution [shown as 1 − cumulative distribution function (CDF)]. Cin8-mGFP was used at 20 to 30 pM. Stated errors and error bars represent SEM.

was surface-immobilized, whereas the other was cross-linked to it by Cin8-mGFP (Fig. 2, A and B) (*14*). Cin8-mGFP accumulated in antiparallel microtubule overlap regions (Fig. 2B and movie S2). Antiparallel microtubules always moved with their plus end lagging, which is indicative of plus-end–directed Cin8 motility (Fig. 2C), as observed for *Xenopus* kinesin-5 (*7*, *17*). The measured sliding velocities (16-17 nm/s) (Fig. 2D) agreed well with the speed of the first, Cin8-dependent phase of anaphase spindle elongation in vivo (around 15 nm/s) (*12*). Furthermore, we observed Cin8-mGFP accumulation at minus ends of single microtubules outside the overlap regions (Fig. 2, B and C), confirming that under identical conditions, but in a different context, Cin8 moved toward the minus end. Thus, although single Cin8 motors are minus-end–directed on individual microtubules (Figs. 1 and 2, B and C) teams of Cin8 motors cross-linking antiparallel two microtubules move toward the plus end. Cin8 thus behaves as a bidirectional motor whose directionality depends on the microtubule-motor configuration.

The switch in Cin8 directionality could be caused, for example, by communication between the two ends of the tetramer when cross-linking two microtubules or, alternatively, by a collective phenomenon: Multiple motors simultaneously binding to an antiparallel microtubule pair could influence each other. We performed microtubule gliding experiments in which multiple surface-immobilized motors collectively transport microtubules (Fig. 3A). Immobilized purified Cin8 motors were found to be plus-end–directed (Fig. 3B and movie S3), which is in agreement with previous gliding assays with surface-adsorbed Cin8 from crude yeast extract (*18*). The speed derived from MSD and MD analysis was between 4 and 5 nm/s (Fig. 3B). Thus, Cin8 does not need to cross-link two microtubules to be plus-end–directed. Next, we reduced the surface density of Cin8 by lowering the protein concentration from 250 to 10 nM and keeping buffer conditions constant. This resulted in fast, minus-end–directed motility, with intermittent pause phases (speeds of 50 nm/s and 31.9 nm/s from MSD and MD analysis, respectively) (Fig. 3D and movie S3). At intermediate motor concentrations (50 nM), microtubule transport was bidirectional, showing phases of both plus- and minus-end–directed motility (Fig. 3C and movie S3) with characteristic switching times in the range of a minute (fig. S4). The speed of transport depended on the nucleotide concentration (fig. S5). As expected for such heterogeneous motility, the transport speeds deduced from MSD (13 nm/s) versus MD (3.8 nm/s) analysis (Fig. 3C) varied considerably. The switch in the directionality depended also on microtubule length (Fig. 3E). This demonstrates that not the density itself but rather the number of motors interacting with a microtubule critically determines the direction of transport. Therefore, large Cin8 ensembles that are mechanically coupled via surface attachment switch to plus-end–directed motility.

To test this further, we varied in the gliding experiments the ionic strength while keeping the motor concentration constant. We observed a transition from plus- to minus-end–directed microtubule transport via an intermediate unstable regime upon increasing the ionic strength (figs. S6 and S7). This switch in directionality was again microtubule-length–dependent: Shorter microtubules underwent the transition from plus- to minus-end–directed motility at lower salt concentrations (fig. S6D) than did longer microtubules. This demonstrates that

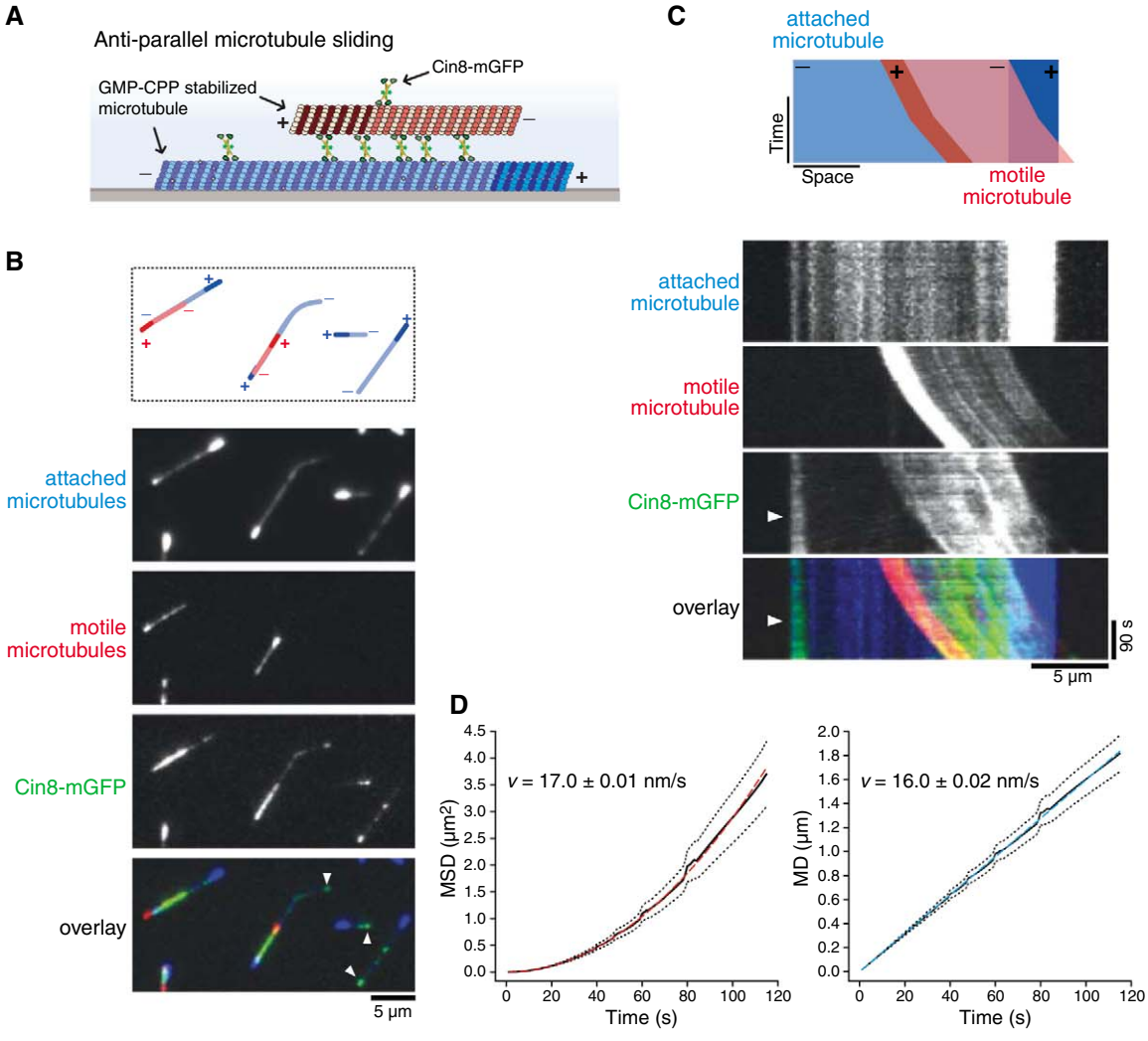

Fig. 2. Cin8 slides antiparallel microtubules apart in a plus-end–directed manner. (**A**) Scheme of the antiparallel sliding assay. (**B**) TIRF microscopy images showing (red) polarity-marked Alexa568-microtubules cross-linked to (blue) surface-immobilized polarity marked Alexa647-microtubules by (green) 4.5 nM of Cin8-mGFP in an antiparallel orientation. White arrowheads indicate Cin8-mGFP accumulation at the minus ends of surface-immobilized microtubules. (**C**) Example kymographs of a sliding antiparallel microtubule pair. (**D**) Quantification of antiparallel microtubule sliding. MSD and MD curves were calculated from tracks of sliding microtubules (n = 38 microtubules; n = 96 respective instantaneous velocities). Mean velocities (v) were derived by fitting the functions (dashed blue line) $MD = vt$ and (dashed red line) $MSD = v^2t^2$ to the data. Stated errors represent SEM. Dotted black lines in (D) are 95% confidence intervals.

the crucial parameter determining directionality of transport is not the ionic strength itself but rather is the number of mechanically coupled motors on the glass surface that interact with a microtubule. Increased salt concentrations weaken the motor-microtubule interaction and hence lower the number of microtubule-bound motors at a given surface density (*19*), supporting this interpretation. Directional switching did not require the entire tetrameric Cin8 protein, as demonstrated by using a C-terminally truncated Cin8 construct previously shown to be dimeric (fig. S8 and table S1) (*5*).

Minus-end–directed movement of Cin8 has not been observed in vivo. Because individual spindle microtubules cannot be visualized easily inside the yeast nucleus, we targeted GFP-labeled Cin8 to the cytoplasm by deleting the C-terminal nuclear localization signal (NLS) (*10*, *20*). This enabled us to observe Cin8 along single cytoplasmic microtubules. In all cells, Cin8 accumulated near the minus ends of cytoplasmic microtubules that are organized by the spindle pole body (SPB) (Spc72-mCherry) (Fig. 4, A and B, and fig. S9). Microtubule plus-end binding of Cin8 as reported previously (*10*) was rarely observed (<1%). The localization of cytoplasmic Cin8 was strongly microtubule-dependent (Fig. 4, A and B), making the possibility of a direct interaction of Cin8 with SPB components unlikely. Time-lapse imaging revealed short-lived microtubule binding events of Cin8 (Fig. 4C), which is in agreement with its in vitro dwell time and in contrast to the very processive plus-end–directed motility of Kip3 in vivo (Fig. 4D) (*21*, *22*). Thus, it is likely that Cin8 acts as a minus-end–directed motor on individual microtubules in vivo.

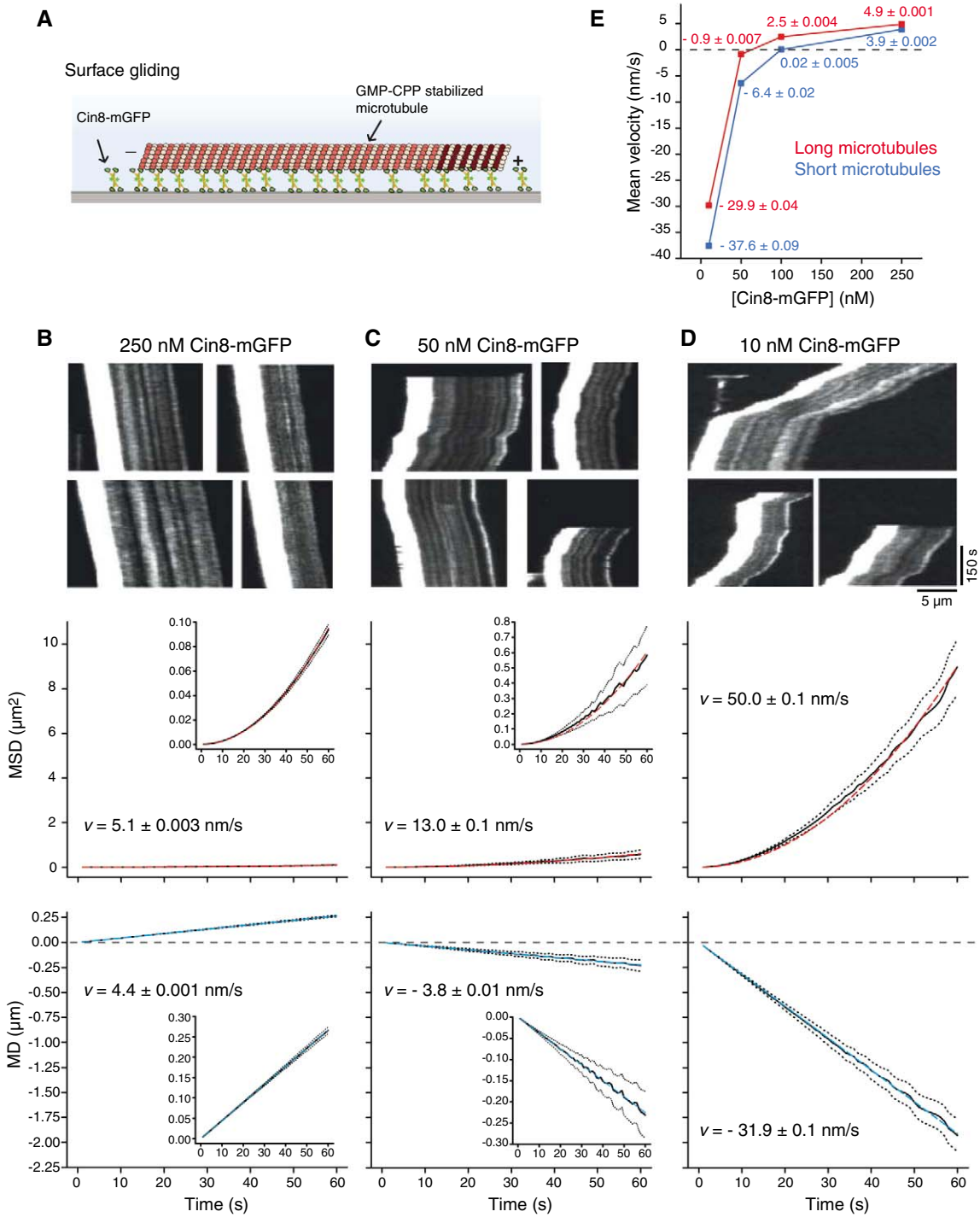

Fig. 3. Cin8 changes directionality depending on the number of microtubule-interacting motors. (**A**) Scheme of a surface gliding assay. (**B** to **D**) Example kymographs and quantifications of surface gliding assays performed at (B) 250, (C) 50, and (D) 10 nM Cin8-mGFP. MSD and MD curves were calculated from tracks of gliding microtubules. (**E**) Comparison of mean velocities between short (<8 µm) and long (>8 µm) microtubules at different motor concentrations (10, 50, 100, and 250 nM). Mean velocities were derived from MD fits, as described in Fig. 2D. Stated errors and error bars represent SEM. Dotted black lines on (B) to (D) are 95% confidence intervals.

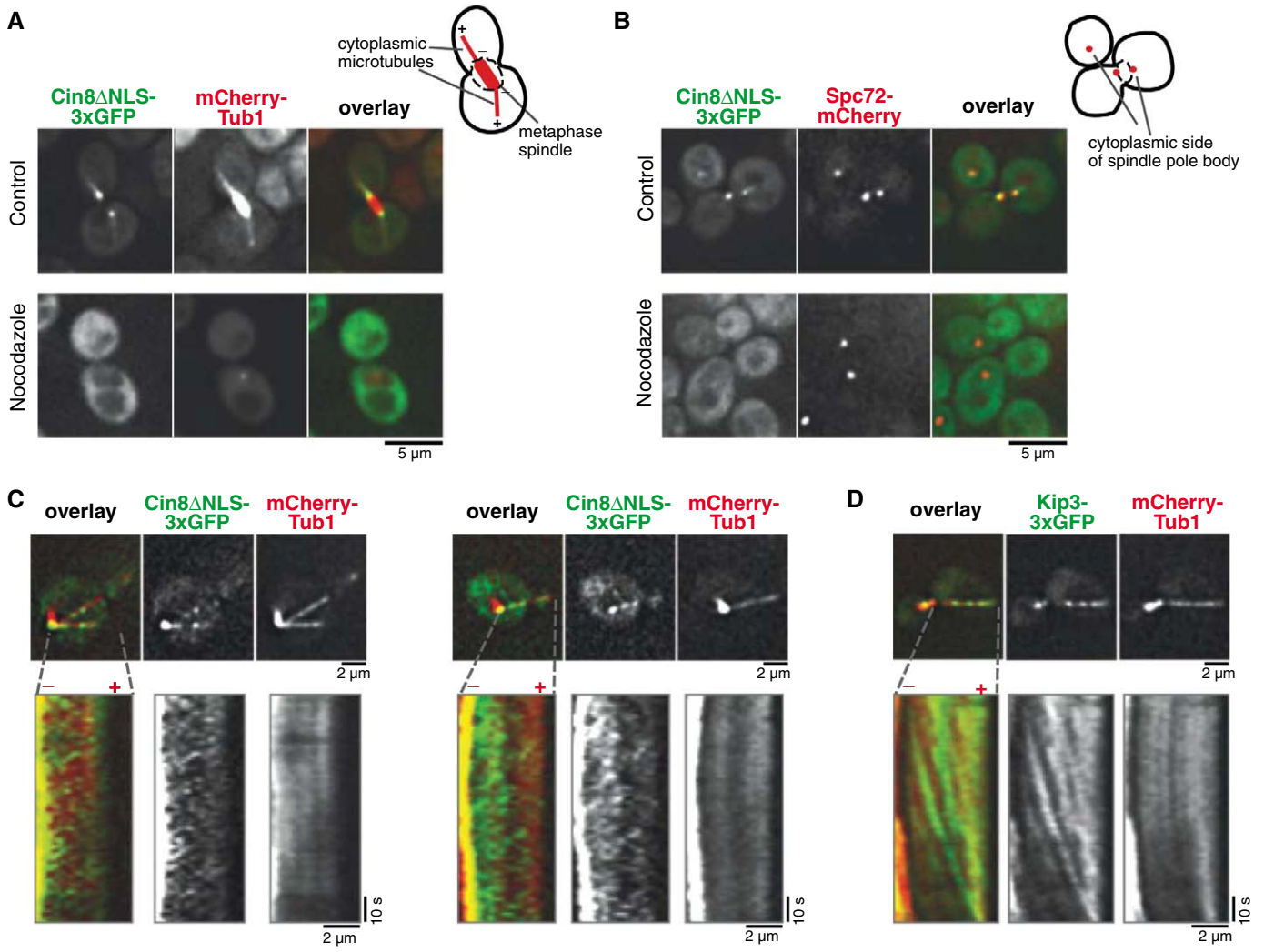

Fig. 4. Cin8 accumulates toward microtubule minus ends in vivo. Localization of cytoplasmic Cin8 (Cin8ΔNLS-3GFP) in cells with (**A**) labeled cytoplasmic microtubules (mCherry-Tub1) or (**B**) labeled cytoplasmic SPB component Spc72 (Spc72-mCherry; red) that anchors cytoplasmic microtubule minus ends. Dimethyl sulfoxide–treated control cells were compared with cells treated with the microtubule-depolymerizing drug nocodazole. Time-lapse analysis of (**C**) Cin8ΔNLS-3GFP and (**D**) Kip3-3GFP on cytoplasmic microtubules (mCherry-Tub1).

Similar to Cin8, kinesin-5 motors from fission yeast (*23*), *Xenopus* (*24*), and *Drosophila* (*25*) concentrate near spindle poles. Accumulation of plus-end–directed *Xenopus* kinesin-5 at the poles depends on the minus-end–directed motor dynein (*26*), which does not have a nuclear function in yeast. The minus-end–directed motility of Cin8 might bypass one of the functions that dynein has in higher eukaryotes.

Microtubule cross-linking promotes directional over diffusive motility of plus-end–directed *Xenopus* kinesin-5 (*27*). Here, Cin8 motors switched directionality in response to team size, suggesting that the ability to sense and respond to mechanical constraints might be a property of kinesin-5 motors, possibly because of specific features of this kinesin family (*28*, *29*). However, Cin8 is also an unusual member of the kinesin-5 family in containing a multitude of insertions and mutations in usually conserved regions (*29*, *30*).

In conclusion, Cin8 can switch between two distinct states of directional motility. On individual microtubules, single Cin8 motors preferentially move toward the minus end, whereas they switch to plus-end–directed movement when part of a large team of mechanically coupled motors cross-linking antiparallel microtubules. Such a context-dependent change in directionality is different from previously studied cases of bidirectionality (*14*, *31*).

References and Notes

1. N. Hirokawa, Y. Noda, Y. Tanaka, S. Niwa, *Nat. Rev. Mol. Cell Biol.* **10**, 682 (2009).
2. S. A. Endow, K. W. Waligora, *Science* **281**, 1200 (1998).
3. U. Henningsen, M. Schliwa, *Nature* **389**, 93 (1997).
4. H. Miki, Y. Okada, N. Hirokawa, *Trends Cell Biol.* **15**, 467 (2005).
5. E. R. Hildebrandt, L. Gheber, T. Kingsbury, M. A. Hoyt, *J. Biol. Chem.* **281**, 26004 (2006).
6. A. S. Kashina *et al.*, *Nature* **379**, 270 (1996).
7. L. C. Kapitein *et al.*, *Nature* **435**, 114 (2005).
8. M. A. Hoyt, L. He, K. K. Loo, W. S. Saunders, *J. Cell Biol.* **118**, 109 (1992).
9. D. M. Roof, P. B. Meluh, M. D. Rose, *J. Cell Biol.* **118**, 95 (1992).
10. M. K. Gardner *et al.*, *Cell* **135**, 894 (2008).
11. J. D. Tytell, P. K. Sorger, *J. Cell Biol.* **172**, 861 (2006).
12. A. Khmelinskii, J. Roostalu, H. Roque, C. Antony, E. Schiebel, *Dev. Cell* **17**, 244 (2009).
13. W. S. Saunders, D. Koshland, D. Eshel, I. R. Gibbons, M. A. Hoyt, *J. Cell Biol.* **128**, 617 (1995).
14. Materials and methods are available as supporting material on *Science* Online.
15. B. H. Kwok *et al.*, *Nat. Chem. Biol.* **2**, 480 (2006).
16. A. F. Straight, J. W. Sedat, A. W. Murray, *J. Cell Biol.* **143**, 687 (1998).
17. C. Hentrich, T. Surrey, *J. Cell Biol.* **189**, 465 (2010).
18. L. Gheber, S. C. Kuo, M. A. Hoyt, *J. Biol. Chem.* **274**, 9564 (1999).
19. P. Bieling, I. A. Telley, J. Piehler, T. Surrey, *EMBO Rep.* **9**, 1121 (2008).
20. E. R. Hildebrandt, M. A. Hoyt, *Mol. Biol. Cell* **12**, 3402 (2001).
21. M. L. Gupta Jr., P. Carvalho, D. M. Roof, D. Pellman, *Nat. Cell Biol.* **8**, 913 (2006).
22. V. Varga, C. Leduc, V. Bormuth, S. Diez, J. Howard, *Cell* **138**, 1174 (2009).
23. I. Hagan, M. Yanagida, *Nature* **356**, 74 (1992).
24. K. E. Sawin, K. LeGuellec, M. Philippe, T. J. Mitchison, *Nature* **359**, 540 (1992).
25. D. K. Cheerambathur, I. Brust-Mascher, G. Civelekoglu-Scholey, J. M. Scholey, *J. Cell Biol.* **182**, 429 (2008).
26. T. M. Kapoor, T. J. Mitchison, *J. Cell Biol.* **154**, 1125 (2001).
27. L. C. Kapitein *et al.*, *J. Cell Biol.* **182**, 421 (2008).

28. A. G. Larson, N. Naber, R. Cooke, E. Pate, S. E. Rice, *Biophys. J.* **98**, 2619 (2010).
29. J. Turner *et al*., *J. Biol. Chem.* **276**, 25496 (2001).
30. A. J. Bodey, M. Kikkawa, C. A. Moores, *J. Mol. Biol.* **388**, 218 (2009).
31. T. Guérin, J. Prost, P. Martin, J. F. Joanny, *Curr. Opin. Cell Biol.* **22**, 14 (2010).
32. We thank D. Pellman and M. Knop for plasmids; I. Hagan, J. Ellenberg, and M. Kaksonen for critically reading the manuscript; and the Deutsche Forschungsgemeinschaft, the European Commission (Marie Curie Research Training Network "Spindle Dynamics"), and the Swiss National Science Foundation for financial support.

Supporting Online Material
www.sciencemag.org/cgi/content/full/science.1199945/DC1
Materials and Methods
Supporting Text
Figs. S1 to S9
Tables S1 to S2
References
Movies S1 to S3

3 November 2010; accepted 11 February 2011
Published online 24 February 2011;
10.1126/science.1199945

The C-Terminal Domain of RNA Polymerase II Is Modified by Site-Specific Methylation

Robert J. Sims III,[1]*† Luis Alejandro Rojas,[1]* David Beck,[1] Roberto Bonasio,[1] Roland Schüller,[2] William J. Drury III,[1] Dirk Eick,[2] Danny Reinberg[1]‡

The carboxy-terminal domain (CTD) of RNA polymerase II (RNAPII) in mammals undergoes extensive posttranslational modification, which is essential for transcriptional initiation and elongation. Here, we show that the CTD of RNAPII is methylated at a single arginine (R1810) by the coactivator-associated arginine methyltransferase 1 (CARM1). Although methylation at R1810 is present on the hyperphosphorylated form of RNAPII in vivo, Ser2 or Ser5 phosphorylation inhibits CARM1 activity toward this site in vitro, suggesting that methylation occurs before transcription initiation. Mutation of R1810 results in the misexpression of a variety of small nuclear RNAs and small nucleolar RNAs, an effect that is also observed in *Carm1*$^{-/-}$ mouse embryo fibroblasts. These results demonstrate that CTD methylation facilitates the expression of select RNAs, perhaps serving to discriminate the RNAPII-associated machinery recruited to distinct gene types.

The carboxy-terminal domain (CTD) of the major subunit of RNA polymerase II (RNAPII) in mammals comprises 52 repeats of the consensus sequence Tyr-Ser-Pro-Thr-Ser-Pro-Ser (*1*). Although site-specific CTD phosphorylation mediates recruitment of other proteins to RNAPII, how this recruitment facilitates distinct processing events remains poorly understood (*2*–*4*). Nonconsensus repeats of the RNAPII CTD contain two arginine and seven lysine substitutions that primarily occur at position seven of the heptad motif. We hypothesized that such arginine and/or lysine residues might be targets for modification of the CTD of RNAPII and, as a consequence, engage activities associated with RNA production.

A glutathione *S*-transferase (GST)–CTD fusion protein containing repeats number 24–52 was not acetylated by HeLa-S3 nuclear extract as a source of enzymes, but specific methylation of the GST-CTD was observed, and its level correlated with increasing amounts of the extract (Fig. 1A). We purified the CTD methyltransferase enzyme from this extract (Fig. 1, B and C), detecting a band at ~65 kD that was crosslinked to a S-adenosyl methionine (SAM) after ultraviolet exposure (fig. S1B) (*5*). Mass spectrometric analysis revealed the presence of coactivator-associated arginine methyltransferase 1 (CARM1), which migrates at a molecular mass of approximately 65 kD by means of SDS–polyacrylamide gel electrophoresis (SDS-PAGE). To ascertain whether CARM1 was the enzyme that methylates the CTD, we performed methylation reactions using increasing amounts of recombinant CARM1 in the presence of the CTD and confirmed that CARM1 is capable of catalyzing this modification (Fig. 1D). Western blot analysis of the Superose 6 gel filtration fractions derived from conventional purification revealed that CARM1 and the CTD methyltransferase activity co-eluted (fig. S1C) (*5*). Given that we did not detect any CTD methyltransferase activity that fractionated apart from CARM1 during the purification and that nuclear extracts derived from *Carm1*$^{-/-}$ mouse embryonic fibroblasts (MEFs) were devoid of this activity (Fig. 1E), we concluded that CARM1 is the enzyme responsible for methylating the CTD. CARM1 is a type I protein arginine methyltransferase (PRMT) that catalyzes a methyltransferase reaction, producing asymmetric dimethylated arginine. Its substrates include histone H3 and p300, and it has been implicated in co-activation of nuclear receptor–directed transcription as well as in mRNA splicing (*6*, *7*), although the underlying mechanisms are largely obscure.

The largest subunit of RNAPII contains two arginine residues within the CTD; one is present within the N-terminal half of the CTD (R1603, second repeat), and the other within the C-terminal half (R1810, repeat number 31) (*8*). We tested whether both arginines are targets of CARM1 using methylation assays with GST fusion proteins containing either the N-terminal (GST-N-CTD) or C-terminal (GST-C-CTD) portions of the CTD. Only the GST-C-CTD substrate was methylated by recombinant CARM1, indicating that CARM1 targets R1810 (Fig. 2A). An alignment of the residues surrounding R1810 from different species suggests that CARM1 methylation may be conserved throughout evolution (Fig. 2B).

CARM1 methylated highly purified RNAP II derived from HeLa-S3 cells (Fig. 2C): Only the hypophosphorylated (IIA) form of RNAPII was methylated; the hyperphosphorylated form of RNAPII (IIO) was not. Methylation experiments by use of the CTD fusion protein that was prephosphorylated by Ser5- (CAK) or Ser2-specific (P-TEFb) kinases suggest that CARM1 methylation is sensitive to Ser2 and Ser5 phosphorylation (Fig. 2D). Furthermore, CARM1 was ineffectual when provided with synthetic peptides that were phosphorylated at Ser2 or Ser5 as substrates (Fig. 2, E and F). Phosphatase treatment of these peptides restored their ability to be methylated by CARM1 (Fig. 2G). The CTD of RNAPII is phosphorylated during the initiation of transcription; CARM1-mediated methylation probably takes place before phosphorylation, which is consistent with its recruitment during the early phases of transcriptional activation (*9*, *10*).

Immunofluorescence analyses performed on MEF cells by using a polyclonal antibody against a CTD peptide containing R1810me2a (fig. S2, A and B) showed that this modification is localized in the nuclei, which is similar to the case of phosphorylated CTD (anti-pSer5, clone 4H8) (Fig. 3A). *Carm1*$^{-/-}$ MEFs were devoid of CARM1, as expected (Fig. 3B) and also devoid of methylated CTD, as evidenced by the absence of signal using antibodies to CTDRme2a (anti-CTDRme2a) (Fig. 3A), which supports the conclusion that the CTD is methylated in vivo by CARM1. The anti-CTDme2a signal observed by using MEF cells was blocked by CTDme2a peptide but not by other synthetic peptides that are analog to CARM1 products, namely H3R26me2a or a symmetrically methylated peptide H4R3me2s (Fig. 3C). Using this antibody on Western blots, we detected methylation on hyperphosphorylated RNAPII purified from HeLa cells (Fig. 3D). Thus, CARM1

[1]Howard Hughes Medical Institute (HHMI), Department of Biochemistry, New York University School of Medicine, 522 First Avenue, Smilow 211, New York, NY 10016, USA. [2]Department of Molecular Epigenetics, Helmholtz Center Munich, Center of Integrated Protein Science Munich (CIPSM), Marchioninistrasse 25, 81377 Munich, Germany.

*These authors contributed equally to this work.
†Present address: Constellation Pharmaceuticals, Cambridge, MA 02139, USA.
‡To whom correspondence should be addressed. E-mail: danny.reinberg@nyumc.org

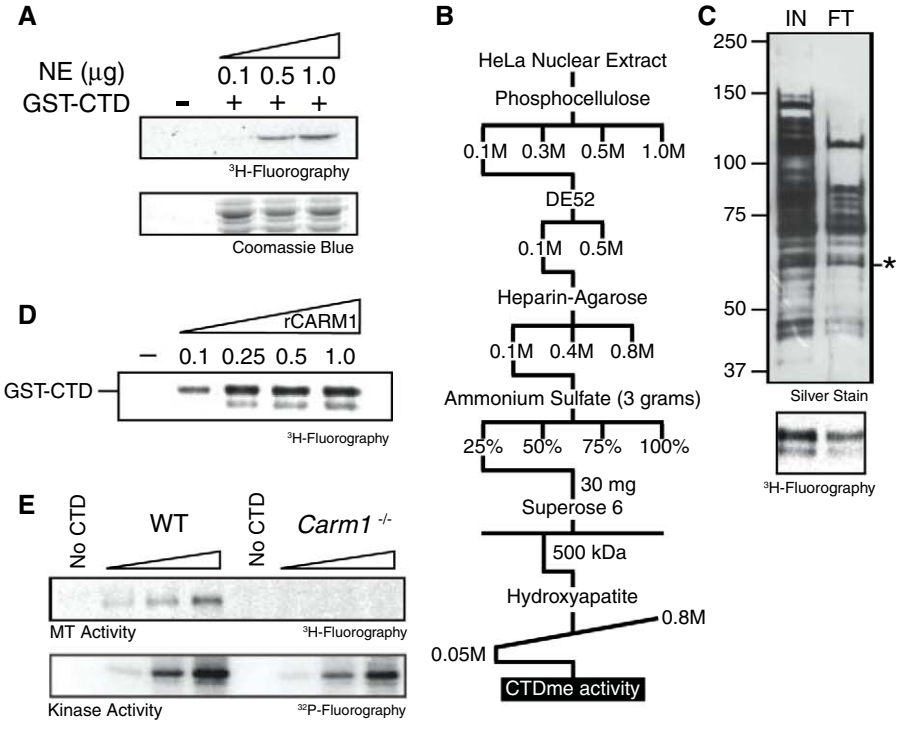

Fig. 1. CARM1 methylates the CTD of RNAPII. (**A**) (Top) Fluorography after SDS-PAGE analysis of GST-CTD protein methylated by increasing amounts of nuclear extract. (Bottom) Coomassie blue staining as a loading control for the substrate. (**B**) Schematic showing the chromatographic strategy that was used to identify the CTD methyltransferase activity. (**C**) (Top) Silver stain of the input and flow-through fractions of the hydroxyapatite chromatographic step. (Bottom) CTD methyltransferase activity of the fractions indicated above. The flow-through fraction was subjected to mass spectrometry, and CARM1 was identified as the CTD methyltransferase activity. The asterisk denotes the molecular weight of CARM1. (**D**) GST-CTD methylation assay performed in vitro using increasing amounts (micrograms) of recombinant CARM1 (rCARM1). (**E**) (Top) GST-CTD methylation assay using nuclear extract from WT or *Carm1*$^{-/-}$ MEF cells. (Bottom) GST-CTD phosphorylation assay with the same extracts.

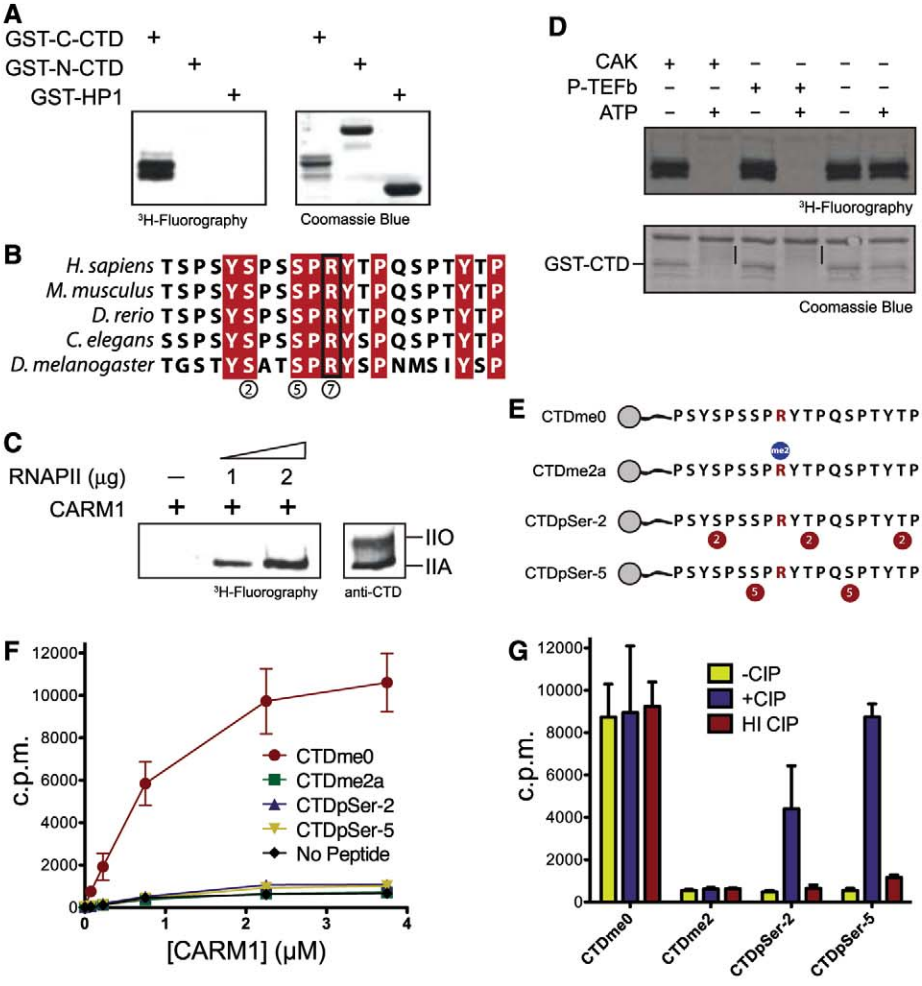

Fig. 2. The hypophosphorylated form of the RNAPII CTD is methylated on a single arginine residue, and phosphorylated CTD cannot be methylated in vitro. (**A**) In vitro methylation assays with rCARM1 using GST-C-CTD and GST-N-CTD, with GST-HP1 as control. The reaction products were detected with fluorography (left). (**B**) Alignment of human CTD-R1810 with CTD sequences from the species indicated. Red columns indicate conserved residues. (**C**) (Left) Methylation assay using recombinant CARM1 and highly purified RNAPII from HeLa-S3 nuclei. (Right) Western blot using highly purified RNAPII and an antibody to the CTD that recognizes both IIA and IIO forms. (**D**) Methylation assays on GST-CTD phosphorylated by the indicated kinases. (Bottom) Black bars denote the change in mobility when the CTD is phosphorylated. (**E**) Schematic of biotinylated CTD peptides used. Red circles indicate phosphorylation sites, and the blue circle indicates the methylation site. (**F**) Methylation of CTD peptides shown in (E) in the presence of increasing amounts of rCARM1, as scored with scintillation counting. Points represent the mean ± SD of three different experiments. (**G**) Scintillation counting of CTD peptide methylation as in (F), after treatment with calf intestine phosphatase (CIP) or heat-inactivated (HI) CIP. Bars represent the mean ± SD of three different experiments.

methylates the CTD of RNAPII in vivo and does so before the CTD is phosphorylated. Yet given that the methylated CTD is a substrate for subsequent phosphorylation and that phosphorylated RNAPII exhibits this methylation state (Fig. 3D), it is highly probable that R1810me is preserved on the transcribing polymerase, not having a major impact on CTD phosphorylation.

To address the function of RNAPII methylation, we generated cell lines expressing an RNAPII resistant to α-amanitin and carrying either wild-type (WT) R1810 or an arginine-to-alanine substitution at that same residue, abolishing R1810 methylation of the CTD (Fig. 4A). In cells cultured in α-amanitin, the α-amanitin–resistant mutants fully replaced the functions of endogenous RNAPII, allowing us to study whether gene expression is affected by the absence of R1810me (*11*). Our transcriptome analysis results suggest that steady-state levels of small nuclear RNAs (snRNAs) as well as small nucleolar RNAs (snoRNAs) are affected in a general manner (Fig. 4B and fig. S3). We confirmed these results for a number of candidate transcripts through quantitative reverse transcription polymerase chain reaction (RT-PCR) using total RNA derived from WT or R1810A cells (Fig. 4C). Because a large number of snRNAs and snoRNAs were affected, we asked whether there was a general correlation between the size of the RNA species whose expression was affected as a consequence of the absence of R1810me (fig. S4). The effect appeared specific to snRNAs and snoRNAs, however, because transcripts of comparable size with that of snRNAs and snoRNAs but belonging to different classes of RNA were not upregulated. Also, expression of RNAPIII-transcribed small RNAs, such as 5S and U6, was not affected (Fig. 4B, bottom plots). The misregulation of snRNA expression was also detected in *Carm1*$^{-/-}$ MEFs through quantitative RT-PCR (Fig. 4D), suggesting that the functions of CARM1 and R1810me are related and that they are conserved, at least in mammals.

The observed de-repression of snRNAs and snoRNAs in the absence of R1810me suggests that this CTD modification functions in opposition to the activating effect of Ser phosphorylation (*12*–*14*). In addition to the direct function of CARM1 in splicing, in which it modulates the recognition of 5′ splice sites through its interaction with U1 small nuclear ribonucleoprotein complex (*15*), CARM1 may also contribute to splicing indirectly through modulating the levels of spliceosome components, such as U1 and U2 (Fig. 4).

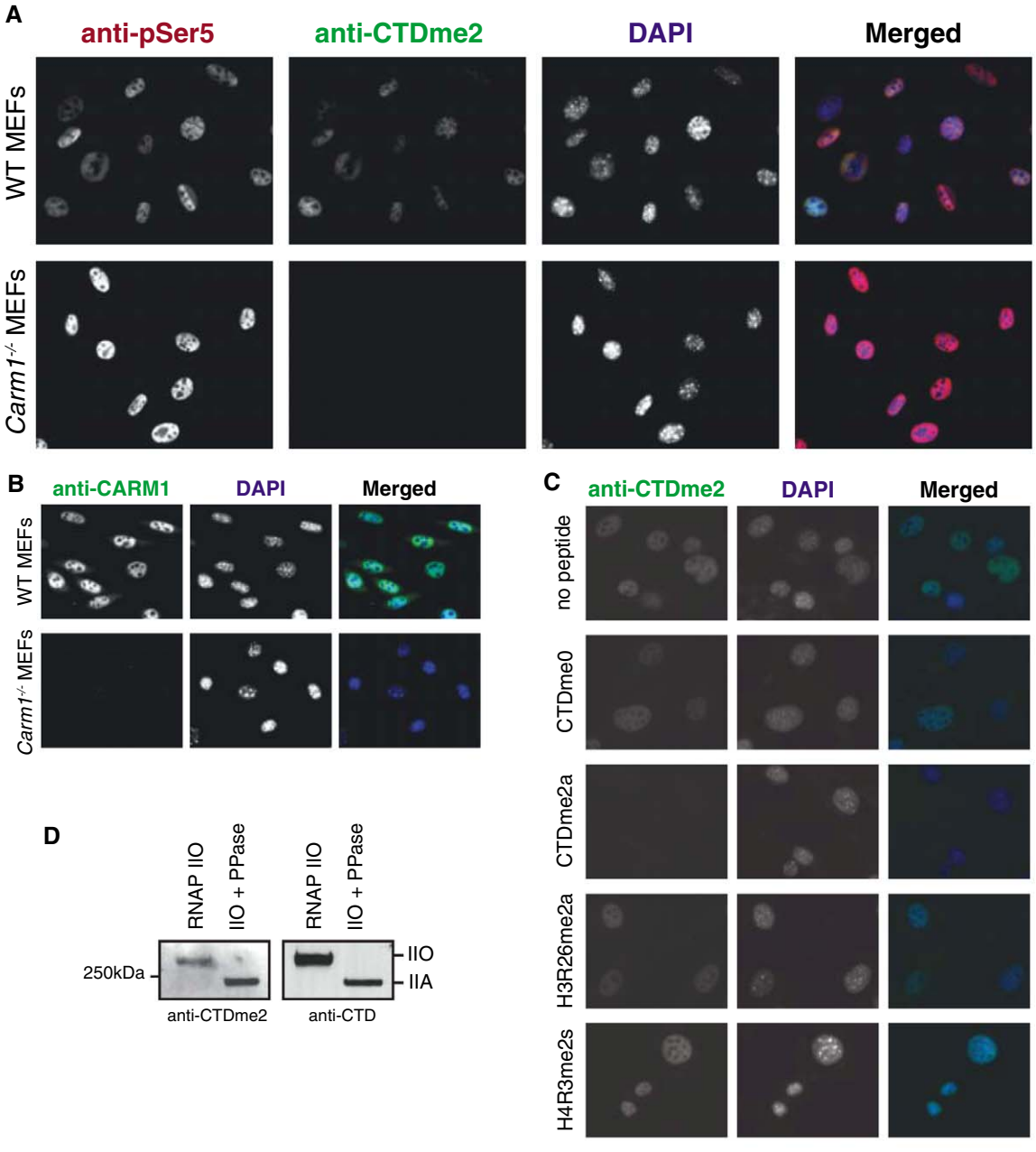

Fig. 3. The CTD of RNAPII is methylated in vivo. (**A**) Immunofluorescence analysis of WT and *Carm1*$^{-/-}$ MEFs using the indicated antibodies. (**B**) Comparison of WT and *Carm1*$^{-/-}$ MEFs using antibody to CARM1. (**C**) The specificity of antibody to CTDme2a is shown as a function of its incubation with the indicated blocking peptides (5 μg/mL) followed by immunofluorescence. (**D**) Western blot of purified hyperphosphorylated RNAPII from HeLa-S3 nuclei as a function of phosphatase treatment as indicated on top, using the indicated antibodies.

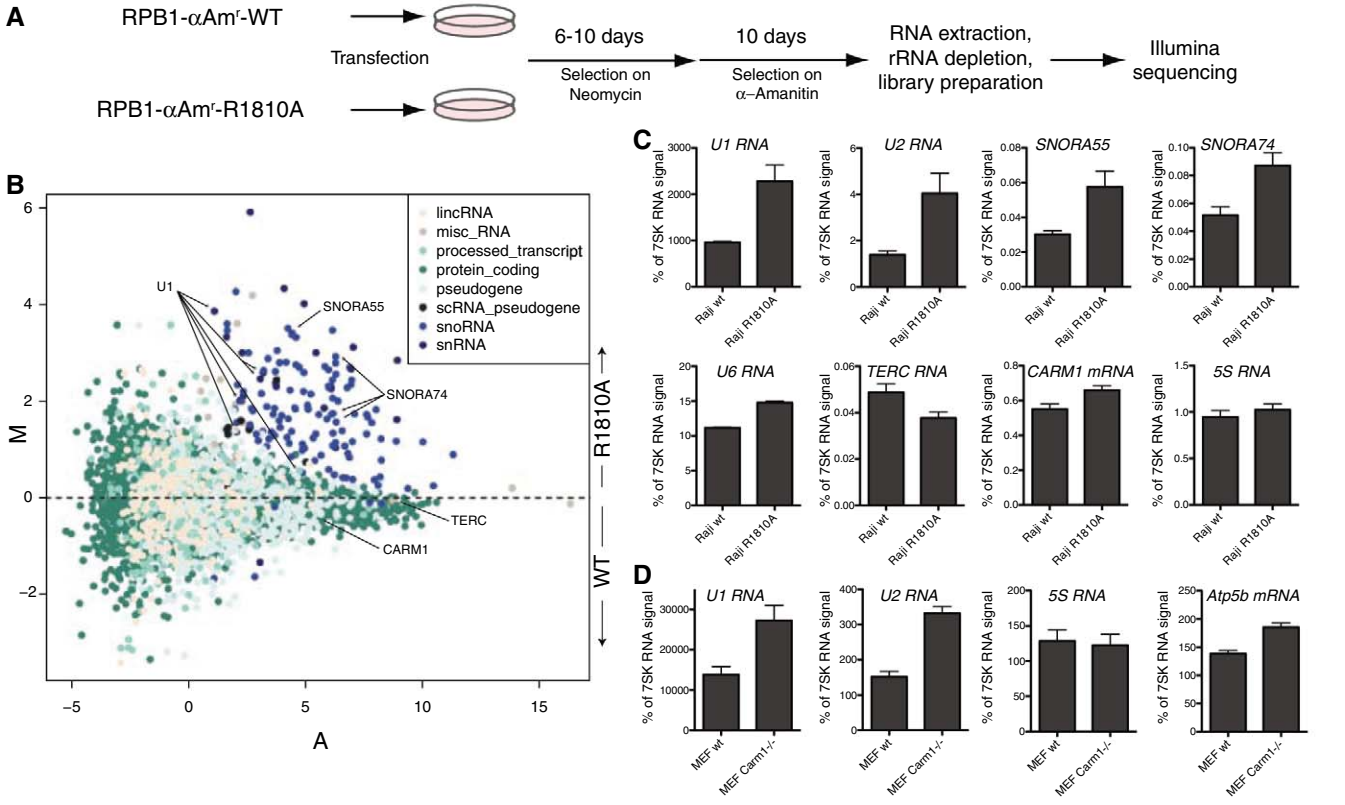

Fig. 4. R1810A mutation affects snRNA and snoRNA expression. (**A**) Schematic of the generation of Raji cells containing R1810A mutation and RNA-seq library preparation. (**B**) MA plot of genome-wide expression changes as determined with RNA-seq. Log_2 fold-changes (M) in normalized number of reads are plotted on the *y* axis, and average intensities (A) are plotted on the *x* axis. Each dot represents a gene from ENSEMBL59. Colors indicate gene biotypes; only the eight most numerous are depicted here. (**C**) Quantitative RT-PCR validation on Raji cells carrying WT or R1810A α-amanitin–resistant RNAPII. Top four plots show affected snRNAs and snoRNAs. Bottom four plots show expression levels of RNAs that were unaffected. Bars represent mean + SEM from two (WT) or three (R1810A) biological replicates and two independent cDNA preparations. (**D**) Quantitative RT-PCR analysis of WT and *Carm1*$^{-/-}$ MEF cells. Bars represent mean + SEM from two independent RNA preparations from MEFs at different passages.

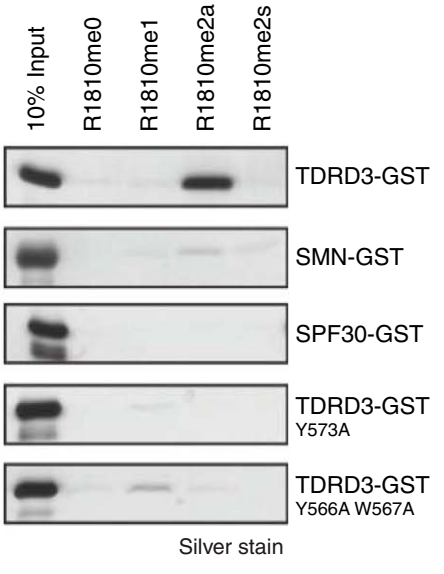

Fig. 5. The methylated CTD is recognized selectively by TDRD3. Shown are silver staining of fractions eluted from the immobilized biotinylated peptides containing different modifications at R1810, as indicated on top. TDRD3 tudor domain selectively recognized the R1810me2a peptide. Mutations at the indicated TDRD3 aromatic residues abolished binding.

The Tudor domains of several proteins specifically associate with methylated arginine residues (*16*–*18*). Tudor domain–containing proteins SMN, SPF30, and TDRD3 bind preferentially to both symmetric and asymmetric dimethyl arginine in the context of Gly-Arg patches (GR motifs). TDRD3 displayed a specific interaction with the R1810me2a-containing CTD peptide, as opposed to the unmodified CTD or mono- or symmetric-dimethylated R1810 (Fig. 5). In contrast, SMN and SPF30 did not exhibit affinity for either the unmodified CTD or any methylated version thereof. TDRD3 can be recruited to chromatin in a CARM1-dependent manner, although it is not clear whether histones or other substrates of CARM1 are recognized by this Tudor domain–containing protein (*19*). On the basis of the crystal structure of the TDRD3 tudor domain (Protein Data Bank ID 2D9T), we mutated residues typically responsible for binding to methylated arginines (Fig. 5, bottom). The relevant TDRD3 mutants did not bind R1810me2a, demonstrating that TDRD3 interaction with dimethyl-R1810 probably depends on an aromatic cage structure within its tudor domain. However, knockdown of TDRD3 did not result in the same genome-wide alterations of snRNA and snoRNA expression as in the case of either the R1810A mutant or *Carm1*$^{-/-}$ cells (fig. S5), suggesting that TDRD3 may be involved in a different function of CTD methylation, unrelated to snRNA and snoRNA regulation.

We have shown here that the CTD of RNAPII is methylated at R1810 by CARM1 in vitro and in vivo. This modification plays a role in the regulation of snRNA and snoRNA expression. In addition, the tudor domain of TDRD3 specifically recognizes CTD-R1810me2a. Although TDRD3 does not play a role in the regulation of snoRNA expression, it could very well participate in different downstream functions of CTD-R1810me2a.

References and Notes

1. S. Egloff, S. Murphy, *Trends Genet.* **24**, 280 (2008).
2. N. Fong, D. L. Bentley, *Genes Dev.* **15**, 1783 (2001).
3. T. Misteli, D. L. Spector, *Mol. Cell* **3**, 697 (1999).
4. K. Ryan, K. G. K. Murthy, S. Kaneko, J. L. Manley, *Mol. Cell. Biol.* **22**, 1684 (2002).
5. Materials and methods are available as supporting material on *Science* Online.
6. D. Cheng, J. Côté, S. Shaaban, M. T. Bedford, *Mol. Cell* **25**, 71 (2007).
7. N. Ohkura, M. Takahashi, H. Yaguchi, Y. Nagamura, T. Tsukada, *Biol. Chem.* **280**, 28927 (2005).

8. Single-letter abbreviations for the amino acid residues are as follows: A, Ala; C, Cys; D, Asp; E, Glu; F, Phe; G, Gly; H, His; I, Ile; K, Lys; L, Leu; M, Met; N, Asn; P, Pro; Q, Gln; R, Arg; S, Ser; T, Thr; V, Val; W, Trp; and Y, Tyr. In the mutants, other amino acids were substituted at certain locations; for example, H134R indicates that histidine at position 134 was replaced by arginine.
9. W. An, J. Kim, R. G. Roeder, *Cell* **117**, 735 (2004).
10. R. Métivier *et al.*, *Cell* **115**, 751 (2003).
11. M. Meininghaus, R. D. Chapman, M. Horndasch, D. Eick, *J. Biol. Chem.* **275**, 24375 (2000).
12. D. Baillat *et al.*, *Cell* **123**, 265 (2005).
13. S. Egloff *et al.*, *J. Biol. Chem.* **285**, 20564 (2010).
14. S. Egloff *et al.*, *Science* **318**, 1777 (2007).
15. N. Ohkura, M. Takahashi, H. Yaguchi, Y. Nagamura, T. Tsukada, *J. Biol. Chem.* **280**, 28927 (2005).
16. J. Côté, S. Richard, *J. Biol. Chem.* **280**, 28476 (2005).
17. N. Shaw *et al.*, *Nat. Struct. Mol. Biol.* **14**, 779 (2007).
18. R. Sprangers, M. R. Groves, I. Sinning, M. Sattler, *J. Mol. Biol.* **327**, 507 (2003).
19. Y. Z. Yang *et al.*, *Mol. Cell* **40**, 1016 (2010).

20. These studies were supported by the HHMI (to D.R.) and grants from NIH (GM-37120 to D.R. and GM-71166 to R.J.S.). R.B. is a fellow of the Helen Hay Whitney foundation. D.E. was supported by Deutsche Forschungsgemeinschaft (SFB/Transregio-5, SFB684) and José Carreras Leukämie-Stiftung eV. We thank L. Vales, E. Lecona, and P. Voigt for careful reading of the manuscript; R. D. Chapman and K. Burger for technical support; and members of the Reinberg lab for critical commentaries during the development of this project. RNA-seq data have been deposited in the National Center for Biotechnology Information's Gene Expression Omnibus as GEO series GSE27315.

Supporting Online Material

www.sciencemag.org/cgi/content/full/332/6025/99/DC1
Materials and Methods
Figs. S1 to S5
References

10 January 2011; accepted 22 February 2011
10.1126/science.1202663

Perception of UV-B by the *Arabidopsis* UVR8 Protein

Luca Rizzini,[1]* Jean-Jacques Favory,[1]* Catherine Cloix,[2] Davide Faggionato,[3] Andrew O'Hara,[2] Eirini Kaiserli,[2]† Ralf Baumeister,[3,4] Eberhard Schäfer,[1,4] Ferenc Nagy,[5,6] Gareth I. Jenkins,[2] Roman Ulm[1,4,7]‡

To optimize their growth and survival, plants perceive and respond to ultraviolet-B (UV-B) radiation. However, neither the molecular identity of the UV-B photoreceptor nor the photoperception mechanism is known. Here we show that dimers of the UVR8 protein perceive UV-B, probably by a tryptophan-based mechanism. Absorption of UV-B induces instant monomerization of the photoreceptor and interaction with COP1, the central regulator of light signaling. Thereby this signaling cascade controlled by UVR8 mediates UV-B photomorphogenic responses securing plant acclimation and thus promotes survival in sunlight.

Sunlight is of primary importance to sessile plants, both as an energy source to fuel photosynthesis and as an informational signal influencing their entire life cycle. Several families of plant photoreceptors have evolved that monitor light ranging from ultraviolet-B (UV-B) to the near infrared and allow optimal adaptation to light (*1*–*3*). Plant perception of UV-B radiation as an environmental stimulus is known to affect growth and development (*1*, *2*, *4*–*8*); however, no photoreceptor protein specifically sensing UV-B radiation has yet been molecularly identified.

We previously provided evidence for a specific pathway mediating molecular and physiological responses of *Arabidopsis* to low-level UV-B, involving the bZIP transcription factor ELONGATED HYPOCOTYL 5 (HY5), the E3 ubiquitin ligase CONSTITUTIVELY PHOTOMORPHOGENIC 1 (COP1), and the β-propeller protein UV RESISTANCE LOCUS 8 (UVR8) (*4*, *9*–*11*). UVR8 contains sequence similarity to the human guanine nucleotide exchange factor Regulator of Chromatin Condensation 1 (RCC1) (*12*); however, available evidence suggests that RCC1 and UVR8 differ in activity and function (*1*).

cop1 and *uvr8* mutants show no UV-B photomorphogenic responses, and COP1 and UVR8 proteins interact within minutes in planta in a strictly UV-B–dependent manner (*4*). Moreover, both proteins were found to accumulate in the nucleus under supplementary UV-B radiation (*11*, *13*). These properties are reminiscent of known photoreceptors (*3*, *4*). In agreement with such a function, we found that the UVR8-COP1 interaction also takes place in protein extracts in a very rapid, UV-B–dependent manner (Fig. 1A), mimicking the in planta situation described before (*4*). This feature allowed us to further investigate the requirements for this early response to UV-B. We UV-B–irradiated separately protein extracts containing either yellow

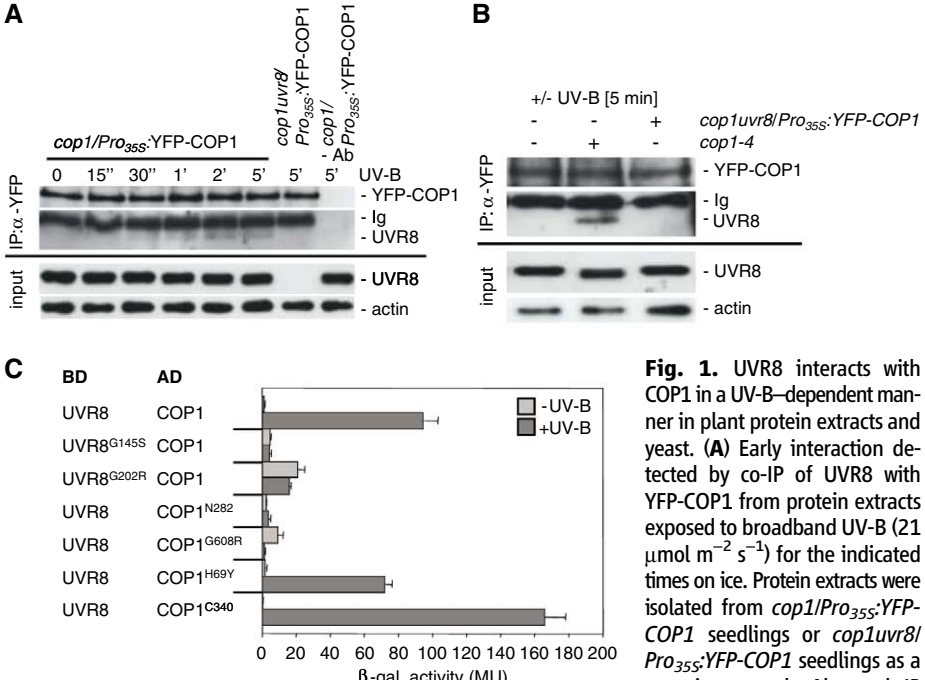

Fig. 1. UVR8 interacts with COP1 in a UV-B–dependent manner in plant protein extracts and yeast. (**A**) Early interaction detected by co-IP of UVR8 with YFP-COP1 from protein extracts exposed to broadband UV-B (21 μmol m^{-2} s^{-1}) for the indicated times on ice. Protein extracts were isolated from *cop1/Pro35S:YFP-COP1* seedlings or *cop1uvr8/Pro35S:YFP-COP1* seedlings as a negative control. -Ab, mock IP without antibodies to YFP; Ig, immunoglobulins. (**B**) Protein extracts were isolated from *cop1-4* and *cop1uvr8/Pro35S:YFP-COP1* seedlings and treated separately with UV-B (+, 21 μmol m^{-2} s^{-1}) or not (-) on ice. In combinations of the extracts, co-IP of UVR8 with YFP-COP1 was detected only when extracts containing UVR8 (*cop1-4*) were UV-B–treated and not when only YFP-COP1 was treated (*cop1uvr8/Pro35S:YFP-COP1*). (**C**) Yeast two-hybrid interaction of UVR8 and COP1 is UV-B–dependent (16 hours, 1.5 μmol m^{-2} s^{-1}) and is impaired in nonfunctional UVR8 and COP1 mutant proteins. β-gal., β-galactosidase; MU, Miller units.

[1]Faculty of Biology, Institute of Biology II, University of Freiburg, D-79104 Freiburg, Germany. [2]Institute of Molecular Cell and Systems Biology, University of Glasgow, Glasgow G12 8QQ, UK. [3]Faculty of Biology, Institute of Biology III, and Faculty of Medicine, ZBMZ, University of Freiburg, D-79104 Freiburg, Germany. [4]BIOSS Centre for Biological Signalling Studies, University of Freiburg, D-79104 Freiburg, Germany. [5]Institute of Plant Biology, Biological Research Centre, H-6726 Szeged, Hungary. [6]School of Biological Sciences, University of Edinburgh, Edinburgh EH9 3JR, UK. [7]Department of Botany and Plant Biology, University of Geneva, Sciences III, CH-1211 Geneva 4, Switzerland.

*These authors contributed equally to this work.
†Present address: The Salk Institute for Biological Studies, La Jolla, CA 92037, USA.
‡To whom correspondence should be addressed. E-mail: roman.ulm@unige.ch

fluorescent protein (YFP)–COP1 but not UVR8 (*cop1 uvr8*/*Pro*$_{35S}$*:YFP-COP1* line), or UVR8 but not YFP-COP1/COP1 (*cop1* mutant), and then mixed them with non-irradiated extracts containing the respective partner protein, followed by coimmunoprecipitation (co-IP) assays of UVR8 using antibodies to YFP (Fig. 1B). The results showed that UV-B irradiation of extracts containing UVR8 was both required and sufficient for the interaction with YFP-COP1 (Fig. 1B), indicating a primary function of UVR8 in UV-B signal perception.

The UVR8-COP1 interaction thus provided a robust readout to test whether an initial UV-B response could be synthetically generated in an heterologous system. We used the yeast two-hybrid test system in *Saccharomyces cerevisiae* to further examine the UVR8-COP1 interaction. It is necessary to note that yeast does not contain a COP1 homolog (*14*) nor a UVR8 protein [a structurally related protein is a bona fide RCC1 homolog (*12*, *15*)]. In yeast, UVR8 also interacted with COP1 in the presence of UV-B but not in its absence (Fig. 1C and fig. S1). This resembles the red- and blue light–specific interactions of phytochrome and cryptochrome photoreceptors with their early targets in yeast (*16*–*18*) and strongly indicates that UVR8 and COP1 are sufficient to constitute an early UV-B–specific response in a nonplant heterologous system.

Consistent with the evidence in planta (*4*, *10*), UVR8 proteins containing mutations that impair UV-B–induced photomorphogenesis in vivo, namely *uvr8-2* (UVR8^{N400}), *uvr8-9* (UVR8^{G202R}) and *uvr8-15* (UVR8^{G145S}), did not interact with wild-type COP1 (Fig. 1C and fig. S1). Similarly, nonfunctional mutant COP1 proteins representing *cop1-4* (COP1^{N282}) and *cop1-19* (COP1^{G608R}) did not interact with wild-type UVR8 (Fig. 1C and fig. S1). The failure of UVR8 interaction with the N-terminal 282 amino acids (COP1^{N282}) in the absence of C-terminal WD40 repeats indicated a requirement for this domain for the interaction. Consistent with this notion, expression of the C-terminal 340 amino acids (COP1^{C340}) comprising only WD40 repeats demonstrated that the WD40 domain of COP1 is sufficient for its interaction with UVR8 under UV-B (Fig. 1C and fig. S1). Moreover, COP1^{H69Y} still interacted with UVR8 in a UV-B–specific manner (Fig. 1C), in agreement with the ability of the corresponding *cop1*^{eid6} mutant to respond to UV-B (*11*). Together with the results from cell-free protein extracts, UV-B–specific interaction of UVR8 with COP1 in yeast further supports the conclusion that UVR8 constitutes a plant UV-B receptor.

Previously, we described constitutive UVR8 dimers in mustard by bimolecular fluorescence complementation (BiFC) in transient assays (*4*). However, reconstitution of a functional YFP in the BiFC assay is practicably irreversible, and thus dynamics cannot be captured (*19*). We therefore turned to more appropriate experimental systems to investigate UVR8 dimer dynamics. First, endogenous UVR8 protein was coimmunoprecipitated with CFP-UVR8 from *Pro*$_{35S}$*:CFP-UVR8* transgenic lines in a wild-type background (Fig. 2A). Negligible endogenous UVR8 was detected in the coimmunoprecipitates under supplemental UV-B, indicating a marked reduction in CFP-UVR8–UVR8 interaction that represents dimer formation (Fig. 2A). This strongly indicated the presence of UVR8 as a dimer in white light without UV-B and its monomerization under supplemental UV-B. In agreement with this indication, analysis of non–heat-denatured protein extracts revealed a marked accumulation of UVR8 monomers under supplemental UV-B as compared with minus–UV-B controls (Fig. 2B, upper panel). In these experiments, however, UVR8 was almost undetectable in the minus–UV-B control (note the weak cross-reacting band that is also detectable in the *uvr8-6* null mutant). In contrast to this observation, but in agreement with previously published data (*4*, *13*), UVR8 protein levels were similar when parallel samples were denatured by boiling (Fig. 2B, upper panel). Thus, our antibodies to UVR8 clearly failed to detect the epitope on non–UV-B-irradiated UVR8. When the gel was irradiated with UV-B before protein transfer to the membrane, a prominent band of higher molecular weight was detected in the same extracts under these conditions. This suggested that UV-B irradiation of UVR8 increased accessibility of the epitope on endogenous UVR8 (Fig. 2B, lower panel) and thus indicated an in-gel conformational change in UVR8 upon UV-B perception linked to the in vivo monomerization of the UVR8 dimers. UVR8 monomerization was found to be a very rapid process detectable after 5 s of UV-B treatment of

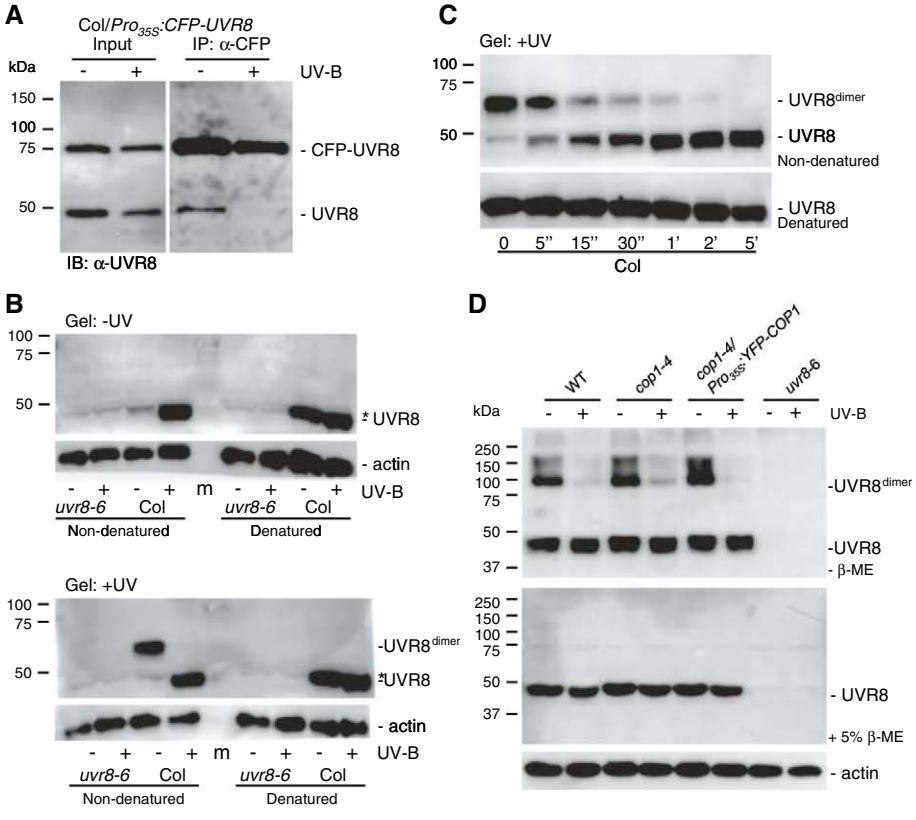

Fig. 2. UVR8 forms dimers in the absence of UV-B and monomerizes in a UV-B–dependent manner. (**A**) Co-IP of endogenous UVR8 with CFP-UVR8 from Col/*Pro*$_{35S}$*:CFP-UVR8* was reduced when seedlings were treated with UV-B (1 hour, 21 μmol m^{-2} s^{-1}). (**B**) UVR8 dimers were detectable in non–heat-denatured samples of *Arabidopsis* protein extracts not treated with UV-B (-), but only if the protein gel was irradiated by UV-B after the gel run (15 min, 21 μmol m^{-2} s^{-1}) and before transfer to a membrane (lower panel). Under non–heat-denatured conditions, the apparent UVR8 dimer size is smaller than the expected 94 kD, indicating that the electrophoretic behavior of the not-fully-denatured UVR8 dimer is anomalous. Treatment of protein extracts by UV-B (5 min, 21 μmol m^{-2} s^{-1}) resulted in UVR8 monomerization. Parallel denatured samples demonstrated equal amounts of UVR8 protein. Actin levels are shown as loading controls. (**C**) Time course analysis of UVR8 monomerization in cell-free plant extracts after exposure to UV-B (21 μmol m^{-2} s^{-1}) on ice for the indicated times. The gel blot of heat-denatured proteins shows equal UVR8 protein amounts. (**D**) UVR8 dimers are cross-linked by DSP, which is reversible by reducing agents (β-ME), showing equal protein amounts. UV-B (5 min, 21 μmol m^{-2} s^{-1}) resulted in a decrease of UVR8 dimers, which was independent of COP1. The UV-B irradiation conditions that result in UVR8 monomerization correspond to the ones causing UVR8-dependent gene expression changes in vivo [SOM and (*4*, *9*, *11*)].

protein extracts on ice (Fig. 2C). Moreover, UVR8 monomerization was fluence rate–dependent and displayed a reciprocal relationship between treatment duration and fluence rate under the tested conditions (fig. S2). Finally, the decrease of UVR8 dimers upon UV-B irradiation was also apparent when proteins were cross-linked using dithiobis(succinimidyl propionate) (DSP) (Fig. 2D, upper panel), which generates reversible protein-protein cross-links that can be cleaved by β-mercaptoethanol (β-ME) (Fig. 2D, lower panel).

To investigate whether COP1 affects UVR8 monomerization, we used DSP cross-linking on protein extracts from *cop1-4* seedlings treated or not treated with UV-B. UVR8 monomerization was similar in *cop1-4* and the wild type, demonstrating that UVR8 monomerization does not require functional COP1 protein (Fig. 2D). Together, these results demonstrate rapid monomerization of UVR8 dimers, probably as the result of the direct perception of UV-B by UVR8 and an associated conformational change (as suggested by epitope detection only after UV-B irradiation of UVR8 before or after electrophoresis, or after heat denaturation).

To further challenge the conclusion that the UVR8 protein has UV-B photoreceptor properties, we examined whether UVR8 monomerization also happens in heterologous systems. Indeed, dimers were detected when UVR8 was expressed in yeast cells grown under conditions devoid of UV-B radiation. In contrast, only UVR8 monomers were found after yeast was irradiated with supplemental UV-B (Fig. 3A). UVR8 mutants that are nonfunctional and incapable of interacting with COP1 were also unable to form dimers (Fig. 3A). Similar to yeast, UVR8 dimers from transfected human embryonic kidney (HEK) 293T cells monomerized in response to UV-B (Fig. 3B).

Aromatic amino acids absorb UV-B radiation. Tryptophan, with an absorption maximum in solution at around 280 nm (which extends to 300 nm and is likely to be further shifted in a protein environment), is particularly suited as a potential UV-B chromophore (*20*, *21*) (UV-B: 280 to 315 nm). This is in agreement with a recent action spectrum for *HY5* gene activation by UVR8 that identified peaks at 280 and 300 nm (*22*). Structure modeling according to the structurally related human RCC1 protein (*12*, *23*) identified 14 tryptophans of UVR8 (the similarly sized human RCC1 contains only four), all located at the top of the predicted UVR8 β-propeller structure (fig. S3), with a particularly intriguing cluster at positions 233, 285, and 337 in the center of the protein structure (Fig. 3C and fig. S3). To examine the potential involvement of these tryptophans in UV-B sensing, they were targeted by mutagenesis, changing them to alanine (UVR8^{W285A} and UVR8^{W337A}) or phenylalanine (UVR8^{W233F}, UVR8^{W285F}, and UVR8^{W337F}). Whereas the W285A, W337A, and W233F mutations abrogated dimerization and W337F still showed UV-B–induced monomerization, mutation of tryptophan-285 to phenylalanine resulted in a constitutive UVR8 dimer with no response to UV-B (Fig. 3D and fig. S4). Yeast two-hybrid analysis revealed a constitutive interaction of UVR8^{W285A} with COP1, although not as strong as the UV-B–induced interaction of the wild-type proteins, and absolutely no interaction of UVR8^{W285F} with COP1 (Fig. 3E). The latter was of particular interest, because dimer formation indicated that the overall structure was largely unaffected by the moderate single tryptophan-to-phenylalanine exchange, whereas UV-B perception was abrogated (absorption maximum of phenylalanine at 257 nm).

Taken together, the results presented here provide strong evidence that plant perception of UV-B is mediated by UVR8 as a UV-B–specific photoreceptor, and they support a tryptophan-based perception mechanism, with tryptophan-285 as a key residue. The UV-B–driven monomerization of the UVR8 dimers signals the receptor activation, which then is followed by interaction with COP1 to relay the signal. The constitutive expression of UVR8 throughout the plant (fig. S5) (*4*, *13*) allows any plant organ to immediately respond to UV-B exposure and to mount protective measures. UVR8 proteins are broadly present and well conserved among plants (fig. S6). This raises the intriguing possibility that, together with the development of an ozone layer in the stratosphere of Earth (*24*), the evolution of terrestrial plants may be coincident with the acquisition of the UV-induced responses mediated by the UVR8 UV-B photoreceptor.

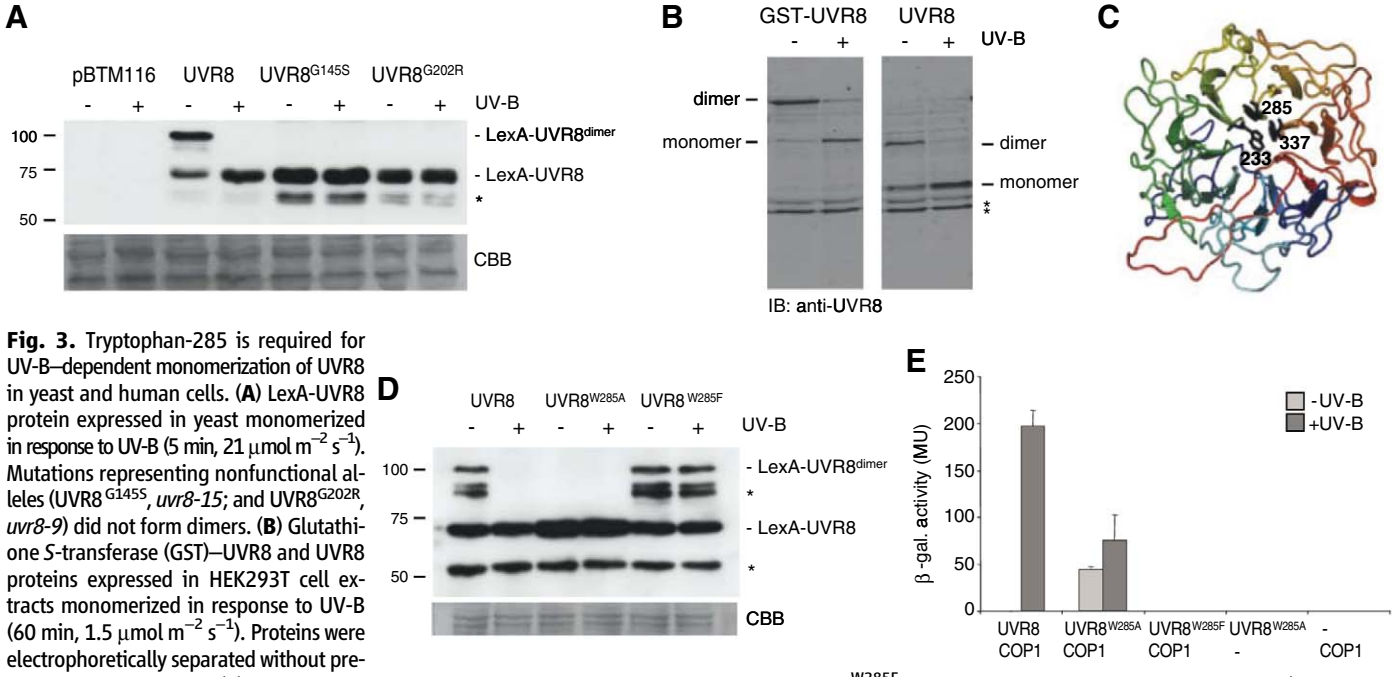

Fig. 3. Tryptophan-285 is required for UV-B–dependent monomerization of UVR8 in yeast and human cells. (**A**) LexA-UVR8 protein expressed in yeast monomerized in response to UV-B (5 min, 21 μmol m^{-2} s^{-1}). Mutations representing nonfunctional alleles (UVR8^{G145S}, *uvr8-15*; and UVR8^{G202R}, *uvr8-9*) did not form dimers. (**B**) Glutathione *S*-transferase (GST)–UVR8 and UVR8 proteins expressed in HEK293T cell extracts monomerized in response to UV-B (60 min, 1.5 μmol m^{-2} s^{-1}). Proteins were electrophoretically separated without previous heat denaturation. (**C**) Predicted structure of UVR8, including in particular the tryptophan cluster with the tryptophan-233, -285, and -337 residues. (**D**) Dependence on tryptophan-285 for UV-B–mediated UVR8 monomerization in yeast. UVR8^{W285A} did not form dimers, whereas UVR8^{W285F} formed dimers but did not monomerize in response to UV-B (5 min, 21 μmol m^{-2} s^{-1}). (**E**) UVR8^{W285A} interacted constitutively with COP1 in a yeast two-hybrid assay, whereas UVR8^{W285F} was impaired in its interaction with COP1 (16 hours of UV-B, 1.5 μmol m^{-2} s^{-1}). (A) and (D) Proteins were electrophoretically separated without previous heat denaturation. The protein gel blot was probed with an antibody to LexA, and the Coomassie brilliant blue (CBB)–stained membrane is shown as a loading control. In (A), (B), and (D), the asterisks indicate degradation products.

References and Notes

1. G. I. Jenkins, *Annu. Rev. Plant Biol.* **60**, 407 (2009).
2. R. Ulm, F. Nagy, *Curr. Opin. Plant Biol.* **8**, 477 (2005).
3. C. Kami, S. Lorrain, P. Hornitschek, C. Fankhauser, *Curr. Top. Dev. Biol.* **91**, 29 (2010).
4. J. J. Favory *et al.*, *EMBO J.* **28**, 591 (2009).
5. J. J. Wargent, V. C. Gegas, G. I. Jenkins, J. H. Doonan, N. D. Paul, *New Phytol.* **183**, 315 (2009).
6. H. Frohnmeyer, D. Staiger, *Plant Physiol.* **133**, 1420 (2003).
7. N. D. Paul, D. Gwynn-Jones, *Trends Ecol. Evol.* **18**, 48 (2003).
8. H. Tong *et al.*, *Proc. Natl. Acad. Sci. U.S.A.* **105**, 21039 (2008).
9. R. Ulm *et al.*, *Proc. Natl. Acad. Sci. U.S.A.* **101**, 1397 (2004).
10. B. A. Brown *et al.*, *Proc. Natl. Acad. Sci. U.S.A.* **102**, 18225 (2005).
11. A. Oravecz *et al.*, *Plant Cell* **18**, 1975 (2006).
12. D. J. Kliebenstein, J. E. Lim, L. G. Landry, R. L. Last, *Plant Physiol.* **130**, 234 (2002).
13. E. Kaiserli, G. I. Jenkins, *Plant Cell* **19**, 2662 (2007).
14. C. Yi, X. W. Deng, *Trends Cell Biol.* **15**, 618 (2005).
15. M. Fleischmann *et al.*, *Mol. Gen. Genet.* **227**, 417 (1991).
16. S. Shimizu-Sato, E. Huq, J. M. Tepperman, P. H. Quail, *Nat. Biotechnol.* **20**, 1041 (2002).
17. A. Hiltbrunner *et al.*, *Curr. Biol.* **15**, 2125 (2005).
18. H. Liu *et al.*, *Science* **322**, 1535 (2008).
19. T. K. Kerppola, *Nat. Rev. Mol. Cell Biol.* **7**, 449 (2006).
20. D. Creed, *Photochem. Photobiol.* **39**, 537 (1984).
21. E. Fritsche *et al.*, *Proc. Natl. Acad. Sci. U.S.A.* **104**, 8851 (2007).
22. B. A. Brown, L. R. Headland, G. I. Jenkins, *Photochem. Photobiol.* **85**, 1147 (2009).
23. L. Renault *et al.*, *Nature* **392**, 97 (1998).
24. J. Rozema, J. van de Staaij, L. O. Björn, M. Caldwell, *Trends Ecol. Evol.* **12**, 22 (1997).

25. We thank L.-O. Essen, J. Paszkowski, and T. Kunkel for helpful comments and advice, and P. King for editing the manuscript. This research was supported by grants from the UK Biotechnology and Biological Sciences Research Council and the Leverhulme Trust to G.I.J.; the Scottish Universities Life Science Alliance and the Hungarian Scientific Research Fund (OTKA-81399) to F.N.; the Sonderforschungsbereich (SFB) 592 to R.B.; the Excellence Initiative of the German Federal and State Governments (EXC 294) and the SFB 746 to R.B., E.S., and R.U.; and the Emmy Noether Programme of the Deutsche Forschungsgemeinschaft (grant UL341/1-1) to R.U.

Supporting Online Material

www.sciencemag.org/cgi/content/full/332/6025/103/DC1
Materials and Methods
Figs. S1 to S7
References

19 November 2010; accepted 18 February 2011
10.1126/science.1200660

Bacteria-Phage Antagonistic Coevolution in Soil

Pedro Gómez[1,2]* and Angus Buckling[1,3]

Bacteria and their viruses (phages) undergo rapid coevolution in test tubes, but the relevance to natural environments is unclear. By using a "mark-recapture" approach, we showed rapid coevolution of bacteria and phages in a soil community. Unlike coevolution in vitro, which is characterized by increases in infectivity and resistance through time (arms race dynamics), coevolution in soil resulted in hosts more resistant to their contemporary than past and future parasites (fluctuating selection dynamics). Fluctuating selection dynamics, which can potentially continue indefinitely, can be explained by fitness costs constraining the evolution of high levels of resistance in soil. These results suggest that rapid coevolution between bacteria and phage is likely to play a key role in structuring natural microbial communities.

Host-parasite antagonistic coevolution—the reciprocal evolution of host defense and parasite counter-defense—is theoretically crucial to a range of ecological and evolutionary processes, including population dynamics and extinction risk, the evolution of diversity and speciation, the evolution of sex and mutation rates, and the evolutionary ecology of pathogen virulence (*1*–*4*). A number of excellent studies have inferred the operation of host-parasite coevolution in natural populations from patterns of local adaptation of parasites to their hosts in space and time (*5*–*10*). However, genetic variation between the host populations in space and time may be driven by parasite-imposed selection but could equally be driven by neutral process or additional selection pressures. A direct demonstration of coevolution requires evidence of host adaptation to parasites as well as parasite adaptation to hosts.

Antagonistic coevolution between bacteria and their ubiquitous parasites, bacteriophage (phage), is likely to be of particularly broad importance because of their extremely rapid rates of evolution (*3*, *11*)—the key role played by bacteria in ecosystem functioning—and the therapeutic use of phages as "evolving" antibiotics in agricultural and clinical contexts (*11*). Both the dynamics and consequences of coevolution between bacteria and viruses have been extensively studied in the laboratory (*12*, *13*), but little is known about the extent or role of rapid bacteria-phage coevolution in natural populations (*14*, *15*). Given that phages are typically highly specific to bacteria species and even genotypes (*11*) and the massive amount of diversity present in microbial communities (*16*), a given interacting bacteria and phage population is likely to make up a tiny fraction of the microbial community. It is therefore unclear whether phages, which only encounter hosts passively, impose sufficient selection on bacteria for rapid coevolution to occur.

We used a "mark-recapture" approach (*17*) to follow the ecological and evolutionary dynamics of a soil bacteria clone, *Pseudomonas fluorescens* SBW25, and a naturally associated lytic bacteriophage clone SBW25ϕ2 (*18*) in soil microcosms. Despite these organisms having been used extensively for in vitro evolution studies (*13*), they were frozen shortly after their original isolation and hence would have undergone little laboratory adaptation before our experiment. The

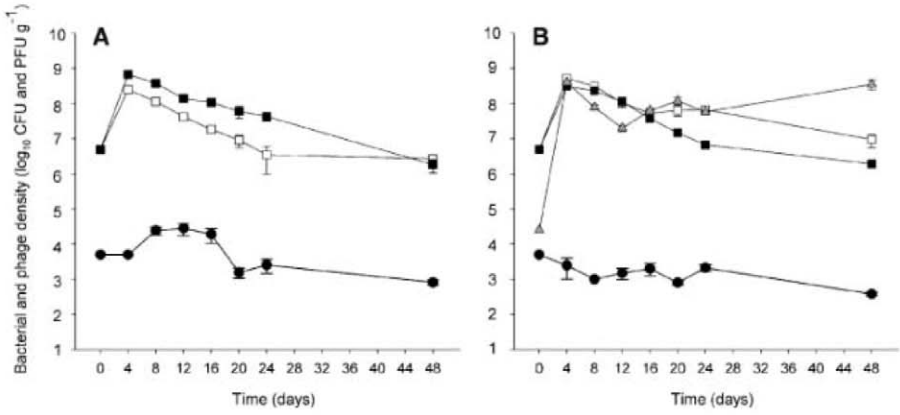

Fig. 1. Population dynamics of the bacterial and phage populations. Connected symbols show densities through time [mean $\log_{10}$(colony forming units/g soil) for bacteria or $\log_{10}$(plaque forming units/g soil) for phage, ± SEM] of phage SBW25ϕ2 (●); *P. fluorescens* SBW25 evolved in the presence (■) or absence (□) of phage; and the culturable fraction of the natural community (▲). Populations were evolved in the (**A**) absence and (**B**) presence of the natural community.

[1]Department of Zoology, University of Oxford, Oxford OX1 3PS, UK. [2]Centro de Edafología y Biología Aplicada del Segura, Consejo Superior de Investigaciones Científicas (CEBAS-CSIC), Murcia (Espinardo) 30100, Spain. [3]Biosciences, University of Exeter, Penryn TR10 9EZ, UK.

*To whom correspondence should be addressed. E-mail: pedro.gomezlopez@zoo.ox.ac.uk

phage, which is infectious to SBW25, can only be transmitted by lysis of the bacterial cell, resulting in the reciprocal evolution of resistant bacteria and infectious phages in nutrient media (*18*). Having established that no culturable bacteria in our soil were resistant to the antibiotic gentamicin (or could be infected by the experimental phage), we used an engineered gentamicin-resistant strain of *P. fluorescens* SBW25 (*3*) to inoculate the soil microcosms. All recovered bacteria that could grow on gentamicin therefore descended from the inoculated ancestral population. Similarly, we established that there were no phages in the soil that were able to infect *P. fluorescens* SBW25; hence, all recovered phages that could infect *P. fluorescens* SBW25 descended from the inoculated phage population. In an attempt to disentangle effects of the physical and biotic components of the soil environment, we cultured our bacteria and phage in sterilized soil, in which the resident microbial community had been reinoculated in some replicate communities but not in others. Samples from the replicate soil communities (eight per treatment combination) were collected every 4 days for 24 days, with a further sample taken after 48 days. At each time point, we determined densities and resistance and infectivity of the focal bacteria and phage, as well as densities of the culturable component of the total bacterial community, by plating onto antibiotic-free agar.

Phages reduced the mean density of the *P. fluorescens* population in the presence of the natural community, whereas in the absence of the natural community phages actually increased mean *P. fluorescens* density (generalized linear mixed model, interaction between presence/absence of natural community and phages: $F_{1,28} = 60$, $P < 0.0001$) (Fig. 1). In cases in which both bacteria and phages were co-inoculated, the presence of the natural community significantly reduced densities of bacteria ($F_{1,14} = 23.5$, $P < 0.001$) and phages ($F_{1,14} = 132.4$, $P < 0.001$) (Fig. 1B). The density-increasing effect of phages in the absence of the natural community is surprising, and its potential implications for the therapeutic use of phages warrants extensive future investigation. However, we speculated that phages selectively killed growing and not stationary cells (*19*), and the presence of high frequencies of growing cells [growth advantage in stationary phase (GASP) mutants] under nutrient limitation reduced population sizes (*20*). In contrast, selective elimination of growing *P. fluorescens* cells by phages did not increase *P. fluorescens* density in the presence of the natural community because this community also inevitably contained growing cells of different species.

Coevolution between this bacteria and phage in laboratory media typically results in the evolution of increased resistance and infectivity ranges through time (arms race dynamics) (*13*). Specifically, bacteria are more resistant to past than contemporary phages and more resistant to contemporary than future phages (*13*, *21*); the same pattern holds for phage infectivity. To determine whether this coevolutionary dynamic occurred in soil, we measured the infectivity to bacteria isolated from day 24 of ancestral (day 0) phages (past) and phages isolated from days 24 (contemporary) and 48 (future) within each replicate. Similarly, we measured the resistance of ancestral (day 0) bacteria (past) and bacteria from days 24 (contemporary) and 48 (future) to phages from day 24. In contrast to results in laboratory media, bacteria were more resistant to their contemporary than past and future phages (Friedman test of effect of time, with replicate fitted as a blocking factor: $P < 0.01$; $n = 16$ populations) (Fig. 2, A and B), and phages were least infective to contemporary than past and future bacteria ($P < 0.01$; $n = 16$ populations) (Fig. 2, C and D), with no effect of the presence of the natural community on resistance/infectivity patterns (Mann-Whitney tests: $P > 0.2$ for resistance/infectivity at each time point, and changes in time). This significantly greater resistance of bacteria to contemporary than to noncontemporary phages (and corresponding lower infectivity of phages) held when comparisons were made only between days 24 and 48 (Wilcoxon paired sample test: $P = 0.02$; $n = 16$ populations). We extended our measurements to all sampled time points and found the frequency of bacteria resistant to the ancestral (time zero) and contemporary phages to be approximately 2 and 10%, respectively (paired t tests of resistance to contemporary versus ancestral phages, averaged through time: $t = 3.5$, $P < 0.01$; $t = 10.2$, $P < 0.001$, $n = 16$ populations, for absence and presence of natural community, respectively) (Fig. 3), with the difference in resistance to contemporary and ancestral phages greater for populations evolved in the presence of the natural community (independent sample t test: $t = 6.0$, $P < 0.01$, $n = 16$ populations). Taken together, these results demonstrate that bacteria and phage rapidly evolve, but that they are not undergoing arms race coevolution.

The data are, however, consistent with coevolution in which parasite genotypes specialize on host genotypes, and fitness of a given genotype fluctuates through time (fluctuating selection dynamics) (*2*, *5*, *6*). If parasites adapt more rapidly than do hosts, fluctuating selection dynamics are on average expected to result in parasites better adapted to their contemporary compared with past and future hosts, and vice versa if hosts adapt more rapidly than do parasites (*6*). Our data show the latter pattern, unequivocally demon-

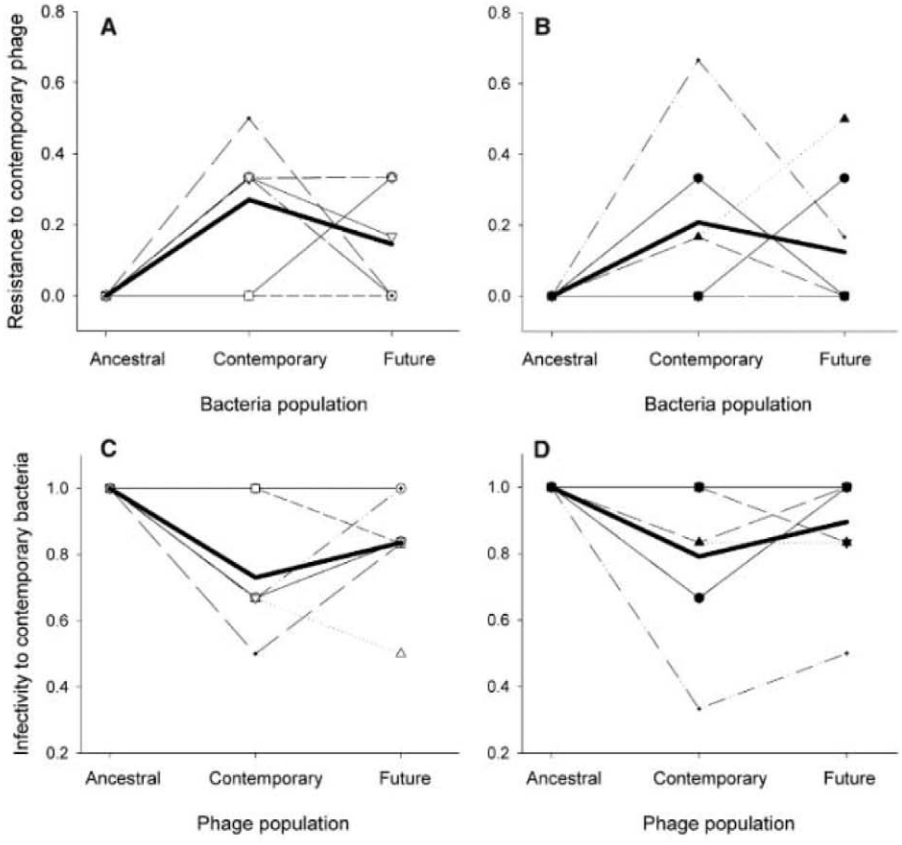

Fig. 2. Coevolutionary dynamics of bacteria and phages. Proportion of *P. fluorescens* isolated from day 24 resistant to ancestral (day 0) phage, contemporary (day 24), and future (day 48) phage populations evolved in the (**A**) absence and (**B**) presence of the natural community. Proportion of ancestral (day 0), day 24, and day 48 *P. fluorescens* susceptible to day 24 phages evolved in the (**C**) absence and (**D**) presence of the natural community. Individual thin lines indicate the eight separate replicates in each treatment; bold lines indicate means for all populations.

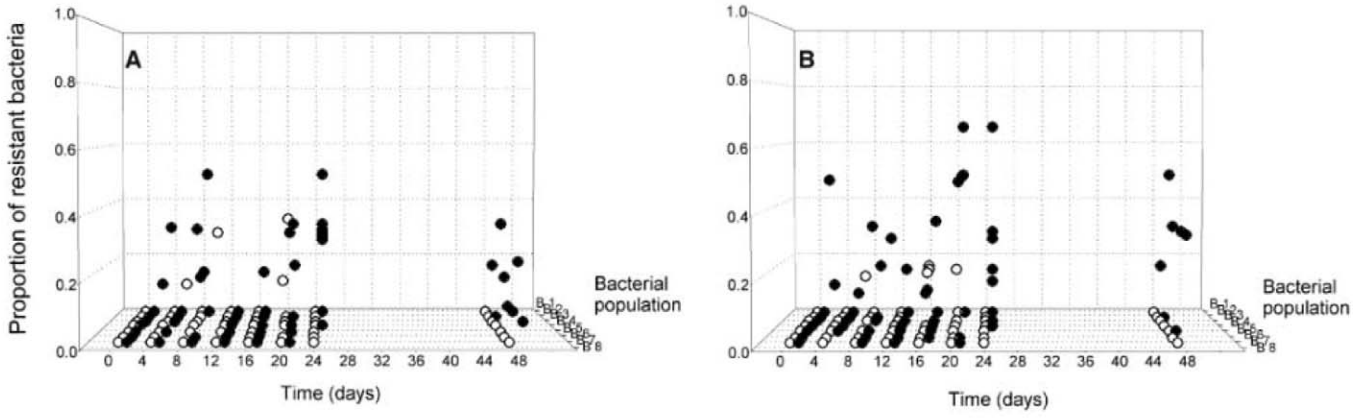

Fig. 3. Resistance of bacteria to ancestral and contemporary phages. Proportion of *P. fluorescens* resistant to the common ancestral (day 0) (○) and contemporary (●) phage populations evolved in the (**A**) absence and (**B**) presence of the natural community for all populations through time. No resistance to phages was detected in *P. fluorescens* populations evolved in the absence of phages.

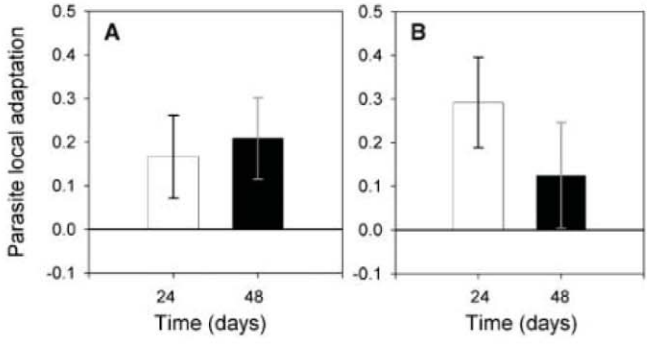

Fig. 4. Phage local adaptation. Mean local adaptation (proportion of local to foreign clones of bacteria susceptible to local phages) ± SEM measured at days 24 and 48 in the (**A**) absence and (**B**) presence of the natural community.

strating adaptation of bacteria populations to the evolving phage populations. Phages require susceptible hosts to propagate; hence, it is almost certain that evolutionary changes in phage infectivity also result from adaptation to evolving hosts. The operation of fluctuating selection dynamics is important because this type of coevolution can potentially continue indefinitely and maintain genetic diversity within populations (*2*), whereas arms race dynamics purge diversity and require a continual supply of novel mutations, so may be short-lived.

In an attempt to obtain more direct evidence of phage adaptation to evolving bacteria, we measured interactions between bacteria and phages in space as well as time by comparing the infectivity of phages to their local bacteria with infectivity to bacteria from replicate microcosms. We found that phages were significantly locally adapted, performing consistently better on local as compared with foreign bacteria (paired *t* test of infectivity to local versus foreign phages, averaged through time: $t = 3.4$, $P < 0.01$, $n = 16$ populations) (Fig. 4), with no difference between communities evolved in the presence or absence of natural communities (*t* test: $P > 0.2$). These data unequivocally demonstrate that phages adapt to changes in bacterial resistance.

Consistent local adaptation in space is commonly used to infer greater rates of adaptation of one evolving partner over the other in putative coevolutionary interactions (*22*, *23*). Our spatial data would therefore suggest phages adapt more rapidly than do bacteria. However, this interpretation is in apparent contrast to the direct measurements of adaptation in time, which suggest that bacteria adapt more rapidly than do phages. These results suggest that host-parasite adaptation in space and time need not be positively correlated (*6*) and that local adaptation in space may tell us little about relative rates of adaptation.

Despite direct evidence for bacteria-phage coevolution in soil, the fluctuating coevolutionary dynamics are markedly different from the arms race dynamics observed in high-nutrient broth, in which bacteria and phages with increasingly broad resistance and infectivity ranges, respectively, are favored through time. What limits the evolution of bacterial resistance and phage infectivity in soil, resulting in the change from arms race dynamics in vitro to fluctuating selection dynamics in soil? Theory suggests that growth-rate costs associated with resistance and infectivity might be important (*24*, *25*), and there is evidence for bacteria bearing costs of resistance to phage (*26*, *27*), and that these costs are greater in less productive environments (*28*). We therefore hypothesized that resistance was more costly in soil, which typically supports lower microbial biomass than does high-nutrient media. To test this hypothesis, we examined the competitive ability (relative to ancestral bacteria) of soil-evolved phage-resistant and -sensitive clones of bacteria in both broth and soil environments in the absence of phages. After competing for 2 days in high-nutrient broth in the absence of phages, no competitive costs associated with resistance were detected [(generalized linear model (GLM), phage-resistant versus -sensitive clones: $P > 0.2$) (fig. S1). In contrast, there was an approximately 36% reduction in relative fitness associated with resistance in soil (GLM, phage-resistant versus sensitive clones: $F_{1,21} = 7.6$, $P = 0.01$) (fig. S1), which did not differ between resistant clones that had evolved in the presence and absence of the natural community (presence versus absence of natural community: $P > 0.2$) (fig. S1). The costs associated with phage resistance in soil may explain why the evolution of resistance in soil is limited to co-occurring phages rather than to a wide range of previously encountered phage populations observed during coevolution in nutrient broth (*18*).

Despite considerable differences between the population dynamics of the focal bacteria and phages in the presence versus the absence of the natural microbial community, coevolutionary dynamics were very similar. There was no difference in the magnitude of parasite local adaptation in space (Fig. 4) and only small differences in patterns of adaptation in time, with an approximately 4% greater resistance to contemporary phages in the presence of the natural community (Fig. 3). If anything, we expected weaker selection for resistance, and less coevolution, in the presence compared with absence of the natural community, in part because of the reduced densities of the focal bacteria and phages (Fig. 1) (*28*). The limited impact of the microbial community on coevolution suggests that intraspecific competition and parasitism play a more substantial role than interspecific competition in driving evolution within microbial soil communities.

Our results show that bacteria and phage rapidly coevolve in soil, with very similar dynamics in the presence and absence of the natural

microbial community. Coevolution altered ecological population dynamics and resulted in bacteria adapted to phages in time and phages adapted to bacteria in space. Unlike coevolution in high-nutrient broth, coevolutionary dynamics in soil appear to be driven by fluctuating selection—a form of coevolution that can potentially continue indefinitely. These results suggest that rapid bacteria-phage coevolution, and not just purely ecological interactions, are likely to be crucial in explaining the structure, population dynamics, and ultimately the function of natural microbial communities.

References and Notes

1. J. J. Bull, *Evolution* **48**, 1423 (1994).
2. W. D. Hamilton, *Oikos* **35**, 282 (1980).
3. C. Pal, M. D. Maciá, A. Oliver, I. Schachar, A. Buckling, *Nature* **450**, 1079 (2007).
4. J. N. Thompson, *The Geographic Mosaic of Coevolution* (Univ. of Chicago Press, Chicago, 2005).
5. E. Decaestecker *et al.*, *Nature* **450**, 870 (2007).
6. S. Gandon, A. Buckling, E. Decaestecker, T. Day, *J. Evol. Biol.* **21**, 1861 (2008).
7. C. M. Lively, M. F. Dybdahl, *Nature* **405**, 679 (2000).
8. M. A. Parker, *Evolution* **39**, 713 (1985).
9. P. H. Thrall, J. J. Burdon, J. D. Bever, *Evolution* **56**, 1340 (2002).
10. D. Ebert, *Science* **265**, 1084 (1994).
11. B. R. Levin, J. J. Bull, *Nat. Rev. Microbiol.* **2**, 166 (2004).
12. B. J. M. Bohannan, R. E. Lenski, *Ecol. Lett.* **3**, 362 (2000).
13. M. A. Brockhurst, A. D. Morgan, A. Fenton, A. Buckling, *Infect. Genet. Evol.* **7**, 547 (2007).
14. M. Vos, P. J. Birkett, E. Birch, R. I. Griffiths, A. Buckling, *Science* **325**, 833 (2009).
15. N. L. Held, R. J. Whitaker, *Environ. Microbiol.* **11**, 457 (2009).
16. J. Gans, M. Wolinsky, J. Dunbar, *Science* **309**, 1387 (2005).
17. Materials and methods are available as supporting material on *Science* Online.
18. A. Buckling, P. B. Rainey, *Proc. R. Soc. Biol.* **269**, 931 (2002).
19. M. H. Adams, *Bacteriophages* (Wiley, New York, 1959).
20. S. E. Finkel, *Nat. Rev. Microbiol.* **4**, 113 (2006).
21. M. A. Brockhurst, A. D. Morgan, P. B. Rainey, A. Buckling, *Ecol. Lett.* **6**, 975 (2003).
22. M. A. Greischar, B. Koskella, *Ecol. Lett.* **10**, 418 (2007).
23. J. D. Hoeksema, S. E. Forde, *Am. Nat.* **171**, 275 (2008).
24. A. Agrawal, C. M. Lively, *Evol. Ecol. Res.* **4**, 79 (2002).
25. A. Sasaki, *Proc. R. Soc. Biol.* **267**, 2183 (2000).
26. A. Buckling, Y. Wei, R. C. Massey, M. A. Brockhurst, M. E. Hochberg, *Proc. R. Soc. Biol.* **273**, 45 (2006).
27. J. T. Lennon, S. A. M. Khatana, M. F. Marston, J. B. H. Martiny, *ISME J.* **1**, 300 (2007).
28. L. D. C. Lopez-Pascua, A. Buckling, *J. Evol. Biol.* **21**, 853 (2008).

29. We thank T. Bell and A. Hall for comments on the manuscript. The work was supported by the European Research Council. P.G. was supported from Ministerio de Ciencia e Innovación (MICINN, Spain) by National Mobility Program of Human Resources "Jose Castillejo." Partial 16*S* ribosomal RNA sequences have been assigned to the European Nucleotide Archive, European Molecular Biology Laboratory—European Bioinformatics Institute, under accession numbers FR746065 to FR746094.

Supporting Online Material

www.sciencemag.org/cgi/content/full/332/6025/106/DC1
Materials and Methods
Fig. S1
References

6 October 2010; accepted 1 March 2011
10.1126/science.1198767

Differences in Thermal Tolerance Among Sockeye Salmon Populations

Erika J. Eliason,[1]* Timothy D. Clark,[1,2,3] Merran J. Hague,[4] Linda M. Hanson,[2] Zoë S. Gallagher,[1] Ken M. Jeffries,[3] Marika K. Gale,[3] David A. Patterson,[4] Scott G. Hinch,[3] Anthony P. Farrell[1,2]

Climate change–induced increases in summer water temperature have been associated with elevated mortality of adult sockeye salmon (*Oncorhynchus nerka*) during river migration. We show that cardiorespiratory physiology varies at the population level among Fraser River sockeye salmon and relates to historical environmental conditions encountered while migrating. Fish from populations with more challenging migratory environments have greater aerobic scope, larger hearts, and better coronary supply. Furthermore, thermal optima for aerobic, cardiac, and heart rate scopes are consistent with the historic river temperature ranges for each population. This study suggests that physiological adaptation occurs at a very local scale, with population-specific thermal limits being set by physiological limitations in aerobic performance, possibly due to cardiac collapse at high temperatures.

Warming oceans and rivers are affecting fish species worldwide (*1*–*4*). In particular, elevated temperatures in streams and rivers are creating lethal conditions for the migration of Pacific salmon to their spawning grounds, raising conservation concerns for these ecologically, economically, and culturally important fish species (*5*–*7*). Because physiological processes are critical in defining temperature-induced mortality (*8*), we investigated whether thermal limits are set at a local level and by physiological limitations in aerobic performance due to cardiac collapse.

The lifetime fitness of millions of sockeye salmon (*Oncorhynchus nerka*) that annually return to the Fraser River (British Columbia, Canada) depends on a physically demanding upriver migration. During this once-in-a-lifetime event, fish swim continuously against a fast flowing river for several weeks at ground speeds of 20 to 40 km day^{-1} (*9*). Feeding ceases in the ocean, and upriver swimming is fueled entirely by endogenous energy stores. Because sockeye salmon return to natal spawning grounds with remarkable fidelity, the Fraser River is home to more than 100 genetically and geographically distinct populations (*10*), each of which experiences variable upriver migration conditions, depending on when they enter the river and where they spawn. Thus, populations vary in migration distance (100 to 1100 km), elevation gain (10 to 1200 m), river temperature (9° to 22°C), and river flow (2000 to 10,000 m^3 s^{-1}) (Fig. 1B and table S1). Reproductively isolated populations can potentially adapt to the environmental conditions that induce maximal aerobic challenges, which for sockeye salmon likely occur during their upriver spawning migration. Indeed, local migratory conditions apparently exert strong selective pressure for adaptation because morphological and behavioral characteristics (gross somatic energy, body morphology, egg number, and swimming behavior) do correlate with river migration distance, elevation gain, and/or work (distance × elevation gain) in sockeye salmon (*11*, *12*). Therefore, we hypothesize that physiological adaptation in sockeye salmon occurs locally at the population level, reflecting upriver migration conditions.

We apply an established conceptual and mechanistic framework for understanding temperature effects on aquatic ectotherms, the oxygen- and capacity-limited thermal tolerance (OCLTT) hypothesis (*13*–*15*). OCLTT attributes the decline in aerobic scope (the difference between resting and maximal oxygen consumption rates) above an animal's optimal temperature (T_{opt}) to capacity limitations of the organ systems that deliver oxygen to tissues. Here, we focus on heat tolerance, given the prevailing warming trend for the Fraser River (fig. S1). The expectation is that local adaptations should extend to multiple levels of the cardiorespiratory system, explaining intraspecific variation in thermal tolerance and aerobic scope.

Our study included eight populations of wild-caught Fraser River sockeye salmon, spanning

[1]Department of Zoology, University of British Columbia, 6270 University Boulevard, Vancouver, BC, Canada, V6T 1Z4. [2]Faculty of Land and Food Systems, University of British Columbia, 2357 Main Mall, Vancouver, BC, Canada, V6T 1Z4. [3]Department of Forest Sciences, University of British Columbia, 2424 Main Mall, Vancouver, BC, Canada, V6T 1Z4. [4]Fisheries and Oceans Canada, Science Branch, Pacific Region, School of Resource and Environmental Management, Simon Fraser University, Burnaby, BC, Canada, V5A 1S6.

*To whom correspondence should be addressed. E-mail: eliason@zoology.ubc.ca

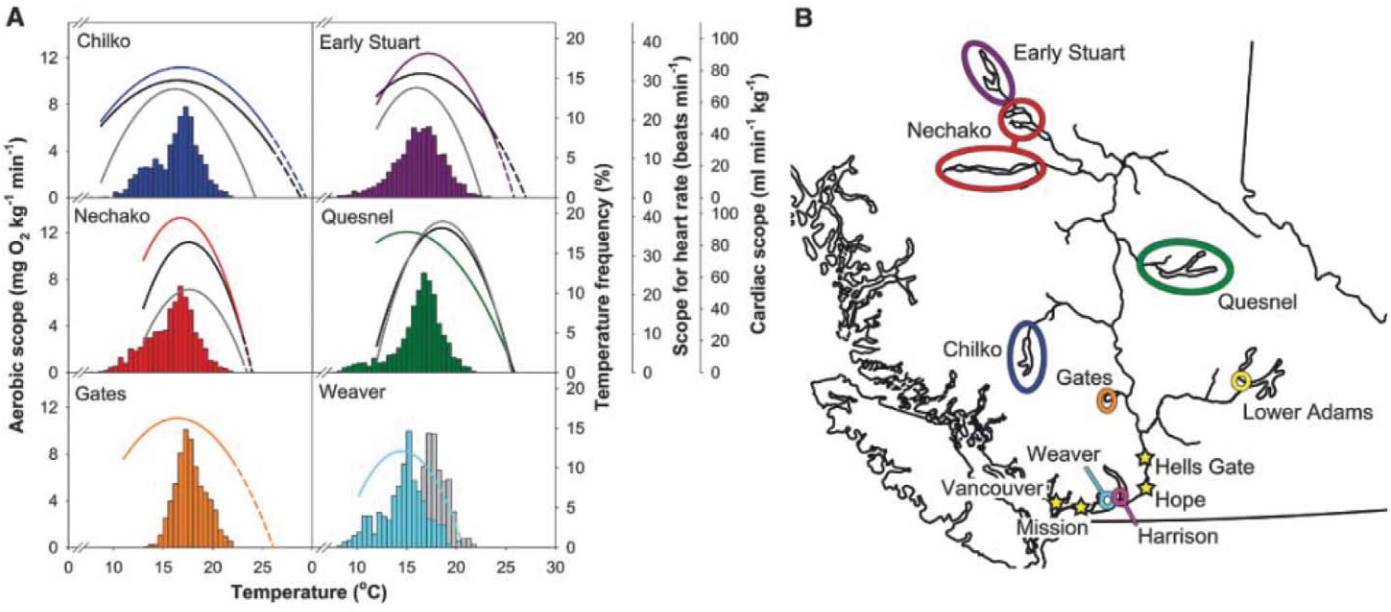

Fig. 1. (**A**) Population-specific estimates of aerobic (colored lines), cardiac (black lines), and heart rate (gray lines) scopes in relation to water temperature. The frequency histogram shows simulated distributions of average river temperatures encountered by individual modeled fish from each population during their upriver migration from 1995 to 2008. For Weaver fish, two temperature histograms are presented, one for the historical river entry (blue), the other for the current early entry phenomenon (gray) (*16*). Aerobic scope data for Gates and Weaver sockeye salmon provided by (*17*). (**B**) Map of the Fraser River, British Columbia, Canada, indicating the spawning locations for the eight sockeye salmon populations included in this study.

a range of river migration difficulties. Populations were first categorized into those that pass through Hells Gate, a hydraulically challenging river segment (upriver populations) and those that do not [coastal populations (table S1)]. Migration difficulty was further quantified using various environmental characteristics: distance, elevation gain, temperature, migration rate, duration, work, river slope, and migration effort (Fig. 1B and table S1). We predicted that migration distance, elevation gain, and work would exert the strongest selection pressure on aerobic scope, given their importance in selecting for morphological traits (*12*). We measured individual cardiorespiratory performance (N = 97) as a function of temperature in four populations (*16*). Many fish could not swim at the highest test temperatures, presumably reflecting a collapse of aerobic scope above T_{opt} (Fig. 1A and fig. S2). Moreover, aerobic scope curves for each population were significantly related to the historic range in river temperature they experienced (table S2), a finding consistent with two additional Fraser River sockeye salmon populations (*17*) (Fig. 1A and table S2). The coastal Weaver sockeye salmon experience the coldest temperatures and had the lowest T_{opt} (14.5°C), whereas the upriver populations experience similar river temperatures and accordingly had a similar T_{opt} [range 16.4° to 17.2°C (Fig. 1A and tables S1 and S3)]. The Chilko population displayed an unusually broad optimal thermal range (Fig. 1A and table S3) that corresponded with the lower temperatures encountered during their difficult migration in the Chilcotin watershed. In addition, significant differences in maximum aerobic scope among the populations (table S4) were positively correlated with the distance to the spawning ground (Fig. 2A and table S5). These results suggest population level adaptation of maximum aerobic scope to the selection imposed by river conditions encountered during migration (*18*–*20*).

Given that cardiac capacity and aerobic scope are tightly related (*21*), we expected populations with the greatest migratory demands to display similar adaptations in cardiac morphology and performance. Relative ventricular mass (RVM), percentage compact myocardium (% compact; the proportion of the ventricle supplied with coronary blood flow), and relative dry compact mass (RDCM) significantly differed among populations (table S4). All three morphological parameters were significantly greater for upriver compared with coastal populations ($P < 0.01$; t test), suggesting that the hydraulically challenging sections of the river impose selection on heart morphology. In addition, correlations between cardiac morphology and migration difficulty (Fig. 2, B to D, and table S5), and maximum aerobic scope with RDCM (table S5), provide promising evidence for local adaptation to river conditions on an even finer scale (*18*–*20*). Furthermore, aerobic scope, cardiac scope, and scope for heart rate were all positively correlated (fig. S3) and varied in parallel with river temperature (Fig. 1A), suggesting that the temperature dependence of cardiac performance is linked to that of aerobic capacity at the population level. Corroborating earlier work (*21*, *22*), scope for heart rate collapsed at a lower temperature than aerobic scope in two populations (Fig. 1A), suggesting that reduced scope for heart rate above T_{opt} may limit maximum cardiac output and the capacity of the cardiorespiratory system to transport oxygen. Interestingly, neither maximum cardiac scope nor maximum scope for heart rate differed significantly among the upriver populations tested (table S4). Therefore, future studies should examine cardiovascular function in coastal populations and consider the possibility of population differences in arterial oxygen-carrying capacity and tissue oxygen extraction ability to provide greater insight into local adaptation of cardiovascular performance.

Next, we sought a mechanistic explanation for the observed intraspecific variation in thermal tolerance. Cardiac adrenergic stimulation protects salmonid cardiac function at low temperatures (*23*, *24*) and against the negative effects of acidosis and hypoxia during exercise (*25*), but protection diminishes at high temperatures associated with declining aerobic scope (*23*–*25*). Therefore, we hypothesized that the unusually broad and high thermal tolerance of the Chilko population would reflect a greater density of adrenaline-binding ventricular β-adrenoceptors compared with the comigrating Nechako population that has a narrower and lower thermal tolerance (Fig. 1A and table S3). We determined ventricular β-adrenoceptor density (B_{max}) and binding affinity (K_d) in fish that had been held for 4 days at 13°, 19°, or 21°C. At all three temperatures, Chilko had a significantly higher B_{max} compared with Nechako sockeye salmon

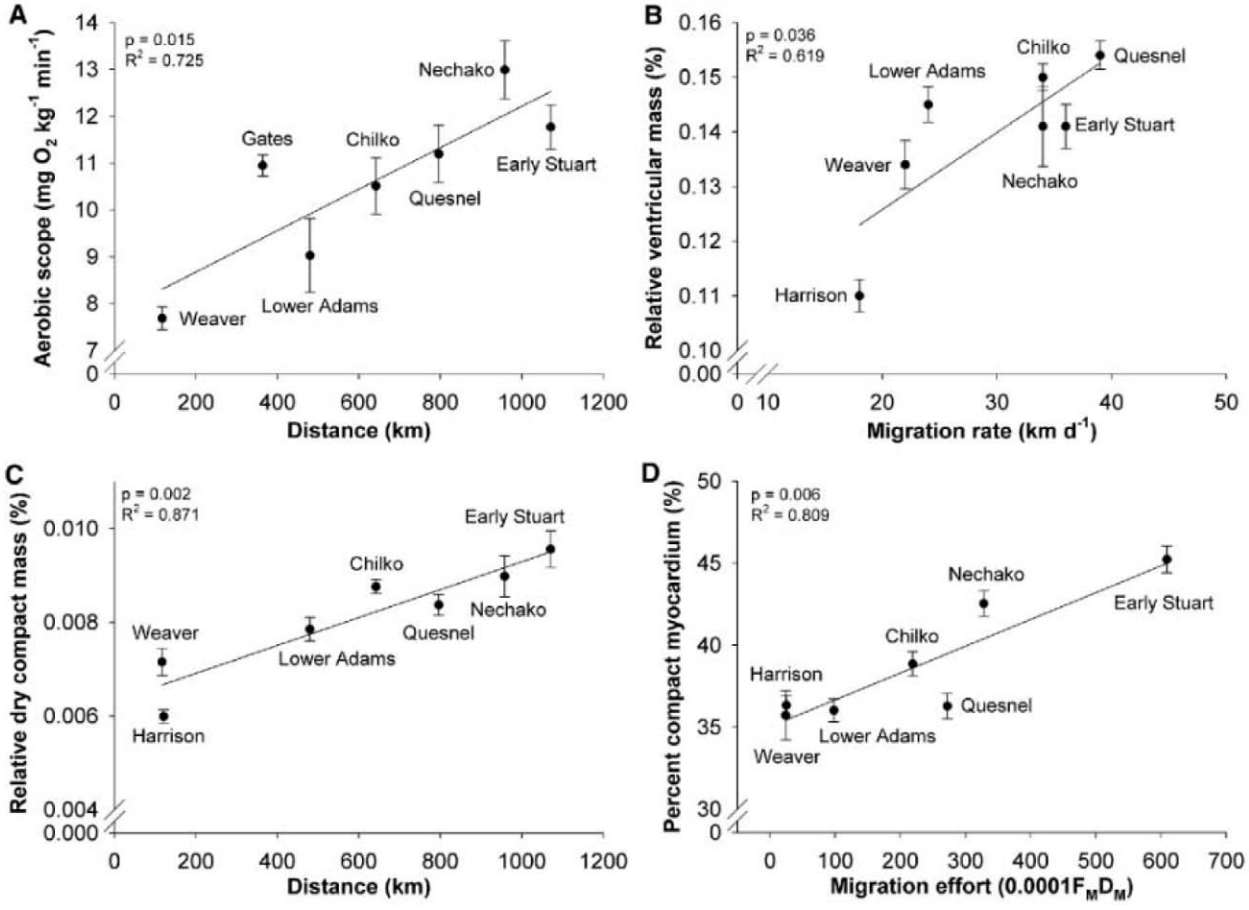

Fig. 2. Linear regressions between migration difficulty indices and (**A**) aerobic scope at T_{opt}, (**B**) relative ventricular mass, (**C**) relative dry compact mass, and (**D**) percentage compact myocardium (tables S1, S3, and S4). Population means ± SEM are presented. The migration difficulty indices with the strongest Pearson correlation coefficient are presented (table S5). F_M, Fraser River discharge; D_M, distance to spawning grounds. Only female sockeye salmon were compared for heart morphology (*16*).

(Fig. 3) [K_d did not differ (fig. S4)] and more than twice that previously measured for salmonids. In contrast to rainbow trout (*24*), B_{max} increased significantly when Chilko sockeye salmon were warmed to 19° and 21°C from 13°C. Consequently, elevated ventricular β-adrenoceptor expression for Chilko sockeye salmon may provide greater cardiac capacity and protection at temperature extremes, expanding their thermal tolerance compared with the Nechako population.

Our results support the hypothesis that continued increases in summer river temperatures will result in population-specific responses of sockeye salmon (*5*). Comparison of temperature profiles for aerobic scope (as a percentage of maximum) among six populations (Fig. 4) reveal clear differences across populations in T_{crit} (when aerobic scope is zero and fish survival is passive, time-limited, and supported by anaerobic metabolism). Although upstream migration is clearly impossible at T_{crit}, exactly how much aerobic scope is required for successful river migration is unknown. A biotelemetry study with Weaver sockeye salmon suggests that at least 50% of aerobic scope is needed [<10% of fish reached their spawning area at 18° to 21°C when aerobic scope is 0 to 68% of maximal (*5*, *26*)]. However, given that all the upriver populations studied here have 89 to 97% of maximum aerobic scope at the upper 90th percentile of historic temperatures encountered (table S3), we suggest that perhaps ~90% of aerobic scope is necessary over a broader time scale for upriver populations experiencing greater migration difficulty. Accordingly, temperatures exceeding the

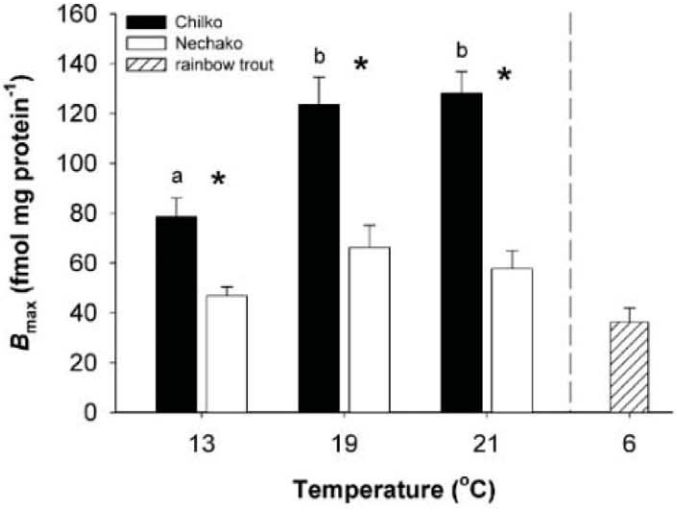

Fig. 3. Ventricular β-adrenoceptor density (B_{max}). Significant differences between populations are indicated by * ($P < 0.001$). Significant differences between temperature treatments existed only for Chilko sockeye salmon and are indicated by differing letters (i.e., a and b; $P < 0.001$, 2-way analysis of variance). Rainbow trout were included as a reference group to confirm the assay technique.

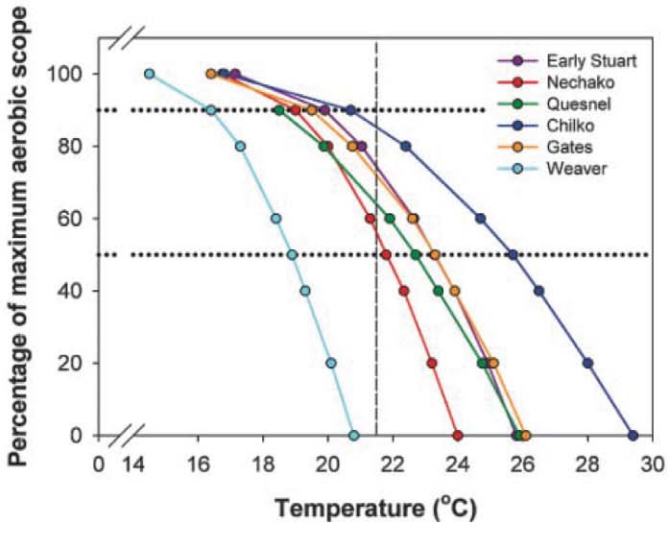

Fig. 4. Percentage of maximum aerobic scope available for each population in relation to temperature. Dashed line at 21.5°C indicates the maximum Fraser River water temperature measured near Hells Gate since the 1940s. Although it is unknown what proportion of aerobic scope is required to successfully ascend the river, 90% and 50% are indicated as guidelines (dotted lines).

population-specific upper T_p [temperature corresponding to 90% of maximum aerobic scope, which includes current temperature maxima of 21.5°C (Fig. 4 and table S3)], could limit successful migrations due to a functional collapse in aerobic scope. Empirically, no sockeye salmon population has initiated river migration at a temperature exceeding 21°C (*27*), nor has a historic mean migration temperature been above 19°C (*6*). However, Chilko sockeye salmon may emerge as "superfish" with greater resilience to climate change by being able to maintain cardiorespiratory performance at higher temperatures. Conversely, Weaver and Nechako populations are especially susceptible to high temperature. If Weaver sockeye salmon continue to enter the Fraser River up to 6 weeks earlier than normal (*28*), exposing themselves to such high temperatures (Fig. 1A), high mortality en route will continue (*5*, *26*, *28*).

Although warming water temperatures are undoubtedly a global issue for fishes at the species level, we propose a concern at the population level for Fraser River sockeye salmon. Because current warming trends in the Fraser River (1.9°C during the past 60 years) (fig. S1) are expected to continue (*29*), survival of sockeye salmon populations will require some combination of behavioral adaptations (to avoid high temperatures by entering the river when it is cooler) and physiological adaptations (a higher T_p to increase high temperature tolerance). Substantial shifts in entry timing are unlikely due to energy and time constraints to achieve highly conserved spawning dates. On the other hand, warming river temperatures could exert strong selective pressure for physiological adaptation. Physiological adaptation requires trait heritability, trait variability, and differential fitness. Evidence of all three have been presented here: local adaptation of cardiorespiratory traits, individual variability in these traits, and zero lifetime fitness for fish failing to complete their upriver migration. The salmonid genome clearly has the capacity for higher thermal tolerance [current thermal extremes are documented for redband trout that experienced 15° to 27°C diurnally, acutely tolerated 29°C, and demonstrated a plateau in aerobic scope at 26°C (*30*)], suggesting that there is potential for future physiological adaptation in Fraser River sockeye salmon. We suggest that adaptations at the level of the heart that sustain cardiac performance at high temperatures, such as the increased ventricular β-adrenoceptor density displayed in Chilko sockeye salmon, could be beneficial in this regard. The current challenge is determining whether the rates and extents of physiological adaptation for Fraser River sockeye salmon will allow them to adapt quickly enough to cope with the current warming trend.

References and Notes

1. K. Brander *et al.*, *ICES Mar. Sci. Symp.* **219**, 261 (2003).
2. A. L. Perry, P. J. Low, J. R. Ellis, J. D. Reynolds, *Science* **308**, 1912 (2005).
3. J. M. Grebmeier *et al.*, *Science* **311**, 1461 (2006).
4. P. Munday, M. Kingsford, M. O'Callaghan, J. Donelson, *Coral Reefs* **27**, 927 (2008).
5. A. P. Farrell *et al.*, *Physiol. Biochem. Zool.* **81**, 697 (2008).
6. S. Hodgson, T. P. Quinn, *Can. J. Zool.* **80**, 542 (2002).
7. L. G. Crozier *et al.*, *Evol. Appl.* **1**, 252 (2008).
8. T. Wang, J. Overgaard, *Science* **315**, 49 (2007).
9. K. K. English *et al.*, *Trans. Am. Fish. Soc.* **134**, 1342 (2005).
10. T. D. Beacham *et al.*, *Trans. Am. Fish. Soc.* **134**, 1124 (2005).
11. S. G. Hinch, P. S. Rand, *Can. J. Fish. Aquat. Sci.* **57**, 2470 (2000).
12. G. T. Crossin *et al.*, *J. Fish Biol.* **65**, 788 (2004).
13. H. O. Pörtner, *Comp. Biochem. Physiol. A* **132**, 739 (2002).
14. H. O. Pörtner, R. Knust, *Science* **315**, 95 (2007).
15. H. O. Pörtner, A. P. Farrell, *Science* **322**, 690 (2008).
16. Materials and methods are available as supporting material on *Science* Online.
17. C. G. Lee *et al.*, *J. Exp. Biol.* **206**, 3239 (2003).
18. J. A. Endler, *Natural Selection in the Wild* (Princeton Univ. Press, Princeton, NJ, 1986).
19. E. B. Taylor, *Aquaculture* **98**, 185 (1991).
20. D. Schluter, *The Ecology of Adaptive Radiation* (Oxford Univ. Press, Oxford, 2000).
21. A. P. Farrell, *J. Exp. Biol.* **212**, 3771 (2009).
22. M. F. Steinhausen, E. Sandblom, E. J. Eliason, C. Verhille, A. P. Farrell, *J. Exp. Biol.* **211**, 3915 (2008).
23. H. A. Shiels, A. P. Farrell, *J. Exp. Biol.* **200**, 1607 (1997).
24. J. E. Keen, D. M. Vianzon, A. P. Farrell, G. F. Tibbits, *J. Exp. Biol.* **181**, 27 (1993).
25. L. M. Hanson, A. P. Farrell, *J. Fish Biol.* **71**, 926 (2007).
26. M. T. Mathes *et al.*, *Can. J. Fish. Aquat. Sci.* **67**, 70 (2010).
27. K. D. Hyatt, M. M. Stockwell, D. P. Rankin, *Can. Water Resour. J.* **28**, 689 (2003).
28. S. J. Cooke *et al.*, *Fisheries (Bethesda, Md.)* **29**, 22 (2004).
29. M. R. Ferrari, J. R. Miller, G. L. Russell, *J. Hydrol. (Amst.)* **342**, 336 (2007).
30. K. J. Rodnick *et al.*, *J. Fish Biol.* **64**, 310 (2004).

31. We thank C. Whitney for assistance with the β-adrenoceptors experiment and field assistance; A. Lotto, G. Cox, E. Sandblom, A. Collins, M. Drenner, C. Wilson, D. Roscoe, M. Donaldson, J. Burt, E. Martins, S. Pieperhoff, L. Thompson, J. Hills, V. Ives, S. Tang, B. Smith, M. Hamer, D. Eliason, G. Eliason, and P. Parsons for field assistance; S. Ballesta and S. Laguë for assistance with the β-adrenoceptors experiment; D. Guo for assistance with heart dissection; S. Cooke for valuable discussions; S. Latham for scale analysis; K. Miller, N. Ginther, C. Wallace, and J. Candy for DNA analysis; and the Department of Fisheries and Oceans (DFO) Environmental Watch Program and the DFO Cultus Lake Salmon Research Laboratory. This research was funded by Natural Sciences and Engineering Research Council of Canada (NSERC) Discovery grants to A.P.F. and S.G.H.; an NSERC Strategic grant to S.G.H. and A.P.F.; Pacific Salmon Forum grants to E.J.E., A.P.F., and S.G.H.; NSERC postgraduate scholarships to E.J.E., K.M.J., and M.K.G.; and a Killam Postdoctoral Fellowship to T.D.C.

Supporting Online Material

www.sciencemag.org/cgi/content/full/332/6025/109/DC1
Materials and Methods
Figs. S1 to S4
Tables S1 to S6
References

15 October 2010; accepted 16 February 2011
10.1126/science.1199158

Lab Devices Get Smaller, More Intuitive, Less Expensive

New instruments that are easier to use, take up less space, and do more work are changing research labs for the better.
By Anne Harding

"It was a pleasure using the device. It's a very odd feeling in the lab, to have fun using the equipment."

Eric Schulze used to think the best lab devices are the ones you don't notice. But **EMD Millipore**'s Scepter, he says, changed his mind.

The first—and only—automated handheld cell counter, released in March 2010, costs less than $3,000. "We referred to it affectionately as an iPod with a pipette attached," says Schulze, who helped beta test the Scepter as a graduate student in Qi-Long Ying's lab at the **University of Southern California's Keck School of Medicine.**

"It was a pleasure to use the device. It's a very odd feeling in the lab, to have fun using the equipment," adds Schulze, who is now with the **U.S. Food and Drug Administration.**

When working with stem cells, Schulze explains, it's often a matter of an individual scientist's intuition to gauge when the cells begin to change and differentiate, which can be tough to explain to someone else. But the Scepter's immediate cell-count readouts and graphs made it possible for him to show colleagues exactly what he was talking about, in real time. "What was previously maybe not obvious to the student, or another scientist or colleague, now became quantifiable," he explains.

The device was so innovative, Schulze adds, that he and his colleagues found themselves designing experiments around it.

The Scepter has received a lot of attention and sold very well, says Grace Johnston, a product manager for the Billerica, Massachusetts-based company. "We've placed instruments globally, pretty much at most major biotechs and most major academic institutions," she adds. According to Johnston, the company sold more than 1,000 units in the first six months after its introduction.

Scepter uses a Coulter principle-based system, with a current across an opening that breaks every time a cell passes through, creating voltage changes that the device records and plots, giving readings within 20 seconds. Its operating range is from 10,000 to 500,000 cells per milliliter. Users can store up to 72 histograms on the device, while its battery will run for at least 72 hours. They can also upload data from the Scepter to a PC. EMD Millipore plans to release a Mac-compatible version this year.

TECHNOLOGY AT YOUR FINGERTIPS

New compact devices like the Scepter are about more than just saving benchtop space, although that's a key consideration. Manufacturers are increasingly building them to be multifunctional, modular, more intuitive, less expensive, and maybe even fun to use. And users like Schulze appreciate how these smaller devices let them have technology at their fingertips, rather than having to wait for a time slot on a large, centralized, and sometimes unreliable monster machine.

EMD Millipore also offers another compact device: a family of Guava benchtop flow cytometry systems. "By putting a system on a benchtop, it makes them much more accessible," Greg Hoff, media relations manager at EMD Millipore, explains. "It really makes flow cytometry an every day lab tool rather than something scientists need to schedule with the core lab." The portability, ruggedness, and ease-of-use of Guava systems are especially beneficial in developing countries. The company has sold more than 300 instruments to laboratories in rural areas of Africa for monitoring HIV therapy. The instruments are not currently approved for HIV monitoring in North America, Europe, or Japan.

Most of these new devices feature touch screen interfaces and many, like **Illumina**'s MiSeq DNA sequencing system, have dramatically simplified sample preparation and workflow. The MiSeq takes up two square feet on the bench, and continued »

UPCOMING FEATURES

Cell Separation Technologies—May 6

Food Safety—June 24

Proteomics: Protein Folding—August 26

FEATURED PARTICIPANTS

Bio-Rad
www.bio-rad.com

BioTek Instruments
www.biotek.com

EMD Millipore
www.emd-millipore.com

Illumina
www.illumina.com

Integra
www.integra-biosciences.com

Luminex Corporation
www.luminexcorp.com

Olympus
www.olympusamerica.com

Redd & Whyte
www.reddandwhyte.com

University of Southern California's Keck School of Medicine
www.keck.usc.edu

U.S. Food and Drug Administration
www.fda.gov

costs less than $125,000, compared to the company's previous generation HiSeq, which is five to six times larger in volume and costs about $690,000. Run prices for MiSeq will range from $400 to $750.

"The concept is to make sequencing personal so that individual labs can afford to use the new system routinely for lower-end experiments," says Jay Flatley, president and CEO of the San Diego company, which will begin taking orders for the MiSeq in April 2011. And while a capillary electrophoresis run would typically yield 100,000 bases of information, Flatley added, "here you're getting a billion…it's certainly an order of magnitude, if not two orders of magnitude, cheaper per base."

Preformatted cartridges containing all the necessary reagents have helped cut down preparation from nine steps requiring about eight to 10 hours of work, to four steps that take two hours.

LEDS INSTEAD OF LASERS

Luminex Corporation slashed the size—and the price—of its biological testing instrumentation in response to marketing research that showed space and budget constraints were stopping many research and clinical scientists from adding multiplexing capabilities to their labs.

Introduced in April 2010, the MAGPIX uses the company's color-coded magnetic microspheres, like earlier generations of devices, for analysis. But rather than lighting up the beads with a laser one by one as they pass through a cuvette, the beads are loaded with a smaller amount of fluid into a chamber within the device. Light-emitting diodes (LEDs) illuminate all of the beads at once after they've been locked into position with a magnet. A digital camera then snaps several images of the beads for analysis. The device weighs less than 40 pounds and, with a list price of $35,000, is half the cost of Luminex's previous generation of multiplexing devices. It also allows users to perform up to 50 tests with a single reaction volume.

"The combination of common LEDs and the camera technology produces much lower costs, high reliability, a smaller footprint, and an easier-to-use platform," explains Tim Dehne, vice president of systems research and development at the Austin, Texas-based company. "Out of the box the user, the scientist, the technician can install the system, literally in minutes," with no need for a field service technician, as required in the past, to ensure the lasers are aligned properly. In fact, he notes, the very first MAGPIX device the company sold went to Papua New Guinea for field research on malaria.

Brian McFarlin, an associate professor in exercise physiology, nutrition, and immunology at the University of Houston, says the MAGPIX has dramatically cut the time it takes his lab to analyze samples for circulating cytokines and chemokines. Before buying the MAGPIX, McFarlin explains, he and his colleagues would buy individual enzyme-linked immunosorbent assay (ELISA) kits to run their analyses, which was time consuming, expensive, and used up too much sample.

But the new device allows McFarlin to do all the measurements he needs on a single sample. He used to run through 342 96-well plates for ELISA analysis of a thousand samples, about nine to 10 weeks of work. MAGPIX multiplex can do the same thing with 26 plates, in three weeks.

Lab instruments can sometimes come with less than desirable software, McFarlin says, but he's very happy with the package that came with the MAGPIX. After you instruct the program on what format you would like the data in, he explains, "it makes a compact CSV file you can put right in Excel for further analysis."

Dehne said Luminex's future plans include finding ways to reduce up-front sample preparation. "The ultimate [goal] would be [where] all you have to do is introduce the patient sample and nothing else, and the device gives you the answer," he explains.

TAKING UP LESS SPACE WITH MORE FUNCTIONALITY

Many smaller devices actually do more than their bigger, costlier predecessors. For example, **BioTek**'s MultiFlo Microplate Dispenser, introduced in September 2010, combines syringe pump and peristaltic pump technology in a single instrument. The device offers a broad volume range, from one microliter to several milliliters, and can be used with a range of plate types.

While a typical dispensing instrument may allow the use of just one reagent at a time and require a 21x 20 inch spot on a benchtop with 12 inches of height clearance, the MultiFlo allows for up to four reagents to be used in parallel and is only 16 x 11 inches with a base height of less than eight inches. The compact size is especially useful with robotic systems, notes Product Manager Jason Greene, which have a limited deck size and reach.

"We understand that size is a very, very important parameter to customers," Greene continues. "We're always trying to keep that in mind, particularly with the liquid handling products, because it's very easy for them to grow. We're constantly keeping that in mind and catching that before it happens."

This January, **Integra** introduced the Viafill, a multifunctioning reagent dispenser requiring only a 14 x 12 x 9.5 inch space. "Many labs require a dispenser, washer, and a serial diluter," explained Product Manager Jonathan Harkins. "Due to the scarcity of bench space, we've combined these into one instrument. It's about the same size as a lot of dispensers, but you don't need

three separate instruments to dispense, wash, and serial dilute. There's quite a bit more functionality to it."

The company also introduced a 96-channel pipette, the Viaflo 96, last January. The device works just like a regular Viaflo pipette, times 96, Harkins explains. "Rather than create a large piece of automated equipment that is difficult to operate, we combined the well-known Viaflo pipette user-interface with the effortless control of a joystick-like pipette handle." The handle "acts just like a handheld pipette," he adds, allowing users to easily move between multiple standard plates and reservoirs. The handheld approach also allows for touching off and for partial loading of pipette tips. It takes up a square foot of bench space and is about a foot and a half tall.

"People don't need to read the manual to know how to use it," Harkins says. "Between the ease of use and the price point, we think it's something that any lab could really benefit from." The base cost is less than $15,000; other 96-channel instruments for similar applications can cost three times as much, Harkins estimates.

"People don't need to read the manual to know how to use it."

TEACHING AN OLD ROBOT NEW TRICKS

Redd & Whyte's Preddator S1 Microplate Dispenser offers yet another entry into the compact dispensing market. "Its really key features are that it can dispense all types of reagents," explains the virtual start up's CEO, Roger Poole. "It can do that accurately and repeatedly, and that's the key. That's what scientists have been missing out on."

The Preddator can dispense cells, gels and matrigels, oils and greases, and other complex materials, and has been specifically designed to avoid the tip blockage that plagues other dispensing devices.

Designed as a "value-added" version of a robot long used in the automotive and printed circuit board market, the Preddator is now available in four-channel and single-channel versions. "One of the reasons why we chose that specific robot is it has a very small footprint and a very open architecture, so the research scientists can get at it," Poole says.

Compactness has been key for **Olympus** in developing two new products: the FluoView FV10i, a completely self-contained laser-scanning microscope that sits comfortably on the benchtop, and the FSX100 Bio Imaging Navigator, another compact microscope. The first generation FV10i uses an oil-based objective, and Olympus has developed a new version with components "inside the box" that will allow the user to do long-term, live-cell imaging, while using carbon dioxide, heat, a water objective, and hardware to ensure that the sample will stay hydrated.

"This allows researchers to accomplish almost everything that they would typically want with confocal microscopy, but with a very small footprint and for less than $150,000," explains Dennis Donley, group manager for laser scanning confocal microscopes at Olympus. Compared to some conventional confocal microscopes that always seem to require tuning and tweaking, he added, "the FV10i is a shift in the workflow that brings the technology to the people—like when cars stepped up to auto transmission."

COMPACT IMAGER SLASHES PROCESSING TIME

Bio-Rad's Gel Doc EZ Imager is another newly compact device with major advantages in terms of ease of use. The EZ Imager has about half the footprint of the Gel Doc XR+, while the new device is just 15 inches tall, compared to about 38 inches for its predecessor. "It's also significantly smaller than every other integrated gel documentation system on the market," says Ryan Short, imaging marketing manager at Bio-Rad Laboratories.

What's more, says Short, "it truly is a one-button-push imaging system." The user places a gel on a tray, inserts it into the machine, pushes a green button that will run a predefined protocol (which can include multiple analyses), and gets a publication-quality image back within five seconds. "To acquire an image on most systems and to do an analysis can take five minutes per gel," Short adds. "In this case, we're doing it in about 10 seconds." The device can also perform stain-free imaging using precast gels, saving time by transforming traditional two-hour staining protocols into one five-minute step.

The device offers four trays in all: a UV tray, a white tray (for Coomassie blue, copper, silver, and zinc stains), a blue tray for nondestructive nucleic acid applications (SYBR Green), and a stain-free tray for use with stain-free gels. Prices can range from $9,000 to $13,000, depending on desired applications; Short says an EZ Imager well equipped for most applications would run about $10,000.

"It's safe to say that we see this as the way of the future," says Short. "Our customers appreciate the smaller format. We'll continue to develop products down this line."

The FDA's Schulze says he'd love to see more lab devices that look like consumer electronics; in fact, he argues, why not an app that allows scientists to collect data and beam it to a colleague, or beam it up into "the cloud" for sharing with the scientific community as a whole.

"The fact that smartphones aren't used for this kind of thing, it kind of blows my mind," he says.

Anne Harding is a freelance science writer based near New York City.

DOI: 10.1126/science.opms.p1100054

YEAST COLONY COUNTER

The new ProtoCOL 2 automated colony counting and zone measurement system can be used for quick and easy analysis of standard and large plates. The system offers a combination of a unique lighting method and a new total viable count (TVC) software that makes counting colonies as small as a pinprick, fast and accurate. Because the ProtoCOL 2 has an integrated processor there is no need to purchase a separate computer. The five separate ProtoCOL 2 software modules can all be integrated into a CFR 21 Part 11 environment, allowing scientists to purchase only those needed for their laboratory. The available software modules include colony counting, spiral plate counts, AMES test counts, and inhibition zone measurements. The new ProtoCOL 2 is perfect for microbiology laboratory scientists looking for a sensitive, easy-to-use, yet inexpensive colony counter or zone sizing system.

Synbiosis

For info: 800-686-4451 | www.synbiosis.com

BENCHTOP EVAPORATOR

The EZ-2 Elite is designed to remove high boiling point solvents and deliver enhanced solvent recovery thereby improving final drying of stubborn samples and enabling fast lyophilization of HPLC fractions. The high-performance scroll pump used with the EZ-2 Elite delivers deeper vacuum than the diaphragm pumps used on other EZ-2 systems. This advance plus internal enhancements to the heat vapor duct and system components enable the EZ-2 Elite to routinely evaporate challenging high boiling solvents including DMSO and NMP. In addition, these enhancements ensure that such challenging solvents only condense in the SpeedTrap. The EZ-2 Elite is designed to concentrate or completely dry samples. The system will accommodate a wide selection of sample holders enabling evaporation from most common sample container formats including round-bottom flasks up to 500 ml, tubes up to 160 mm long, custom reaction blocks, and shallow or deep-well microplates.

Genevac

For info: 845-255-5000 | www.genevac.com

BACTERIAL TRANSFORMATION

The new Eppendorf Eporator offers a fast, simple, and safe option to transform bacteria, yeasts, and other microorganisms with DNA/RNA. When bacteria or yeast strains are exposed to short high-voltage pulses, macromolecules such as plasmid DNA can diffuse into the cell through temporary pores in the cell membrane. The results are highly reproducible, and in comparison with chemical methods, electroporation yields up to 10 times higher transformation efficiency. Two new program buttons, designed for storage and recall of most commonly used parameters, along with the simple one-button operation, guarantee intuitive use for faster sample handling. State-of-the-art electronics and an integrated electroporation chamber offer higher safety for the user and minimize the risk of sample loss. Eppendorf offers electroporation cuvettes with three different gap widths. Due to its compact design, the Eporator can be transported easily within the lab and stored during times when it is not in use.

Eppendorf

For info: 800-645-3050 | www.eppendorf.com

AUTOMATIC FUSION MACHINE

Sample preparation by the fused bead technique is widely accepted as giving better precision and accuracy than most other techniques when analyzing minerals, ceramics, and similar samples by X-ray fluorescence (XRF). The Vulcan fusion system uses automatic fusion control to achieve better sample uniformity and repeatability. The Vulcan MA comes in several different versions. The basic XRF version has two, four, or six fusion stations, with automatically controlled flame temperatures under microprocessor control and the facility to store up to 10 different melting programs. Stable flame temperatures and simplicity of operation ensure good sample-to-sample repeatability. Controlled temperature ramping is also possible. Other configurations are designed for sample preparation for ICP or AAS, or even a mixture of XRF and ICP or AAS, and it is possible to combine the Vulcan with a dedicated fume extraction system to provide an integrated sample preparation workstation.

Analysco Limited

For info: +44-(0)-1993-831792 | www.analysco.co.uk

BIOCHEMICAL DETECTOR

The SpectroSens monitoring and data analysis control unit is a benchtop control center capable of monitoring up to eight independent inline SpectroSens optical sensors. SpectroSens sensors employ an innovative technology that interprets changes in refractive index to provide real-time process monitoring. The new data-monitoring unit advances the company's systems by providing a built-in, touch-screen interface while reducing the footprint by over 50 percent. Due to its new ergonomic form and smaller size, the SpectroSens unit is perfectly suited for use in a range of environments, from a small process-development laboratory up to industrial scale requirements. The multichannel capabilities of the device allow it to be connected to a number of SpectroSens sensors, whether in a single, multistage process or in situations where multiple processes are running in parallel.

Stratophase

For info: +44-(0)-1794-511226 | www.stratophase.com

Electronically submit your new product description or product literature information! Go to **www.sciencemag.org/products/newproducts.dtl** for more information.

Newly offered instrumentation, apparatus, and laboratory materials of interest to researchers in all disciplines in academic, industrial, and governmental organizations are featured in this space. Emphasis is given to purpose, chief characteristics, and availability of products and materials. Endorsement by *Science* or AAAS of any products or materials mentioned is not implied. Additional information may be obtained from the manufacturer or supplier.

POSITIONS OPEN

OPEN FACULTY SEARCH
Dorothy M. Davis
Heart and Lung Research Institute
The Ohio State University

The Dorothy M. Davis Heart and Lung Research Institute (DHLRI) at The Ohio State University Medical Center is a 100,000 square foot, comprehensive, state-of-the-art research facility opened in October 2000. The DHLRI is under new leadership and initiating a search for outstanding scientists for tenure-track faculty positions at the **ASSISTANT** or **ASSOCIATE PROFESSOR** level. Candidates should have a relevant doctoral degree, at least two years of postdoctoral training, a commitment to basic/translational cardiovascular or pulmonary science, and a history of strong research productivity. Individuals will be evaluated on their ability to establish innovative independent research programs as well as develop collaborative areas of focus with existing programs. Individuals must have strong communication and interpersonal skills.

Applications should include a detailed curriculum vitae, a description of research experience, and statement concerning the nature of the planned independent research program. Information about the University and the DHLRI can be obtained by accessing our **websites: http://www.osu.edu** and **http://heartlung.osu.edu.**

Application material should be sent to:

Lorri A. Fowler, MBA
Administrative Director
473 West 12th Avenue
Columbus, Ohio 43210-1252
E-mail: fowler.142@osu.edu

The Ohio State University is an Equal Opportunity/Affirmative Action Employer. Women and members of underrepresented minority groups are especially encouraged to apply.

POSTDOCTORAL POSITION
School of Molecular Biosciences
Washington State University

Postdoctoral position to study the role of chromatin structure in regulating DNA repair in yeast (e.g., **Kyriss et al.,** *Mol. Cell. Biology* **30:**3503, 2010; **Nag et al.,** *Nucleic Acids Res.* **38:**1450, 2010; **Chaudhuri et al.,** *Nucleic Acids Res.* **37:**1690, 2009). The successful applicant will investigate the role of histone domains and modifications in excision repair as part of a joint collaborative project between **Dr. John Wyrick** (**website: http://www.wsu.edu/~jwyrick**) and **Dr. Michael Smerdon** (**website: http://www.wsu.edu/~smerdon/index.html**) in the School of Molecular Biosciences at Washington State University. Candidates should have a Ph.D. in molecular biology, biochemistry, or genetics. Prior experience with yeast is not required. Send statement of interests, curriculum vitae, and names of three references to **e-mail: dsmerdon@wsu.edu.** *WSU is an Equal Opportunity/Affirmative Action Educator and Employer.*

TENURE-TRACK VISITING ASSISTANT OR ASSOCIATE PROFESSOR of Dental Sciences and Biological Sciences

The Departments of Dental Sciences (**website: http://www.isu.edu/dentsci/**) and Biological Sciences (**website: http://www.isu.edu/departments/bios**) at Idaho State University seek applicants for a tenure-track Visiting Assistant/Associate Professor position to begin August 2011. Applicants must have a Doctorate (postdoctoral experience preferred). For a complete job description, requirements, and application instructions visit us at **website: http://www.isujobs.net.** Priority consideration will be given to those who apply by May 1, 2011; position will remain open until filled. *ISU is an Equal Opportunity/Affirmative Action Employer. We have an institution-wide commitment to inclusion and diversity and encourage all qualified individuals to apply. Veterans' preference. Upon request, reasonable accommodations in the application process will be provided to individuals with disabilities.*

POSITIONS OPEN

FACULTY POSITION OPENING at Hunan University

The College of Biology at Hunan University is expanding and will recruit up to 10 faculty in 2011. We welcome applicants in the following three widely defined areas: Life Sciences (plant molecular biology and plant biotechnology), biomedical engineering, and molecular medicine. Applicants should have a Ph.D. or M.D. in related areas such as biology, medicine, biomedical engineering, and chemistry, etc. Applicants at all academic levels are welcome to apply with the following materials: curriculum vitae, research and teaching statements, and the names of five references. These materials can be sent to **e-mail: hudabiology@gmail.com.** Competitive salary and startup will be offered based on qualifications. Review of applications will begin on May 1, 2011, and continue until the positions are filled. Hunan University is a 985 Project University with intensive research and teaching programs.

ASSISTANT PROFESSOR ACADEMIC PATHOLOGIST

New York College of Osteopathic Medicine (NYCOM) of New York Institute of Technology (NYIT) seeks an Academic Pathologist/Assistant Professor (rank negotiable) for its Biomedical Sciences department. Under the leadership of a new Chair, the department of Biomedical Sciences seeks to build competitive research programs. The successful candidate will focus primarily on research (60 to 75 percent effort) with the remaining effort in teaching and service. The preferred area of research is Cardiovascular but other areas will be considered.

A private, non-profit, independent institution of higher education, NYIT attracts students from 106 nations and 50 states. NYIT's 15,000 students are enrolled in seven schools and attend classes at the university's New York campuses in Manhattan (at Columbus Circle) and on Long Island (on 300 beautiful, wooded acres in Old Westbury), at five sites/campuses around the world, and online. Offering more than 90 courses of study leading to undergraduate, graduate, and professional degrees, NYIT has conscientiously followed its mission of providing career-oriented professional education. Its academic programs, in areas including engineering, architecture, business, communication and graphic arts, and medicine, prepare students for some of the most in-demand careers in today's global economy. NYIT has been recognized by The Chronicle of Higher Education as a "Great College to Work For 2010" and has been consistently ranked in Tier 1 by U.S. News & World Report for more than a decade.

The successful candidate will possess a D.O., M.D., D.V.M., and/or Ph.D. in Pathology and two or more years of postdoctoral teaching experience. NYCOM offers a competitive salary and attractive benefits package including tuition remission, along with a professional environment designed to enhance your career development. To apply, please electronically send your cover letter and resume to: **Dr. A. Martin Gerdes,** Chair of Biomedical Sciences at **e-mail: agerdes@nyit.edu** or mail to: **P.O. Box 8000 Northern Blvd, NY 11568-8000.** *Equal Opportunity Employer for Minorities/Females/Persons with Disabilities/Veterans.*

SENIOR POSTDOCTORAL ASSOCIATE
Boston University

Required expertise in transgenic rats, ultrasound molecular imaging, arterial stiffness analysis, and sonoporation, FACS, MoFlo, confocal microscopy. M.D. or Ph.D., $40,000/year. Send curriculum vitae to **Nancy Clinton, nclinton@bu.edu.** *Equal Opportunity Employer/Affirmative Action.*

ETH

Eidgenössische Technische Hochschule Zürich
Swiss Federal Institute of Technology Zurich

Professor of Physical Chemistry

The Laboratory of Physical Chemistry of the Department of Chemistry and Applied Biosciences at ETH Zurich (www.chab.ethz.ch) invites applications for the position mentioned above.

The applicant's research field should preferably focus on the characterization and study of matter at the atomic and molecular level with spectroscopic or microscopic methods including studies at the single-molecule level and nano-optics. Responsibilities include teaching in all areas of physical chemistry. The new professor will be expected to teach undergraduate level courses (German or English) and graduate level courses (English).

Please apply online at **www.facultyaffairs.ethz.ch**. Your application should include your curriculum vitae and list of publications. The letter of application should be addressed **to the President of ETH Zurich, Prof. Dr. Ralph Eichler. The closing date for applications is June 30, 2011.** With a view towards increasing the number of women in leading academic positions, ETH Zurich specifically encourages women to apply.

RIKEN

The RIKEN Initiative Research Unit Program Unit Leader

Targeted Research Areas:
Research field is not specified. We require the applicant to pioneer his or her own curiosity-driven, internationally-oriented interdisciplinary research field.

Contract Period: Maximum of five years
Upon completion of the initial five-year term and following a midterm evaluation, the unit leader may be recommended for a limited-term PI position, or a permanent PI position as Associate Chief Scientist, allowing continuation of research, if desired.

Remuneration and Allowances, Research Budget:
(1) Salary will be 10.9 million yen/year (pre-tax) and commuting and housing allowances will be provided as per RIKEN policy.
(2) A research budget of approximately 38.5 million yen/year from which the unit leader is expected to recruit and hire several research and technical staff persons will be provided. Depending on the circumstances, the first year budget may be supplemented with 10 million yen as startup funds.

Application Deadline: 5pm on June 30, 2011, Japan Standard Time

Details can be found at:
http://www.riken.jp/iru/

If you have questions regarding application, please send an email to **iru@riken.jp**

Faculty Positions

The Center for Immunology and Microbial Disease at Albany Medical College invites applications for multiple tenure-track Assistant Professor, Associate Professor, and full Professor positions from individuals who have a doctoral degree, postdoctoral experience, and demonstrated research productivity. Applicants for a senior faculty position should have an internationally-recognized research program in microbiology and/or host-pathogen interactions. The basic science departments at Albany Medical College are organized as interdisciplinary research centers and the Center for Immunology and Microbial Disease has a focus on microbial pathogenesis and immune defense, particularly as related to biothreat agents and emerging infections. Our faculty comprises a highly collaborative research group that last year received $8.4M in NIH funding, ranking it within the top half of all Microbiology and Immunology programs in the country. The successful candidates will receive attractive start-up packages and will have an opportunity to lead a focus group in new laboratory space, with access to all departmental core facilities including the Center's fully-staffed ABSL-3/BSL-3. We have established a close relationship with the New York State Department of Health Wadsworth Laboratories, providing a diverse environment that is rich in infectious disease expertise. Albany Medical College is located in a mid-sized city within the upstate New York Capital Region, and has easy access to Boston, New York City, and the Adirondack Mountains.

Applicants should send their curriculum vitae, a statement of research plans, and contact information for three references to:

Faculty Search Committee
Center for Immunology and Microbial Disease
Albany Medical College
47 New Scotland Avenue, MC-151
Albany, NY 12208

For further information about the Center, visit **www.amc.edu/Academic/Research/imd.htm**.

An Equal Opportunity/Affirmative Action Employer.
Women and minorities are encouraged to apply.

Call for applications for FY2012 Foreign Postdoctoral Researcher (FPR) RIKEN, Japan

RIKEN is one of Japan's largest research organizations with institutes and centers in various locations. RIKEN carries out advanced basic and applied research in a wide range of fields, including physics, chemistry, medical science, biology, and engineering.

RIKEN is now accepting applications for the position of Foreign Postdoctoral Researcher (FPR) for FY2012. This position is for young foreign scientists who have demonstrated creative and innovative ideas and who can be expected to achieve broad international recognition in the future.

The FPR program will provide an opportunity for young foreign scientists to apply their creative and innovative ideas, under the direction of RIKEN's laboratory heads, to research currently being conducted at RIKEN.

Job Description Summary
1. Number of openings: Around 18
2. Qualifications:
   (1) Applicants should be non-Japanese citizens.
   (2) Applicants must have a PhD in the natural sciences awarded in or after 2006, or expect to be awarded a PhD by the date of hire.
   (3) Applicants must be able to start working at RIKEN within fiscal year 2012 (April 1, 2012 to March 31, 2013).
3. Contract duration;
   (1) From date of hire to March 31, 2013
   (2) This contract may be renewed for up to a maximum of 3 years.
4. Remuneration:
Salary is 487,000 yen per month. Commuting and housing allowances are also available. An annual research budget of 1 million yen will be allocated to the host laboratory.

Send an e-mail indicating your desire to apply for the position of FPR to RIKEN by **Friday, May 20, 2011**. Reference material will be sent to those with an interest in applying.

Application Deadline : 5pm on Friday, May 20, 2011 (Japan Standard Time)

Additional information on the program and application procedures is available at **http://www.riken.jp/fpr/**

FPR Desk, Global Relations Office, RIKEN, 2-1 Hirosawa, Wako, Saitama 351-0198 Japan, Fax +81-48-463-3687 Email: **fpr@riken.jp**

Tenure-Track/Tenure-Eligible Investigator
Hepatitis Virus Vaccine Research

The Laboratory of Infectious Diseases (LID), Division of Intramural Research (DIR), National Institute of Allergy and Infectious Diseases is seeking an outstanding individual to study the molecular biology and pathogenesis of hepatitis C virus and to develop and test candidate vaccines, immunotherapy, and immunoprophylaxis strategies. Studies of other human hepatitis viruses are also encouraged.

The incumbent will be expected to conduct a vigorous research program that includes molecular virology, studies of protective immunity, production and characterization of candidate vaccines, and testing of vaccines and antibodies in animal models including nonhuman primates. The incumbent will benefit from unique opportunities to interact with other members of LID and DIR who perform basic and translational research on hepatitis and other viruses.

LID has a diverse portfolio of virus vaccine research and an extensive collection of hepatitis specimens from humans and nonhuman primates. Access to nonhuman primates, state-of-the-art core research support, and the NIH Clinical Center—a premier research hospital on the main NIH campus—is available.

Additional information about LID is available online at **www.niaid.nih.gov/LabsAndResources/labs/aboutlabs/lid**.

DIR provides support for salary, technical personnel, postdoctoral fellows, equipment, and research supplies. Salary is dependent on experience and qualifications.

Applicants must have an M.D., Ph.D., M.D./Ph.D., or equivalent degree in a relevant field with extensive postdoctoral experience, as well as a strong publication record demonstrating potential for creative research.

Interested candidates may contact Jeffrey Cohen, LID Chief, at 301-496-5265 or **jcohen@niaid.nih.gov** for additional information about this position.

To apply, submit your curriculum vitae, bibliography, and a detailed statement of how your expertise can contribute to the success of the hepatitis virus program to Ms. Bao-Hahn Ngo at **LIDViralHepatitisSearch@niaid.nih.gov**. In addition, three letters of reference must be sent directly from the referee to Dr. Bernard Moss, Chair, NIAID Search Committee, c/o Ms. Bao-Hahn Ngo at **LIDViralHepatitisSearch@niaid.nih.gov** or 10 Center Drive, MSC 1356, Building 10, Room 4A22, Bethesda, MD 20892-1356. E-mail is preferred.

Applications will be reviewed starting on **April 25, 2011** and will be accepted until the position is filled. Further information regarding DIR laboratories is available at **www.niaid.nih.gov/about/organization/dir**, and information on working at NIAID is available at **www.niaid.nih.gov/careers/dat**.

A full package of benefits (including retirement and health, life, and long-term care insurance) is available. Women and minority candidates are especially encouraged to apply. U.S. citizenship is not required.

NIAID

National Institute of Allergy and Infectious Diseases

ASSISTANT PROFESSOR OF MEDICINE

Computational Biology – Dana-Farber Cancer Institute

The Department of Medical Oncology at Dana-Farber Cancer Institute (DFCI) invites applications for a full-time appointment as Assistant or Associate Professor of Medicine, Harvard Medical School, to establish a research program in cancer genomics and computational biology. Successful candidates will have a proven track record of innovative methodological research in computational biology as well as collaborative basic and translational cancer research. It is expected that candidates will have received doctoral and post-doctoral training in biostatistics, mathematics or computer science as well as in cancer genomics and cancer biology. The candidate should have expertise in analyzing cutting-edge large-scale cancer genomics datasets and utilizing such information to address cancer-relevant questions. Track records in collaborative research with cancer biologists and clinicians are desirable.

Interested applicants should direct their letter of application, 3-page research plan, curriculum vitae, and letters from three qualified references to: Dr. Lynda Chin, Chair, Search Committee, Dana-Farber Cancer Institute, 4 Blackfan Circle, HIM Room 220, Boston, MA 02115; Email: lynda_chin@dfci.harvard.edu. Applicants should ask their three referees to write or email their letters of recommendation independently to this address. Complete application packages submitted after May 2, 2011 may not be considered.

DANA-FARBER/BRIGHAM AND WOMEN'S

CANCER CENTER

HARVARD MEDICAL SCHOOL

Dana-Farber Cancer Institute/Harvard Medical School are Equal Opportunity/Affirmative Action Employers actively committed to increasing the diversity of our faculty: women and members of underrepresented minority groups are therefore strongly encouraged to apply.

Director
Gastrointestinal Immunology Program

The Department of Medicine at the Georgetown University Medical Center is seeking a dynamic founding director of the Gastrointestinal Immunology Program. The ideal candidate will have an MD or MD/PhD degree, and an established track record of NIH – supported research of gastrointestinal immunology. The candidate will establish and lead a translational effort in immunology to be integrated with clinical and basic science investigators within the Georgetown scientific community, and the Georgetown - Howard Universities Center for Clinical and Translational Science. A clinical focus and the ability to collaborate with other investigators will be advantageous. Appointment will be at the Professor or Associate Professor level.

Please send curriculum vitae to **Tolise Miles** at **tcm9@georgetown.edu**, and contact Ms. Miles for questions via e-mail or by phone at **(202) 444-7309**.

Georgetown University is an Affirmative Action/Equal Opportunity Employer.

Nutritional Sciences
UNIVERSITY OF TORONTO

Assistant Professor in Nutritional Sciences

The Department of Nutritional Sciences in the Faculty of Medicine invites applications for a tenure-track Assistant Professorship. The research interests of the Department range from basic science to clinical investigation and population health. Applications are encouraged from candidates with an excellent record of research accomplishments in any one of our four core research platforms: healthy human development and aging; nutrigenomics and personalized nutrition; chronic disease prevention and treatment; and nutrition, food and public policy, profiled on **www.utoronto.ca/nutrisci/**. Successful candidates will be expected to mount an independent, externally funded research program and to participate in some teaching at the undergraduate or graduate level.

Applicants should send curriculum vitae, description of research interests and the names and addresses of 3 references by **April 30, 2011** to:

Dr Mary L'Abbé, Chair,
Department of Nutritional Sciences
Faculty of Medicine, University of Toronto
150 College St., FitzGerald Building
Toronto, ON, Canada M5S 3E2
Mary.Labbe@utoronto.ca
Phone: 416-978-7235 Fax: 416-971-2366

The University of Toronto is strongly committed to diversity within its community and especially welcomes applications from visible minority group members, women, Aboriginal persons, persons with disability, members of sexual minority groups and others who may contribute to further diversification of ideas. All qualified candidates are encouraged to apply; however, Canadians and permanent residents will be given priority.

FRED HUTCHINSON CANCER RESEARCH CENTER

A LIFE OF SCIENCE

FACULTY POSITION

The Vaccine and Infectious Disease Division (VIDD) at the Fred Hutchinson Cancer Research Center (FHCRC) is soliciting applications to fill a faculty position with an individual conducting innovative translational research in pathogen-associated cancers. Areas of research interest may include viral immunology, mechanisms of oncogenesis of cancer-related pathogens, vaccine development or virus/pathogen discovery.

VIDD is one of five divisions within the FHCRC that focuses on a wide range of infectious pathogens. There are opportunities for translational research as the Seattle Cancer Care Alliance (SCCA) provides treatment and care for international and domestic patients with a wide variety of cancers, including the hematopoietic stem cell transplant population. Valuable resources will be available to the candidate through ongoing collaborations between the FHCRC, SCCA and the Uganda Cancer Institute. These collaborations provide a rich source for translational research in HIV-related malignancies, especially Kaposi's sarcoma and Burkitt's lymphoma. Candidates at any rank will be considered. Opportunities exist for joint (secondary) appointment in the Divisions of Clinical Research, Public Health Sciences or Human Biology at FHCRC, as well as an affiliate appointment at the University of Washington.

VIDD occupies state-of-the-art research laboratories on a beautiful lakeside campus. The Center offers outstanding shared resources, including computational biology, genomics, proteomics, and imaging facilities. The Center has active training programs for graduate students and postdoctoral fellows and offers exceptional opportunities for scientific interactions with other investigators in the Seattle area. Additional information about VIDD and Center can be found at: **http://www.fhcrc.org/science/vidd/about.html** and **http://www.fhcrc.org/science/**.

Candidates should submit a curriculum vitae, a concise statement of research plans, and names of three references to **Dr. Corey Casper, 1100 Fairview Ave. N, M1-B140, Seattle, WA 98109**. The application deadline is open until filled.

The Fred Hutchinson Cancer Research Center is an Equal Opportunity Employer committed to work force diversity. Applications from female and minority candidates are strongly encouraged.

Imperial College London

School of Public Health

Applications are Invited for Academic Positions in Imperial College London's new School of Public Health

Department of Epidemiology and Biostatistics

- Lecturer/Senior Lecturer/Reader in Environmental Epidemiology and Exposure Assessment (MRC-HPA Centre for Environment and Health) **(Ref: SM028-11a)**
- Lecturer/Senior Lecturer/Reader in Cancer Epidemiology **(Ref: SM028-11b)**
- Lecturer/Senior Lecturer/Reader in Statistical Genetics **(Ref: SM028-11c)**

Department of Genomics of Common Disease

- Lecturer/Senior Lecturer/Reader in Human Genomics **(Ref: SM028-11d)**

Salary Range:
Lecturer: £42,500 - £47,450 p.a.
Senior Lecturer/Reader: £52,400 minimum p.a. (level of appointment dependent on experience)

The School of Public Health was recently launched with the aim of addressing the major public health challenges of the 21st Century. It undertakes world-class research at local, national and international levels, with translation into improvements in disease prevention. The School's research scored in the top two epidemiology and public health submissions to the UK's 2009 Research Assessment Exercise and has a significant research portfolio with total grants and contracts in excess of £25 million per year.

Applications are now sought for four academic positions in the School of Public Health. The three posts in the Department of Epidemiology and Biostatistics are based at the College's St. Mary's campus, while the post in the Department of Genomics of Common Disease is based at the Hammersmith campus. The successful candidates will be appointed at Lecturer, Senior Lecturer or Reader level and will have a proven, world-class research track record.

For further details on the School of Public Health see our website: www.imperial.ac.uk/publichealth

For informal discussions please contact Professor Elio Riboli, (Director School of Public Health, e-mail: e.riboli@imperial.ac.uk), Professor Paul Elliott (Department of Epidemiology and Biostatistics, e-mail: p.elliott@imperial.ac.uk), Professor Philippe Froguel (Department of Genomics of Common Diseases, e-mail: p.froguel@imperial.ac.uk), Professor Sylvia Richardson (Department of Epidemiology and Biostatistics, e-mail: sylvia.richardson@imperial.ac.uk).

All posts are full time permanent contracts based at Imperial College London within the School of Public Health. Further details on the positions can be found at the College website and our preferred method of application is online via our website http://www3.imperial.ac.uk/employment Please complete and upload an application form as directed **quoting the relevant reference number.**

Stonewall TOP 100 EMPLOYERS 2011

Closing date: 27 April 2011.

Committed to equality and valuing diversity. We are also an Athena Silver SWAN Award winner and a Stonewall Diversity Champion.

UNIVERSITY OF LOUISVILLE
SCHOOL OF MEDICINE

Two Assistant/Associate Professor positions in Neurological Surgery

Neurobiologist

The Department of Neurological Surgery and the Kentucky Spinal Cord Injury Research Center at the University of Louisville announces a search for an Assistant or Associate Professor with interests including, but not restricted to, developmental neurobiology, immunology, inflammation, plasticity, and/or regeneration. Candidates should have an M.D. and/or Ph.D. degree and demonstrated productivity excellence in their graduate, postdoctoral, and/or early faculty research careers. It is expected that a strong extramurally funded research program will be developed. The successful candidate will join a highly collaborative and productive faculty with strengths in molecular, cellular, and rehabilitative aspects of SCI. Outstanding core facilities will enable new collaborations. This tenure track position is supported by a substantial endowment to be used at the discretion of the successful candidate with the potential to become an endowed chair at tenure. Membership in the graduate faculty will be through a secondary appointment in an appropriate basic science department.

Basic and/or Clinical Aspects of Plasticity after SCI

The Department of Neurological Surgery, Frazier Rehabilitation Institute and the Kentucky Spinal Cord Injury Research Center at the University of Louisville announce a search for an Assistant or Associate Professor with research interests including, but not restricted to, clinical, translational or basic models of rehabilitation, neuroplasticity, motor control (posture, locomotion, respiration) and/or autonomic regulation after brain or spinal cord injury. Candidates should have an M.D. and/or Ph.D. degree and demonstrated productivity in their graduate, postdoctoral, and/or early faculty research careers. It is expected that a strong extramurally funded research program will be developed. The successful candidate will join a highly collaborative and productive faculty with strengths in molecular, cellular, and rehabilitative aspects of SCI. Outstanding clinical, rehabilitation and basic science facilities will facilitate new collaborations. This tenure track position is supported by a substantial endowment to be used at the discretion of the successful candidate with the potential to become an endowed chair at tenure. Membership in the graduate faculty will be through a secondary appointment in an appropriate basic science department.

Submit curriculum vitae, statement of research interests, contact information for four references to **Mr. Jeffrey Leis, Unit Business Manager, Dept. Neurological Surgery, University of Louisville, 401 E. Chestnut St., Suite 580, Louisville, KY 40292** or submit e-mail application to **jeffrey.leis@louisville.edu**. Applications will begin to be evaluated on **April 4, 2011**. Search will close **June 1, 2011**.

Equal Employment Opportunity. The University of Louisville is an Affirmative Action, Equal Opportunity, Americans with Disabilities Employer, committed to diversity and in that spirit, seeks applications from a broad variety of candidates.

FACULTY POSITIONS IN PLANT AND MICROBIAL BIOLOGY

The Institute of Plant and Microbial Biology, Academia Sinica, Taipei, Taiwan, is inviting applications for several research-oriented faculty positions at the levels of Assistant, Associate, and Full Research Fellow (equivalent to Assistant, Associate, and Full Professor at a university). Successful candidates must have demonstrated expertise in studies of plant-microbe interaction OR the mechanisms of plant function. Excellent facilities and starter funds will be provided for the new fellows. Please visit the websites for details of the Institute (**http://ipmb.sinica.edu.tw/**) and Academia Sinica (**http://www.sinica.edu.tw/**). Applicants are expected to have a Ph.D. degree plus postdoctoral training. Chinese Language is not essential. International scientists are encouraged to apply. The application folder should include curriculum vitae, a statement of research accomplishments, and research plans. The application folder and, separately, three letters of recommendation should be sent to Drs. Shu-Hsing Wu and Wolfgang Schmidt, Co-chairs of Search Committee, Institute of Plant and Microbial Biology, Academia Sinica, 128, Sec 2, Academia Rd, Nankang, Taipei, Taiwan 11529. E-mail: **wsearch@gate.sinica.edu.tw** Fax: (+886)2-2782-1605. The review of applications will begin on May 15, 2011 and continue until the positions are filled.

BIO-PROCESSING UNIT
(NATIONAL AGRI-FOOD BIOTECHNOLOGY INSTITUTE)

(An Autonomous Institute of Department of Biotechnology, Ministry of Science and Technology, Government of India)
C-127, Industrial Area, S A S Nagar, Phase 8, Mohali, Punjab, India-160071

CHIEF EXECUTIVE OFFICER

(Advt. No.BPU-1/2011)

The Department of Biotechnology, Government of India has established an agri-food cluster in the "Knowledge City", at Sector-81, SAS Nagar, Mohali, Punjab. We are looking for a dynamic **CEO** to spearhead the establishment of a Bio-Processing Unit (BPU) in the cluster.

The BPU shall link the innovations and emerging technologies with entrepreneurs in the area of bioprocess applications for enhancing the value of agri-products. It will function in close linkage with other institutes, and agri-food industry as a 'Not-for-Profit Company' and aim at becoming self-sufficient through 'Fee-for-Service' and private equity.

This is a position of highest leadership (at the basic pay Rs.80000/- per month with allowances, perks and benefit sharing as per Government of India norms). **Interested candidates may visit www.nabi.res.in for details and apply as per format or be nominated by April 30, 2011 to the following address:**

Executive Director, National Agri-Food Biotechnology Institute, C-127, Phase-8, Industrial Area, SAS Nagar, Mohali-160071, Punjab, India. Phone No.0172-2290100; Fax No. 0172-4604888. E-mail: edoffice-ceobpu@nabi.res.in. A format for the application and other details can be taken from www.nabi.res.in.

Imperial College London

Faculty of Medicine

Chair or Reader in Preclinical Imaging and Physiology

A competitive salary will be agreed depending on qualifications and experience. The minimum salary for a Professor is £66,830 p.a. and for a Reader is £52,400 p.a.

The Faculty of Medicine of Imperial College London wishes to invite applications for a Professor or Reader in Preclinical Imaging and Physiology, based on the Hammersmith campus. The successful applicant will be appointed in the National Heart and Lung Institute (NHLI), if a cardiovascular researcher, or in alternative departments as most appropriate. The Faculty of Medicine is organised into six Schools, Institutes and Departments (SIDs), details of which can be found at http://www1.imperial.ac.uk/medicine/divisions

The post will be full-time and will provide a leadership role for large mammal research and education by investigators throughout Imperial College London.

The post holder will be responsible for initiating and sustaining research in the new Preclinical Imaging Centre (PCIF), based on the Hammersmith campus. This was commissioned in 2010 and houses an angiography suite integrated with 3T MRI, as well as an integrated PET-CT and a state-of-the-art facility comprised of a digital Siemens Artis Zee fluoroscopy system with full haemodynamic monitoring. In addition to its local role, the PCIF is intended to provide a national facility for large mammal research, in particular using porcine and ovine *in vivo* models, with users drawn both from academia and industry.

The successful candidate will be a leader in the field of large mammal physiology, with extensive research experience, including hands on experience of acute and chronic animal models of cardiovascular disease. The post holder will also be expected to have hands on experience in one or more of the following: animal imaging with MRI, PET-CT or percutaneous cardiovascular catheterisation. The successful candidate will also have gained high achievement in a chosen field, reflected in national and international reputation.

A proven record of extensive publications and successful research funding is essential, as is experience of undergraduate and postgraduate teaching, and with also a proven ability to supervise research staff and students.

Evidence of successful management at a group/departmental level should be demonstrated. Experience within subject specialism, supported by relevant qualification (PhD plus optional teaching qualification) is required. The successful candidate will also have substantial quality and quantity of research output.

The appointed individual will be expected to develop a personal program of competitive, peer-reviewed research relevant to the Institute's cardiovascular strategy, and also to champion, facilitate and promote the use of the PCIF both within Imperial College London and by appropriate external users. You will play a major role in enabling the translation of biomedical research outcomes from rodents into clinical research and eventually clinical practice.

The level of the appointment will be determined by the appointed candidate's level of attainment.

For informal enquiries please contact Professor Michael D. Schneider on +44 (0)207 594 3027; e-mail: m.d.schneider@imperial.ac.uk

Our preferred method of application is online via our website at the following link: http://www3.imperial.ac.uk/employment (select "Job Search"). Please complete and upload an application form as directed and submit any other relevant supporting documents such as your full CV. **Please quote reference number: RB016-11.**

Alternatively, you may e-mail your application and CV to Maria Monteiro; m.monteiro@imperial.ac.uk; tel: +44 (0)207 594 5498.

Stonewall TOP 100 EMPLOYERS 2011

Closing date: 7 June 2011.

Committed to equality and valuing diversity. We are also an Athena Silver SWAN Award winner and a Stonewall Diversity Champion.

Yale CANCER CENTER
A Comprehensive Cancer Center Designated by the National Cancer Institute

SMILOW CANCER HOSPITAL AT YALE-NEW HAVEN

Yale Cancer Center
Cancer Biology Institute

The Yale Comprehensive Cancer Center, its brand new Cancer Biology Institute, and the Yale School of Medicine invite applications from basic science investigators for junior or senior appointments with interests in cancer biology, in the areas of cancer genetics and genomics, signal transduction, structural biology, proteomics, and mass spectrometry, as well as drug discovery. The Cancer Biology Institute is one of 5 newly formed multi-disciplinary research institutes at Yale's West Campus, a 136 acre parcel located 7 miles from Yale's New Haven campus that includes 20 buildings and 1.6 million square feet of research, office, and warehousing space. Additional West Campus assets include the Institute of Chemical Biology, Institute of Microbial Diversity, Institute of Systems Biology, Institute of Biodesign, as well as core facilities in high throughput cell biology, small molecule discovery, and genomic analysis. The position will have a role in defining and implementing the vision for cancer biology research at Yale going forward. This includes developing translational research opportunities with the recently opened Smilow Cancer Hospital at Yale-New Haven. Appointment at Yale Medical School is available in a number of departments and will be commensurate with a demonstrated record of scholarly achievement. Of particular importance is experience in one or more of the following; a record of original research in cancer biology, independent extramurally funded laboratory investigation for senior applicants, engagement in translational research activities, and/or the development of strong cooperative teams across disciplines. Women and minority candidates are urged to apply.

Please submit a letter describing qualifications, with a CV and three letters of reference by [30 days from publication date] to: **Dr. Joseph Schlessinger, Director, Cancer Biology Institute, Yale Cancer Center, c/o Vickie Johnson, 333 Cedar St., PO Box 208028, New Haven, CT 06520-8028**.

Yale University is an Equal Opportunity/Affirmative Action Employer.

NATIONAL AGRI-FOOD BIOTECHNOLOGY INSTITUTE

Department of Biotechnology, Govt. of India C-127, Phase-VIII, Industrial Area, SAS Nagar, Mohali-160071 (PUNJAB), India

DEANS: Three Posts – Direct Recruitment or Deputation

(Advt. No.NABI-5/2011)

The Department of Biotechnology, Government of India has established National Agri-Food Biotechnology Institute (NABI) in the 'Knowledge City' at Mohali, Punjab. The institute will establish three Centres of Excellence for research and for preparing human resource with expertise in high-end knowledge and technology at the interphase of agriculture, food and nutrition.

NABI invites applications and nominations for the position of Deans in three departments. The Deans will be responsible for the development of centres for knowledge creation and high learning at NABI.

(i) Dean, Department of Agricultural Biotechnology
(ii) Dean, Department of Food Biotechnology
(iii) Dean, Department of Nutritional Biotechnology.

The positions are in PB-4 in the Scale Rs. 37400-67000 plus Grade pay 12000 plus allowances and IP related benefits as per government norms. Interested candidates may visit www.nabi.res.in for details and apply or be nominated by April 30, 2011 to the following address:

Executive Director, National Agri-Food Biotechnology Institute, C-127, Industrial Area, Phase-8, SAS Nagar, Mohali-160 071, Punjab, India. Fax No. 0172-4604888. E-mail edoffice-deannabi@nabi.res.in. A format for the application and other details can be taken from www.nabi.res.in.

Get a Career Plan that Works.

An exceptional career requires insightful planning and management. That's where *Science* Careers comes in. From job search to career enhancement, *Science* Careers has the tools and resources to help you achieve your goals. Get yourself on the right track today and get a real career plan that works. Visit **ScienceCareers.org**.

Science Careers
From the journal *Science* AAAS

ScienceCareers.org

NATIONAL AGRI-FOOD BIOTECHNOLOGY INSTITUTE

(Dept. of Biotechnology, Ministry of Science & Technology, Govt. of India)

SCIENTISTS IN FOOD AND NUTRITIONAL BIOTECHNOLOGY AND BIOINFORMATICS – DIRECT RECRUITMENT OR ON DEPUTATION

(Advt. No. 3/2011)

The Department of Biotechnology, Government of India has established National Agri-Food Biotechnology Institute (NABI) in the 'Knowledge City' at Mohali, Punjab. The institute nurtures skills and state-of-art infrastructure for plant genomic, nutritional and food science research. The research programmes are meant to catalyse knowledge-driven growth of agri-food sector in India.

A number of positions for faculty at several levels of seniority are available in the areas of nutritional biotechnology, genomics, nanoscience and bioinformatics applications to food science. Scientists with creativity, and drive for applied research may apply individually or as teams in the specified areas of research.

Interested candidates may visit **www.nabi.res.in** for details and apply or be nominated by April 15, 2011 to the following address:

Executive Director, National Agri-Food Biotechnology Institute, C-127, Industrial Area, Phase-8, SAS Nagar, Mohali-160071, Punjab, India. Fax No: 0172-4604888. E-mail: **edoffice@nabi.res.in**. A format for the application and other details can be taken from **www.nabi.res.in**.

Call for applications for the positions of Research Scientist Permanent position, RIKEN, JAPAN

RIKEN has openings for research scientists at the following laboratories.

1. Quantum Metrology Laboratory
http://www.riken.jp/engn/r-world/info/recruit/k110615_e_asi.html

2. Cellular Memory Laboratory
http://www.riken.jp/engn/r-world/info/recruit/k110615_e_asi_2.html

3. Spin-Isospin Laboratory
http://www.riken.jp/engn/r-world/info/recruit/k110615_e_rnc.html

4. Quantum Hadron Physics Laboratory
http://www.riken.jp/engn/r-world/info/recruit/k110615_e_rnc_2.html

[Application] The required documents differ according to the laboratory. Refer to the each URL mentioned above for more details.

[Deadline] 5pm on Wednesday June 15, 2011 (Japan Standard Time)

[Start of Employment] April 1, 2012 or later, but negotiable.

http://www.riken.jp/engn/r-world/info/recruit/index.html

QUINNIPIAC UNIVERSITY FACULTY OPENINGS

WE'RE BUILDING A MEDICAL SCHOOL FROM THE GROUND UP—JOIN US.

An exciting opportunity is unfolding at Quinnipiac University. Work has begun on our School of Medicine, and we are looking for people who will join us in first developing and then implementing a program of study that is not just practical, relevant, and comprehensive, but visionary as well. We are committed to creating a School of Medicine that embraces our core values—excellent academic programs, an environment that focuses on the student, and a strong sense of community.

We seek faculty members who are broadly trained in their disciplines and passionate about educational excellence: faculty members who can contribute to multi-discipline, integrated medical instruction in lectures, laboratories, and conferences as well as facilitate problem-based learning with small groups of students. We plan to welcome students in the Fall of 2013.

Currently, we are accepting applications for faculty positions within the Department of Basic Medical Sciences at the **PROFESSOR, ASSOCIATE PROFESSOR, AND ASSISTANT PROFESSOR LEVELS.** Previous experience in undergraduate medical education is required for consideration for appointment at the ranks of associate professor or professor. We are especially interested in receiving applications from individuals with broad training and experience in the basic medical sciences, including curriculum and course development Candidates must have training and experience in one of the following areas:

- **ANATOMY**
- **BIOCHEMISTRY**
- **CELL BIOLOGY**
- **GENETICS**
- **MOLECULAR BIOLOGY**
- **MICROBIOLOGY AND IMMUNOLOGY**
- **NEUROSCIENCES**
- **PATHOLOGY**
- **PHARMACOLOGY**
- **PHYSIOLOGY**
- **BEHAVIORAL SCIENCE**

Applicants should submit a letter of interest, a curriculum vitae, a statement describing your teaching philosophy, a statement of plans for ongoing scholarly activity, and at least three references with complete contact information.

For complete job description and to apply, please visit
http://www.quinnipiac.edu/medschool.xml

Just 90 minutes from New York City and two hours from Boston, Quinnipiac University is a private, coeducational university with 5,900 undergraduate and 2,000 graduate students. Consistently ranked among the best universities by U.S. News & World Report. The Medical School is located at Quinnipiac's North Haven, Connecticut campus—already home to all of the School of Health Sciences' programs. For more information about our plans for Quinnipiac University's School of Medicine, please visit our website at www.quinnipiac.edu.

Quinnipiac University has a strong commitment to the principles and practices of diversity throughout the University community. We welcome candidates who would enhance that diversity.

FACTS & FICTION

Careers in Industry and Academia

Trying to figure out the next step in your career? Join us for a roundtable discussion that will look at facts and fiction surrounding academic and industry career options for PhD-level scientists. Get some nuts and bolts advice on how to research career options, what questions to ask, and how to best prepare for various careers.

- Do industry and academic careers require different skill sets?
- Do industry jobs have better compensation? Less autonomy?
- Do academic scientists have less work/life balance?

For answers view our roundtable discussion for free at:

ScienceCareers.org/webinar

Science Careers
From the journal *Science* AAAS

Produced by the *Science*/AAAS Business Office.

Nontraditional Careers: Opportunities Away From the Bench

Webinar

Want to learn more about exciting and rewarding careers outside of academic/industrial research? View a roundtable discussion that looks at the various career options open to scientists and strategies you can use to pursue a nonresearch career.

Now Available On Demand
www.sciencecareers.org/webinar

Produced by the *Science*/AAAS Business Office.

Science Careers
From the journal *Science* AAAS

POSITIONS OPEN

Cornell Laboratory for Accelerator-based Sciences and Education (CLASSE)

SENIOR RESEARCH ASSOCIATE
Cornell Laboratory for Accelerator-based Sciences and Education

The Cornell Laboratory for Accelerator-based Sciences and Education (CLASSE) seeks an individual to take a lead role in the management and development of major accelerator systems. The specific research and development activities will be in one of the accelerator-associated fields that are part of the mission of CLASSE (X-ray science, accelerator science, or elementary particle physics). These activities will be determined in consultation with the CLASSE Director, to whom this position reports. Duties will also include overseeing accelerator radiation protection and safety systems; performing radiation shielding calculations using Monte Carlo codes such as MARS, FLUKA, EGS5, or MCNPX; calculating radioactivity induced in materials by stray radiation fields around electron accelerators; assessing radiation damage in electronics; making measurements of photon and neutron spectra over a wide energy range; and reviewing and approving safety analysis documents for laboratory operations, working with staff at all levels to analyze and set procedures for unusual or new safety issues.

Requirements: A Ph.D. in one of the physical sciences or engineering, and several years of experience in experimental high-energy accelerator physics or nuclear science and engineering. Must be familiar with biological effects from natural and man-made sources of environmental radioactivity; federal, state, and local laws governing radiation; photon and neutron dosimetry; and occupational, chemical, biological, and laser safety. A high level of people skills and mature judgment are essential.

Please send a cover letter, including curriculum vitae and a publications list to **Dr. Maury Tigner,** Newman Laboratory, Cornell University, Ithaca, NY 14853, and arrange for three letters of recommendation to be sent. Correspondence may be directed to **e-mail: search-classe@cornell.edu.** *Cornell University is an Equal Opportunity/Affirmative Action Educator and Employer.*

POSTDOCTORAL FELLOW positions are available at University of California, Los Angeles (UCLA) to study chromatin remodeling in cardiovascular disease. Ongoing research projects are examining the role of histone variants, global chromatin structure, and histone modifying enzymes in controlling complex cardiac phenotypes during health and disease. The projects employ a systems approach utilizing proteomics, genomics, network biology, imaging, and animal/cell physiology. Strong collaborations exist in this highly creative environment, which spans multiple basic and clinical Departments at UCLA, and training opportunities exist in the aforementioned high throughput biology techniques as well as in cardiovascular physiology. Successful candidates should have a Ph.D. or MD, exceptional motivation, and demonstrated research experience in chromatin regulation and/or proteomics/genomics. Individuals with extensive credentials in molecular imaging in eukaryotes are also encouraged to apply. Please send curriculum vitae, cover letter, and contact information for three references to: **Thomas Vondriska, Ph.D.** (**e-mail: tvondriska@mednet.ucla.edu**).

MEDICAL SCHOOL FACULTY POSITIONS

The Saint James School of Medicine, an international medical school (**website: http://www.sjsm.org**), invites applications from candidates with teaching and/or research experience in any of the basic medical sciences for its Caribbean campuses.

SENIOR FACULTY positions currently available in Pharmacology, Biochemistry, and Physiology. Applicants must be M.D., D.O., and/or Ph.D.

Teaching experience in the U.S. system is desirable but not required. Retired persons are encouraged to apply. Attractive salary and benefits. Submit curriculum vitae electronically to **e-mail: sjsmcoordinator@sjsm.org** or mail to: **HRDS Inc., 1480 Renaissance Drive. Suite 300, Park Ridge, IL 60068.**

POSITIONS OPEN

ANATOMY FACULTY

The Basic Sciences Division, Osteopathic Medical Program of the Georgia Campus of Philadelphia College of Osteopathic Medicine (625 Old Peachtree Road NW, Suwanee, Georgia) seeks a full-time anatomist at the **ASSOCIATE PROFESSOR** level.

Duties include: teaching in the anatomical sciences including gross anatomy, histology, and embryology; serving in leadership and membership capacities on committees; actively pursuing scientific research or other scholarly activity; participating in professional and scientific meetings; preparing and delivering presentations; evaluating student progress; communicating evaluations to students and administrative/faculty members; publishing results of scientific research or other scholarly activity in professional journals.

Candidates must have five to eight years of experience, be capable of teaching medical gross anatomy, including dissection instruction in a cadaver-based laboratory. Teaching experience in histology and embryology preferred, with experience in neuroanatomy/biomechanics/kinesiology is strongly preferred.

This position offers a competitive salary and an excellent benefits package. The minimum level of formal education required for this position is an earned doctorate (i.e., Ph.D., D.O., M.D.) in an appropriate or related field.

Applicants should submit curriculum vitae that include the names of three references and a description of teaching experience to: **Rita C. Forde, Director of Human Resources, Philadelphia College of Osteopathic Medicine, 4190 City Avenue, Philadelphia, PA 19131. E-mail: ritaforde@pcom.edu.**

PCOM is an Equal Opportunity Employer.

MARKETPLACE

2012 AAAS ANNUAL MEETING
16–20 February ▸ Vancouver, Canada

Call for Symposium Proposals

Flattening the World: Building the 21st Century Global Knowledge Society

We live in a time when collaborations between countries and continents have never been easier, at least from a technical standpoint. A stunning example is the Large Hadron Collider, which is being used by a multinational group of physicists to understand the fundamental building blocks and laws of nature, from subatomic to cosmic. Stores of information and knowledge can be accessed from anywhere by anyone. Remote sensing technology enables the detailed observation of virtually every aspect of our planet's surface, subsurface, and climate. Technology and the Internet are transforming education. Learning is, in principle, available to everyone everywhere.

The 21st century is shaping up to be a challenging one. The issues that face us are many: climate change, energy, agriculture, health, water, biodiversity and ecosystems, population growth, and economic development. The 2012 program will focus on the complex challenges of the 21st century that are both global in their scope and profoundly interconnected as well as ways to tackle them on a global scale through international, multidisciplinary efforts.

Symposium proposals for the 2012 meeting are now being solicited. To submit a proposal, visit **www.aaas.org/meetings**. The deadline for submission is Tuesday, 26 April 2011.

Call for Poster Submissions

Student Poster Competition

Open to college undergraduate and graduate students only

The competition recognizes the individual efforts of students who are actively working toward a college-level degree. Winners in each category receive a cash award and framed certificate, and are listed in *Science*.

General Poster Session

Open to postdocs and professionals

This session provides an opportunity for postdocs and professionals to present their research to the broad community of scientists attending the AAAS Annual Meeting.

Information about the call for poster submissions for the 2012 Annual Meeting will be available at **aaas.org/meetings** on 12 May 2011.

AAAS
ADVANCING SCIENCE, SERVING SOCIETY

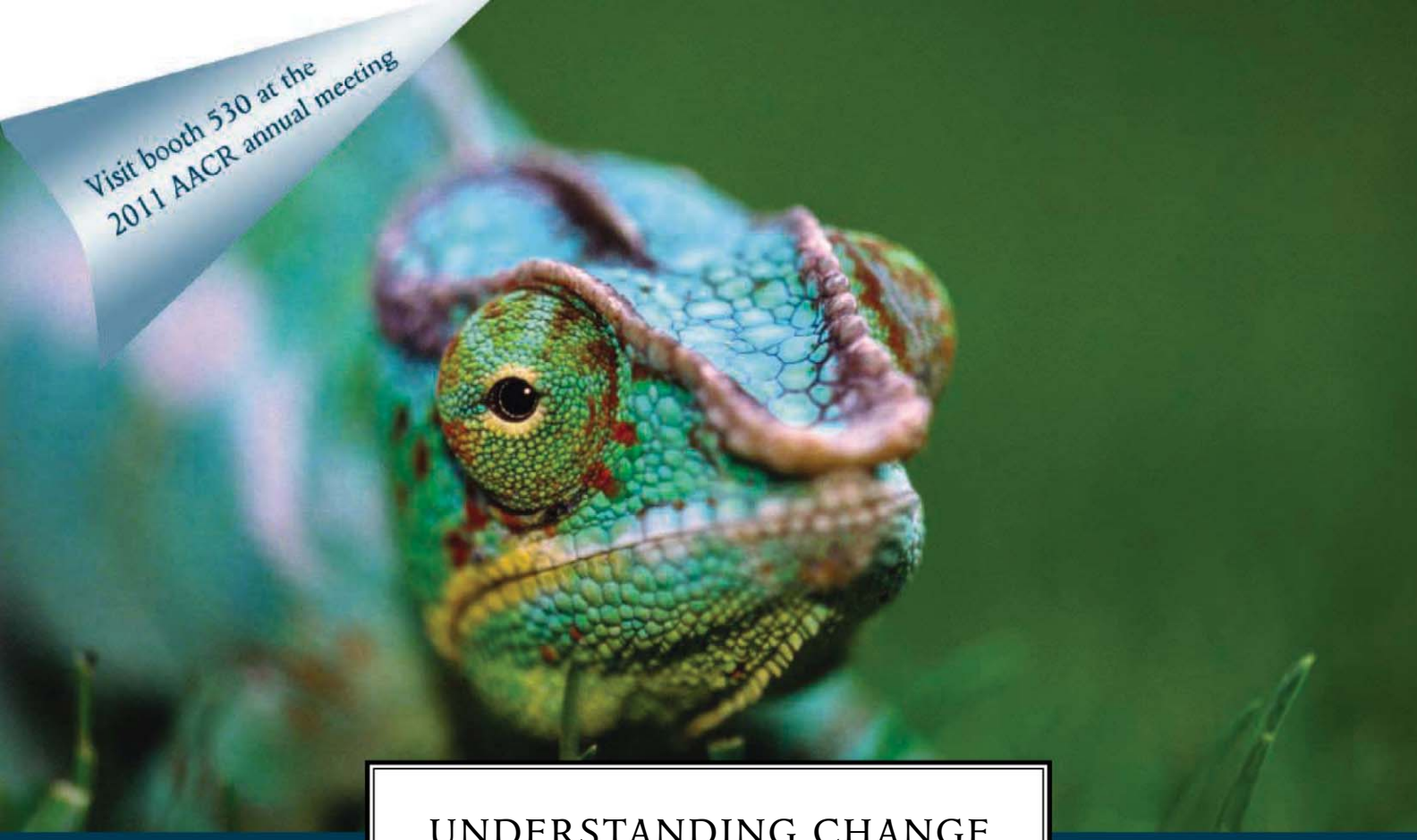

UNDERSTANDING CHANGE

Streamline epigenetics research with EpiMark™

When looking to simplify epigenetics studies, turn to EpiMark™ validated reagents from New England Biolabs. This suite of products is designed to address some of today's challenges when studying histone and DNA modifications, and expands the potential for biomarker discovery.

Identify and quantitate methylation states with the EpiMark™ 5-hmC and 5-mC Analysis Kit

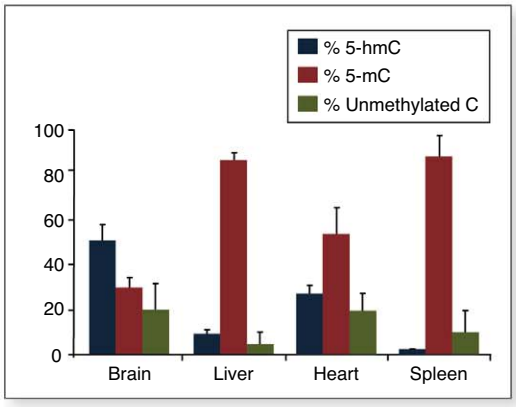

Analysis of the different methylation states in Balb/C mouse tissue samples shows a variation in the amount of 5-hmC present at locus 12.

New products:

- Novel kit for 5-hmC and 5-mC analysis
- Highly sensitive method for enrichment of methylated DNA
- Recently discovered methylation-dependent restriction enzymes
- New hot start polymerase and conversion kit for bisulfite sequencing

For more information, visit **www.epimark.com**

NEW ENGLAND BioLabs® Inc.
enabling technologies in the life sciences

www.neb.com